Microstructurally Controlled Mechanical Properties of Al-Mg-Si Alloys for Warm Forming Applications

PhD thesis

Manojit Ghosh

Delft University of Technology

Microstructurally Controlled Mechanical Properties of Al-Mg-Si Alloys for Warm Forming Applications

Proefschrift

ter verkrijging van de graad van doctor
aan de Technische Universiteit Delft,
op gezag van de Rector Magnificus prof. ir. K.C.A.M. Luyben,
voorzitter van het College voor Promoties,
in het openbaar te verdedigen op woensdag 6 april 2011 om 10.00 uur

door

Manojit GHOSH

Master of Technology in Metallurgical Engineering
Indian Institute of Technology, Kharagpur, India
geboren te Kolkata, India

Dit proefschrift is goedgekeurd door de promotor:

Prof. dr. ir. L.A.I. Kestens

Samenstelling promotiecommissie:

Rector Magnificus, voorzitter

Prof. dr. ir. L.A.I. Kestens, Technische Universiteit Delft, promotor

Prof. ir. L. Katgerman, Technische Universiteit Delft

Prof. dr. ir. J. Sietsma, Technische Universiteit Delft

Prof. dr. ing. B. Holmedal, Norwegian University of Science and Technology, Noorwegen

Dr. ir. A. Van Bael, Katholieke Universiteit Leuven, België

Dr. ir A.H. van den Boogaard, Universiteit Twente

Dr. A. Miroux, Materials innovation institute

Prof. dr. I.M. Richardson, Technische Universiteit Delft, reservelid

My Mother and Alexis

CONTENTS

_____

ACKNOWLEDGEMENTS
_____

xi

Microstructurally Controlled Mechanical Properties of Al-Mg-Si Alloys for Warm Forming Applications

_____

SUMMARY

_____

Aluminium and its alloys are mainly handicapped by poor room temperature formability compared to steel. Owing to their light weight and excellent corrosion resistance the use of aluminium alloys in automobile industries is increasing progressively. Therefore, the main challenge to the extension of aluminium alloys application is the improvement of their formability. Sheet forming at warm temperature has been reported as one of the promising solutions of the formability problem. Warm forming may reduce the flow stress and rate of work hardening and can improve ductility and toughness. Warm forming investigations on 5xxx aluminium alloys showed considerable improvement of drawability. 5xxx alloys, however, can only be hardened by strain hardening and they suffer from stretcher strain. Precipitation hardened alloys like 6xxx aluminium alloys may offer a promising alternative since they are free of Lüdering along with the possibility of strengthening by control of precipitates. Although 6xxx aluminium alloys are not the strongest among the aluminium alloys, still they contribute the maximum share of aluminium products. Nearly 90% of the aluminium extrusions are with 6xxx aluminium alloys. Unfortunately little is known about warm forming of 6xxx. This was the primary motivation for the present investigation. Finite element models (FEM) became a common tool to simulate forming operations. Information about the material work hardening and plastic anisotropy is required for the simulation and is obtained from experimental measurement or other numerical models. Since temperature influences the material response in a complex way, its effect needs to be included in the models for accurate simulation. Therefore, the objective of this work was first to experimentally study the mechanical behaviour of 6xxx aluminium alloys from room temperature to 250°C and then to develop temperature dependent numerical models for work hardening and plastic anisotropy that can be linked to FEM. Deep drawing of cylindrical cups is used to illustrate the performance of the coupled models.

Two aluminium alloys were used during this investigation. 6016 with Si excess (Mg/Si=0.4 in wt.%) is considered as one of the promising alloys while the other alloy, 6061, is balanced in terms of Si and Mg content. Chapter 2 deals with the characterization of the as-received materials. The two as-received recrystallized alloys were found similar in respects to grain size distribution, nature and distribution of constituent particles, and crystallographic texture. The main

difference among them was in chemical composition and small precipitate distribution. This difference is visible in the ageing kinetics measured by hardness tests during artificial isothermal ageing at 150°C, 180°C and 250°C.

The procedure for the mechanical tests used for the present investigation is described in chapter 3. Tensile and plane strain compression (PSC) tests were performed using the Gleeble 3800 at Delft University of Technology. Deep drawing (DD) tests were done at TNO Science and Industry, Eindhoven, while the bi-axial (BA) tests were done at Tata Steel (at the time of the tests Corus) Research Development and Technology, IJmuiden. In section 3.2 the description of the tensile specimen, test procedure, temperature distribution inside the deformation zone and accuracy of the tests is discussed. Same issues are addressed for PSC, DD and BA tests in section 3.3, section 3.4 and section 3.5. It has been observed that all tests were highly repeatable.

The effect of solutes and precipitates on strength and work hardening is investigated experimentally in chapter 4 by varying temper state, holding time before deformation, alloy composition and strain rate. The observed higher work-hardening rate for naturally aged material (T4) compared to artificial aged one (T6) could be explained as the result of solute depletion during ageing. The effect is more pronounced with increasing temperature. Higher yield strength for T6 specimens compared to T4 ones could be related to the presence of stronger precipitates after artificial ageing. Long holding time influences precipitate state and morphology in the same way than artificial ageing and thereby exhibit strength and work-hardening rate close to T6 state. In T4 condition, 6061 is stronger than 6016 during tensile and bi-axial experiments for all the respective temperatures, in line with hardness measurements. The effect of alloy composition in T6 state is, however, more complex as it also depends on the deformation temperature. Strain rate variations within the investigated range do not influence the flow stress at room temperature resulting in zero strain rate sensitivity. At higher temperatures the impact of strain rate was also small except for extremely slow deformation rate (0.0001 s^{-1}) in which evidences of dynamic precipitation has been noticed. During DD the punch force-punch displacement response was found consistent with ageing curves, i.e. W temper being the softest and T6 the strongest material. With longer holding time before drawing the initial force increase is steeper and interestingly the maximum force for all the curves was found to be the same.

In chapter 5 the influence of temperature and strain rate on work hardening is studied from tensile and deep drawing tests and subsequently the results were used to develop a temperature dependent work hardening model. The experimental results presented in section 5.3 show that both yield strength and work hardening rate decrease with increasing temperature and logically so does the punch force during DD. Microstructure evolution during deformation was also observed by Scanning

Electron Microscopy (SEM), Electron Back Scattered Diffraction (EBSD) and Gallium Enhanced Microscopy (GEM). The final purpose of this chapter was to propose a strain hardening model that can accurately simulate the material behaviour at various temperatures and strain rates. The *Nes* model was selected because it calculates the flow stress from a microstructure description similar to the one observed in aluminium alloys. The description of the work hardening model is presented in section 5.4. The original *Nes* model had been tested for different non heat-treatable aluminium alloys at room temperature only. For the present investigation this model needed to be extended to larger temperature range and to 6xxx series. The model has then been modified in terms of contribution of shearable precipitates to the yield strength and dislocation mean slip length. The transition radius shear-by pass has been fitted as a function of temperature as well as two solute content dependent parameters. Despite the limited number of fitted parameters the model was found to reproduce reasonably well the materials response during deformation.

Chapter 6 aims to generate a temperature dependent yield locus to be used as an input for FEM modeling. Therefore, the first objective of this chapter is to understand the anisotropic behaviour of heat treatable 6xxx aluminium alloys from room temperature to 250°C both from experiment and modelling results. The shape of the r-value profile measured from tensile testing (section 6.3.1) and the position and number of cup ears during DD (section 6.3.2) were found independent of forming temperature. The average r-value and ear amplitude, however, depend on temperature. Efforts have been made to investigate any textural change (section 6.3.3) during deformation that might be related to anisotropic effects. Although the deformed and initial textures are different for all modes of deformation, no significant effect of the deformation temperature on texture evolution could be observed. The possible activation of extra slip systems with increasing temperature has been determined from the analysis of EBSD maps and subsequently, this possibility has been implemented into a *crystal plasticity Visco-Plastic Self-Consistent (VPSC)* model. *VPSC* model successfully predicts the deformed texture after 35% PSC deformation at room temperature and 250°C for both alloys using the CRSS ratios of different slip systems determined after fitting the r-value profiles (section 6.5). Good match is obtained between the experimental and calculated yield locus at room temperature and the model is then used to predict the yield locus at 250°C (section 6.6).

The main objective of the project was to develop physically based models that should predict the work hardening and plastic anisotropy behaviour of 6xxx aluminium alloys, and that can be used as a potential resource for FE simulation of warm forming operation. Chapter 7 presents an example of such FE simulation applied to warm deep drawing of cylindrical cups. Finite element code DiekA

developed at University of Twente, The Netherlands, was linked with *Nes* and *VPSC* models. The punch force-punch displacement curves and cup thickness distribution predicted by the FEM for different conditions were compared with the experimental results. The simulation results show a good agreement with experiment and illustrate the potential interest of the modeling approach.

SAMENVATTING

Aluminium en zijn legeringen worden voornamelijk gehinderd door slechte vervormbaarheid bij kamer temperatuur in vergelijking met staal. Dankzij hun lage gewicht en uitstekende corrosie bestendigheid neemt het gebruik van aluminium in de automobielindustrie steeds verder toe. Daarom is het verbeteren van de vervormbaarheid de belangrijkste uitdaging om de toepasbaarheid van aluminium legeringen te vergroten. Het warm vervormen van plaatwerk wordt genoemd als een van de veelbelovende oplossingen voor het vervormbaarheidsprobleem. Warm vervormen kan de vloeispanning en verstevigingsnelheid verminderen en de vervormbaarheid en taaiheid verbeteren. warmvervormonderzoek naar 5xxx aluminium legeringen heeft een aanzienlijke verbetering van de trekbaarheid laten zien. 5xxx legeringen kunnen alleen verstevigd worden door vervorming, waarbij bandvorming aan het oppervlak optreedt. Precipitaat verstevigde legeringen, zoals de 6xxx aluminium legeringen, kunnen een veelbelovend alternatief zijn, aangezien *Lüder*-banden hier niet optreden, terwijl zij bovendien te verstevigen zijn door precipitaten. Hoewel 6xxx aluminium legeringen niet de sterkste zijn van de aluminium legeringen, hebben zij wel het grootste aandeel in de aluminium producten. Bijna 90% van de aluminium extrusies wordt gedaan met 6xxx aluminium legeringen. Helaas is weinig bekend over het warm vervormen van 6xxx. Dit was de primaire motivatie voor dit onderzoek. Eindige elementen modellen (EEM) wordt veel gebruikt om vormingsprocessen te simuleren. Informatie over de versteviging van het materiaal en de plastische anisotropie is benodigd voor deze simulaties. Deze informatie is verkregen door experimentele metingen of andere numerieke modellen. Omdat temperatuur de reactie van het materiaal op een complexe manier beinvloed, moet dit effect worden meegenomen in de modellen om te komen tot accurate simulaties. Daarom was het doel van dit onderzoek om eerst het mechanisch gedrag van 6xxx aluminium legeringen experimenteel te onderzoeken van kamer temperatuur tot 250°C. En daarna temperatuursafhankelijke numerieke modellen te ontwikkelen voor de versteviging en plastische anisotropie, die kunnen worden gekoppeld aan EEM. Dieptrekken van cilindrische bekers is gebruikt om de prestaties te laten zien van de gekoppelde modellen.

Twee aluminium legeringen zijn gebruikt tijdens dit onderzoek. 6016 met een Si overschot (Mg/Si = 0.4 in wt.%) wordt beschouwd als een veelbelovende legering, terwijl bij de andere legering, 6061, de hoeveelheid Si en Mg is gebalanceerd. Hoofdstuk 2 behandelt het karakteriseren van de ontvangen materialen. De twee ontvangen gerekristalliseerde legeringen waren gelijksoortig voor wat betreft de, type en verdeling van de al aanwezige deeltjes en kristallografische textuur. Het

belangrijkste verschil was de chemische samenstelling en de verdeling van de kleine precipitaten. Dit verschil is zichtbaar in de verouderingskinetiek, gemeten door hardheidstesten tijdens kunstmatig isotherm verouderen op 150°C, 180°C and 250°C.

De procedure voor de mechanische testen in dit onderzoek is beschreven in hoofdstuk 3. Trekproefen en plane strain compression (PSC) testen zijn uitgevoerd met de Gleebe 3800 op de Technische Universiteit Delft. Dieptrek (DT) tests zijn gedaan bij TNO Science and Industry, Eindhoven, terwijl de bi-axiale (BA) tests zijn gedaan bij Tata steel (op het moment van de tests Corus) Research Development and Technology, IJmuiden. In paragraaf 3.2 is het proefstuk voor de trekproef, de test procedure, de temperatuursverdeling in de deformatie zone en de accuraatheid van de tests besproken. Dezelfde zaken worden ook besproken voor de PSC, DT en BA tests in paragraaf 3.3, paragraaf 3.4 en paragraaf 3.5. Alle tests bleken in hoge mate herhaalbaar.

Het effect van opgeloste atomen en precipitaten op de sterkte en versteviging is experimenteel onderzocht in hoofdstuk 4 door het variëren van de ontlaten toestand, gloeitijd voor deformatie, legeringsamenstelling en reksnelheid. De waargenomen grotere verstevigingsnelheid voor natuurlijke veroudering (T4) vergeleken met de kunstmatige veroudering (T6) kan worden verklaard door de afname van opgeloste atomen ten gevolge van veroudering. Dit effect is sterker met toenemende temperatuur. De hogere vloeigrens voor het T6 proefstuk vergeleken met het T4 proefstuk kan gerelateerd zijn aan de aanwezigheid van sterkere precipitaten na kunstmatige veroudering. Een langere gloeitijd beïnvloedt de staat en morfologie van het precipitaat op dezelfde manier als kunstmatige veroudering en vertoont daarom een sterkte en verstevigingsnelheid die vergelijkbaar is met de T6 situatie. Onder T4 condities is 6061 sterker dan 6016 tijdens trekproef en bi-axiale experimenten voor alle respectievelijke temperaturen. Dit is in lijn met de hardheidsmetingen. Het effect van de legeringsamenstelling onder T6 condities is echter compliceerder, omdat het ook afhangt van de deformatietemperatuur. De onderzochte reksnelheden hebben geen invloed op de vloeispanning bij kamertemperatuur, dus de reksnelheidsgevoeligheid is nul. Op hogere temperaturen was het effect van de reksnelheid ook klein, behalve voor extreem langzame reksnelheden (0.0001 s^{-1}), waarbij tekenen van dynamische precipitatie zijn waargenomen. Tijdens DT was de kracht – verplaatsing respons consistent met de verouderingscurves, dat is W is het zachtste en T6 is het sterkste materiaal. Met langere gloeitijden voor het vervormen is de initiële kracht toename steiler. Opmerkelijk genoeg was het maximum kracht voor alle curves hetzelfde.

In hoofdstuk 5 is de invloed van temperatuur en reksnelheid op de versteviging onderzocht met trekproeven en dieptrektests en vervolgens zijn de resultaten gebruikt om een temperatuur afhankelijk verstevigingsmodel te ontwikkelen. De

experimentele resultaten gepresenteerd in paragraaf 5.3 laten zien dat zowel de vloeigrens als de verstevigingssnelheid afnemen met toenemende temperatuur en logischerwijze ook de kracht tijdens DT. De ontwikkeling van de microstructuur tijdens deformatie is ook onderzocht met Scanning Electron Microscopy (SEM), Electron Back Scattered Diffraction (EBSD) en Gallium Enhanced Microscopy (GEM). Het doel van dit hoofdstuk was om een verstevigingsmodel te ontwikkelen dat het materiaalgedrag op een accurate wijze simuleert bij verschillende temperaturen en reksnelheden. Het *Nes* model is gekozen omdat het de vloeispanning berekend op basis van een microstructuur, die vergelijkbaar is met de microstructuur van aluminiumlegeringen. De beschrijving van het verstevigingsmodel is gepresenteerd in paragraaf 5.4. Het oorspronkelijke *Nes* model is alleen getest op verschillende niet-warmte-behandelbare aluminium legeringen op kamertemperatuur. Voor het huidige onderzoek moest het model worden uitgebreid naar een groter temperatuursbereik en de 6xxx series. Het model is vervolgens aangepast voor wat betreft de bijdrage van afschuifbare precipitaten op de vloeigrens en de gemiddelde dislocatie glij-afstand. De straal waarbij dislocaties om het deeltje heen gaan is gefit als een functie van temperatuur en twee parameters afhankelijk van de hoeveelheid opgeloste atomen. Ondanks het beperkte aantal fit-parameters, was het model redelijk goed in staat de respons van het materiaal tijdens deformatie te voorspellen.

Het doel van hoofdstuk 6 is om een temperatuursafhankelijke vloeioppervlak te verkrijgen, die als invoer kan worden gebruikt voor EEM modeling. Daarom is het eerste doel van dit hoofdstuk om het anisotropische gedrag van warmte behandelbare 6xxx aluminium legeringen te begrijpen van kamertemperatuur tot 250°C, zowel via experimentele als modelleer resultaten. De vorm van het r-waarde profiel gemeten met rekproeven (paragraaf 6.3.1) en het aantal en de positie van de oren tijdens DT (paragraaf 6.3.2) was onafhankelijk van de vormingstemperatuur. Echter, de gemiddelde r-waarde en oor amplitude hangen af van temperatuur. Er zijn pogingen zijn gedaan om textuurveranderingen (paragraaf 6.3.3) tijdens deformatie te onderzoeken, die gerelateerd kunnen zijn aan anisotropische effecten. Hoewel de gedeformeerde en initiële textuur verschillend zijn voor alle deformatie modes, is er geen significant effect van de deformatietemperatuur op de textuurevolutie waargenomen. De mogelijke activatie van extra glijsystemen met toenemende temperatuur is bepaald door middel van EBSD maps en vervolgens is deze mogelijkheid geïmplementeerd in een *kristalplasticiteit Visco-Plastic Self-Consistent (VPSC)* model. Het *VPSC* model voorspelt met succes voor beide legeringen de gedeformeerde textuur na 35% PSC deformatie op kamertemperatuur en 250°C, gebruik makende van de CRSS ratio's van verschillende glijsystemen, die bepaald zijn na het fitten van de r-waarde profielen (paragraaf 6.5). Een goede match is verkregen tussen het experimentele en berekende vloeioppervlak op kamer

temperatuur. Het model is vervolgens gebruikt om het vloei-oppervlak te voorspellen op 250°C (paragraaf 6.6).

Het belangrijkste doel van het project was om een fysisch gebaseerd model te ontwikkelen dat de versteviging en het plastische anisotropie gedrag van 6xxx aluminium legeringen kan voorspellen, en dat kan worden gebruikt als een potentiële bron voor een FE simulatie van een warmvormingsoperatie. Hoofdstuk 7 presenteert een voorbeeld van een dergelijke FE simulatie, toegepast op warm dieptrekken van cilindrische bekers. Het eindige elementen programma DiekA, ontwikkeld aan de Universiteit Twente, Nederland, is gekoppeld aan *Nes* en *VPSC* modellen. De kracht – verplaatsing curves en bekerdikte verdeling die voorspeld zijn door het EEM voor verschillende condities zijn vergeleken met de experimentele resultaten. De simulatieresultaten vertonen een goede overeenkomst met de experimenten en illustreren het mogelijke belang van deze modelmatige benadering.

Chapter 1

INTRODUCTION

1.1 Warm Forming of Aluminium Alloys

The demand for aluminium alloys has been increasing in brisk pace in recent years in automotive industries owing to their light weight and corrosion resistance. For instance, the use of aluminium sheet material for typical automobile body could provide a mass reduction of up to 50pct compared to current steel construction. However, despite having high strength to weight ratio aluminium and its alloys are lagging far behind in this sector primarily because of their poor formability at room temperature [1] which is approximately 2/3 of that of steel. Improvement of formability is of special interest for the automotive industries, where weight reduction is compulsory on the one hand and panels have intricate shapes on the other hand. Super plastic aluminium alloys can address this issue by offering extremely high tensile ductility but with the drawback of high material cost, low production rates and requirement of new forming equipment. Recent investigations into the phenomenon of increased tensile ductility of Al-Mg and Al-Mg-Si alloys showed a practical alternative to superplasticity. It has been documented [2] that the room temperature tensile elongation is at a minimum, as compared to both cryogenic and elevated temperatures [3]. At cryogenic temperatures the increment of tensile elongation of many aluminium alloys is attributed mainly to the enhancement of work hardening and the same effect at elevated temperatures is principally due to increased strain rate hardening. Forming at elevated temperature seems one of the most promising solutions [4] because forming at cryogenic temperature needs higher energy consumption and leads to increased spring back compared to elevated temperature deformation. The interest towards warm forming also derives from the reduction in flow stress, increase in ductility and increase in toughness of the material when compared with cold forming. Moreover, for temperatures lower than those involved during hot forging it is easier to obtain close tolerance and high quality surface finish. Increasing formability by warm forming is still a challenge to the industry. This process is industrially more challenging and more complex in terms of the microstructure-mechanical behaviour relationship. In elevated

temperature forming the most important issue is the selection of the temperature range. There should be few structure changes and almost a stable microstructure during operation. Hot forming is accompanied by significant structural changes associated with deformation-induced recrystallization and growth of grains or particles. In addition, creep may affect the forming deformation and cavitations at the grain boundaries can lead to permanent failure at low strain rate. So, warm forming is preferable for aluminium alloys compared to hot forming in order to improve the room temperature formability.

Forming of aluminium alloys at elevated temperatures has been reported by many researchers [5-10] but mostly on 5xxx series alloys. Finch **[5]** investigated the potential of warm forming by deep drawing of both rectangular and circular cups from annealed and hardened aluminium alloy sheets early in 1946. Their results showed significant improvement in the drawability (in terms of cup height) at a relatively moderate temperature of about 150°C even for the precipitation hardened alloys (like 2024-T4 and 7075-T6). In the 1950's an aluminium alloy containing 3-4% Mg was generally employed for warm press forming panels for the more expensive ranges of cars. In the 1970's it was discovered that an aluminium-6% Mg alloy could give a total elongation of about 300% at about 250°C at an appropriate strain rate. It was observed that [7-8] the cup height increased with increasing forming temperature and / or decreasing punch speed for an Al–2Mg and 5182-O alloy. Warm forming of alloy 5182-O at 120°C was successfully used by General Motors [9] to produce inner door panels and a V-6 oil pan at commercial press speeds, by heating both the die and the blank and using a mica lubricant and a MoSi2/graphite release agent. According to their results, some precipitation hardened alloys could also be warm formed successfully to produce components at 250°C at a cycling rate of 5 parts/min. The optimum forming temperatures were found to be 200°C and 250°C for the precipitation hardened and the strain hardened alloys, respectively. In a more recent study with 5083, Tetsuo and Fusahito [10] found that the limit drawing ratio increases with increasing die temperature and decreases with increasing forming speed. Bolt and his co-workers [11] also conducted comparative warm drawing tests on 5754 and 6016. They concluded that warm forming offers a good possibility for drawing complicated aluminium sheet products which cannot be made at room temperature without extra forming or joining operation. They also found that the minimum die temperature required for a significant deeper product is lower for the 6016-T4 compared to 5754-O alloy. At a temperature of 175°C the increase in maximum height for 6016-T4 is 30% while it is only 11% for 5754-O.

Although 5xxx series alloys exhibit higher strength than 6xxx alloys in annealed condition they suffer from the problem of dynamic strain ageing effects resulting in stretch marks, which affect the surface quality. Also they are not heat treatable and

can only be hardened by mechanical working. On the other hand, 6xxx alloys are heat treatable and free of Lüdering. This arises from the lower Mg content compared to the 5xxx series. Also other solute elements such as Si and Cu are either energetically bound to Mg in the form of coherent clusters or have too low diffusion rates to enable the formation of effective solute atmospheres that pin dislocations. Typically 5xxx alloys are used for inner panels because of their better formability and 6xxx alloys for outer panels because of the absence of stretcher lines. It would be, however, preferable to use only one type of alloy for the entire application.

The 6xxx series are not the strongest among the aluminium alloys although they contribute to the highest share of aluminium products (~20%) [12]. In extrusion industry the share is even higher as 90% of the extruded aluminium profiles are made from 6xxx series alloys. [13] A renewed interest in Al–Mg–Si and Al–Mg–Si–(Cu) alloys in recent years has been led by the prospect of applications of 6xxx alloys in the automotive industry. Al-Mg-Si alloys with no or very little Cu are the materials of choice in Europe and 6016 is considered as the most promising system [14]. A material with low yield strength (<130 MPa) and good formability yields low springback and relative ease for production of complex forms with accuracy. In service, a demand for higher yield strength (>200 MPa) is placed. The alloys harbour a huge potential for improvement of strength by precipitation hardening during the paint baking cycle, typically in the range of 170 – 200°C for time up to 30 minutes [1]. The age-hardening response of these alloys is very significant and hence the control of precipitation during thermo-mechanical treatment is critical for attaining an optimal alloy performance.

As previously mentioned little is known about warm forming of 6xxx and also on the effect of temperature on work hardening and plastic anisotropy, which are two important properties related to formability. Therefore, exploration of warm forming potential of existing and new 6xxx aluminium alloys becomes essential. Finite element modelling (FEM) has been a very effective method to simulate the forming processes with accurate prediction of deformation behaviour. FEM can be used not only in process analysis but also in the product design to estimate the optimum conditions of the forming processes [1,2]. In order to access the warm formability of 6xxx alloys it is necessary to combine the FEM with an appropriate constitutive model describing the material work hardening. FE analysis is also complicated due to the material dependence on plastic anisotropy which can be measured under multiple loading conditions [15]. Plastic anisotropy can be largely controlled by crystallographic texture and a texture derived yield locus combined with FEM has been used to explain the anisotropy during drawing. Further complications arise when the effect of temperature on hardening and plastic anisotropy is introduced

into FEM through material models. The use of an appropriate material model is, therefore, of vital importance for the accurate numerical simulation of sheet metal forming. Moreover, temperature dependent metallurgical phenomena like dynamic recovery, change in precipitate state, activation of extra slip systems, etc., are expected to have a huge influence on the characteristics of plastic deformation during warm forming and should also be considered in the models. Despite their potential large application range in terms of alloying systems and process conditions, such combined FEM and material model approaches are still being developed and no fully validated version is available yet.

1.2 Objective of the Thesis

Although warm forming is regarded as a promising process to improve formability of 6xxx aluminium alloys compared to room temperature forming, existing data are still limited and temperature dependent models for plastic deformation are not yet fully predictive. Generation of knowledge in terms of warm formability of 6xxx alloys and influence of temperature on work hardening and plastic anisotropy is the first objective of the thesis. The two alloys selected purposefully for the present investigation are 6016 and 6061. Alloy 6016 is a Si excess alloy, while alloy 6061 is almost balanced. Several mechanical tests are used to identify the temperature dependence of work hardening and plastic anisotropy in relation to the microstructure and texture characteristics. The performance of these alloys for warm forming applications is also studied. The second objective aims to generate physically based material models describing plastic deformation and anisotropy. This includes a unified model of work hardening irrespective of alloy conditions, temperature and strain rate. The effects of change in precipitates state are part of the work hardening model. A crystal plasticity based model that takes into account the effect of plastic anisotropy also needs to be adapted to both room and warm temperatures and validated. Finally, the material models are aimed to be coupled with FEM and applied to the simulation of warm forming of 6xxx sheets.

1.3 Outline of the Thesis

Chapter 2 describes the characterization of the as-received materials used for the present investigation. 6016 and 6061 rolled and annealed sheets of 1 and 3 mm thickness were chosen mainly in naturally aged (T4) and artificially aged (T6) conditions. The grain size was measured from optical microscopy micrographs and electron back scattering diffraction (EBSD) maps. Particles and second phases were characterized on optical microscopy and scanning electron microscopy micrographs and by energy dispersive X-ray spectroscopy. In section 2.1.5 the crystallographic

texture of the materials were calculated from the results of X-ray diffraction. The age hardening behaviour of the alloys at the different temperatures of interest was also measured.

The description of the mechanical tests used throughout the thesis is presented in chapter 3. For achieving the final goal of the project it was necessary to carry out tensile, plane strain compression, deep drawing and bi-axial tests at room and warm temperatures. The description of the machines, test procedures and accuracy of the measurements are presented. After the introduction in section 3.1, tensile test procedures, test conditions, accuracy and a comparison between bulk and sheet materials are reported in section 3.2. Likewise plane strain, deep drawing and bi-axial tests are described in section 3.3, section 3.4 and section 3.5 respectively.

Combining the techniques described in chapter 2 and 3, chapter 4 has been constituted to study the effect of solutes and precipitates on mechanical properties principally on strength and work hardening. Three test results namely tensile, deep-drawing and bi-axial were considered to explain this effect in section 4.3.1, section 4.3.2 and section 4.3.3, respectively. The precipitate state was varied by changing temper, holding time and strain rate and subsequent effects are reported both at room and warm temperatures. Bi-axial tests, however, were carried out only at room temperature. From the results of the tensile tests, the possibility of dynamic precipitation at different strain rates was investigated.

Chapter 5 investigates the effect of temperature and strain rate on strength and work hardening mainly from a microstructure point of view. The results from the tensile and deep-drawing tests are analyzed in this chapter. The gallium enhanced microscopy and EBSD results of the deformed samples provide information about the substructure formation and level of misorientation between the subgrains. A work hardening model has been adapted to heat treatable aluminium alloys and used to simulate the experimental stress-strain curves under different conditions for both alloys.

Chapter 6 is dedicated to the effect of plastic anisotropy both at room and warm temperatures. Anisotropy was investigated by measuring the changes in r-value with tensile direction (section 6.3.1), earing (section 6.3.2), texture (section 6.3.3) and yield locus (section 6.6). Experimental r-value and texture have been used for validating a crystal plasticity based *Visco-Plastic Self-Consistent (VPSC)* model and subsequently the model has been used in predicting the yield locus at 250°C.

The general objective of the project is to develop physically based models that should predict the material constitutive relationships needed as input for FE simulation of forming processes. The *Nes* work hardening model described in

chapter 5 and the *VPSC* crystal plasticity model presented in chapter 6 were linked to the FEM software program DiekA. The results of the FE simulations of cold and warm forming of cylindrical cups are presented in chapter 7. Thickness distribution of the drawn cups along with their force-displacement response were simulated and compared with experimental measurements.

References

1. **Ayres R.A., Wenner M.L.**, Strain and strain-rate hardening effects in punch stretching of 5182-O aluminum at elevated temperatures. *Metallurgical Transactions A*, **10**, 1979, p.41

2. **Flanigan A.E., Tedsen L.F. and Dorn J.E.**, Tensile properties affecting the formability of Aluminium alloy sheet at elevated temperature, *Journal of the Aeronautical Sciences*, **13** 1946, p.475

3. http://www.eaa.net/en/about-aluminium/aluminium-history/

4. **Li, D., Ghosh, A.**, Tensile deformation behavior of aluminum alloys at warm forming temperatures, *Materials Science and Engineering A* **352**, 2003, p.279

5. **Finch D.M., Wilson S.P. and Dorn J.E.**, Deep Drawing aluminium alloys at elevated temperatures, part I – Deep Drawing cylindrical cups, *Transactions ASM*, **36**, 1946, p.254

6. **Li D and Ghosh A. K.**, Effects of Temperature and Bland Holding Force on Biaxial Forming Behaviour of Aluminium Sheet Alloys, *Journal of Materials Engineering and Performance*, **13**(3), 2004, p.348

7. **Shehata F., Painter M.J. and Pearce R.**, Warm forming of Aluminium/Magnesiun alloy sheet, *Journal of Mechanical Working Technology*, **2**, 1978, p.279

8. **Ayres R.A. and Wenner M.L**, Strain and strain rate hardening effects in punch stretching of 5182-O aluminium at elevated temperatures, *Metallurgical and Materials Transactions A*, **10**, 1979, p.41

9. **Ayres R.A. and Wenner M.L**, Warm forming the GM V-6 oil pan in aluminium, *SAE paper 780180*, Society of Automotive Engineers, 1978, p.702.

10. **Tetsuo Naka and Fusahito Yoshida**, Deep Drawability of type 5083 aluminium-magnesium alloy sheet under various conditions of temperature and forming speed, *Journal of Materials Procesing Technology*, **89-90**, 1999, p.19.

11. **Bolt P.J., Lamboo N. A. P. M and Rozier P. J. C. M.**, Feasibility of warm Drawing of Aluminium Products, *Journal of Materials Processing Technology*, **115**(1), 2001, p.118

12. **Andersen S.J., Zandbergen H.W., Jansen J., Treholt C., Tundal U. and Reiso O.**, The crystal structure of the β" phase in Al-Mg-Si alloys, *Acta Materialia*, **46**(9), p.3283

13. **Parson N. C. and Yiu H. L.**, *Proceedings of Light Metals Conference*, Las Vegas, February 1989, ed. by P. G. Campbell (TMS/AIME), Warrendale, Pennslvania, United States, 1989, p. 713

14. **Kleiner. S, Henkel. Ch., Schulz. P and Uggowitzer. P.J.**, Paint bake response of aluminium alloy 6016, *Aluminium*, **77**, 2001, p. 185

15. **Chung, K., Lee, S.Y., Barlat, F., Keum, Y.T., Park, J.M.**, Finite element simulation of sheet forming based on a planar anisotropic strain-rate potential. *International Journal of Plasticity*, **12** (1), 1996, p.93

CHAPTER 2

CHARACTERIZATION OF THE AS-RECEIVED MATERIALS

This chapter provides a description of the as-received materials used for the present investigation. The alloys, denominated EN AW-6016 and EN AW-6061, each available with a thickness of 1 mm and 3 mm, were used mainly in naturally aged (T4) and artificially aged (T6) conditions. The characterization has been performed using Optical Microscopy, Scanning Electron Microscopy, Energy Dispersive X-ray Spectroscopy, Electron Back Scattered Diffraction and X-ray Diffraction. The as-received recrystallized alloys are very much similar in many respects, e.g. grain size and grain size distribution, nature of constituent particles and their distribution, and texture. The main difference among them is in the chemical composition and small precipitate distribution. The static ageing response of these materials is also discussed.

2.1   Microstructure and Texture Characterization

The as-received materials have been characterized in terms of microstructure and texture.

2.1.1   Initial material

Aluminium alloys EN AW-6016 and EN AW-6061 in the form of rolled sheets have been used for the present research. These materials have been supplied by Aleris Aluminum Duffel BVBA via Corus, IJmuiden, The Netherlands. The sheets have been cold rolled, solution treated, quenched and naturally aged (T4). Two different thicknesses of each material has been received. The thickness and the composition of these materials are shown in table 2.1. Alloy 6016 is a Si excess alloy (Mg/Si=0.4 in wt.%) while alloy 6061 is almost balanced[1] (Mg/Si=1.5). Another noticeable difference between the two alloys is the higher Cu content of alloy 6061.

Table 2.1: Sheet thickness, t [mm], chemical composition [wt%], and designation of the investigated materials

Name	Alloy	t	Si	Fe	Cu	Mn	Mg	Cr	Others
16-S	6016	1.01	1.03	0.25	0.06	0.15	0.42	0.02	< 0.15
16-B	6016	2.91	0.99	0.26	0.06	0.15	0.43	0.02	< 0.15
61-S	6061	1.20	0.62	0.35	0.20	0.08	0.95	0.15	< 0.15
61-B	6061	3.09	0.63	0.35	0.21	0.07	0.98	0.15	< 0.15

In the entire thesis, materials with thicknesses close to 1 mm are referred as S and those close to 3 mm are referred as B material.

Heat treatment

Naturally aged material has been converted to peak aged condition or T6 by applying a heat treatment, at 150°C for 4 hours followed by annealing at 170°C for 4 hours in a salt bath and quenching in water.

---

[1] Conventionally a 6xxx aluminium alloy is said balanced when its Mg:Si ratio corresponds to the stoichiometry of the Mg_2Si precipitate, i.e. 1.73 in weight fraction.

2.1.2   Microstructure

The microstructures of the as-received and heat treated materials have been characterized by means of Optical Microscopy (OM), Scanning Electron Microscopy (SEM) and Electron Back Scattered Diffraction (EBSD).

Optical microscopy

Tucker's etchant (10.6 ml HCl, 6 ml HNO$_3$, 4.6 ml HF, 178.8 ml H$_2$O; electroetching for 15 s to 30 s with 18 V) has been used to reveal the grain boundaries when observed under OM (Although Barker's etchant has been the most common etchant for most aluminium alloys, it does not give good results for these two 6xxx alloys).

(a)   (b)
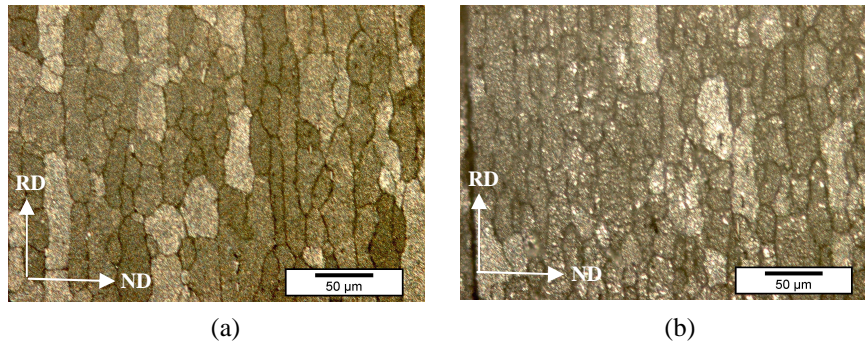
Figure 2.1: OM micrograph of the grain structure revealed using Tucker's etchant for (a) 16-T4-B: 500 µm from the surface and (b) 16-T6-S: close to the surface

(a)   (b)
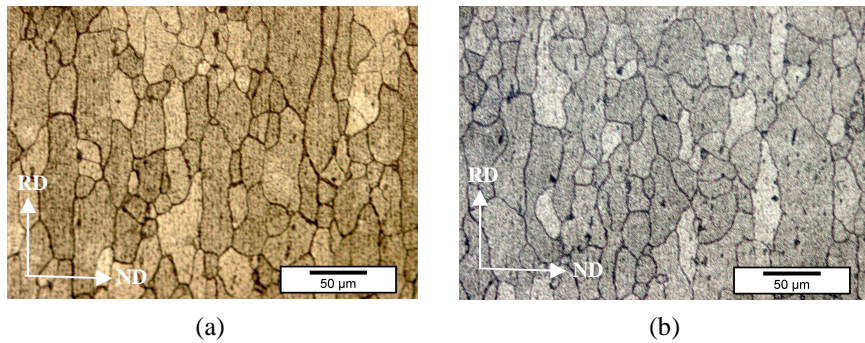
Figure 2.2: OM micrograph of the grain structure revealed using Tucker's etchant for (a) 61-T4-B: close to the surface and (b) 61-T6-B: 300 µm from the surface

Looking at the grain structure in figure 2.1 and figure 2.2, of the initial materials in T4 and T6 states it can be said that the grains are elongated along the rolling

direction (RD). Also, there is no obvious difference among the four materials in terms of grain shape. Observations on different locations show that the microstructure is homogeneous throughout the entire material.

Scanning Electron Microscopy

6061 and 6016 alloys of both tempers and thickness have been examined in backscatter mode in a Field Emission Gun Scanning Electron Microscope of type JEOL JSM 6500F. After fine cloth polishing up to a quarter micron the samples were electro-polished using A2 solution (78 ml perchloric acid, 90 ml H_2O, 730 ml ethanol, 100 ml butylglycol) with a voltage of 20 V and a flow rate of 18 ml/s for 50 s at -12°C.

(a)   (b)

(c)   (d)
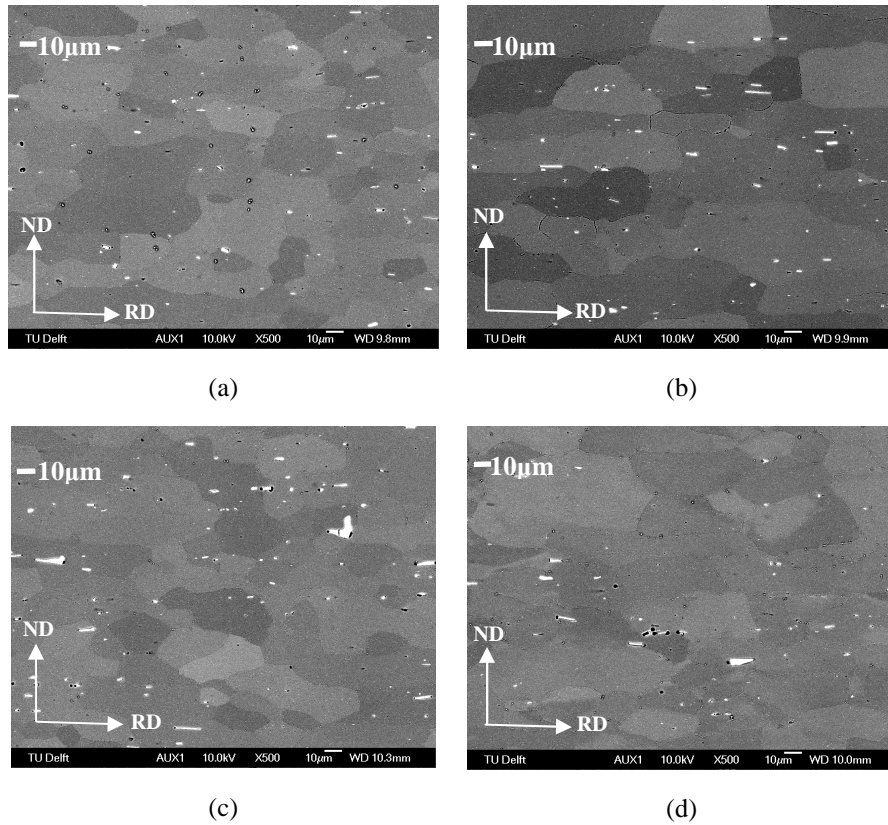
Figure 2.3: SEM micrographs of the initial materials at the centre of the cross-section for (a) 16-T4-S (b) 16-T4-B (c) 16-T6-S (d) 16-T6-B

From figure 2.3 it can be noticed that, like OM, SEM observations also show grains elongated along the rolling direction and that the average grain size for the four

different conditions are very close to each other. No qualitative difference is observed between T4 and T6, which implies that there is no effect of the heat treatment on the grain structure. The uniform contrast within a grain revealed by back-scattered image confirms a fully recrystallized microstructure. Similar features have been noticed with 6061 B and S materials.

Electron Back Scattered Diffraction

EBSD measurements were performed on a JEOL JSM 6500F scanning electron microscope employing the Channel5 acquisition system of HKL. The samples for the EBSD observations were prepared by grinding to 800, 1000 and 2400 grit silicon carbide papers followed by cloth polishing in 9 µm, 6 µm, 3 µm, 1 µm and ¼ µm diamond suspension and finally electro-polishing with A2 solution at 20 V for 50 s at -12°C at a flow rate of 18 ml/s. EBSD measurement of the as-received materials has been performed for both tempers and on cross-sections perpendicular to RD (RD cross-section) and perpendicular to TD (TD cross-section) with a step size of 1 µm. Each EBSD map typically consists of 200 to 400 grains. The average indexation rate obtained was 90% and the average mean angular deviation (MAD) was 0.5. The orientation image maps (OIM) presented in this section are after wild spikes correction (replacement of the orientation of isolated highly mis-orientated pixel by the orientation of one of the neighbouring pixels) and complete removal of the zero solution points. This procedure does not alter the morphology of the grains.

(a)

(b)

(c)
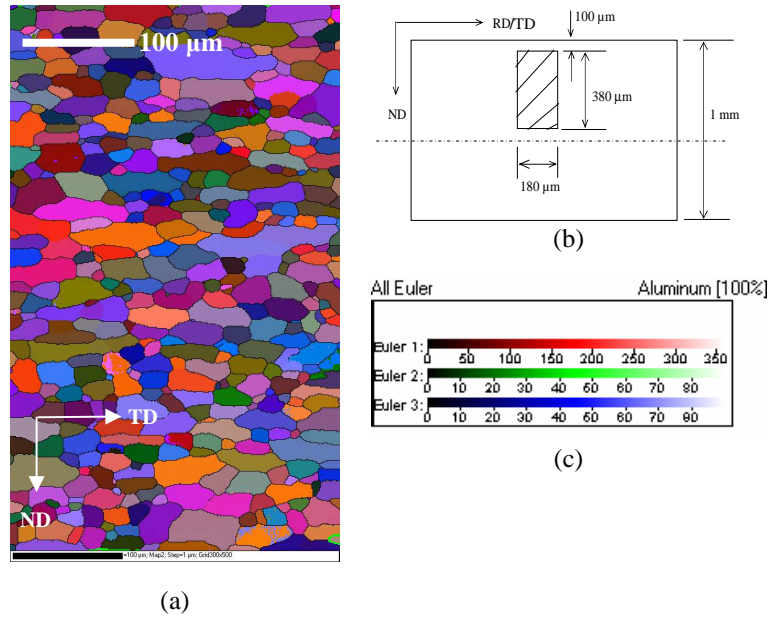
Figure 2.4: Sample 16-T4-S: (a) OIM (b) position of scanned area on sample cross-section and (c) color code used for all EBSD maps.

In sample 16-T4-S, it is clear from the OIM (figure 2.4) that the as-received material is fully recrystallized owing to the uniform crystallographic orientation inside each grain. This fact can also be corroborated by looking at the band contrast map, where grains look completely strain free without any detectable defects. All the as-received materials show similar recrystallised microstructures.

(a)   (b)
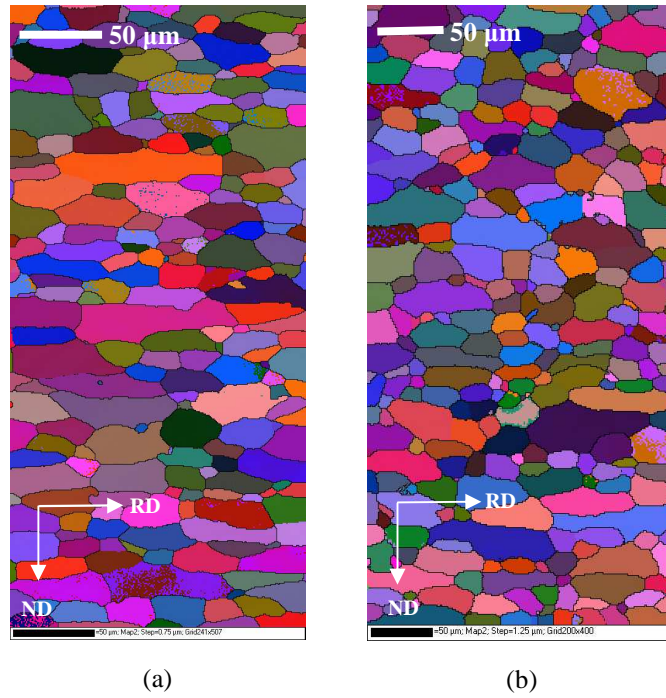
Figure 2.5: OIM for (a) 16-T4-S and (b) 16-T6-S

The comparison of the transverse sections of figure 2.5a and figure 2.5b confirms that the heat treatment did not bring any change in grain shape and size, meaning that grain coarsening was very sluggish or prevented by precipitates on grain boundaries. For both occasions the grains are elongated along TD and RD (figure 2.4a and figure 2.5a), which means they grains are flat ellipsoids or *pancaked*.

(a)   (b)
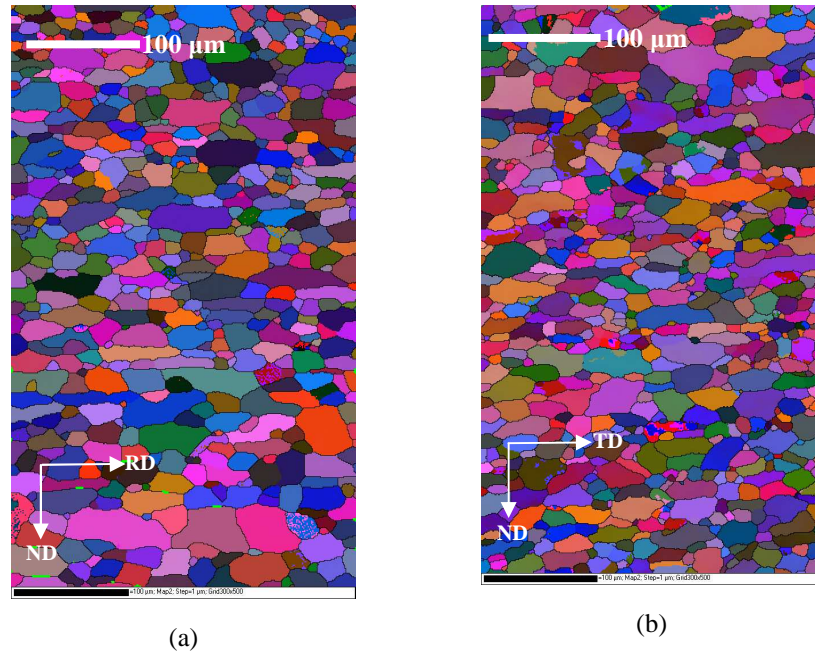
Figure 2.6: OIM for (a) 61-T4-S and (b) 61-T4-S for two different cross-sections

Similar to alloy 6016 (figure 2.4a and 2.5a), two cross-sections RD and TD have been investigated for alloy 6061 under T4 condition (figure 2.6) and the conclusions are also identical in almost every respect. Observation of similar grain size and shape for both the cross-section truly speaks about the flat and ellipsoidal nature of the grains. The observations on the B materials are very much similar to the results obtained on the S materials.

2.1.3   Grain size

The grain size of the as-received materials has been measured from the OM micrographs and EBSD maps.
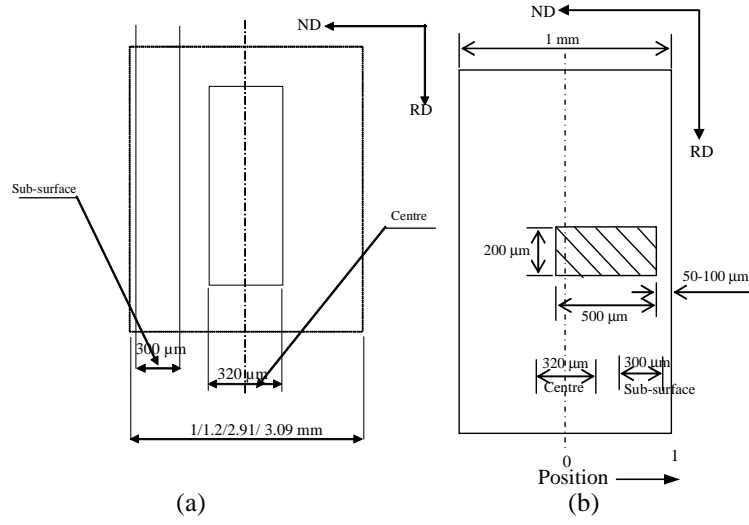
Figure 2.7: Location of sub-surface and centre for (a) OM and (b) EBSD samples

Figure 2.7 shows the locations on the samples observed by OM and EBSD chosen in order to define the centre and sub-surface areas. The sub-surface is restricted up to 300 µm deep for both the techniques.

Grain size by optical microscopy

(a)

(b)

(c)

(d)
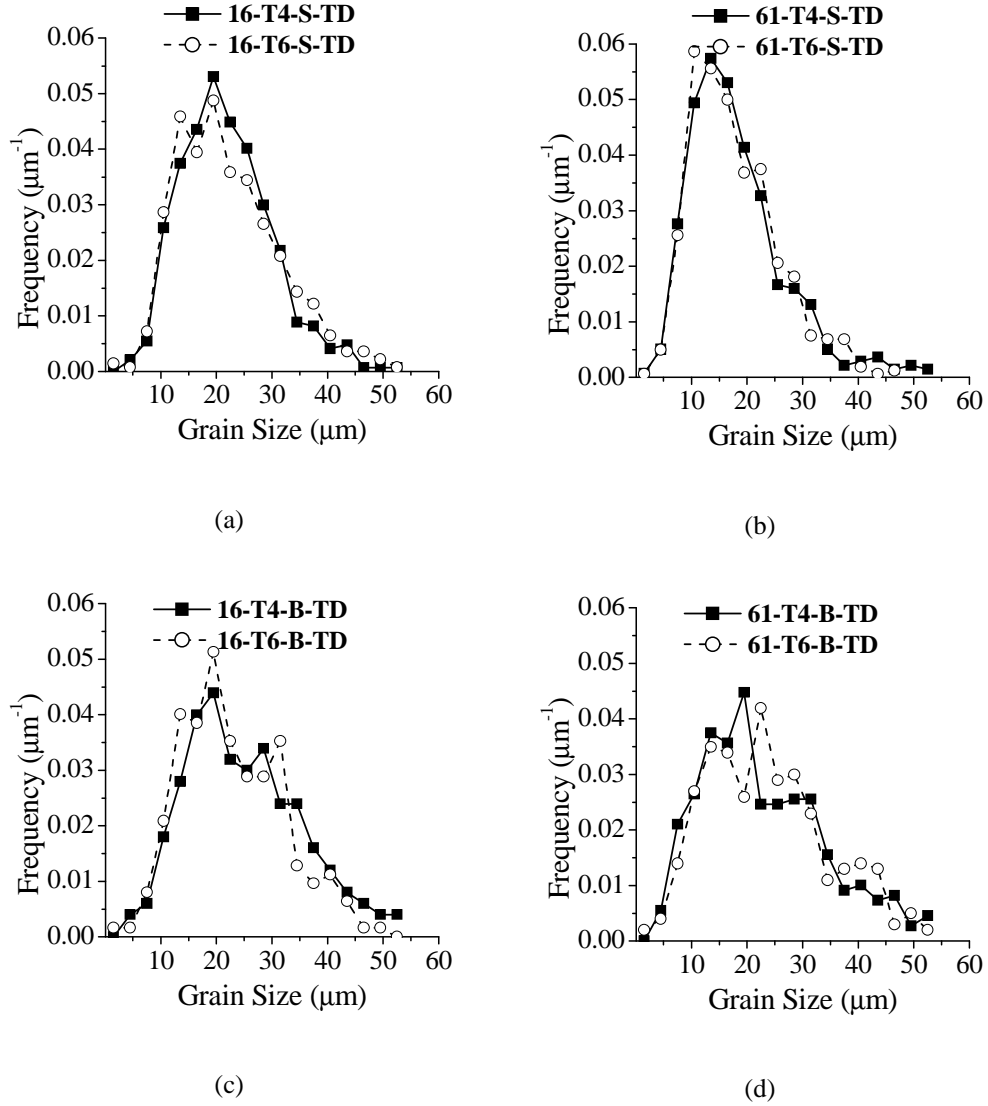
Figure 2.8: Comparison of grain size distribution measured on OM micrograph

OM micrographs have been analyzed by using the software called Analysis developed by analySIS FIVE[®], to obtain the equivalent circular diameter (ECD) and aspect ratio of each individual grain. The grain size distributions represented in figure 2.8, have been calculated using the following equation for the frequency:

Frequency = $\dfrac{N_i}{N_t \Delta}$ where,

N_i is the number of grains in size class i, Δ is the class width (3µm for all cases) and N_t is the total number of grains involved in the analysis.

Figure 2.8 shows the grain size distribution and table 2.2 the average grain size and aspect ratio. The number of grains involved in the analysis varied between 100 and 500 depending on the micrograph. The results show that the grain size for T4 and T6 state for both alloys are the same, which confirms the previous conclusion from OIM that the heat-treatment did not bring any change in grain size and its distribution.

Table 2.2: Average grain size on cross-section (C-S) TD in the center (Cen), sub-surface (Sur) and through thickness average (Avg) and aspect ratio (AR) measured by OM

Sample	C-S TD [µm]			AR
	Cen	Sur	Avg	
16-T4-S	21.5	20.9	21.6	2.0
16-T6-S	21.6	22.8	22.2	2.2
61-T4-S	19.9	20.5	19.2	2.0
61-T6-S	17.4	18.4	17.7	1.9
16-T4-B	22.7	22.7	23.9	2.4
16-T6-B	21.9	24.1	22.8	2.1
61-T4-B	24.9	21.2	24.4	2.1
61-T6-B	23.4	25.9	24.4	2.1

(a)   (b)
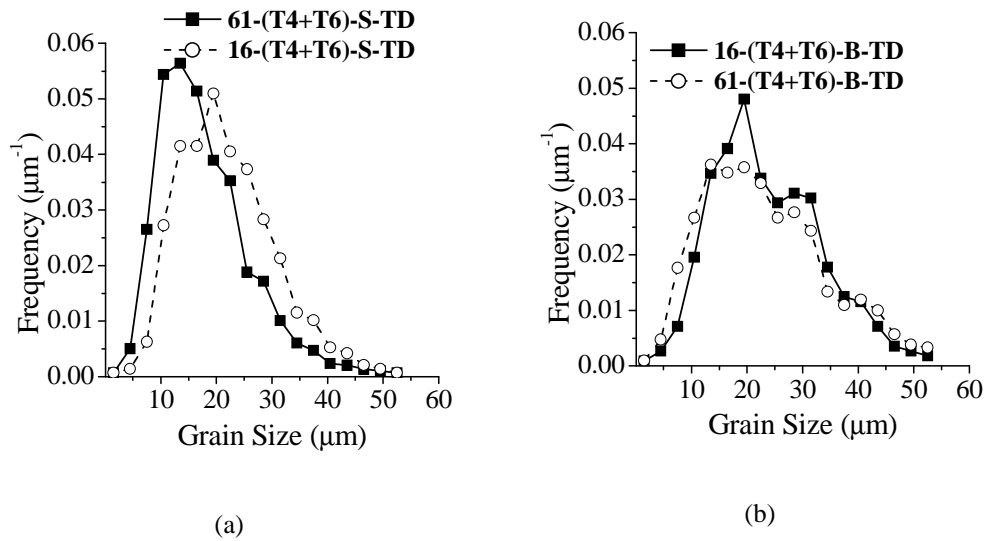
Figure 2.9: Comparison of grain size distribution for two alloys by OM

For each material, the data for T4 and T6 state have been combined to increase the statistical relevance of the size distribution (figure 2.9). From figure 2.9 and table 2.2, it can be seen that the 61-S material has smaller grains than the other three materials, which are similar. The frequency of small grains (in the range of 0 and 20 μm) of 61-S is higher than in 16-S alloy. The aspect ratios for all the conditions are close to 2 except for alloy 16-T4-B-TD where it is 2.4.
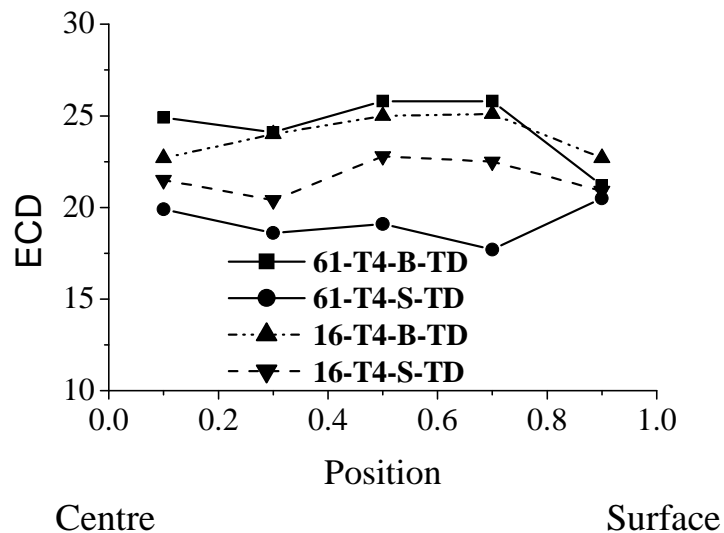
Figure 2.10: Grain size from centre to the surface

Figure 2.10 shows the average grain size variation from centre to surface for all T4 conditions. Comparing the four alloys no clear systematic variation of grain size can be noticed. For alloy 61-T4-B a layer (around 200 µm) of larger grains has been noticed at 150 µm away from the surface (close to position 0.7) from the OM micrograph. This is not well reflected in the graph because the effect of these large grains is compensated by the presence of very fine grains close to the surface.

Grain size by EBSD

The equivalent circular diameter and the aspect ratio have been measured from EBSD maps in the same way than that for OM micrographs. The number of grains involved in the measurement varies in between 70 and 500 grains depending on the size of the OIM maps.

Table 2.3: Grain size and aspect ratio measurement data obtained by EBSD

Sample	C-S TD [µm]			AR
	Cen	*Sur*	*Avg*	
16-T4-S	17.8	18.6	17.9	2.4
16-T6-S	19.6	20.4	19.5	2.0
61-T4-S	15	19.8	16.4	2.0
61-T6-S	16.9	14.5	15.4	1.9
16-T4-B	19.8	-	19.8	2.5
61-T6-B	19.4	-	19.4	2.1
Sample	C-S RD [µm]			
	Cen	Sur	Avg	
16-T4-S	19.2	20.3	19.4	2.2
61-T4-S	15.3	15.3	15.1	2.0

Table 2.3 represents the average grain size and aspect ratio on RD and TD sections for 6016 and 6061 materials. The results are similar for both alloys. It is confirmed that the heat treatment to form T6 does not affect the grain structure and that 6061-S has smaller grains compared to other materials. The results also confirm the observation from OM results in that the average grain size across RD and TD sections are similar for both the alloys.
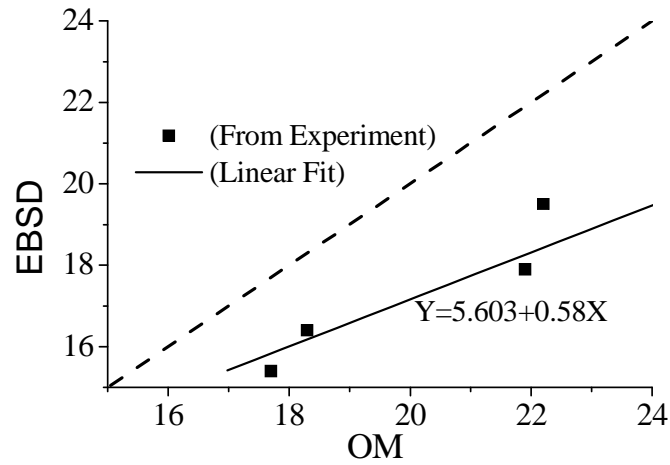
Figure 2.11: Comparison of average grain size (in μm) measured by EBSD and OM

Grain size measurement from OM and EBSD are compared in figure 2.11. It is evident that the grain size is overestimated by OM. This shows that not all the grain boundaries have been revealed during etching of the samples for OM observations.

2.1.4   Particles and second phases

In order to reveal the size, morphology, orientation, composition and quantify the second phase particles OM, SEM and EDXS have been used.

(a)   (b)
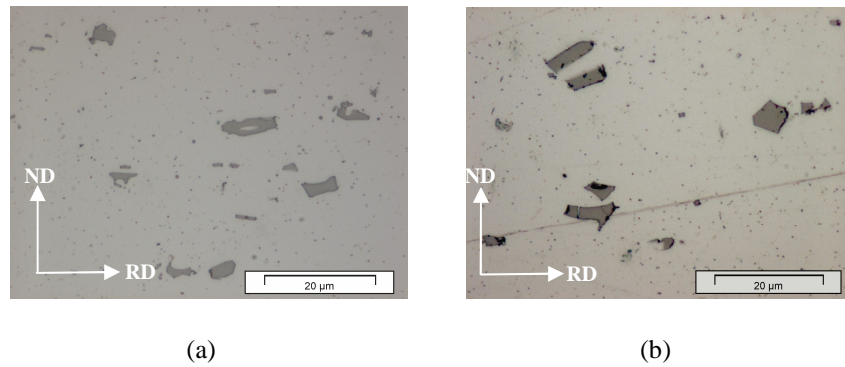
Figure 2.12: Optical micrograph of the grain structure revealed by using Keller's etchant for (a) 61-T6-S and (b) 16-T4-S

Keller's etchant (performed better than 0.5% HF) was used to reveal the shape and morphology of the second phase particles by OM. There are various shapes of particles some being fragmented during rolling and mostly aligned along the rolling direction (Figure 2.12). These particles are mainly constituent particles generated during casting with a size in the range from 5 to 30 μm. They are present all over the grains and on grain boundaries also. Using optical micrographs it was practically not possible to indentify any remarkable differences among the alloys or the tempers from particle size, shape or density point of view.

<p align="center">(a)   (b)</p>

<p align="center">(c)   (d)</p>
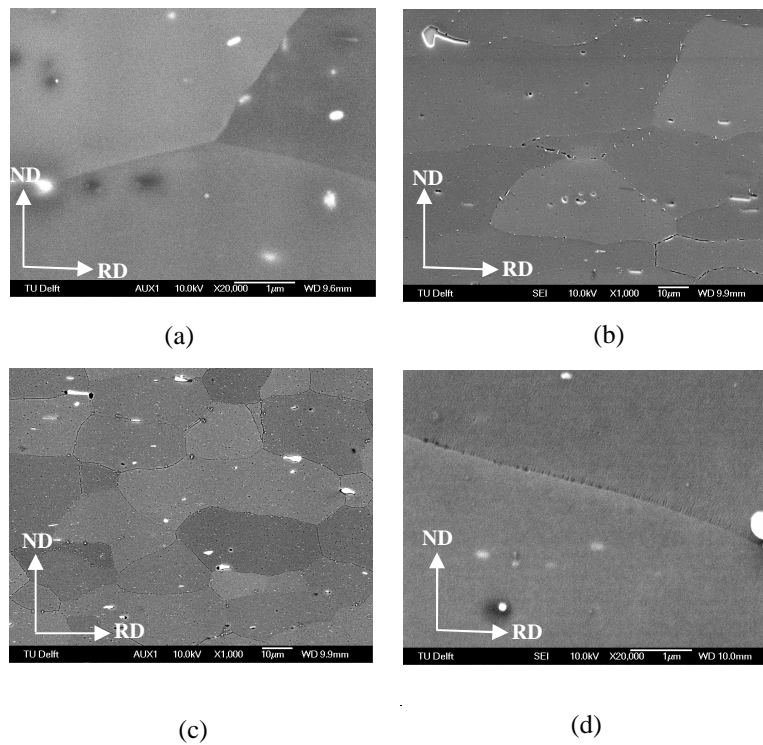
Figure 2.13: Scanning micrographs for (a) 16-T4-S (b) 16-T4-B (c) 16-T6-S and (d) 16-T6-B at the sub-surface

In addition to the constituent particles SEM micrographs (figure 2.13) also clearly reveal the presence of smaller particles or dispersoids prominent along the grain boundaries. They are distributed inside the grains as well. These particles have spherical or ellipsoid shape with a size ranging from 0.02 to 0.5 μm and form during heat-treatments. For the sample 16-T6-B (figure 2.13d), it is seen that small particles on the grain boundary have been scored off probably during polishing leaving small voids. The voids can also be due to the chemical attack on the particles during electro-polishing.

Quantification of the constituent particles has been performed for alloy 61-T4-S on the TD plane using pictures from SEM acquired in back-scattered mode. The acceleration voltage was 10 kV with magnification 3000X and 10 mm working distance. The software used to analyze the data is the Noran Vantage Software. The detailed description of the process can be found in the work of Anselmino [1]. The particles with length 0.01 μm and more and area 0.1 $μm^2$ and more have been considered for the present calculations. From the analysis the average 3D radius, volume density and volume fraction are found to be 0.66 μm, 5.3 $x10^{15}$ particles/m^3 and 0.0064 respectively.

EDXS has been performed with the same SEM equipment. An accelerating voltage of 15 kV and working distance of 25 mm was used for these measurements. A limited number of particles were analyzed on 16-T4-S and 16-T6-S samples. It shows that the main elements are Si, Fe, Mn and Al. Also α particles with composition Al_5FeSi and β particles with $Al_2(FeMn)Si$ have been found [2].

The small precipitates that are responsible for the precipitation hardening of these alloys have a size in the range of a few tens of nanometer and are therefore not visible with the technique applied here.

2.1.5   Texture

The texture of the as-received materials has been derived from XRD measurements. The ND surface of the samples for XRD measurement (size 38 mm × 38 mm) were first polished up to the desired thickness levels before the final polishing by smooth polishing paper (2400). Samples were dipped in 15%NaOH for 10 min and then transferred under running water very quickly before they were cleaned by 25% HNO_3 for 20 s. After cleaning they were again placed under running water. On average 50 μm has been removed due to the chemical action.

Texture measurements have been performed using the Bruker-AXS D8 Discover equipped with a Co tube (45 kV, 25 mA). The goniometer radius is 300 mm. The parallel beam optics consists of a PolyCap (divergence: 0.25°, 4 mm x 2 mm) in the incident beam in combination with a parallel sollerslit (divergence: 0.35°) in the diffracted beam. The advantage of this setup is that it is virtually free of defocusing and insensitive for specimen displacement. The pole figures measured were {100}, {110}, {111}, and {311}. The integration time is close to 1 s (per measuring point) for pole figure measurement and 10 s for background measurement. 16 circles were measured with $\Delta\chi = 5°$ and $\chi_{max} = 75°$ (χ: tilt). The beam mode is set in point focus with continuous measurement in φ (azimuth) and a step size of $\Delta\varphi = 5°$ (72 segments). Measured data have been processed with the *MTM-FHM* software

system developed by P. Van Houtte. After background subtraction poles figures were used to calculate the orientation distribution function (ODF) following the spherical harmonic method (L_{max} = 22) and applying the orthorhombic sample symmetry which is suitable for rolled sheets. Equal weights were given to each pole figure. The ODFs are plotted as sections through Euler space (φ_1, ϕ, φ_2) for constant values of φ_2, using Bunge's notation [3] with ND, RD and TD the sample reference axes.
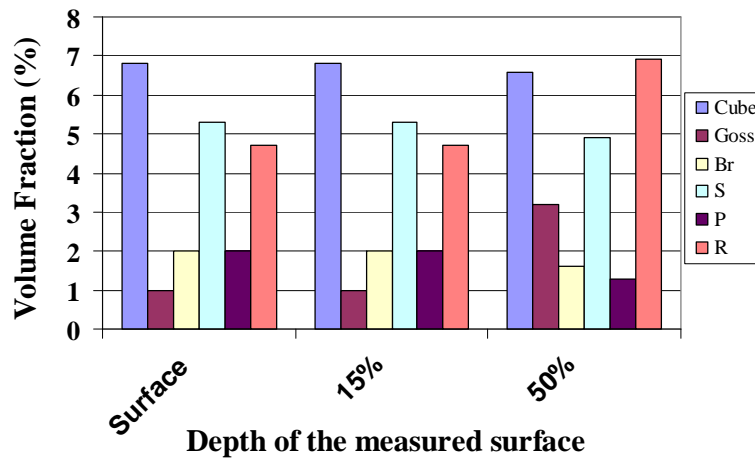
Figure 2.14: Volume fraction of the texture components at different levels of thickness for 61-T4-S.

Figure 2.14 shows the variation of the volume fraction of the main texture components across the thickness for 61-T4-S material. It can be noticed that the texture components do not vary a lot throughout the thickness. This remains true for other materials as well. The average through thickness texture of the materials has been calculated using a weighted average of the C-coefficients of surface, sub-surface (15%) and mid-thickness (50%) textures. The weights were chosen as 10, 30 and 60% respectively, based on the volume of material assumed to be represented by each measured texture.
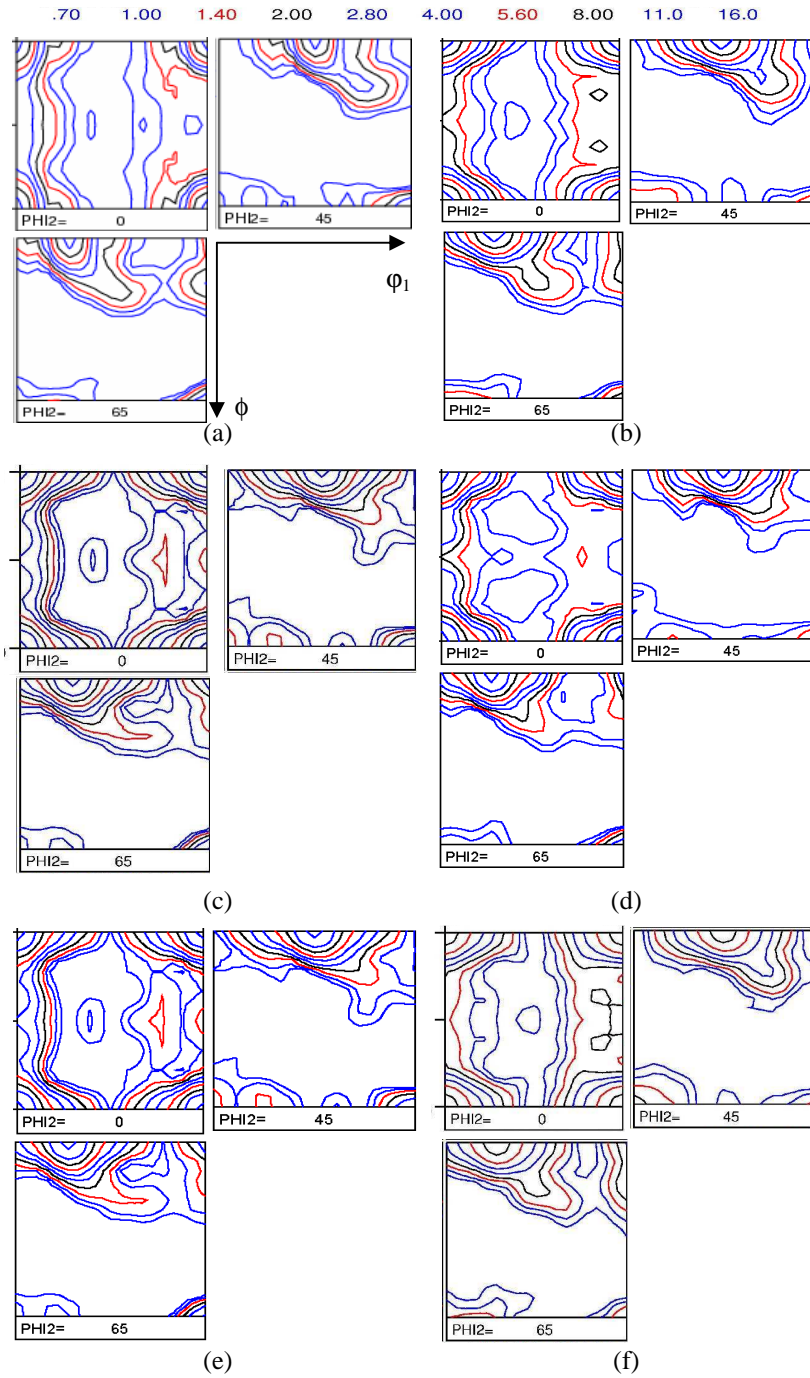
Figure 2.15: Through thickness ODF from XRD shown by three cross-sections of constant φ_2 angle for (a) 61-T4-S (b) 61-T4-B (c) 61-T6-B (d) 16-T4-B and (e) 16-T6-S and (f) 16-T6-B.

Table 2.4: Volume fraction (%) of most important texture components calculated with the software of Van Houtte. For calculation from EBSD data a spread of 11° is assumed around each orientation and G is the number of grains involved in the calculation.

	Sample	G	Cube	Goss	Br	S	Cu	P	R	I-G	D
E B S D	16-T4-S-TD	130	6.9	2.8	1.2	4.6	1.8	1.6	5.0	0.9	2.3
	16-T4-S-RD	274	4.0	5.4	1.3	4.6	2.0	1.5	5.3	0.4	2.5
	Com-16-T4-S	404	5.1	4.4	1.3	4.6	1.9	1.6	5.2	0.6	2.4
	16-T6-S-TD	220	4.2	2.9	1.4	4.7	2.1	3.0	5.2	0.4	2.3
	61-T4-S-TD	413	5.2	1.8	2.1	6.2	2.2	1.2	6.8	0.9	2.7
	61-T4-S-RD	459	5.1	1.2	2.2	6.9	2.8	1.8	6.6	1.1	3.2
	Com-61-T4-S	872	5.2	1.5	2.2	6.6	2.5	1.5	6.7	1.0	2.9
	61-T6-S-TD	457	6.8	1.9	1.6	6.3	2.7	1.7	6.7	0.4	3.1
X R D	16-T4-S	-	5.7	4.5	1.5	5	1.8	3	4.5	0.5	2.3
	61-T4-S	-	6.7	2.3	1.7	5	2	1.5	6	1.2	2.7
	16-T4-B	-	9.7	1.7	1.7	3.7	1.5	1.9	4.1	1.1	2.2
	16-T6-B	-	9.3	2.6	1.6	4.1	1.7	1.8	4.2	1.4	2.2
	61-T4-B	-	7.3	1.4	1.7	5	1.9	1.8	5.2	1.7	2.6
	61-T6-B	-	6.3	1.1	1.3	4.3	1.5	1.8	4.4	1.9	2.1

From figure 2.15 it can be noticed that all the ODFs are qualitatively very similar. All the textures are dominated by cube oriented grains. They can also be characterized by the presence of the η-fibre, from Cube to Goss, and S/R oriented grains (Table 2.4). Comparing the four as-received materials, it is observed that alloy 16-B has the highest cube volume fraction while alloy 16-S has the lowest cube volume fraction and the highest Goss volume fraction. For both alloys it is observed that S material has lower volume fraction of cube and higher volume fraction of Goss than B material. No change in texture due to the conversion from T4 to T6 has been noticed. As observed in section 2.1.2 the grain size does not

change due to heat treatment during the formation of T6 from T4, consequently any texture change due to this conversion is also not expected.

Texture characterization has also been performed using EBSD measurements. The sample preparation and EBSD settings have been described in section 2.1.2. The ODF has been calculated by the series expansion method included in the HKL CHANNEL5 system using $L_{max} = 22$ and half Gaussian spread of 7°. Orthorhombic sample symmetry has been applied during the calculation which is a valid assumption for rolled material. Wild spike correction and partial noise reduction has been performed before the calculation of the ODFs. ODFs calculated from EBSD measurements on RD and TD cross-sections of the same material show some small quantitative differences, which can be explained by the limited area of the EBSD maps. For the sake of better statistics, measurements on RD and TD cross-sections were therefore merged by combining the series expansion coefficients (C-coefficients) and using weight factors proportional to the map areas (indicated by "com-" in Table 2.4). The volume fractions of texture components generated from the EBSD measurements produce a very good agreement with the ones from the XRD data for both alloys (Table 2.4). The ODFs generated from XRD are considered for future references in this thesis.

2.2   Static Ageing Kinetics

The ageing kinetics of the as-received materials has been measured from Vickers hardness tests using the micro-hardness tester Buehler from Olympus. The load used was 500 gf. Each result is an average of 7 measurements and the accuracy is ± 2.5 for a confidence level of 0.95.

It is reminded here that the as-received materials (T4) were heated to 150°C for 4 hours followed by 170°C for 4 hours in an salt bath and water quenched to form the T6 temper. The natural ageing response has been measured over a period of more than several years. Artificial isothermal ageing has been performed by heating the as-received (T4) and heat treated materials (T6) at three different temperatures (150°C, 180°C and 250°C) for different time periods and then quenching in water. At 250°C annealing was done in a salt bath whereas an oil bath was employed for the other two temperatures.

(a)   (b)
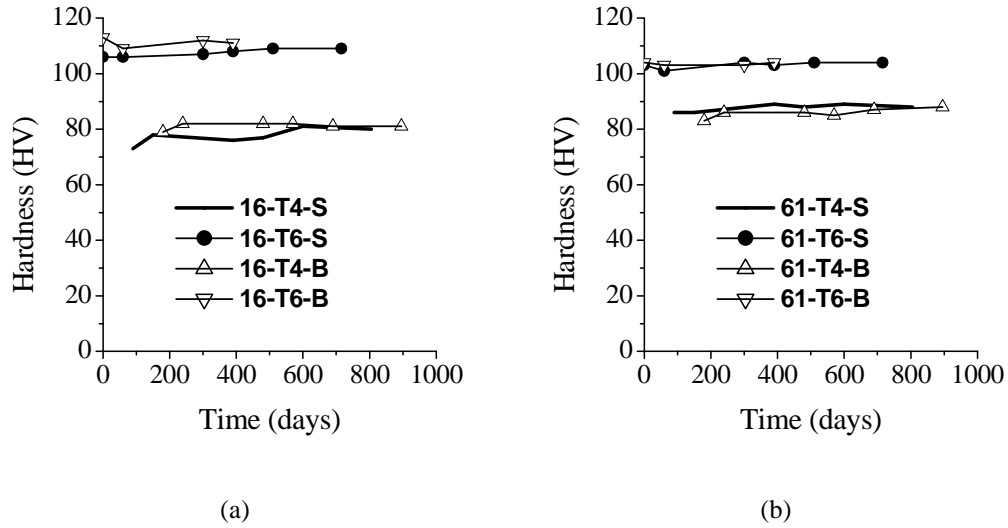
Figure 2.16: Natural ageing response of the as-received and heat-treated materials
(a) 6016 (b) 6061

The natural ageing response for T4 state is presented in figure 2.16. There is only a
negligible change in hardness over the long time period and 6061-T4 is found to be
harder compared to 6016-T4.
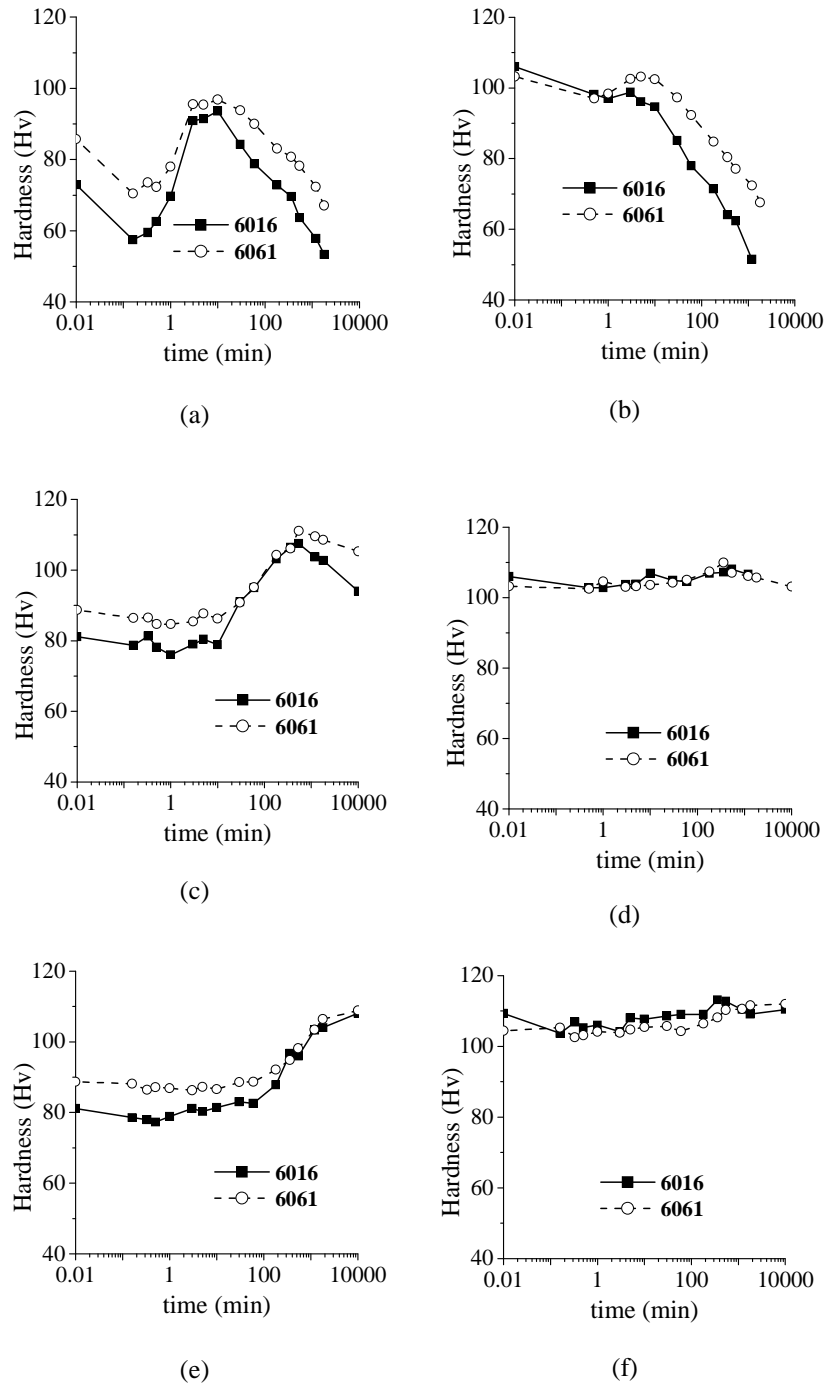
Figure 2.17: Artificial ageing response of 6016 and 6061 S materials (a) T4 at 250ºC (b) T6 at 250ºC (c) T4 at 180ºC (d) T6 at 180ºC (e) T4 at 150ºC (f) T6 at 150ºC

The artificial ageing response for the T4 state is presented in figure 2.17a, 2.17c, and 2.17e. An initial drop of hardness for both the alloys of T4 state is observed at 250°C, while the drop is absent for ageing at 180°C and 150°C. This initial drop in hardness has already been reported [4, 5]. An et al. [4] found that the depth of the drop increases with temperature and that the time to reach the lowest hardness is shorter at higher temperature. The following reason was put forward by An and his co-workers: small clusters called natural ageing (NA) clusters, are expected to form at room temperature and are responsible for the strength increase during natural ageing. During artificial ageing the NA clusters need first to dissolve to release the solutes required to form GP zones, which delays the formation of hardening particles upon heating [5, 6, 7]. This is the reason for the dip in the hardness curve at 250°C for the alloys in T4 state. There is no such dip for the ageing curves obtained at 180°C or 150°C in the present investigation. The probable reason is the slower dissolution of the NA clusters at lower temperature and the simultaneous development of the GP zones that compensates the hardness drop. Both 6016-T4 and 6061-T4 alloys have similar ageing kinetics and reach the same peak hardness. The main difference between the two alloys is the faster hardness decrease of 6016-T4 compared to 6061-T4 during overageing.

The natural ageing for the T6 stage also shows (figure 2.16) the least change in hardness value with time. Alloy 6016 is found to be slightly harder in T6 state compared to alloy 6061, whereas the opposite is true for the T4 state.

The artificial ageing response for the T6 state is presented in figure 2.17b, 2.17d and 2.17f. As expected, the T6 state of both alloys was already at peak aged or even overaged state as the ageing curves do not show any clear initial hardness increase. The peak hardness values of the two alloys are comparable. When plotted on the same graph, the T6 curves follow the overaged part of the T4 curves for all cases meaning that overageing kinetics are the same for both tempers. Ageing curves at 250°C clearly show that also in T6 state alloy 6016 overages quicker than alloy 6061.

Three factors have to be considered when comparing the strength and ageing kinetics of the two investigated alloys: the total amount of Mg and Si alloying elements, the Mg/Si ratio and the Cu content. 6061 is a balanced alloy that can potentially form a higher volume fraction of Mg_2Si, GP zones or NA clusters than alloy 6016. This can explain the higher hardness of 6061 in T4 state. The higher Cu content in 6061 also contributes to its higher T4 hardness. On the other hand, 6016 is a Si excess alloy. Excess Si changes the stoichiometry of Guinier Preston (GP) zones and increases their number density [8]. Together with the higher amount of Si left in solid solution, this will increase the strength [9] and partially reduce the difference in hardness between 6061 and 6016. Both addition of Si and Cu are

known to speed up the artificial ageing kinetics in the underaged regime [10, 11]. The very similar ageing kinetics of 6016-T4, with higher Si content, and 6061-T4, with higher Cu content, can then be explained by the balance between the effect of these two elements. The stoichiometry of the β'' precipitates responsible for the strength in peak hardness or T6 state is usually close to Mg_5Si_6 [12]. At T6 state 6061 becomes a Mg excess alloy and 6016 is still a Si excess alloy. It is then not possible to qualitatively comment about the relative strength of the two alloys. Cu addition has negligible effect on peak strength [10] but has been found to improve the thermal stability of the precipitates [11]. This can explain the slower coarsening rate, hence hardness decrease, during overageing of 6061 compared to 6016. A quantitative comparison of the effect of the chemical composition of the two alloys on their mechanical properties requires the use of numerical models and will be done in chapter 5.

That 6061-T4 is stronger than 6016-T4, is evident from the tensile and deep drawing test results discussed in chapter 4.

References

1. **Anselmino E.**, **Miroux A**. and **van der Zwaag S**, "Dispersoids quantification and size distribution in hot and cold processed AA3103", *Materials Characterization,* vol. 52/4-5, 2004 p. 289

2. **Kuijpers N.**, "Kinetics of the β-AlFeSi to α-Al(FeMn)Si transformation in Al-Mg-Si alloys" , (Ph.D. thesis), Delft University of Technology, Delft, The Netherlands, p. 52

3**. Bunge H.J.**, *Texture analysis in Materials Science*, Butterworths, London, 1982

4. **An Y.G., Zhuang L., Vegter H. and Hurkmans A**., Fast ageing kinetics of the AA6016 Al-Mg-Si alloy and the application in forming process, *Metallurgical and Materials Transactions A*, **33A**, 2002, p. 3121

5. **Kleiner S., Henkel Ch., Schulz P. and Uggowitzer P.J**., Paint bake response of aluminium alloy 6016, *Aluminium, 77*, 2001, p. 185

6. **Murayama M. and Hono K**., Pre-precipitate clusters and precipitation processes in Al–Mg–Si alloys, *Acta Materialia* **47**, 1999, p. 1537

7. **Edwards G.A., Stiller K., Dunlop G.L. and Couper M.J**., The precipitation sequence in Al–Mg–Si alloys, *Acta Materialia* **46**, 1998, p. 3893

8. **Murayama M. and Hono K.**, Pre-precipitate clusters and precipitation process in Al-Mg-Si alloys, *Acta materialia,* **47**, 1999, p. 1537

9. **Sachdev A.K.**, Development of an aluminium sheet alloy with improved formability, *Metallurgical Transactions A,* **21**, 1990, p. 165

10**. Murayama M., Hono K., Miao W.F. and Laughlin D.E.**, The effect of Cu additions on precipitation kinetics in an Al-Mg-Si alloy with excess Si, *Metallurgical and Materials Transactions A*, **32A**, 2001, p. 239

11. **Man J., Jing L. and Jie S.G.**, The effect of Cu addition on the microstructure and thermal stability of an Al-Mg-Si alloy, *Journal of Alloys and Compounds,* **437**, 2007, p. 146

12. **Chen J.H., Costan E., van Huis M.A., Xu Q. and Zandbergen H.W.**, Atomic pillar-based nanoprecipitates strengthen AlMgSi alloys, *Science,* **312**, 2006, p. 416

CHAPTER 3

MECHANICAL TEST PROCEDURES

This chapter describes the procedures of all the mechanical tests performed for the present investigation at both room and warm temperatures. The reported procedures pertain to Tensile, Plane Strain Compression, Warm Deep-Drawing and Biaxial tests. The procedures for measurement of ear profile and thickness distribution from the centre of the cup to flange are described as part of the post drawing analysis. Tensile and PSC tests were performed on the thermo-mechanical simulator Gleeble 3800 and deep drawing at TNO Science and Industry, Eindhoven, The Netherlands. The accuracy of the tests was determined and all the tests were found highly repeatable.

3.1. Introduction

The principle objective of this chapter is to describe the mechanical test procedures used throughout the investigation. Tensile, plane strain compression (PSC), deep-drawing (DD) and biaxial (BA) tests have been selected in the present scope of research. The objective of these tests was to investigate the influence of process parameters on mechanical response and to use the results to validate a work hardening model and form an experimental yield locus used as input of a finite element code. Tensile, PSC and DD tests were performed at room temperature (RT), 150°C, 180°C and 250°C.

Tensile and PSC tests were done with the thermo-mechanical simulator Gleeble 3800[®]. The advantage of using this machine was the accurate control of temperature and simultaneous heating and loading, so that deformation could start immediately after achieving the desired temperature. Apart from generating usual stress-strain curves, the results of the tests were used to investigate the work hardening response of the materials. The tensile curves were also used for the validation of the work hardening model that has been coupled with FEM in order to incorporate the effect of work hardening. The description of the work hardening model and subsequent validation are discussed in chapter 5.

Force displacement response, ear profile and cup thickness distribution were measured to study the effect of process conditions on DD. These results are also used for validating the FEM simulations in chapter 7.

3.2. Tensile Test

3.2.1. Introduction

The uniaxial tensile test is the most common and popular among all the screening tests principally because of its easier control over the test parameters. The test results are typically important in estimating various parameters that influence formability [1,2,3,4] under simple loading conditions.

In the present investigation, tensile tests were carried out using the thermo-mechanical simulator Gleeble 3800. Tests were performed with 6016 and 6061 specimens of T4 and T6 tempers under different conditions. The chemical composition and characteristics of these materials are described in chapter 2.

3.2.2.   Procedure and test conditions
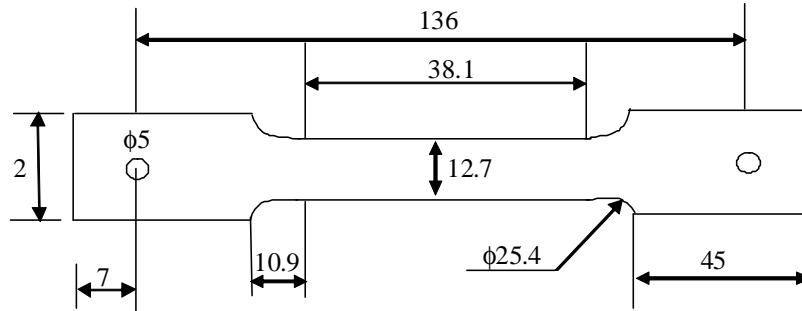
Figure 3.1: Design and dimension (in mm) of the tensile test specimen

The design and dimension of the tensile specimens are presented in figure 3.1. The function of the two holes at either end of the specimen is to hold the specimen between the grips. An extensometer was attached at the middle of the specimen and the test was gauge controlled so that the measurement of deformation was restricted to the length within the two arms of the extensometer. The initial distance between the two arms of the extensometer was 10 mm, each maintaining 5 mm distance from the centre of the specimen.
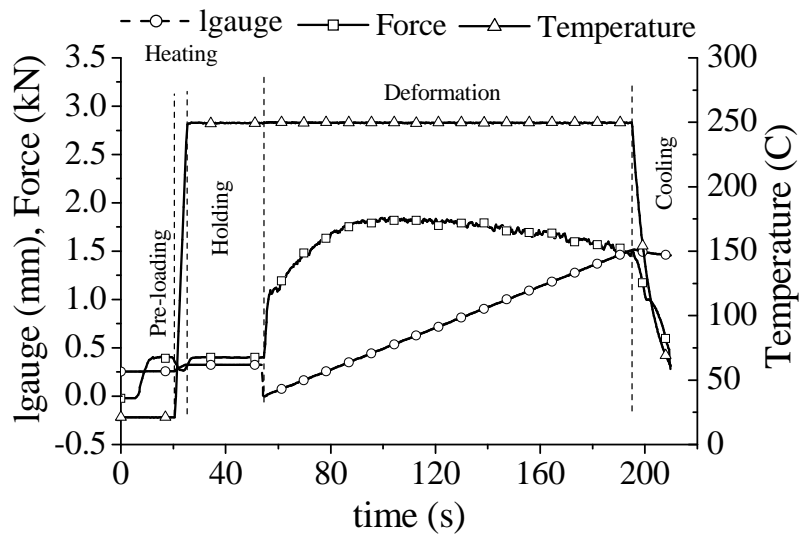
Figure 3.2: Description of a typical tensile test

The general description of a warm temperature tensile test can be found in figure 3.2. The specimens were pre-loaded to 0.5 kN pressure at the beginning of the test. The temperature started then to increase keeping the force constant till the beginning of deformation. After deformation the specimens were simultaneously cooled by compressed air and unloaded. For the tests performed at RT, the same sequence has been maintained without heating and cooling by compressed air. From the load-gauge length curves so generated, the true stress-true strain response of the materials was calculated and subsequently the 0.2 % offset yield point was determined. Finally, the work hardening response was plotted against true stress. Work hardening coefficients (n) was calculated from the slope of the true stress-true strain plot. The Lankford R-values were calculated from the specimen dimension changes along the gauge length and width.

The two alloys were tested approximately one year after their production in the form of sheets. Tests were carried out at RT, 150°C, 180°C and 250°C for T4 and T6 tempers. The heating rate was 50°C/s for all cases. Tensile specimens were taken from rolled sheets with the tensile direction parallel to the rolling direction for most of the tests. Some tests were also performed with the tensile axis parallel to the transverse, 45°, 30° and 60° directions with respect to the rolling direction to study the influence of plastic anisotropy. The details about anisotropy results are discussed in chapter 6. In order to investigate the effect of strain rate, tests were performed at 0.1 s^{-1}, 0.01 s^{-1} and for few occasion 0.001 s^{-1}. The purpose of an extremely slow rate was to observe the occurrence of any dynamic precipitation. Effect of holding time at test temperature before deformation was investigated at 250°C for T4 temper by using holding times of 2 s, 30 s and 600 s.

Temperature distribution inside the deformation zone
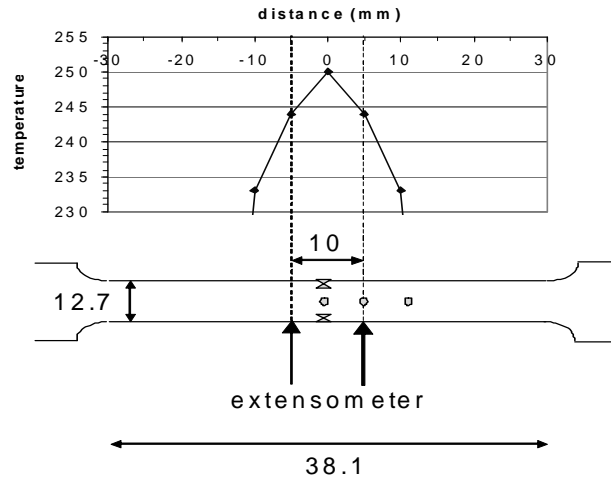
Figure 3.3: Position of the thermocouples for the temperature profile test

For the warm temperature tests, maintaining the desired temperature between the two arms of the extensometer (i.e. deformation zone) was an important issue. The specimens were heated by the resistance Joule effect and the grips were kept cold by the water cooling system. Consequently a temperature gradient forms during heating. Therefore, it was necessary to measure the temperature profile inside the deformation zone. To this purpose, three thermocouples were placed at the locations indicated by the circle marks in figure 3.3. Thermocouple TC1 was placed at the middle of the sample, thermocouples TC2 and TC3 were placed horizontally 5 mm and 10 mm away from TC1.

Table 3.1: Measured temperature by the thermocouples placed at different positions on the tensile specimen.

Sample	Temp°C	HR (°C /s)	TC1 (°C)	TC2 (°C)	TC3 (°C)	$\Delta*$ (°)
16-T4-S	250	50	250	244	233	6
16-T4-S	150	50	150	146	140	4
16-T4-B	250	50	250	247	133	3
16-T4-B	150	50	150	148	140	2

---

[*] Temperature difference between TC1 and TC2.

Table 3.1 presents the measured temperatures and their differences. The difference has been found to be 6°C between TC1 and TC2 for a nominal temperature of 250°C (i.e. within the deformation zone) for 6016-T4 S material. At lower temperature (150°C) this difference is even lower (4°C). For B materials, the temperature distribution inside the deformation zone was found even better compared to S and the difference was found to be 3°C and 2°C for higher (250°C) and lower temperatures (150°C) respectively. Therefore, the maximum temperature difference within the deformation zone is 6°C, which is within the accepted range reported by other researchers [5]. Tests were also conducted placing the thermocouples at the edges of the specimen (marked as x in figure 3.3) within the deformation zone. For a 6016-T4 specimen, the difference between them was found to be 1°C, which is well within the measurement accuracy. The temperature distribution is assumed to be the same for 6016-T6, 6061-T4 and T6 specimens.

3.2.3.   Accuracy of the test

(a)   (b)
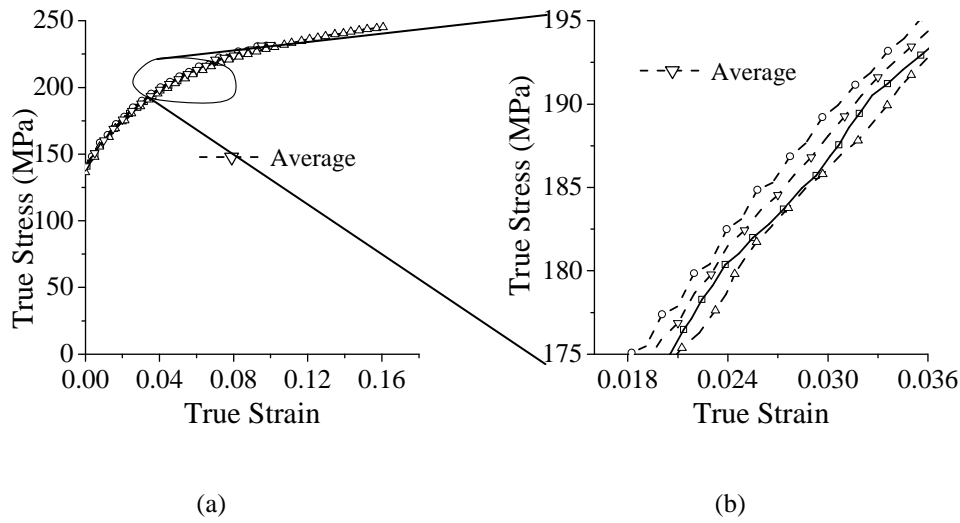
Figure 3.4: Measure of repeatability for 16-T4-S at 150°C. Tensile direction along RD.

Figure 3.4 shows three tensile tests with identical conditions carried out on sample 6016-T4-S at 150°C and with a strain rate of 0.1 s^{-1}. The average scatter from the average plot is ±1 MPa for the same value of strain. Therefore, the process is highly repeatable. All the test results presented in this thesis are average results of at least two tests.

3.2.4.   Comparison between S and B samples
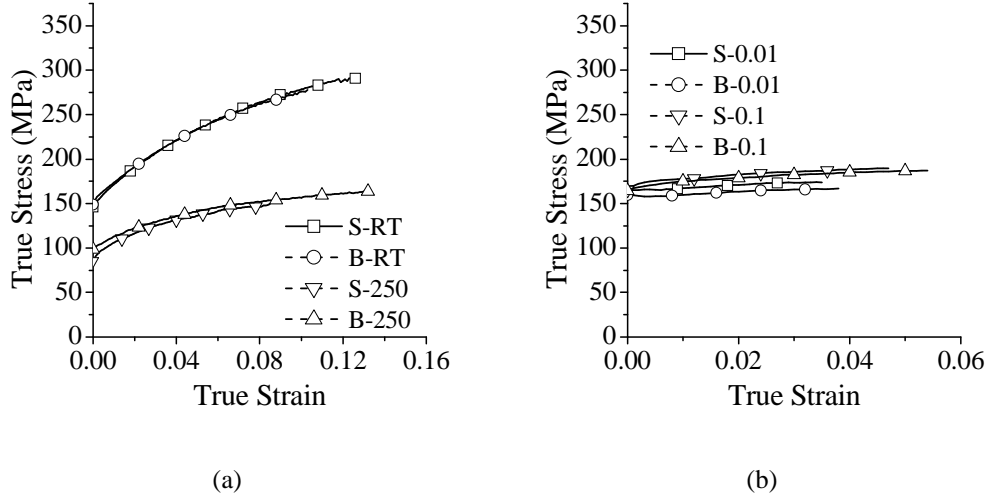
Figure 3.5: Tensile tests along RD with B and S specimens for (a) 6016-T4 at RT and 250°C with a strain rate of 0.01 s^{-1} after 30 s holding (b) 6061-T6 at two different strain rates after 30 s of holding at 250°C

Tensile tests were carried out with B and S materials in order to check the effect of specimen thickness on tensile test results. With almost same chemical composition (refer chapter 2) and after same heat-treatment it is interesting to note from figure 3.5 that thickness has negligible effect on stress-strain plot for all process conditions meaning the tests carried with S and B materials are comparable.

3.3. Plane Strain Compression

3.3.1   Introduction

Orowan [6] first proposed Plane Strain Compression (PSC) tests as a simulation of material flow behaviour experienced during plate and strip rolling. Since then, extensive investigations have been carried out by different researchers using different machines with standard principle testing parameters [7-10]. In the current investigation, PSC tests are used to observe and measure the microstructure and texture evolution at larger strains than the ones obtained in tensile tests. This information will contribute to the development of physically based models that include microstructural parameters such as the dislocation substructure.

3.3.2   General description
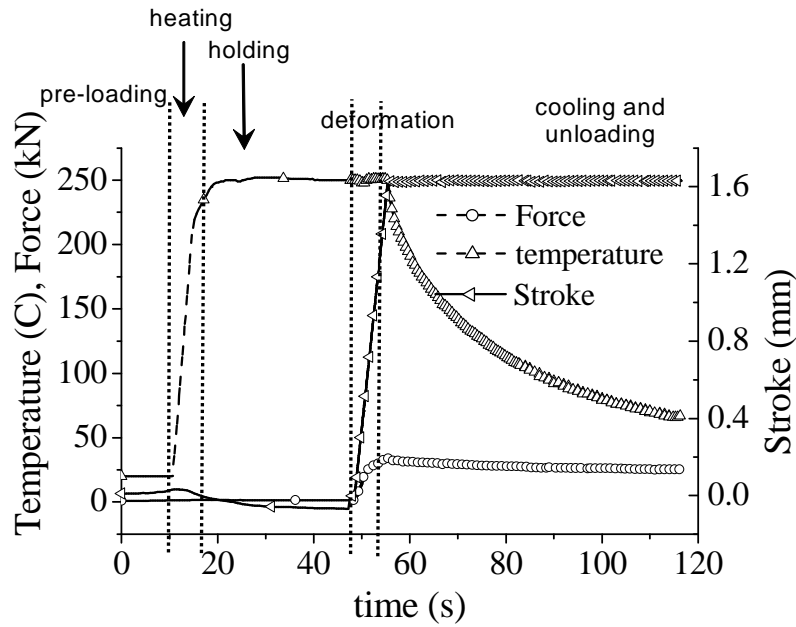
Figure 3.6: Schematic of the PSC test

PSC tests have been done using the thermo-mechanical simulator Gleeble 3800 under controlled conditions of temperature and strain rates. That the alloys were tested approximately one year after their production date is believed to have negligible influence on the test performance. Test pieces of desired dimensions were cut from as received sheets of 3 mm (B samples) by spark erosion technique. The loading direction (LD) is perpendicular to the sheet (parallel to ND) and the extension occurs along the rolling direction (RD) for most of the tests.

L = 40 mm
b = 20 mm
w = 8 mm
a = 30 mm

(a)

(b)
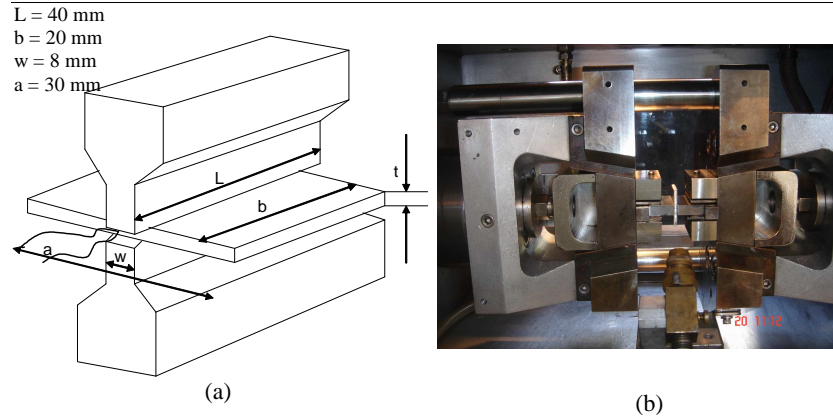
Figure 3.7: (a) Schematic diagram of the PSC anvil (b) Gleeble 3800 chamber

The specimen and anvil dimensions along with the chamber of the Gleeble 3800 hot forging simulator are presented in figure 3.7. To ensure a uniform deformation of the test specimen lateral rigidity and accurate alignment between the anvils were checked carefully. It was found that flow pattern could be asymmetric due to misalignment [11,12]. The compression has been performed with 8 mm width (w) anvils, made of Tungsten Carbide. Anvils are longer than the specimen. Tungsten Carbide is strong enough to sustain the load requirement during deformation and does react neither with the test piece nor with the lubricant. The ratio of anvil width to sample thickness is always more than 2. As the anvils move during deformation the material is compressed (along, say, the z-axis) and extended along the anvil width (say, x). The friction between the anvils and the sample has been reduced by applying a paste made of chemically pure Ni and graphite that can withstand a temperature up to 1400°C. The samples were pre-loaded with 1.5 kN force during heating and holding before the deformation starts. The thermocouples were spot welded at the middle of side of the specimen (in the (x,z)-plane). The heating occurs following the principle of the Joule effect at 50°C/s, ensuring a very fast temperature homogenization all over the sample. Strictly speaking, the displacement was not restricted only to the (x,z) plane as lateral widening (along y), though small, was unavoidable. After deformation, the specimens were simultaneously cooled by compressed air and unloaded. The entire process is represented graphically in figure 3.6. The maximum deformation imposed was 35% of the initial thickness.

3.4. Deep-Drawing

3.4.1   Introduction

Deep drawing of sheets is a widely accepted method for the production of carbody panels. It is also an important and popular process in the assessment of formability of sheet metals. The objective of the deep-drawing tests was to investigate the influence of process parameters on the force-displacement curves, foot print[1] of the drawn cups used to characterize the earing profile, and on the thickness distribution along the cup cross section. Moreover, the results were also used for validation of the coupled work hardening, crystal plasticity and Finite Element (FEM) models. During cup drawing, the majority of the deformation occurs in the flange region and the average r-value, r_{avg}, is a good measure of the drawability. Higher r_{avg} values prevent thinning in the cup wall by increasing planar flow in the flange resulting in delayed onset of necking. Thus, higher r_{avg} increases the drawing depth. This parameter was measured from the tensile tests presented in section 3.2. Foot print measurements were used to characterize the type and amplitude of planar plastic anisotropy. In case of four fold symmetry anisotropy, Δr also gives a good estimation of the drawability. The higher the Δr value the more pronounced the ears leading to a reduction in drawing depth as ears must be trimmed. Thickness variation along the cup is also an important parameter as extensive thinning can result in tearing. The change in thickness of drawn cups was observed and analyzed by some researchers [13-16]. However, the full theoretical description of the drawing operation is less documented, as the conditions of straining are complex and vary from point to point in type and magnitude. Metal drawn inwards over the die is subjected to an enormous amount of hoop compressive strain, while the part formed over the punch profile is under biaxial tension. Experimental investigation of strains for drawing cylindrical cups from a flat circular blank was first done by Chung and Swift [14]. In their analytical investigation for the cup thickness, they assumed the strain rate to be constant during drawing which is not a tangible assumption. Mahdavian and He [13] developed an analytical model to calculate the thickness of the drawn cup taking the friction force between the blank and the tool

---

[1] Equivalent to earing, i.e. a wavy projection formed at the open end of a cup or shell in the course of deep drawing because of differences in directional properties. Also termed as scallop. An important consequence is inhomogeneous distribution of mechanical properties and wall thickness due to volume conservation.

into account. The reduction of frictional force was found to prevent the thinning of the cup wall.

3.4.2   Procedure and test conditions

Warm deep drawing tests were carried out at TNO Science and Industry laboratories in Eindhoven (The Netherlands) on sheets of 6016 and 6061 of T4, T6 and W (as solutionized) tempers. A 1000 kN hydraulic press was used to perform the tests. The general view of the tool and the press is shown in figure 3.8 and basic data are given in table 3.2.

(a)   (b)
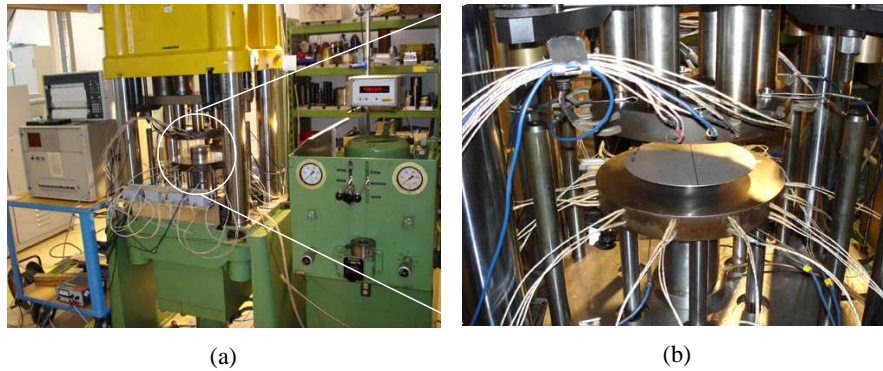
Figure 3.8: Picture of the applied tool set-up (a) overall view (b) tool set-up with blank, blank holder, die, punch and heating arrangements. The white wires are connected to the heating rods while the blue wires are connected to the thermocouples.

Table 3.2: Dimensions of the tool

Parameters	Values (mm)
Punch diameter (d_p)	110
Punch nose radius (r_p)	10
Inside die diameter (d_d)	113
Draw in radius	15
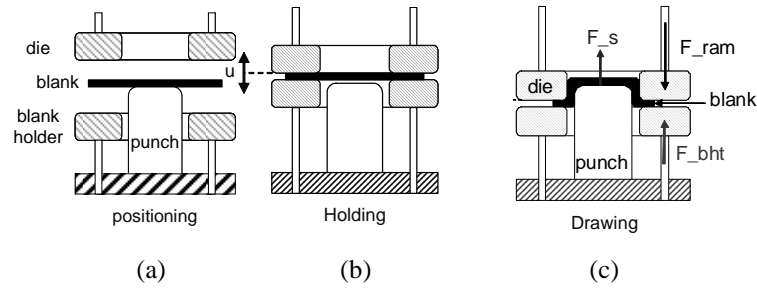
Figure 3.10: Schematic deep-drawing operation

A short description of the deep-drawing procedure is presented schematically in figure 3.10. The blanks were placed on top of the cold punch, which was little shifted vertically from the blank holder (figure 3.10a). The blanks were lubricated with a water based paste that contained Mo_2S. The paste was applied on both sides of the blank before being placed on top of the cold punch. For drawing at warm temperature, the die and blank holder were heated by means of electrical resistance heating arrangements while the punch remained cooled by internal water flow throughout the entire process. The blanks were assumed to be heated up and reach the desired temperature very quickly (in seconds) as soon as they were in contact with the die and the blank holder (figure 3.10b). The holding time, which is the time during which the blank is maintained at the drawing temperature before the drawing starts, is counted from the moment the hot die and blank holder were in contact with the blank. Other press parts were not warmer than 30°C. During heating the water of the lubricant evaporates leaving only the lubricant on the blank. Drawing was performed by moving down simultaneously the die and blank holder while the punch remained immobile (figure 3.10c). Drawing was stopped when the die reached the desired depth, which was set before the blank completely flows inside the die. The cups were water quenched after warm drawing. There was a time lapse of around 5 s between the completion of drawing and water quenching. For drawing at RT the sequence of operations remained exactly the same, except the heating and cooling steps.

The drawing tests were carried out for 6016 and 6061 alloys of W, T4 and T6 tempers. Tests were performed at RT, 180°C and 250°C for different holding times (10 s, 30 s and 600 s) and punch velocities (between 10 and 120 mm/s). The drawing depths were fixed either at 65 or 80 mm. The blank holding pressure (BHP) was adjusted to ensure flowing of the material pressed under the blank holder without tearing while preventing wrinkling. All the above parameters were varied in one series of tests, denominated test A. Another series of experiments termed as series B, were performed to dissociate possible effects of tool geometry from the ones of

plastic anisotropy. In test series B, the rolling direction of the blanks were put at different angles with respect to a reference direction of the tool. Series C was done to examine the effect of friction between the blank and the tool by varying the lubrification conditions. The results from series A are presented in chapter 4 and chapter 5 to study the effect of precipitates, temperature and deformation rate while series B and series C tests are reported in chapter 6 explaining the effect of anisotropy.

3.4.3   Test output and accuracy

Apart from generating the force displacement response, ear profile and thickness distribution from the bottom to the flange of the drawn cups were the two most important outputs from the drawing tests.

Force displacement response

The machine recorded the data for ram force (F_ram) and blank holding force (F_bht), the difference of which is the punch force (F_s). During holding F_ram and F_bht are equal and the blank remains immobile. During drawing F_ram increases and F_bht also increases to counter F_ram. When F_bht reaches the chosen blank holding force, only F_ram continues to increase so that drawing starts. This moment defines the origin for the force-displacement plot.
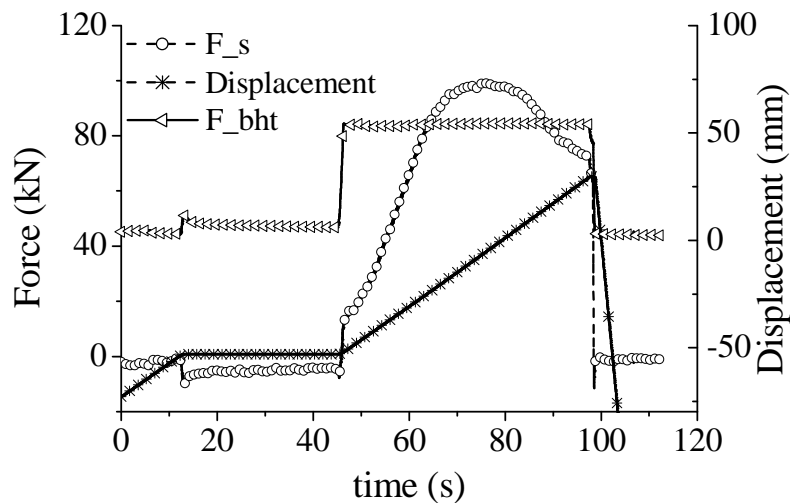
Figure 3.11: Typical drawing plot showing the force-displacement response for the material (F_s), the blank holding force (F_bht) and the displacement of the die (u) at different stages of drawing

A schematic of the forces acting during the drawing operation can be seen in figure 3.11. The plot represents the changes of force (F_s), BHP (F_bht) and punch displacement (u) with time. There was a small value of positive BHP even during the time of closing and holding.

Ear profile

(a)   (b)
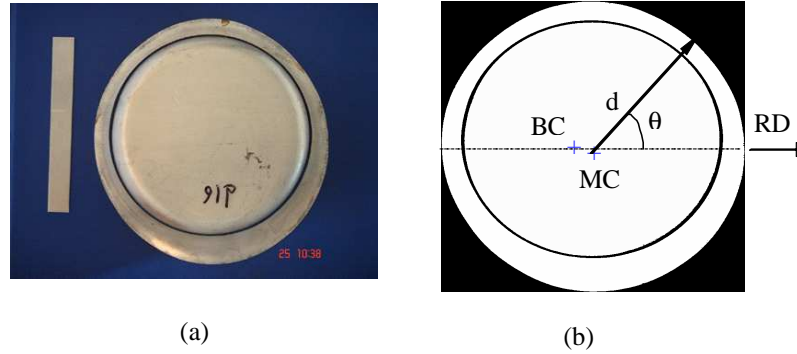
Figure 3.12: (a) Digital picture of the cup and (b) binarized picture with BC and MC.

The plastic flow anisotropy was characterized by measuring the foot-print of the cup. The digital pictures (figure 3.12a) of the cups were binarized and the distance between the pixels of the outer circumference and the central axis of the cup was plotted as a function of the angle from the rolling direction (θ). A linear rule was placed next to the cup and the length of the rule was used for calibration purpose. All the cups were placed keeping the rolling direction horizontally. So angles at 0°, 180° and 360° are along the rolling direction and 90° and 270° correspond to the transverse direction. As noticed from figure 3.12 the centre of the bottom of the cup (referred to as BC) and the centre of the outer circumference of the cup (named MC) may be different. Both centres were considered. A software named "QWin" was used to binarize, clean and fill up holes of the colour picture, find BC and the pixels at the outer circumference. A second program, "GetPix", was used to find MC and calculate the distance (d) of the pixels from the outer circumference from either BC or MC as a function of the angle from the rolling direction (θ) (figure 3.13).
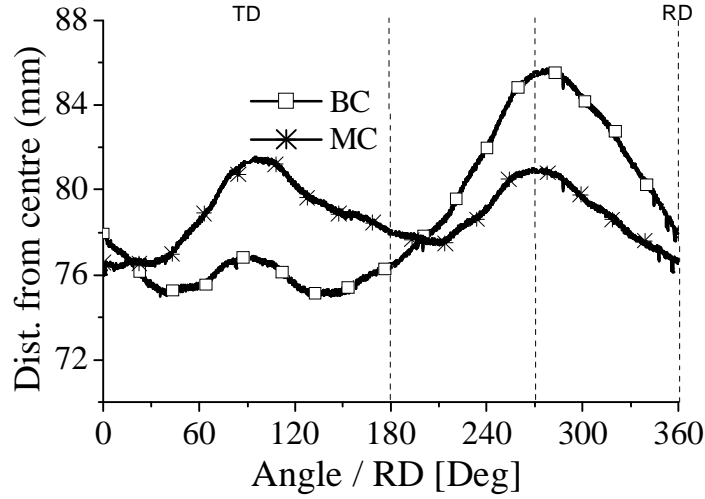
Figure 3.13: Earing with BC and MC

MC is directly linked to the blank center and the ear profile from MC is then only sensitive to the plastic flow anisotropy effect. The point BC corresponds to the punch center and, therefore, the ear profile from BC also depends on the possible shift between blank and punch centers**.** The less the misalignment the more symmetric the ear profile from BC and the appearance of both plots converges. The two centers (BC and MC) should merge together if blank and punch centers were aligned perfectly. During drawing at RT the problem of centre shifting was absent and hence both plots were identical.

Thickness measurement

The thickness of the cups along a radial line going from the bottom center to the flange was measured by using a micrometer. The thickness profile along RD, TD, 30° or 45° from RD has been measured depending on the cup anisotropy. Standard deviations have been calculated by repeating the measurement 10 times at three significant locations: middle of the cup bottom, i.e. between [*s,a*], middle of the first curvature, i.e. between [*a,b*] and middle of the wall, i.e. between [*b,d*] in figure 3.14. The measurement accuracy was found to be ±0.012 mm for all three locations and the same value has been assumed valid for the entire profile.
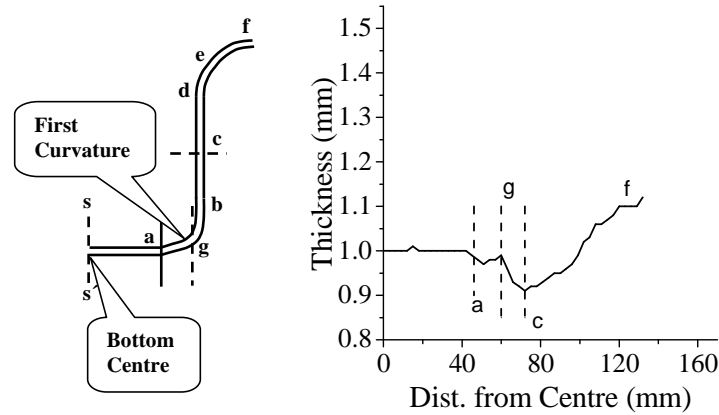
Figure 3.14: General pattern of the thickness profile for half the cross-section of a cup; *sa*: cup bottom, *ss*́: punch axis, *ab*: zone around the punch radius, *bd*: cup wall, *d*: die throat, *e*: die profile radius, *f*: flange

Looking at the nature of all the plots some general comments can be made. The first noticeable reduction of thickness has been found at [*a,b*]. This part was under tension and bended around the punch radius when the punch moves at the time of drawing. The minimum of the thickness plot is seen at position "*c*" which is almost halfway of the wall. The thickness increases from that point up to the flange (*f*). During drawing the reduction of the blank circumference under the die and blank holder generated a tangential compressive force and due to volume conservation of the material this results in thickening. When the metal flows around the die radius, it experiences a bending and unbending under tension which makes the sheet thinner. The final thickness is then the result of a competition between these deformation modes. In between the part of the blank that bends around the punch radius [*a,b*] and the part that flow around the die radius [*b,d*] there is a small ring of the blank where the thickness is close to the initial thickness, hence the local maximum at *g* [15] has been seen. The thickness at the bottom of the cups was found slightly lower than the initial thickness for most of the cases. This difference (maximum 0.05 mm) actually represents the stretching at the bottom of the cups. The difference is, however, small for most of the cases as the friction between the punch and the blank prevents stretching.

Accuracy of force displacement
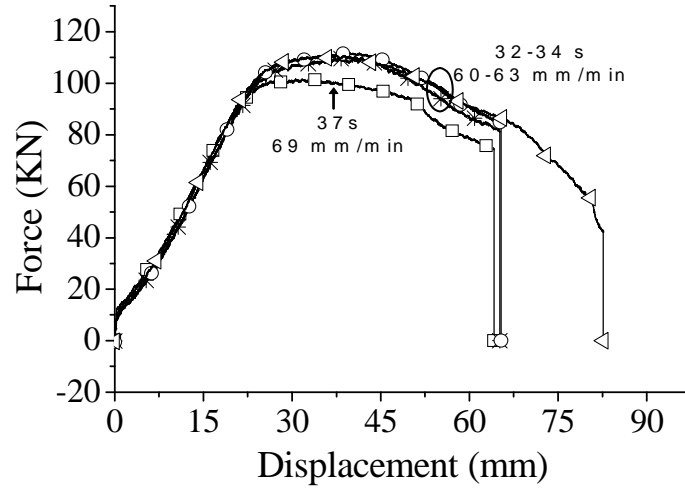
Figure 3.15: Reproducibility for 6061-T6 sheet drawn at 250°C

The general trend for the force-displacement plot shows a sharp increase up to a maximum before the force starts to decrease. The process was found to be highly repeatable, as depicted in figure 3.15. 6061-T6 blanks of drawing ratio 2.0 were drawn at 250°C with various punch velocities ranging from 60 to 69 mm/min. It was found that for a holding time difference of 2 s the force variation is ±1 kN for the same punch velocity and ±2.5 kN for different punch velocities. In general, all forces are within ±1 kN at RT and ±2 kN at 250°C for tests done under the same conditions.

Accuracy of ear and thickness profile

(a)   (b)

(c)   (d)
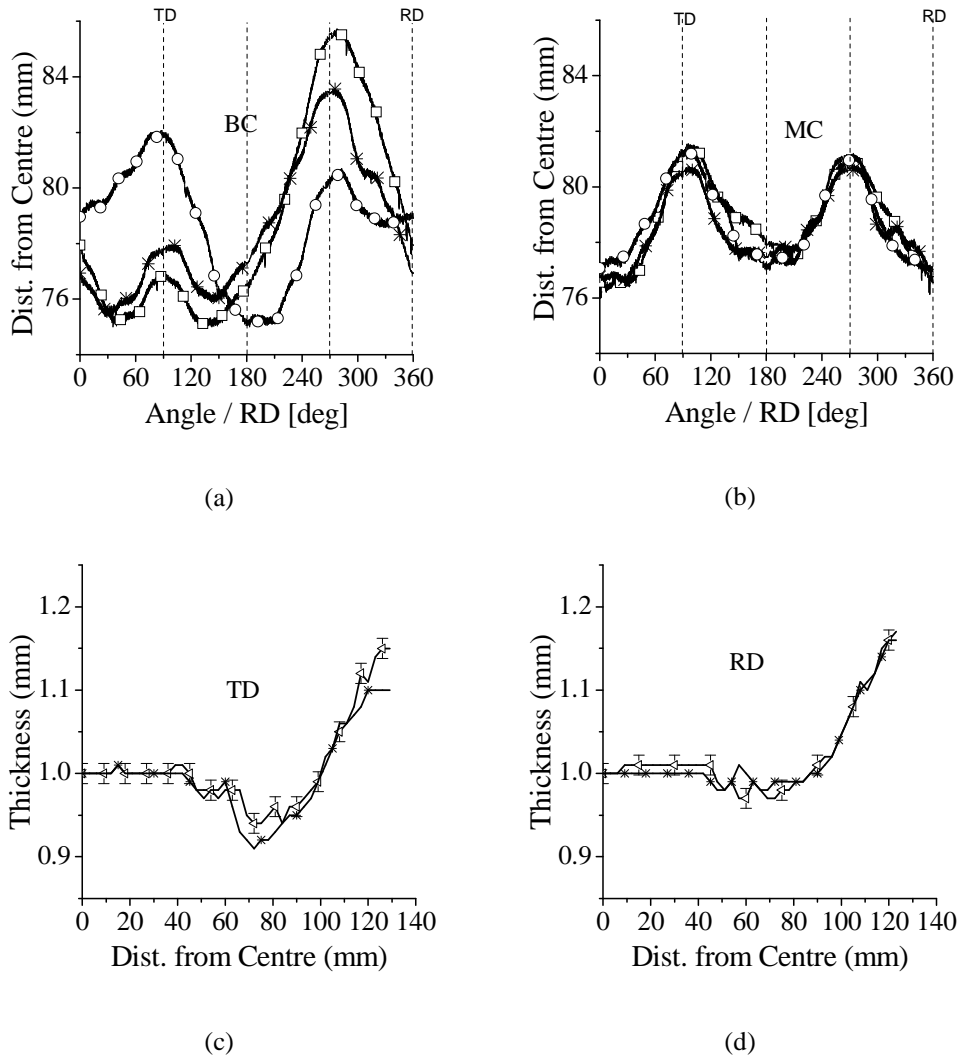
Figure 3.16: Reproducibility of data corresponding to sample 6016-T4 drawn at
250°C for three different tests with similar conditions. The earing profile was
calculated from (a) BC and (b) MC, whereas the thickness was assessed along (c)
TD and (d) RD

The earing profile calculated from MC, figure 3.16(b), shows that the results are
highly repeatable with a maximum variation of about ±0.9 mm although the exact
distance depends on the depth of the drawn cup. The departure of BC from MC due
to the misalignment (maximum 6.49 mm and minimum 1.31 mm within all tests) of
the blank does not affect the repeatability for the foot-print measurement from MC.

The earing profile curves formed with BC were not symmetric because of the misalignment (figure 3.16a). Consequently, earing profiles calculated from MC are used for the remaining of the thesis. The difference in thickness between cups drawn under identical conditions is lower than the thickness measurement accuracy, which confirms the reproducibility of the drawing tests (figure 3.16c and d).

3.5. Bi-axial Tests

3.5.1   Introduction and objective

Bi-axial (BA) tests by means of through-thickness compression were performed in order to achieve larger strain deformation at RT than in tensile tests. The BA yield point would be also useful to construct the experimental yield locus at RT.

3.5.2   Procedure and test conditions

The equi-biaxial tests were performed at Tata Steel (Corus Research Development and Technology at the time of the tests), IJmuiden, The Netherlands. A stack of eleven square sheets have been glued with a PTFE-layer (figure 3.17a) combined with preserving oil as a lubricant [16]. By applying a compressive stress perpendicular to the plane of the glued sheets as shown in the figure 3.17a, the stress state can be compared with an equi-biaxial stress state. With this configuration it is possible to achieve a stress-strain plot with very high strain levels. A friction correction has been applied after the test. A ratio of height-to-width of 1.25 was found to be suitable in order to keep a frictional stress minimum [17]. The tests were carried out in a MTS hydraulic testing machine and to measure the displacement along both in-plane directions a cross extensometer was used, cf. figure 3.17b. Three strain rates 0.001 s^{-1}, 0.01 s^{-1} and 0.1 s^{-1} were used at RT for both alloys of T4 temper.

(a)   (b)
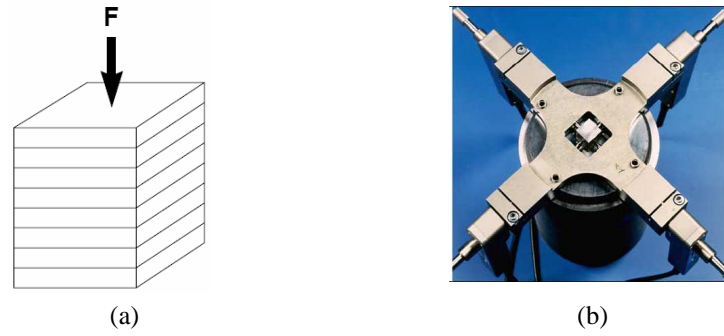
Figure 3.17: (a) Stacked sheet specimens (b) View of cross extensometer

Accuracy of bi-axial tests

(a)   (b)
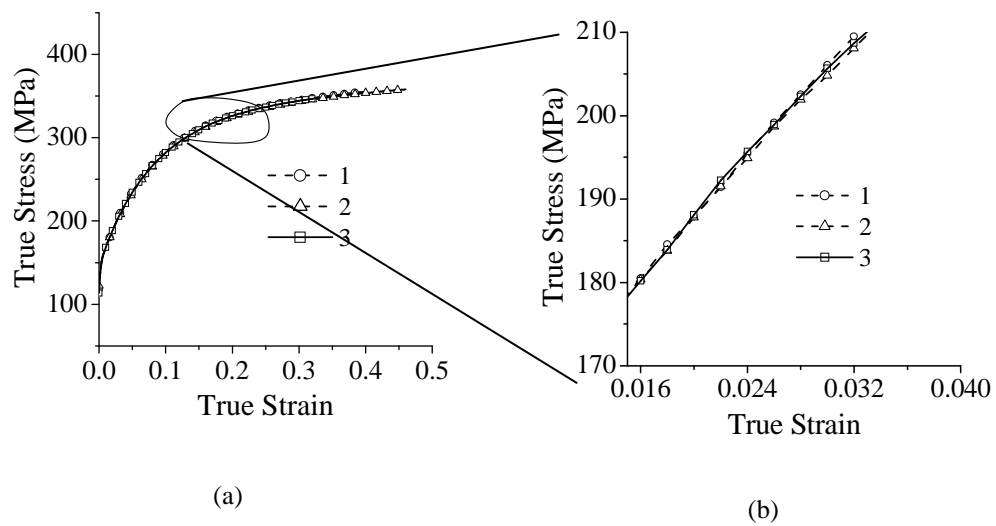
Figure 3.18: Tests for repeatability with 61-T4-S-RT

Figure 3.18 shows that the bi-axial tests are highly repeatable and the stress difference between tests with identical conditions is less than 1 MPa.

References

1. **Stevenson R.**, The low temperature deformation behaviour of 5182-O and 2036-T4 aluminium, *Report GMR-3865*, General motor research Laboratories (Warren, MI), 1981

2. **Ghosh A.K.**, Strain localization in diffuse neck in sheet metals, *Metallurgical and Materials Transactions*, **5A**, 1974, p.1607

3. **Ghosh A.K.**, The influence of strain hardening and strain rate sensitivity on sheet metal forming, *Transactions ASME*, **99**, 1977, p.264

4. **Chan K.S., Koss D.A. and Ghosh A.K.**, Localized necking of sheet at negative minor strains, *Metallurgical and Materials Transactions*, **15A**, 1984, p.323

5. **Burford D.A., Narasimhan K. and Wagoner R.H.**, A theoretical sensitivity analysis of full-dome formability tests: parameter study for n, m, r, and μ, *Metallurgical Transactions*, **26**, 1978, p.103

6. **Orowan. E**, The calculation of roll pressure in hot and cold flat rolling, *Proceedings of the Institution of Mechanical Engineers*, **150**, 1943, p.140

7. **Watts A.B. and Ford H**. An experimental investigation of the yielding of strip between smooth dies, *Proceedings of the Institution of Mechanical Engineers*, (B) **1**, 1952, p.448

8. **Watts A.B. and Ford H.**, On the basic yield stress curve for a metal, *Proceedings of the Institution of Mechanical Engineers*, **169**, 1995, p.1141

9. **Shi H., McLarer A.J., Sellars C.M., Shahani R. and Bolingbroke R.,** Hot plate strain compression testing of aluminium alloys, *Journal of Testing Evaluation*, JTEVA, **25** (1), 1997, p.61

10. **Shi H., McLarer A.J., Sellars C.M., Shahani, R. and Bolingbroke, R.**, Constitutive equations from high temperature flow stress of aluminium alloys, *Materials Science and Technology*, **13**, 1997, p.210

11. **Duckham, A. and Knutsen, R.D.,** Asymmetric flow during plane strain compression testing of aluminium alloys, *Materials Science and Engineering A*, **256**, 1998, p.220

12. **Loveday M.S., Mahon G.J., Roebuck B., Lacey A.J., Palmiere E.J., Sellars C.M. and van der Winden M.R**., Measurement of flow stress in hot plane strain compression tests, *Materials at high temperatures*, **23** (2), 2006, p.85

13. **Mahdavian S.M. and He D.**, Product thickness analysis in pure cup-drawing, *Journal of Materials Processing Technology*, **51**, 1995, p.387

14. **Chung S.Y. and Swift H.W.**, Cup drawing from a flat blank, *Proceedings of the Institution of Mechanical Engineers*, **165**, 1951, p.199

15. **Padmanabhan R., Oliveira M.C., Alves J.L and Menezes L.F**., Influence of process parameters on deep-drawing of stainless steel, *Finite Elements in Analysis and Design,* **43**, 2007, p.1062

16. **Vegter H., ten Horn C.H.L.J., An Y., Atzema. E.H., Pijlman H.H., van den Boogaard A.H. and Huétink J**., Characterization and modelling of the plastic material behaviour and its application in sheet metal forming simulation, in COMPLAS VII, *VII International Conference on Computational Plasticity*, Barcelona 2003, 1

17. **An. Y.G. and Vegter H.**, Analytical and experimental study of fractional behaviour in through-thickness compression test, *Journal of Materials Processing Technology,* **160**, 2005, p.148

CHAPTER 4

EFFECT OF SOLUTES AND PRECIPITATES ON MECHANICAL BEHAVIOUR

This chapter provides a description of the effect of solutes and precipitates on the mechanical response of 6xxx aluminium alloys through tensile, biaxial and deep-drawing tests. Different solute and precipitate states were obtained through variation in temper, holding time before deformation and strain rate. Precipitates are found to have a large influence on the yield strength of the materials while solutes predominantly control the work hardening rate. It is also shown that at extremely slow deformation rate evidence of dynamic precipitation has been revealed.

4.1 Introduction

Most pure metals are soft at ordinary temperature as their crystal structure offers hardly any resistance to dislocation motion along slip planes. The strength increases after appearance of obstacles to hinder the motion of dislocations. The obstacles may be in the form of grain boundaries, second phase particles, solute atoms and dislocation arrays. Precipitation hardening, where small particles inhibit the motion of dislocations and hence strengthen the metal, has been applied since long to improve the mechanical strength of aluminium alloys. In general the precipitates should be present with high density to maximize the strength increment. The stress during plastic deformation, called flow stress, increases with accumulated plastic strain. The entanglement of dislocation motion by various sources, and hence the dislocation accumulation, is the most important structural phenomenon associated with plastic deformation. The dislocations tend to form three dimensional arrays which depend on strain, strain rate, temperature as well as materials features like stacking fault energy, crystal structure, solute content etc. Dislocations also interact with existing precipitates or with precipitates forming on dislocations during deformation, i.e. dynamic precipitation [1]. When second phase particles are sufficiently strong and cannot be sheared by dislocations, they give rise to an improvement of flow stress and work hardening. These hard particles complicate the slip in the matrix resulting in a rapid build up of dislocation density.

In aluminium alloys the dependence of the flow stress on the Peierls-Nabarro stress is small. The main contribution comes from the solute atoms, shearable and non shearable precipitates or dislocation-dislocation interaction. The change in nature and density of the obstacles changes the evolution of work hardening. The strongest aluminium alloys are produced by age hardening of heat treatable alloys (2xxx, 6xxx and 7xxx). The improvement of the mechanical properties is obtained by the precipitation of a fine dispersion of nano scale precipitates from a supersaturated solid solution during ageing. The presence of fine nano scale precipitates is more effective in blocking dislocation motion as compared to dispersoids (50 to 500 nm) and hence precipitation strengthening is more effective than strength effects from dispersoids. Precipitation hardenable alloys generally exhibit low strain hardening rates. Strain rate hardening plays a more important role in improving the resistance to strain localization and the increase of strain rate sensitivity with temperature becomes a key mechanism in improving the warm formability. One important observation of precipitation hardenable alloys is that the increase of the forming temperature produces only a slightly improved performance for stretching operations while it greatly improves the formability in drawing operation [2]. The principle aim of this chapter is, therefore, to identify the effect of precipitates on

yield strength and work hardenig under different ageing conditions and deformation modes. The data generated are used in a work hardening model in chapter 5.

Precipitation in 6xxx system occurs through a sequence of several metastable phases up to the stable ones. These metastable phases are important since the optimum mechanical properties are usually obtained in presence of a distribution of metastable phases. Concerning the sequence and structure of the precipitates quite a large number of results have been published. Approximately 20 structures have been proposed between the initial supersaturated solid solution and equilibrium β phase. The structure of precipitates at the early stage is not well established owing to the difficulty of observing and quantifying the microstructure on such an ultra-fine scale. Drastic quenching from homogenization or extrusion temperature produces a solid solution supersaturated with Mg and Si. Owing to the higher solubility of Mg in Al, Si comes out of the solution and forms clusters when stored at room temperature. Formation of Mg clusters has also been reported [3]. Further storing or heating causes diffusion of Mg and formation of Mg-Si natural ageing clusters (NA). The first phases to precipitate are called *GP* zones. Formation of *GP* zones occurs with the help of quenched-in vacancies. A study by Edwards et al. [4] revealed the presence of two types of *GP* zones namely *GP-I* and *GP-II* or alternatively called β''. Fully coherent spherical *GP-I* zones exhibit a size range of 1 to 3 nm. Partially coherent *GP-II* zones appear as needles having up to 5 nm in width and 50 nm in length. The next phase in the transformation sequence is β'. β' has a rod shape and a lower Mg/Si ratio than β. The stable phase is β (Mg_2Si). 6xxx aluminium alloys obtain their maximum strength by precipitation of β'' metastable phase. An excess Si (Mg[wt%]:Si[wt%]<1.7), as in the case of 6016, is found to [5] enhance the age hardening response by increasing the number density of β'' metastable precipitates. It also reduces the Mg:Si ratio in early *GP* zones and co-clusters. For a Cu containing alloys like 6061, Cu is found to accelerate the kinetics of precipitation and increase the strength during artificial ageing. The effect is large in the underaged region and smaller but noticeable on the value of peak hardness [6]. Extra precipitation of β'' has been identified apart from *GP* zones resulting in a much finer precipitate distribution for the alloy with a higher Cu content. The maximum hardness in these alloys is obtained by the combination of small *GP* zones with approximately 2.0 nm diameter and needles of β'' with typical length size of 10 to 15 nm. The density of these precipitates is high and for β'' needles a value of $10^4/\mu m^3$ has been reported [6]. The determination of the ageing sequence for such alloys is also complicated by the presence of more than one co-existing phase in one particular heat-treatment stage. The increased precipitation kinetics is supported by the formation of the Q' phase in addition to the precipitates formed in the ternary alloys. Q' is the precursor phase of the equilibrium Q phase [6]. The addition of Cu

also reduces the deterioration of the age-hardening response arising from natural ageing of Al-Mg-Si alloys. It is also reported [6] that Cu addition increases the level of supersaturation of Mg and Si by retarding the formation of Mg-Si clusters during natural ageing. In 6061 alloy the sequential appearance of precipitates is mostly the same than in the ternary Al-Mg-Si alloys, only the kinetics may be faster due to the presence of Cu. Also Q ($Al_wCu_xMg_ySi_z$) is expected to form due to the same reason. Pre-deformation also influences the precipitation kinetics. Initially the ageing kinetics of deformed materials is similar to the one of undeformed materials but it decreases rapidly due to progressive annihilation of the quenched-in vacancies towards dislocations. Precipitation during deformation, conventionally known as dynamic precipitation, occurs when deformation is performed in a supersaturated solid solution. Precipitation can appear at a much faster rate than that in conventional conditions at temperature over 170°C [7].

The variety of precipitates that can form in 6xxx alloys, depending on the process condition, shows the necessity to investigate the effect of precipitates on mechanical properties under different conditions. Several precipitate distributions have been obtained by changing the temper or holding time at deformation temperature before deformation. A variation of the deformation rate was used to reveal the effect of dynamic precipitation. The chapter starts with investigating the effect of precipitates during tensile (section 4.3.1) and by bi-axial (section 4.3.2) tests followed by their effect during a deep-drawing forming operation (section 4.3.3). The chapter concludes with a detailed discussion of the subsequent effects. The influence of precipitates on plastic anisotropy is presented in chapter 6.

4.2   Experimental Conditions

Tensile tests were mostly conducted at room temperature (RT) and 250°C for 6016 and 6061 specimens of both S and B with 1 mm and 3 mm thicknesses respectively and T4 and T6 conditions. Some additional tests were also done at 150°C and/or 180°C. The strain rates chosen were 0.01 and 0.1 s^{-1} under normal circumstances and in some cases 0.001 s^{-1} to study the effect of dynamic precipitation. Biaxial tests at a strain rate of 0.1, 0.01 and 0.001 s^{-1} were carried out only at RT for S materials. Deep-drawing tests were also conducted at RT and 250°C for T4 and T6 conditions. Additional tests were done at 250°C immediately after solutionizing the blanks at 540°C for 1 h (W temper). The Blank Holding Pressure (BHP) has been kept constant at 4.1 MPa for the tests conducted at RT and 2.5 MPa for tests at 250°C while the punch velocity (PV) varied between 60 mm/min and 78 mm/min for the standard tests. Additional tests were done with a PV around 10 mm/min to study the effect of a low PV and 120 mm/min for high PV. The mechanical test procedures were described in detail in chapter 3.

4.3   Results

4.3.1   Tensile tests

The effect of solutes and precipitates on tensile properties has been investigated by varying successively temper, holding time before the test and strain rate.

Effect of temper

(a)

(b)

(c)

(d)
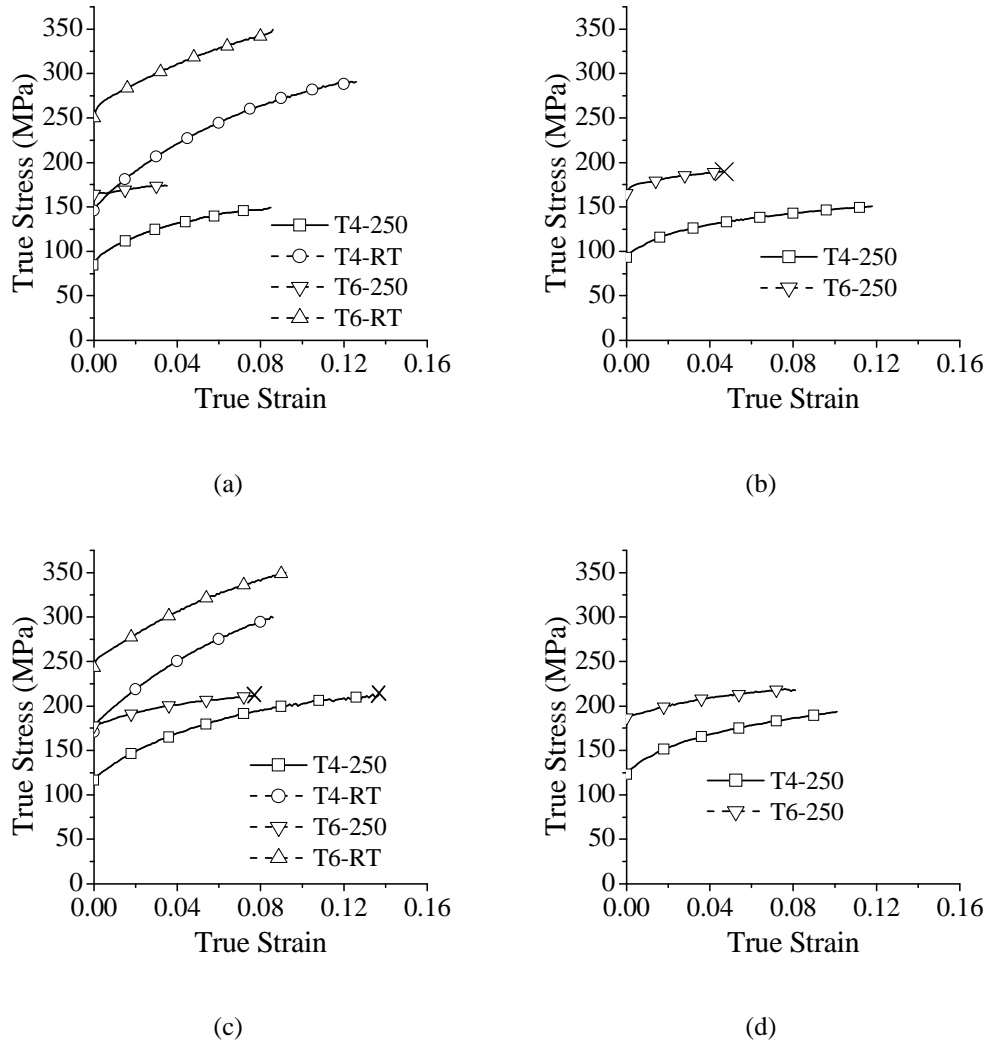
Figure 4.1: Effect of temper on true stress-true strain plots for (a) 6016 alloy at a strain rate of 0.01 s^{-1} (b) 6016 at a strain rate of 0.1 s^{-1} (c) 6061 at a strain rate of 0.01 s^{-1} (d) 6061 at a strain rate of 0.1 s^{-1}. The tensile direction is parallel to RD. The cross marks in the figure indicate the end of uniform elongation

Figure 4.1 illustrates the effect of temper for both alloys at two strain rates and two temperatures. As expected, for all conditions T6 material is stronger compared to T4, although the rate of work hardening is higher for the T4 state at both temperatures (figure 4.2). The difference in work hardening rate is smaller at room temperature than at 250°C. For T6 state deformed at 250°C there is practically no

work hardening and the true stress true strain curve appears almost like a plateau before the onset of necking.

(a)

(b)
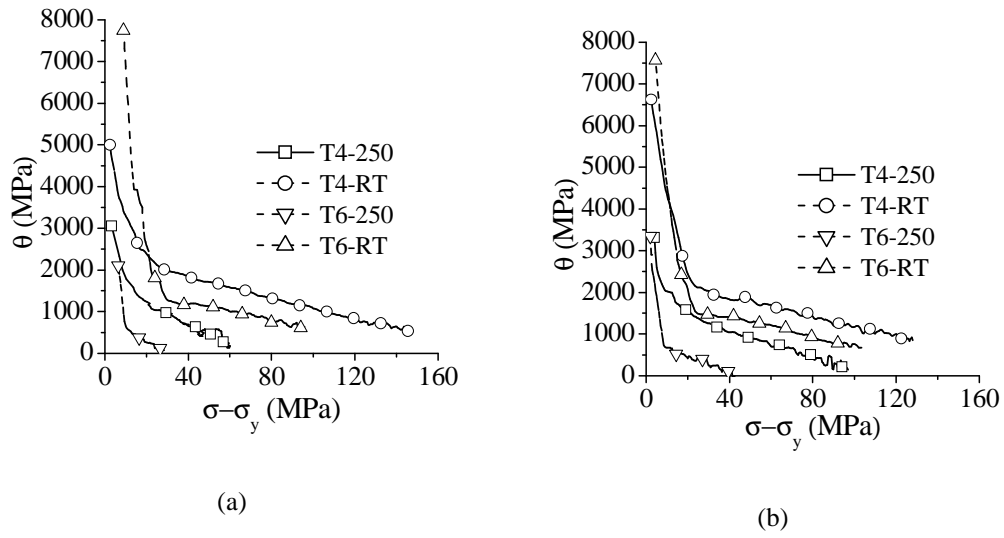
Figure 4.2: Effect of temper on work hardening rate (θ) for (a) 6016 at a strain rate of 0.01 s^{-1} and (b) 6061 at a strain rate of 0.01 s^{-1}. The tensile direction is parallel to RD. σ is flow stress and σ_y is yield strength

Effect of holding time

(a)   (b)
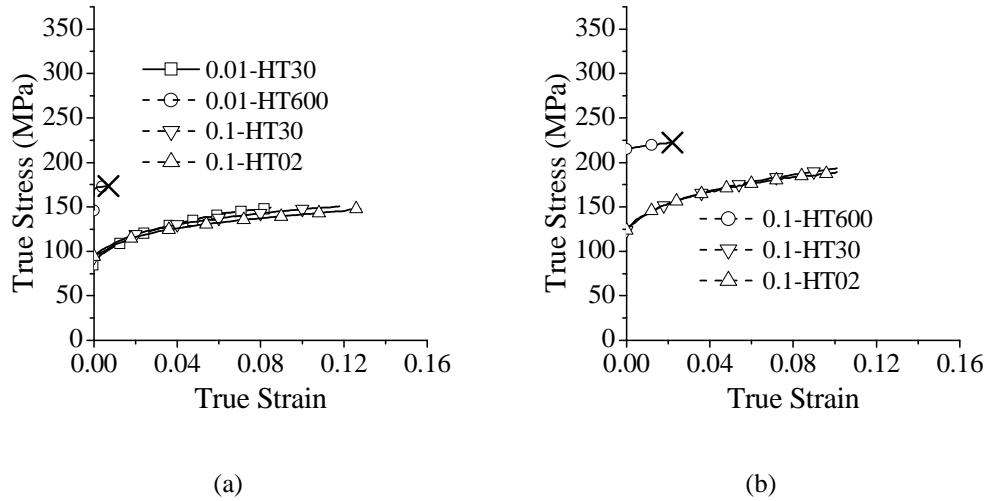
Figure 4.3: Effect of holding time at 250°C on true stress-true strain plot for (a)
6016-T4 (b) 6061-T4. The tensile direction is parallel to RD.

The effect of holding time, i.e. the time period between the end of heating of the specimen to the desired test temperature and the start of deformation, is shown in figure 4.3 for two strain rates. The holding time at 250°C has been varied from a very short period (2 s) to a long period (600 s) with an intermediate standard (30 s) holding in accordance with the static ageing kinetics as reported in chapter 2. At 250ºC, from the static ageing plot of T4 materials it has been observed that the hardness value decreases slightly between 2 and 30 s of holding and this evolution corresponds to the dissolution of small natural ageing clusters. Figure 4.3 shows, however, that this dissolution has almost no effect on the stress-strain plot as the "HT02" and "HT30" plots are completely superimposed.

(a)
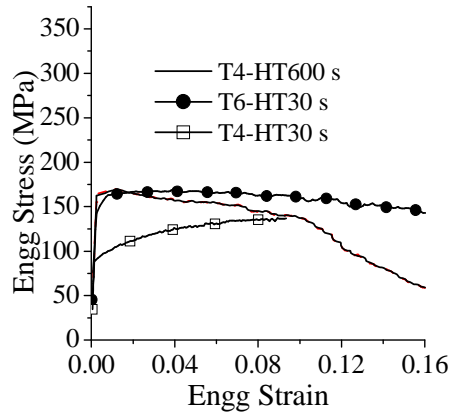
Figure 4.4: Evidence of prolonged necking for alloy 6016-S at 250°C for (a) tests with different holding time before the tensile test (b) Specimen with diffused necking tested after a holding time of 600 s.

Increasing further the holding time to 600 s results in a clear change in mechanical behaviour for T4 materials. With a positive strain hardening response only for a short initial part and higher yield point, the material shows the character of prolonged diffused necking (figure 4.4). Similar stress-strain curves are found for T6 material held for 600 s before deformation. For T4 materials, this situation corresponds to peak hardness according to the static ageing curves. There is a continuous evolution of work hardening behaviour when changing from T4 material with a holding time of 30 s to T6 material and then to T4 and T6 materials with a holding time of 600 s; the uniform elongation decreases and the total elongation becomes dominated by post uniform elongation. From figure 4.4b, it seems that crack initiated from the centre of the specimen and spreads towards the edges.

Effect of strain rate

(a)   (b)
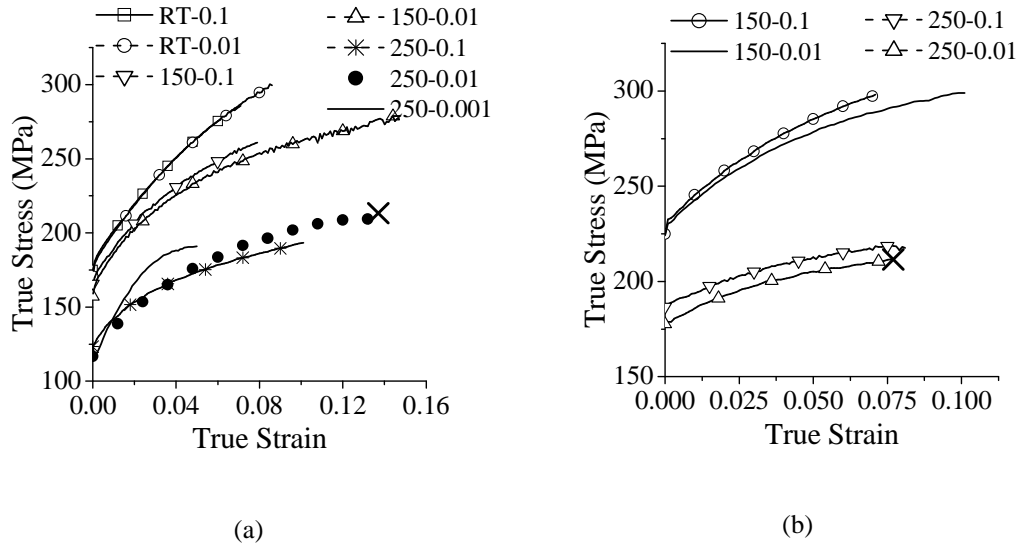
Figure 4.5: Effect of strain rate on true stress-true strain curve, with tensile direction parallel to RD, of (a) 6061-T4-S and (b) 6061-T6-S. Tests at 250°C were started after 30 s holding at this temperature

The effect of strain rate has been investigated for both alloys and temper at RT, 150°C and 250°C by comparing results at two strain rates: 0.1 s^{-1} and 0.01 s^{-1} (figure 4.5). For T4 materials there is no difference in materials response under different strain rates at room temperature resulting in zero strain rate sensitivity. At 150°C the rate of work hardening slightly increases with strain rate for both tempers T4 and T6; T4 specimens deformed at 250°C clearly show a distinct behaviour; with decreasing the strain rate down to 0.001 s^{-1} the yield strength decreases but the work hardening rate becomes initially higher before saturating rapidly, resulting in a lower uniform elongation (figure 4.5a). The above observations are found equally true for 6061-B, 6016-S and 6016-B materials.

4.3.2   Biaxial Tests

(a)

(b)

(c)

(d)
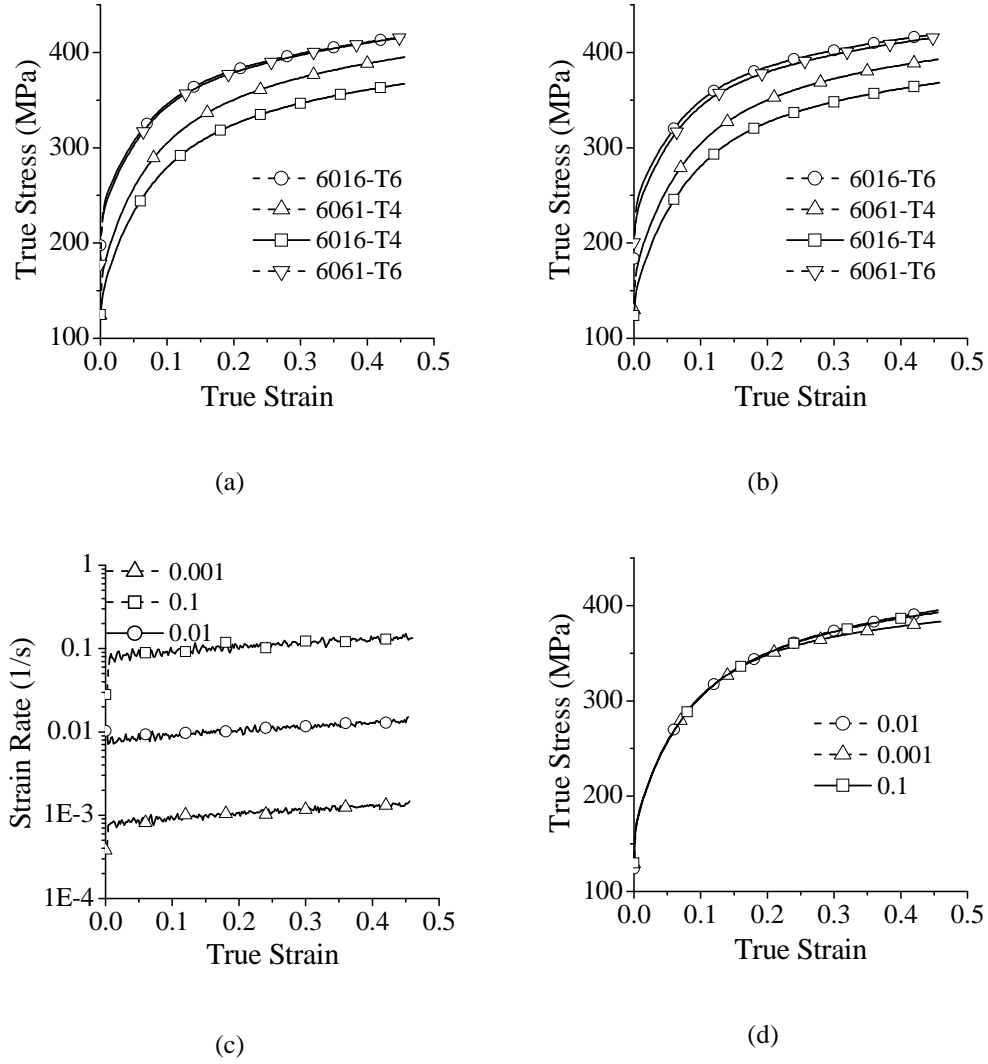
Figure 4.6: Effect of temper on true stress-true strain plots for 6016 and 6061 alloys at RT, at a strain rate of (a) 0.01 s^{-1} (b) 0.1 s^{-1} and (c) evolution of strain rate during the test with 6061-T6 (d) response of strain rate for 6061-T4

The results of the compression tests of stacked plates, used to represent the equi-biaxial behaviour as described in section 3.5, are presented in figure 4.6. The higher strain could be reached with the biaxial test compared to the tensile test. The strain rate has been nicely maintained stable throughout the test as shown in figure 4.6c. Figure 4.6a and figure 4.6b confirm that in T4 condition, 6061 is significantly

stronger than 6016 but the difference is reduced for T6 temper. Figure 4.6d shows that the strain rate also has a negligible effect on the stress-strain response at RT.

4.3.3   Deep-Drawing

It is not possible to achieve the full theoretical description of the deep-drawing process because of its complex straining condition and its variation from point to point in magnitude and type. The metal drawn inwards undergoes substantial hoop compressive strain while the part over the punch profile undergoes bi-axial tension. The effect of precipitates on force-displacement, foot-print and thickness under different conditions of drawing are presented for two sheet alloys.

Effect of temper

(a)   (b)
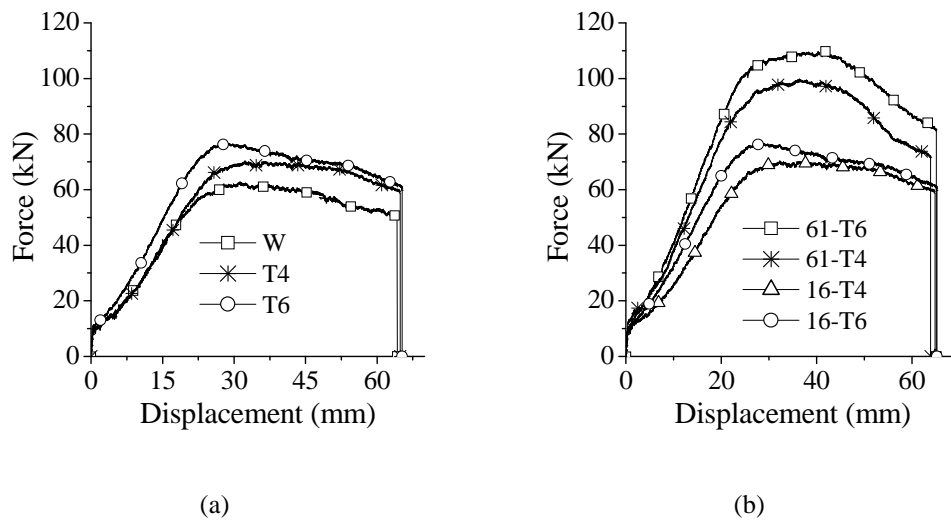
Figure 4.7: Effect of temper on force-displacement plots at 250°C for (a) 6016 and (b) 6016 and 6061

The punch force – punch displacement plots (figure 4.7) are found consistent with the ageing curves and as expected W condition represents the softest and T6 the strongest material. The force response of T4 and W conditions at the beginning of deformation are the same before T4 gets stronger and departs after some point (figure 4.7 a).
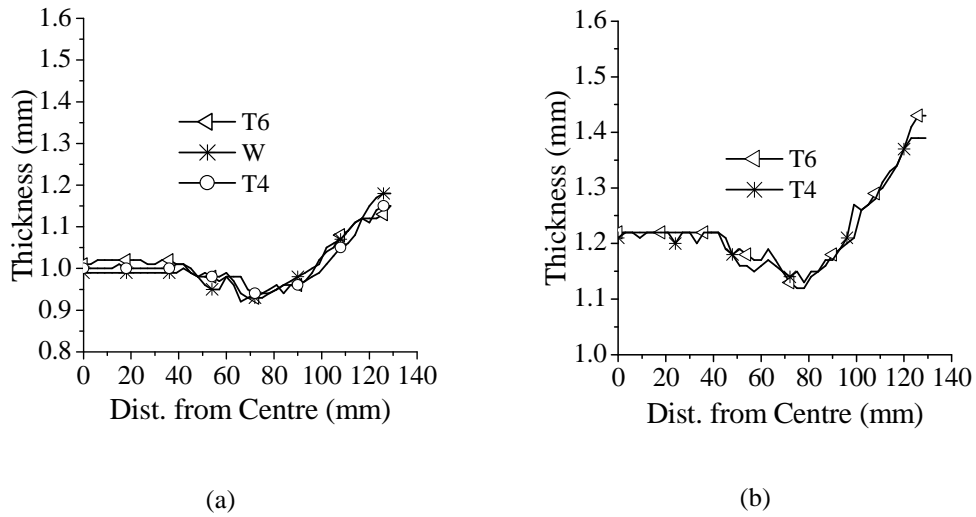
Figure 4.8: Effect of temper on thickness distribution at 250°C for (a) 6016 and (b) 6016 alloys.

The basic nature of the thickness distribution (figure 4.8) is found independent of alloy and temper. More stretching at the bottom along TD is observed for W compared to T4 and T6 tempers but this is well within the accuracy limit of the experiment.

Effect of Holding Time

(a)   (b)
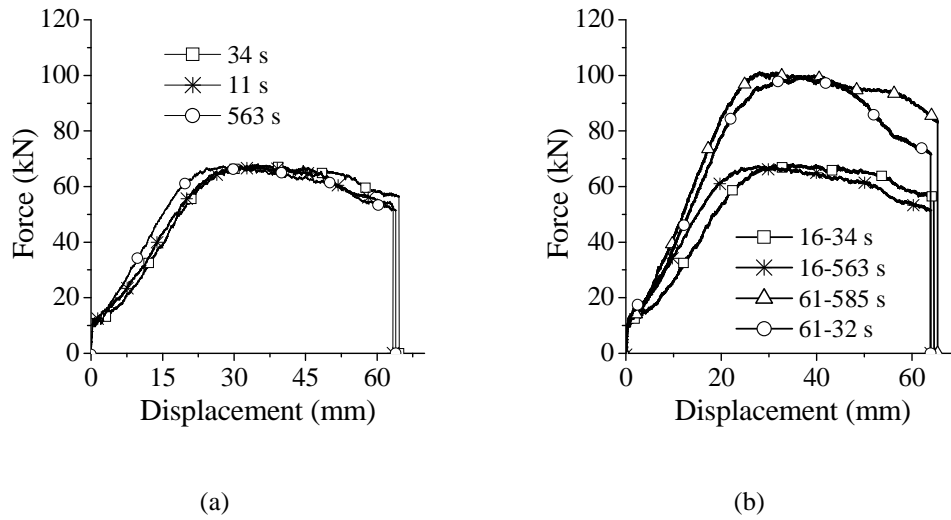
Figure 4.9: Effect of holding time at test temperature before drawing on force-
displacement plot at 250°C for (a) 6016-T4 and (b) 6016-T4 and 6061-T4

The effect of holding time has been investigated for both alloys by holding the plates
between the die and blank holder heated to 250°C for different time spans before
drawing but keeping the same punch velocity and blank holding pressure conditions.
The holding time has been varied from 32 s to 10 min under T4 state. The effect of
precipitates on the drawing force is clearly very limited as there is no significant
difference among the plots of different holding time (figure 4.9). Although for
longer holding time the initial force increase is steeper, interestingly the maximum
for all the plots has been found to be the same. Thickness plots were also found to
overlap with each other. Only for alloy 6061 the cup drawn after a longer holding
time was found thinner along the TD direction after the first curvature.

Effect of Punch Velocity

(a)   (b)
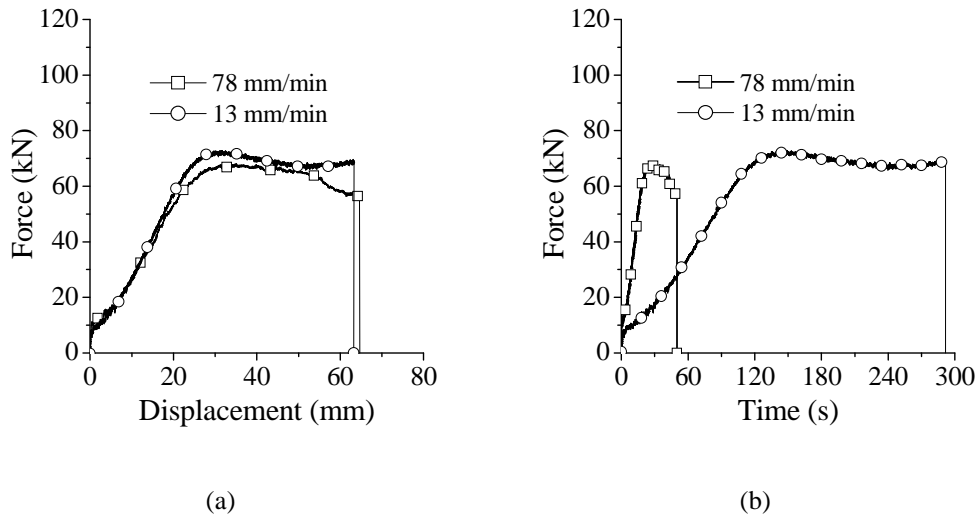
Figure 4.10: Effect of PV during drawing of 6016-T4 sheet at 250°C on (a) force-displacement plot and (b) force-time response

Figure 4.10 compares the results obtained with a low PV (13 mm/min) to the standard case (78 mm/min) for 6016 in T4 state at 250°C keeping the holding time and blank holding pressure constant. It can be noticed from figure 4.10a, that the drawing force is higher for lower PV. Like other parameters, the PV has no influence on thickness plots.

4.4   Discussion

4.4.1   Effect of solutes and precipitates on the mechanical response

The effect of solutes and precipitates has been investigated by varying the temper or the holding time at warm temperature before deformation. T4 (naturally aged) materials have been subjected to a heat-treatment of 150°C for 4 hours followed by 170°C for 4 hours to achieve the T6 state. According to results in chapter 2 (figure 2.17), T4 specimens held for 600 s at 250°C before warm deformation have also reached the peak aged condition although the precipitates (population, morphology and size) is expected to be different than for T6 because of the different ageing temperature. The influence of solutes and precipitates on yield point and work

hardening can directly be noticed from the tensile and bi-axial tests while the punch force-displacement response derived from the deep-drawing experiments results from the full stress distribution in the cup making the interpretation more complex.

For all cases the yield strength was found higher for T6 than T4 temper condition (figure 4.1, figure 4.6, and table 4.1). Similarly, holding T4 specimens for 600 s before the test at 250°C drives the material towards the T6 state and naturally the alloy exhibits a similar yield strength than T6 material (figure 4.4). The yield strength is a function of density and size of the obstacles. Values from literature in terms of precipitate density indicate that T4 exhibits a higher density than the T6 condition (e.g. 3×10^{24} and 4.2×10^{24} particles/m^3 for 6016-T4 and 6061-T4 compared to 1.5×10^{23} and 4×10^{22} for 6016-T6 and 6061-T6 [8]). So clearly the size effect of the particles dominates over the density contribution. The precipitates in T6 being larger, they pin dislocations more effectively than the ones in T4.

Table 4.1. 0.2% off set yield stress (YS$_{0.2\%}$) and parameters of the Voce equation fitted to the experimental tensile test results with a strain rate of 0.01 s^{-1}.

	T4 – RT	T4 – 250°C	T6 – RT	T6 – 250°C
6016				
YS$_{0.2\%}$ (MPa)	153	86	261	157
θ_{max} (MPa)	2070	1310	1390	580
$|\beta|$	10.7	18.1	9.0	37.8
6061				
YS$_{0.2\%}$ (MPa)	178	115	247	171
θ_{max} (MPa)	2180	1720	1390	920
$|\beta|$	11.0	17.5	11.3	23.4

The work hardening rate in a precipitation hardened alloy is generally controlled by the interaction of dislocations with the solutes left in the matrix and with the precipitates. The Equivalent Circular Diameter (ECD) of the precipitates in T4 condition is nearly 1 nm while that for T6 condition it was reported to be 2.5 nm and 3.7 nm for 6016 and 6061, respectively [4]. Furthermore, in the T4 stage the precipitates are mostly spherical while they are rod shaped β'' in the T6 stage. The above facts show that a less dense population of bigger precipitates results to a decrease of work hardening rate. At 250°C the work hardening rate for T6 decreases to such an extent that the true stress strain curve becomes practically flat resulting to almost no work hardening. The work hardening rate versus flow stress plot, or

Kocks-Mecking plot, had proved to be an efficient representation to analyse experimental data. The Voce equation has then been fitted to the stage III part of the work hardening curves in order to determine the initial work hardening rate at the beginning of stage III ($\theta_{max} = d\sigma/d\varepsilon_p$) and the dynamic recovery parameter ($\beta = d\theta/d\sigma$ during stage III) (table 4.1). At RT the lower work hardening rate for T6 materials compared to T4 comes from a lower value of θ_{max} since β values are similar. This is in accordance with other experimental data [9,10] that show that the initial work hardening rate (θ_{max}) of T6 or peak-aged materials is minimum, meaning that precipitates do not contribute to the storage of dislocations. Several explanations have been proposed in order to explain this effect. Cheng et al. [9] proposed that precipitates at peak-aged conditions are still shearable while Simar et al. [10] suggested that precipitates at peak-aged conditions are non-shearable but because their size is only slightly larger than the transition radius shear-by pass they can still be sheared after accumulation of Orowan loops. The decrease of θ_{max} from T4 to T6 tempers is therefore usually explained as the result of solution depletion [10,11]. It is also expected that, when going from T4 to T6, the solute depletion should make dynamic recovery faster while the growth of shearable precipitates should make dynamic recovery slower. Literature data show that the dynamic recovery parameter ($|\beta|$) is unaffected or slightly decreased when changing from the T4 to the T6 condition, which means that the effect of precipitates tends to dominate. Our experimental results also show the same at RT. The obtained β values are similar to the ones reported for AA6111 [9] or for AA6005A [10]. This implies that dynamic recovery in AA6xxx series is relatively independent of the exact solute content and precipitate distribution.

At 250°C, the observed decrease of work hardening rate from T4 to T6 condition is due to both a decrease of θ_{max} and an increase of $|\beta|$. Lower θ_{max} values for T6 can be explained by the depletion of solute during ageing as it was at RT while the sharp increase of $|\beta|$ between T4 and T6 tempers suggests that at higher temperature, solutes control dynamic recovery.

There is a clear correspondence between the increase rate of the drawing force during deep drawing and the yield strength or hardness of the material and therefore with the precipitate population; at 250°C the drawing force increases less rapidly during drawing of T4 blanks than during drawing of T6 blanks (figure 4.7b) or T4 blanks held for 600 s at 250°C (figure 4.9b). The two last cases are similar. Furthermore, the effect is more pronounced for 6016 than 6061. The change of hardness between T4 and T6 or after 600 s ageing at 250°C is also higher for 6016 than for 6061 supporting the correlation between material strength and the increase

rate of drawing force. Only drawing of W blanks shows a departure from this observation since drawing of W and T4 blanks requires a similar force at the beginning of drawing while W material has a lower yield strength than T4 one.

Looking at the temper effect, the maximum drawing force increases when following the temper sequence: W to T4 and to T6. This suggests that the maximum force is related to the yield strength or hardness too. However, increasing the holding time before drawing from 30 to 600 s has no effect on the maximum force of T4 blanks, while it was shown it increases the yield strength to the same level of T6 material. Therefore, there is no one-to-one relation between yield strength and maximum drawing force. In the present investigation the maximum force was reached after approximately 30 mm of punch displacement, which is enough for the formation of the cup bottom and the first curvature of the wall. Therefore, the contribution of work hardening becomes important when the maximum force is considered. An interesting observation from the present investigation can be made in support of the above proposition. The lower maximum force during DD for naturally aged material with long holding time, compared to T6 material, can be explained by considering the higher work hardening rate for T6 compared to T4 material with long holding time (figure 4.4).

The results presented in this chapter can be explained on a qualitative basis, but a more detailed analysis of the deep drawing process is presented in chapter 7.

4.4.2   Effect of alloy composition

(a)   (b)
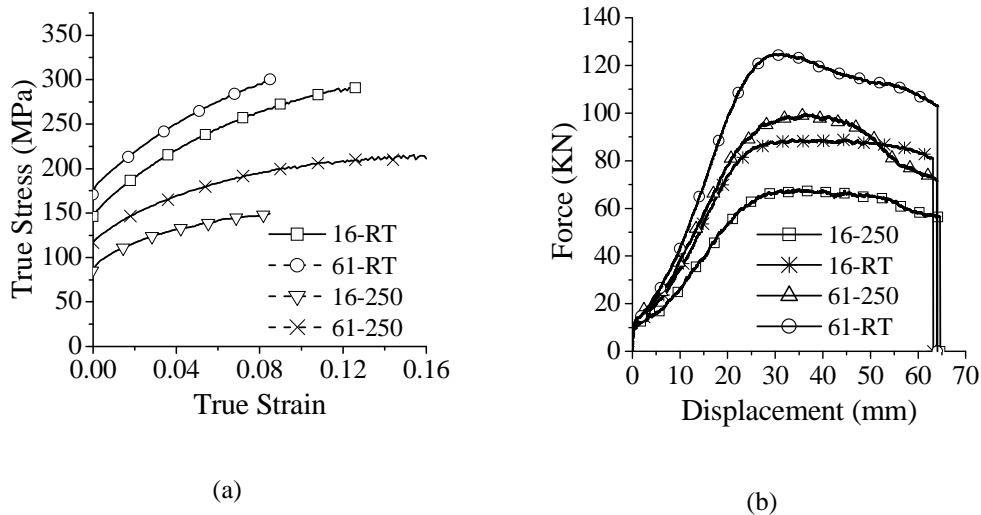
Figure 4.11: Effect of alloy composition on material strength during (a) tensile test of T4 specimens with 0.01 s^{-1} strain rate (b) deep-drawing test of T4 blanks.
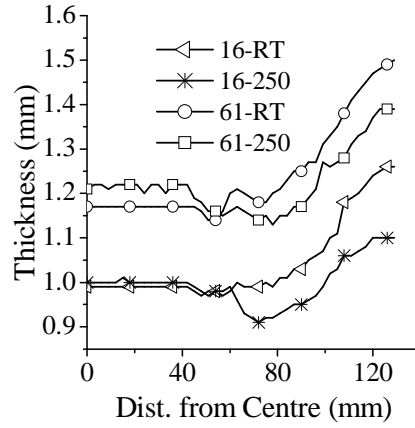
Figure 4.12: Effect of alloy composition on the thickness distribution for T4 conditions.

The effect of alloy composition has been demonstrated for tensile tests (figure 4.11a), bi-axial tests (figure 4.6a and b) and deep drawing tests (figure 4.7b, 4.11b and 4.12). In T4 condition, 6061 is stronger than 6016 material in tensile and bi-axial stress mode for all the respective temperatures, in line with hardness measurements. The work hardening rate is also higher for both temperatures, which is due to the higher initial work hardening rate, θ_{max} (table 4.1). Both observations logically explain the higher drawing forces for 6061-T4. The reason for the higher strength of 6061-T4 compared to 6016-T4 has been explained in chapter 2 (section 2.2). Tensile tests also confirm the RT hardness measurements in T6 condition with lower yield strength for 6061 than for 6016. Interestingly, at 250°C, the yield strength of 6061-T6 is again higher than for 6016-T6 as was the case in T4 condition. It was shown in chapter 2 that explaining these differences requires a quantitative estimation of the solute content and the precipitate distribution. At both temperatures, however, it was observed that the work hardening rate is higher for 6061-T6 compared to 6016-T6, as it was observed for T4. The main difference is the much faster recovery rate (higher $|\beta|$) at 250°C for 6016-T6 compared to 6061-T6 (table 4.1). Concerning the thickness distribution, there is hardly any difference between the two alloys. The thickness profile (figure 4.12) is higher for 6061 owing to its higher initial thickness. Therefore, the difference in composition and hence the precipitate state does not affect the thickness profile for the present investigation.

4.4.3   Effect of dynamic precipitation

The possible effect of dynamic precipitation has been investigated by varying the strain rate and PV of tensile and deep-drawing tests respectively. In case of T4 material deformed at 250°C it has been observed that work hardening becomes faster with lower strain rate during tensile tests (figure 4.5) and that the punch force increases with decreasing PV during deep-drawing (figure 4.10 and figure 4.13a and b) so that the initial soft material gradually becomes harder and approaches the T6 one. Both alloys exhibit qualitatively a very similar behaviour and the difference is only quantitative. These observations can be explained in terms of dynamic precipitation behaviour. Dynamic precipitation is not uncommon in aluminium alloys. E.g. evidence of dynamic precipitation have been reported for 6061, 6111 [12] and Al-Zn-Mg [13] alloys. Since precipitation is a diffusion controlled process slower strain rate allows more time for precipitation to take place. The static ageing curve (cf. chapter 2) at 250°C for 6016-T4 and 6061-T4 showed a drop of hardness after 30 s and a rapid rate of increase after 3 min of annealing. However, the maximum hardness was attained after 10 min of ageing. During tensile tests, after holding at 250°C for 30 s the time to reach the maximum force with a strain rate of 0.001 s^{-1} was about 50 s. The time to reach the maximum force during the drawing test is around 160 s (plus 30 s of holding time) for lowest PV of 11 mm/min (figure 4.10b). This means that during deformation, significant increase of hardness, hence precipitation occurs according to the static ageing curve. Furthermore, it has been reported that dynamic precipitation brings down the over-ageing time from 1000 min to 1 min at 170°C [7] for AA6061 indicating the pronounced effect of deformation. Another study [14] on the same alloy showed that dynamic precipitation by equal channel angular extrusion also brings down the time to reach the peak hardness from 1000 min to 10 min compared to static ageing. Therefore, dynamic precipitation is indeed expected during the slow strain rate tests of this investigation.

(a)   **(b)**
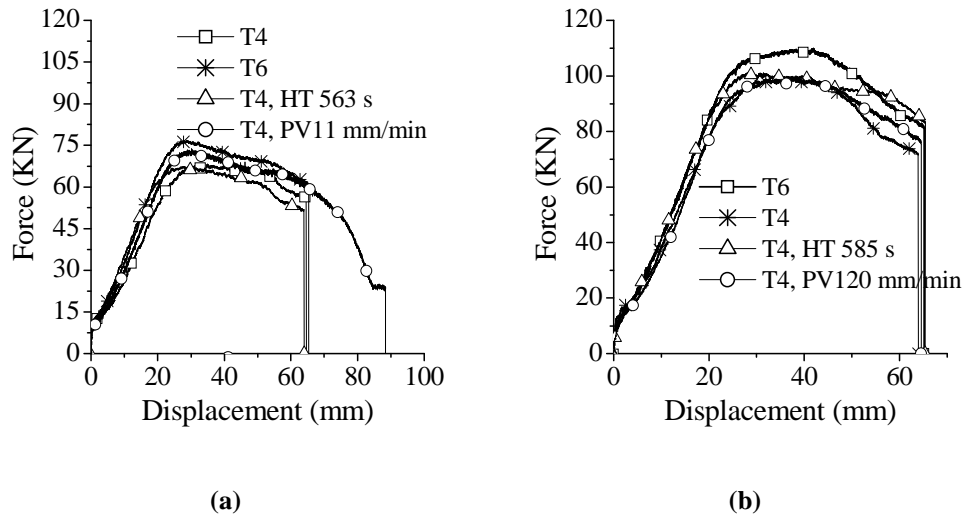
Figure 4.13: Effect of precipitates at 250°C for (a) deep-drawing with 6016 (b) deep-drawing with 6061. Standard holding time is 30 s and PV is 60-80 mm/min.

It can be seen in Figure 4.13b that deep drawing of T4 blanks at 250°C with punch velocities between 60 and 120 mm/min produce the same force displacement response. It shows that no dynamic precipitation takes place in this PV range. Figure 4.13 also compares the effect of different ways to produce precipitates on the drawing force. The interesting fact that can be noticed is that the force displacement response is very similar to the one in T6 condition because of dynamic precipitation at the lower PV rates. On the other hand, precipitates formed by holding the blank at 250°C for 10 min before drawing do not result in higher maximum forces than in T4 condition but only lead to a faster force increase similar to the one observed in drawing T6 sheets.

4.5   Conclusions

The effect of solutes and precipitates on the mechanical properties has been investigated from various perspectives. The results driven from various mechanical tests e.g. tensile, bi-axial and deep-drawing at room and higher temperatures are similar in nature and helped to draw the conclusions.

The higher work hardening rate or increase in drawing force with displacement for the natural ageing state (T4) compared to the artificial ageing one (T6) is attributed to the lower solute content in the matrix in T6 state, which controls the dislocation

storage rate. In both tempers precipitates do not contribute to work hardening. At higher temperature, solute content is also found to influence the rate of dynamic recovery. The higher yield stress for T6 is purely due to the size increase of fine shearable precipitates. The increase of holding time from standard (30 s) to 600 s yields a similar strength response to the one obtained in the T6 state. Longer holding time tests are associated with the occurrence of prolonged diffused necking before failure during tensile tests. With extremely slow deformation rate evidence of dynamic precipitation is revealed. The analysis of the results also show that the increase rate of the force during drawing bears a relation with the material yield strength while the maximum drawing force is also controlled by the work hardening properties. Despite their influence on yield strength and work hardening rate, solutes and precipitates do not have any influence on the thickness distribution plots.

The two alloys did not show any remarkable qualitative differences for the properties under investigation. Alloy 6061 is found to be stronger than alloy 6016 and work-harden faster at all temperatures.

References

1. **Deschamps A., Bréchet Y. and Guyot P.**, Interaction between plasticity and precipitation, *Proceedings of the 7th seminar of the international federation for heat treatments and surface engineering,* Budapest, Hungary, 1999

2. **Finch D.M., Wilson S.P. and Dorn J.E.**, Deep Drawing aluminium alloys at elevated temperatures, part I – Deep Drawing cylindrical cup, *Transactions ASM*, **36**, 1946, p.254

3. **Andersen S.J., Cerezo A., Zandbergen H.W. and Jansen J., Traholt C., Tundal U. and Reiso O.,** The crystal structure of the β'' phase in Al-Mg-Si alloys, *Acta Materialia*, **46**(9), 1998, p.3283

4. **Edwards G.A., Stiller K., Dunlop G.L. and Couper**, The precipitation sequence in Al-Mg-Si alloys, *Acta Materialia*, **46**(11), 1998, p.3893

5. **Gupta A.K., Lioyd D.J. and Court S.A.,** Partition hardening in Al-Mg-Si alloys with and without excess Si, *Materials Science & Engineering*, A**316,** 2001, p.11

6. **Murayama M., Hono K., Miao W.F. and Laughilin D.E.**, The Effect of Cu addition on the Precipitation Kinetics in an Al-Mg-Si Alloy with Excess Si, *Metallurgical and Materials Transactions A*, **32A**, 2001, p.239

7. **Sahehata F., Painter M.J. and Pearce R.**, Warm forming of Aluminium/Magnesiun alloy sheet, *journal of Mechanical Working Technology*, **2**, 1978, p.279

8. **Morley A. I. Zandbergen M. W.; Cerezo A., Smith G. D. W.**, The Effect of Pre-Ageing and Addition of Copper on the Precipitation Behaviour in Al-Mg-Si Alloys, *Materials Science Forum*, **519-521**, 2006, p.543

9. **Cheng L.M., Poole W.J., Embury J.D. and Lloyd D.J.**, The influence of precipitation on the work-hardening behaviour of the aluminium alloys AA6111 and AA7030, *Metallurgical and Materials Transactions*, **34A**, 2002, p.2003

10. **Simar A, Bréchet Y., Meester B. de., Denquin A. and Pardoen T**, Sequentional modeling of local precipitation, strength and strain hardening in friction stir welds of an aluminium alloys 6005A-T6, *Acta Materialia*, **55**, 2007, p. 6133

11. **Llyod D.J.**, The Work Hardening of Some Commercial Al Alloys, Materials Science Forum, **519-521**, 2006, p. 55

12. **Deschamps A., Esmaeili S., Poole W.J. and Militzer M.**, Strain hardening rate in relation to microstructure in precipitation hardening materials, *Journal Physics IV*, France, **10**, 2000, p. 151

13. **Blaz L. and Evangelista**, Strain rate sensitivity of hot deformed Al and AlMgSi alloys, *Materials Science and Engineering A*, **207**, 1996, p. 195

14. **Cai M., Field D.P. and Lorimer G.W**., A systematic comparison of static and dynamic ageing of two Al-Mg-Si alloys, *Materials Science and Engineering A*, **373**, 2004, p.65

CHAPTER 5

WORK HARDENING IN 6XXX ALUMINIUM ALLOYS

This chapter provides a description of the influence of temperature and strain rate on work hardening. Uniaxial tensile and deep-drawing tests have been selected to study the mentioned effects. Gallium enhanced microscopy and EBSD measurements have also been used to reveal the effect of work hardening on microstructure in terms of substructure formation and degree of misorientation. The chapter proposes an adaptation of the *Nes* work hardening model to the case of 6xxx series. The simulated true stress-true strain response of the material is compared with the experimental one over a temperature range from room temperature to 250°C and strain rates varying from 0.01 s^{-1} to 0.1 s^{-1} for both alloys and tempers. The model successfully predicts the material response.

5.1   Introduction

Strain hardening or work hardening is an important phenomenon associated with plastic deformation of polycrystalline materials. Important phenomena in plastic deformation like the development of preferred crystallographic orientations, dislocation cell formation, plastic flow localization, generation of residual stresses, or fracture can be strongly influenced by work hardening properties. Work hardening plays, therefore, a vital role in controlling plastic deformation, flow stress evolution, strain distribution and, consequently, the metal behaviour during forming operations.

The formation of a dislocation substructure is closely associated with the ability to climb or cross slip of the dislocations. For all modes of deformation grains are sub-divided into volume elements that are misoriented with respect to each other. Based on a large number of microstructural observations, Hansen et al. [1,2,3] and Hughes [4,5] distinguished two levels of subdivision in medium to high stacking fault energy metals. Dislocation cells, commonly known as the smallest sub-division units, are constituted due to statistical trapping of glide dislocations together with forest dislocations. Geometrically necessary boundaries and microbands form at a larger sub-division scale. They surround cell blocks in which different combinations of active slip systems operate. In order to accommodate the resulting strain variations between the cell blocks these geometrically necessary boundaries incorporate the lattice rotations. Therefore, the degree of misorientation is larger across the geometrically necessary boundaries compared to cell walls. Because dislocation walls and microbands are distributed throughout the entire volume of a grain, strain accommodation occurs, therefore throughout a grain. Misorientations across the geometrically necessary boundaries will increase during deformation owing to the slip on different slip systems in neighboring cell blocks. The need for extra accommodation due to diverging orientations in neighboring cells is achieved by further sub-division through the creation of microbands and new dense dislocation walls within cell blocks. As further subgrain formation requires climb and cross slip, this is a thermally activated process. So, hot or cold deformation of aluminium alloys is associated with an increase in dislocation density and subsequently a decrease in subgrain size and increase in subgrain misorientation. Deformation at elevated temperatures may be associated with activation of non-octahedral slip systems, which consequently bring changes in work hardening behaviour in terms of formation of dislocation substructure. In general, for most aluminium alloys the work hardening rate decreases with increasing temperature or decreasing strain rate.

The evolution of strain hardening of a material during deformation is usually derived from the stress-strain curves by computing the instantaneous strain hardening rate (θ) and plotting it against flow stress increase (σ-σ_y) where σ_y is the yield stress (Kocks-Mecking plot). Kocks-Mecking plots are usually normalized by a temperature dependent shear modulus (G) and the plots become (θ/G) vs (σ-σ_y)/G. The plots for most fcc metals of medium to high stacking fault energy exhibit four distinct stages of hardening. Stage I or easy glide stage, which depends strongly on the orientation of the crystal, is caused by the activation of a single slip system only [6]. The interaction between dislocations is so weak that the work-hardening rate is low. This stage is only present in single crystals of high purity metals. At room temperature the easy glide stage can account for up to 5% strain [7]. Stage II starts when the dislocation density on the primary slip system becomes high enough to favor dislocation slip on secondary slip plane. The dislocation density in these systems increases rapidly to the same value found in primary slip plane enhancing the extent of dislocation interaction due to the presence of multiple slip systems. So the value of θ is high but is found constant (~G/100,) and weakly sensitive to temperature and strain rate. During stage II, work hardening can be attributed to dislocation pile ups at barriers such as Lomer-Cottrell locks (LC) [8,9], dislocation tangles or glissile dislocations intersecting the sessile one. For most polycrystalline metals stage II is practically absent [10]. At the end of stage II, dislocations start to distribute heterogeneously and form dislocation substructure which continues into the next stage until a stable subgrain structure is reached. During stage III the shear stress-shear strain curve strongly deviates from linearity. It is dependent on temperature and strain rate. At the beginning of stage III the dislocation density inside the cell becomes saturated. The misorientation increases rapidly and the cell size decreases. This stage is characterized by the reduction in hardening rate due to the annihilation of screw dislocations by cross slip known as dynamic recovery. Dynamic recovery during stage III is, however, not sufficient to attain a steady state of deformation, characterized by a dynamic equilibrium between dislocation multiplication (work hardening) and annihilation (work-softening by dynamic recovery). Stage III is then followed by a stage of low but approximately constant work hardening rate called stage IV. Stage IV terminates when the work hardening rate drops to zero due to additional recovery mechanism or the occurrence of failure (stage V). During the later stages of work hardening, the stacking fault energy (SFE) of the material becomes very important as it governs the dislocations ability to cross slip and hence recovery. In materials with high SFE dislocations can easily cross slip and avoid obstacles, as it is the case for aluminium.

The evolution of the crystallographic texture has been considered to be another factor affecting the strain hardening of polycrystalline materials. The grains tend to

rotate towards energetically more stable orientations with straining. This alters the hardening behavior. Crystallographic texture and dislocation substructure has been reported [11] to have significant influence on formability, typically in case of strain path changes. The slip activity at microscopic level influences the substructure at a mesoscopic scale and the grain rotation to stable orientation at a macroscopic level. In order to isolate the effect of texture on formability a specific approach is described in chapter 6.

The purpose of this chapter is to accumulate data for a strain hardening model that can accurately simulate the material behaviour and specially the experimental stress-strain response of AA6xxx alloys at warm temperatures. Models with a better constitutive description of work hardening may yield a more effective optimization of the final process and product. For pure metals a reasonable understanding has been reached to describe the influence of temperature and strain rate on work hardening rate both at low and high temperature [12]. But for alloys the presence of solid solution and precipitates complicates the situation and existing theories are less accurate to explain the experimental data. The work hardening behaviour at room temperature for 6xxx series has been investigated by many researchers, but study of the same phenomenon at warm temperatures is not that frequent. Consequently, the available well established room temperature models are rarely tested at warm temperatures. The *Nes* [13] model, which has been tested for different aluminium series at room temperature only, was used in the present investigation both at room and warm temperatures for 6xxx series. The experimental data are used to validate the model. The effect of temperature and strain rate on the work hardening behaviour in association with substructure formation and degree of mis-orientation of the subgrains are studied in section 5.3. The description of the work hardening model is presented in section 5.4 and the application and validation to the case of 6xxx alloys is reported in section 5.6.

5.2   Experimental Conditions

Tensile tests were mostly conducted at room temperature (RT) and at 250°C with 6016 and 6061 specimens of both S and B with 1 mm and 3 mm thicknesses respectively and T4 and T6 conditions. Some of the tests were also done at intermediate temperatures: 130°C, 150°C and 180°C. The strain rate effect was investigated by comparing tests carried out at 0.01 s^{-1} and at 0.1 s^{-1}. Deep-drawing tests were conducted at RT and 250°C. The blank holding pressure (BHP) has been kept constant at 4.1 MPa for the tests conducted at RT and 2.5 MPa for the tests at 250°C while the punch velocity varied between 58 and 78 mm/min for 6016 and between 74 and 122 mm/min for 6061 (cf. chapter 3 for details of the mechanical test procedures). Following the results of chapter 4, strain rates during tensile tests

and the punch velocity range were selected in a way that the material is free from the effect of dynamic precipitation.

Microstructural characterization was done to relate the microstructure and work hardening based on band contrast maps obtained from EBSD measurements. The microstructure was also investigated by the gallium enhance microscopy (GEM) technique. EBSD measurements were done with a step size of 0.5 μm. The indexation rate varied between 80 and 90%. The maps were enhanced using the "noise reduction" correction procedure in the Tango module of the HKL software. The green pixel represents "zero solutions", i.e. areas where Kikuchi patterns could not be recognised. Band contrast maps give a clear image of the appearance of bands and subgrains and are used to measure the microstructure characteristics and intragranular misorientation. Thick black lines indicate grain boundaries with misorientations equal or larger than 15°, whereas thin black lines represent low angle grain boundaries with misorientations between 5 and 15°. The sample preparation for EBSD samples is described is chapter 2.

GEM has been used in order to reveal grain and subgrain boundaries. The melting point of gallium [30ºC] can be reduced by adding aluminium that forms a low temperature melting eutectic. When liquid gallium is put in contact with the aluminium sample gallium atoms diffuse along the grain boundaries first and then along the subgrain boundaries or small angle boundaries even at room temperature. Addition of a small amount of gallium to aluminium increases the visibility of the grain and subgrain boundaries when observed in the SEM by back scattered electrons [14,15]. One side of the sample was polished for SEM observation. Gallium was applied on the far side of the polished surface, which has been previously scratched to break the oxide layer and ensure a better gallium penetration. Before application gallium has been saturated with commercially pure aluminium (99.5%) to make gallium liquid at room temperature by the formation of the eutectic phase. At the time of application of gallium on the surface the temperature was 40°C to 50°C. Typically after 2 hours, gallium had diffused through the sample thickness. The average rate of propagation for gallium has been found to be approximately 2 mm/hr. The sample was then observed in a SEM of type JEOL–JSM-6500F®. This process has been claimed to give optimum results for revealing small angle dislocation boundaries with misorientations less than 1º. SEM images obtained with back scattered electrons do not produce enough contrast for the very low angle subgrain boundaries in a deformed structure and EBSD is limited by the angular resolution of about 1.5º [16]. The resolution and contrast of GEM-SEM has been reported [14] to be better than conventional back scattered SEM and even EBSD. It is also statistically sound considering the larger area covered compared to TEM. The

high angle grain boundaries show larger contrast compared to sub-boundaries because more gallium atoms are segregated on the boundaries with larger excess free volume. Later they diffuse along the low angle boundaries by dislocation pipe diffusion.

5.3   Experimental study of work hardening

The work hardening response of the investigated alloys was evaluated mainly from the tensile test results while the effect of plastic deformation on microstructure was observed after the plane strain compression and deep-drawing tests.

5.3.1   Tensile tests

Strain rate

Investigation of strain rate effects is closely associated with two parameters namely work hardening index (n) and strain rate sensitivity index ($m = \Delta \ln \sigma / \Delta \ln \dot{\varepsilon}$). Strain rate sensitivity of metals is a property that develops during straining and depends upon the deformation mode along with the dominant hardening and softening processes at the temperature and strain rate of interest [17]. It is an important material property to evaluate the formability of sheet metals. Several authors [18,19] have reported evidence of the strain rate sensitivity index to be either dependent or independent on strain and strain rate. At the beginning of cold deformation the value of $\Delta\sigma/\sigma$ is constant ($\Delta\sigma$ is the instantaneous flow strain increase) making the strain rate sensitivity m constant and stress independent. At higher strain, the m value increases when $\Delta\sigma$ vs σ exhibits a positive deviation. At high temperature (more than $0.5T_m$) the strain rate sensitivity shows an upward trend from very early stages of deformation [10]. Because the construction of substructure depends on various levels of strain and strain rate, strain rate sensitivity is also related to work hardening.

(a)

(b)

(c)

(d)
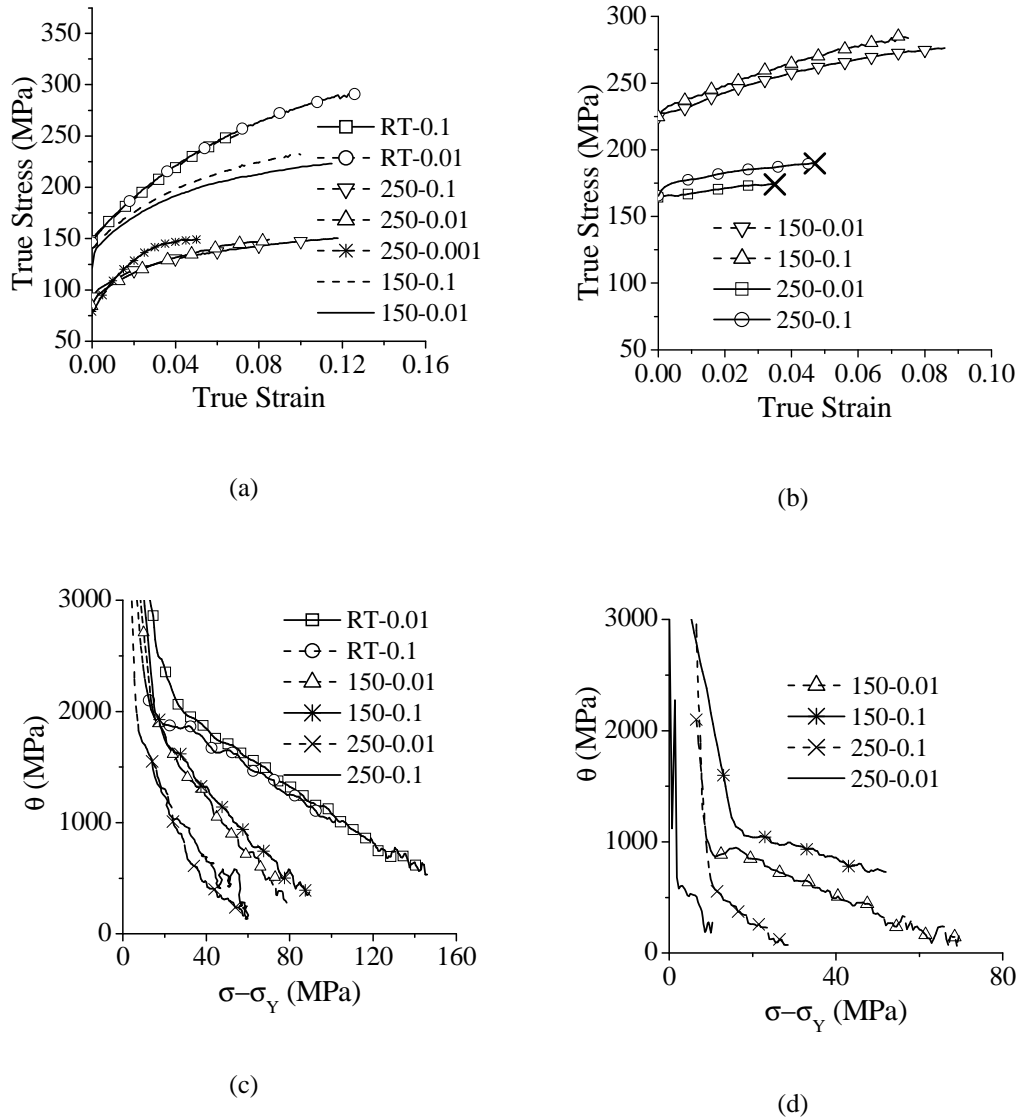
Figure 5.1 Effect of strain rate on true stress-true strain curve for (a) 6016-T4-S (b) 6016-T6-S and on work hardening for (c) 6016-T4-S (d) 6016-T6-S with tensile direction parallel to RD. σ is flow stress and σ_y is yield strength

The effect of strain rate on stress strain response at different temperatures is shown in figure 5.1 for the 6016 alloy. The results are very similar to the ones presented for alloy 6061 in chapter 4 (section 4.3.1). It is confirmed that dynamic precipitation takes place in T4 specimens at 250°C and low strain rate (0.001 s^{-1}). For this reason,

only strain rates over 0.01 s^{-1} are considered in this chapter. It is observed that strain rate has no effect on stress strain response at RT while at higher temperature, stress and work hardening rate tend to increase with increasing strain rate.

Temperature

The increasing deformation temperature has been reported to result in a decrease of yield stress and work hardening rate for 5182 [20,21,22], 6016-T4 and 6061-T6 [23] aluminium alloys. In 5xxx alloys [20,21,22,24] it also corresponds to a decrease of uniform elongation and to a larger strain rate sensitivity and total elongation. That means the increase in total elongation is solely contributed by post-uniform elongation. Decreasing the strain rate even intensifies this effect leading to diffused necking with localized thinning. Dynamic recovery at elevated temperature and low strain rates has been believed to be the mechanism responsible for this behaviour. A similar increase of total elongation with temperature has also been reported for 6xxx. Li and Ghosh [25] found that this effect is weaker for 6111-T4 than for 5754 and Fuchs and Williams [23] also observed less dependency of uniform elongation on strain rate for 6061-T6 compared to 5xxx. In opposition, Bolt and Werkhoven [24] in their warm tensile test experiment with 6016-T4 reported the reduction of total elongation with temperature especially at slower strain rates of 0.002 s^{-1} and to a lesser extent at 0.02 s^{-1}. The effect of temperature on deformation of 6xxx appears, therefore, more complex than in non-heat treatable alloys.

(a)

(b)

(c)

(d)
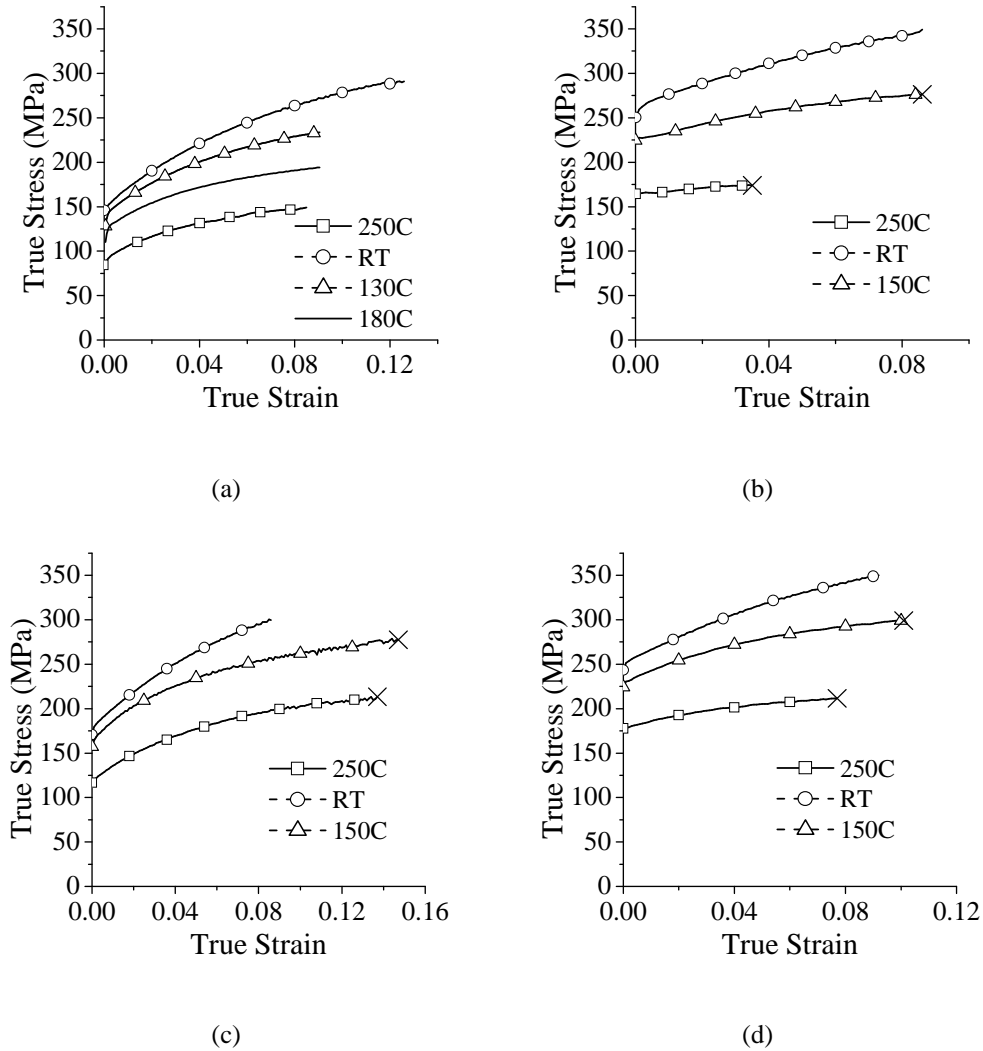
Figure 5.2: Effect of temperature on true stress-true strain response after 30 seconds of holding and elongated along RD for sheet specimens of (a) 6016-T4 (b) 6016-T6 (c) 6061-T4 and (d) 6061-T6 at a strain rate of 0.01 s^{-1}

The effect of temperature on yield strength and work-hardening has been investigated in the temperature range between RT and 250°C. Most of the tests were stopped after 10% or 15% elongation. If the maximum engineering stress was reached within this deformation range the cross (X) mark on the figure 5.2 represents the onset of necking. It is found that both the yield strength and work hardening rate diminish progressively with increasing temperature for both the

alloys and for both T4 and T6 tempers (figure 5.2, figure 5.3 and table 5.1). Under T6 conditions work hardening reduces drastically and becomes severely limited at 250°C. In that case the total elongation is mainly given by the post uniform elongation (see also figure 4.5 of chapter 4). These observations are in good agreement with the literature results reported above.
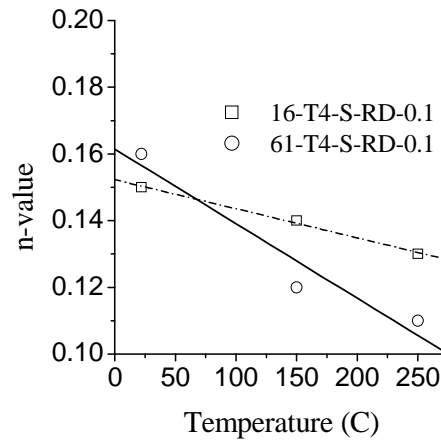
Figure 5.3: Variation of strain hardening index with temperature

The higher yield point at room temperature compared to higher temperatures (table 5.1) results from two effects. First, the strength decreases due to 30 s of holding at warm temperature before the tensile test starts and second the direct effect of temperature on yield point. From the static ageing curves (Chapter 2) it can be seen, for instance, that the hardness values of 6016-T4-S decreases with 4 Hv after holding for 30 s at 150°C and with 18 HV at 250°C. This effect was attributed to the dissolution of small natural ageing (NA) clusters.

Table 5.1. 0.2% off set yield stress ($YS_{0.2\%}$) and parameters of the Voce equation fitted to the experimental tensile test results at a strain rate of 0.01 s^{-1}.

	T4 – RT	**T4 – 250°C**	**T6 – RT**	**T6 – 250°C**
6016				
$YS_{0.2\%}$ (MPa)	153	86	261	157
θ_{max} (MPa)	2070	1310	1390	580
$|\beta|$	10.7	18.1	9.0	37.8
6061				
$YS_{0.2\%}$ (MPa)	178	115	247	171
θ_{max} (MPa)	2180	1720	1390	920
$|\beta|$	11.0	17.5	11.3	23.4

The effect of temperature can be further analysed by looking at the parameters of the Voce equation fitted on the stage III part of the true stress-true strain curves. $\theta_{max} = d\sigma/d\varepsilon_p$ is the initial work-hardening rate at beginning of stage III and $\beta = d\theta/d\sigma$ is related to dynamic recovery during stage III (table 5.1). Table 5.1 shows that the decrease of work hardening rate with increasing temperature is related to both a decrease of dislocation storage efficiency (decrease of θ_{max}) and to the thermal activation of dynamic recovery (increase of $|\beta|$). The lower storage rate can be explained, as for the difference between T4 and T6 tempers, by a weaker effect of solute atoms on dislocation storage at higher temperature.

Work-hardening and microstructure

Specimens for EBSD analysis have been deformed with the tensile direction parallel to RD. The EBSD maps were measured in the middle portion of the gauge length on the (RD, ND) or (tensile direction, TD) cross section.

(a)   (b)
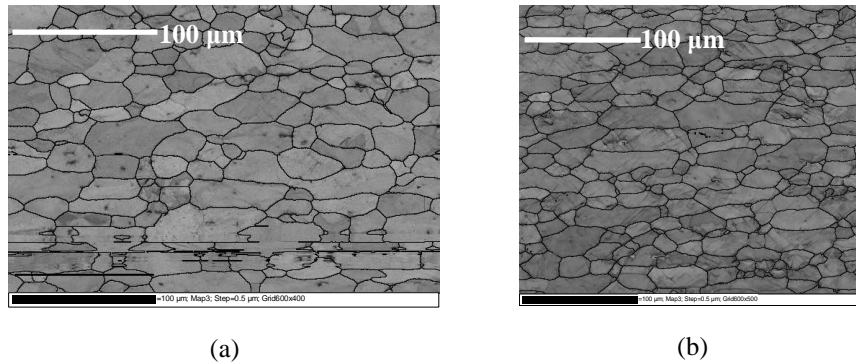
Figure 5.4: Band contrast maps for the tensile specimens 6016 on TD cross section
deformed up to a strain of 10% at (a) RT and (b) 250°C at a strain rate of 0.01 s^{-1}.
The horizontal lines in (a) are a measurement artefacts.

Figure 5.4 shows the development and comparison of band contrast maps after
tensile deformation at RT and 250ºC. It can be clearly noticed that grains are not
much strained and the deformation substructure is under-developed after 10% strain
at both the temperatures although deformation has reached stage III of work
hardening. The average degree of mis-orientation between two successive
measurement points inside a single grain along horizontal and vertical directions is
1° and the misorientation from one end of the grain to another is 6° to 7° for both the
specimens. Lee [26] proposed that owing to easier recovery with increasing
temperature dislocations of the deformed boundaries can rearrange themselves in
low energy configurations resulting in an increased banding tendency. A similar
observation has been noticed in the present investigation (figure 5.4) where the
banding tendency is higher at 250°C compared to that at RT.

(a)

(b)

(c)

(d)
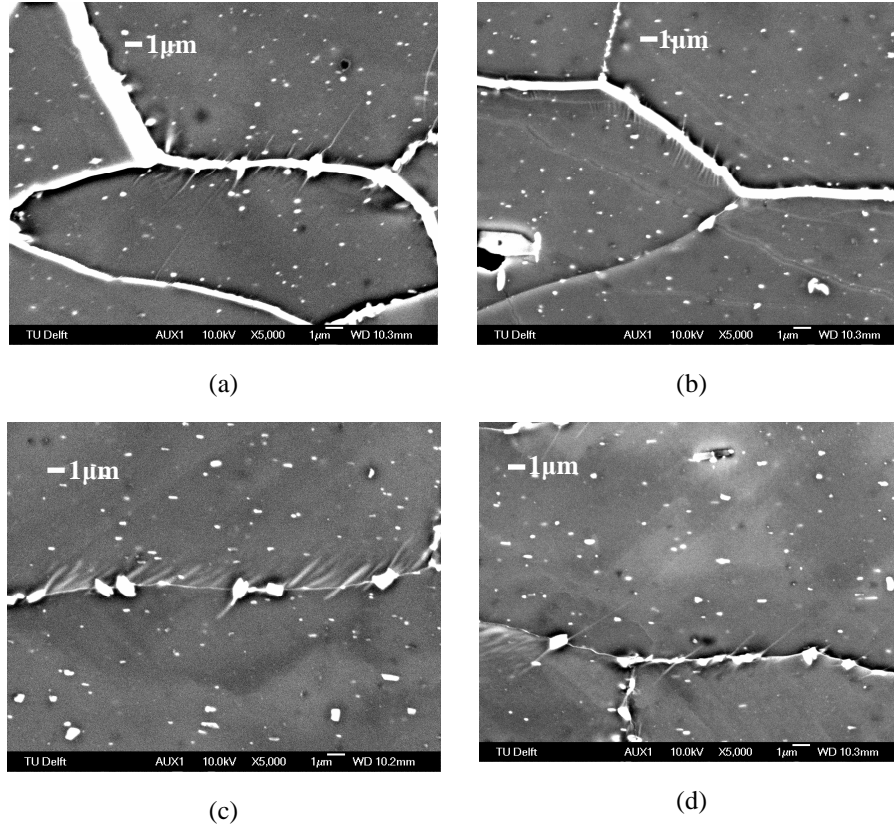
Figure 5.5: GEM-SEM micrographs of the tensile specimen 6016 on the TD plane deformed at (a) RT and observed after Ga deposition of 2 hr. (b) RT and observed after Ga deposition of 1 day (c) 250°C and observed after Ga deposition of 2 hr. (d) 250°C and observed after Ga deposition of 1 day

Figure 5.5 shows that gallium has segregated at the grain boundaries but is not present at the interface between the shaded zones visible inside the grains even not 1 day after its application. This implies that the misorientations between the shades are too small to act as a faster diffusion path for liquid gallium. The non penetration of gallium even after 1 day truly supports the argument for an under-developed substructure already observed by EBSD. The majority of the microbands, primarily composed of dislocation tangles, end at grain boundaries. Restriction of gallium flow inside the grains may be the consequence of limitation in diffusion of gallium at low misorientation.

5.3.2   Plane Strain Compression

Work-hardening on microstructure

(a)   (b)

(c)   (d)
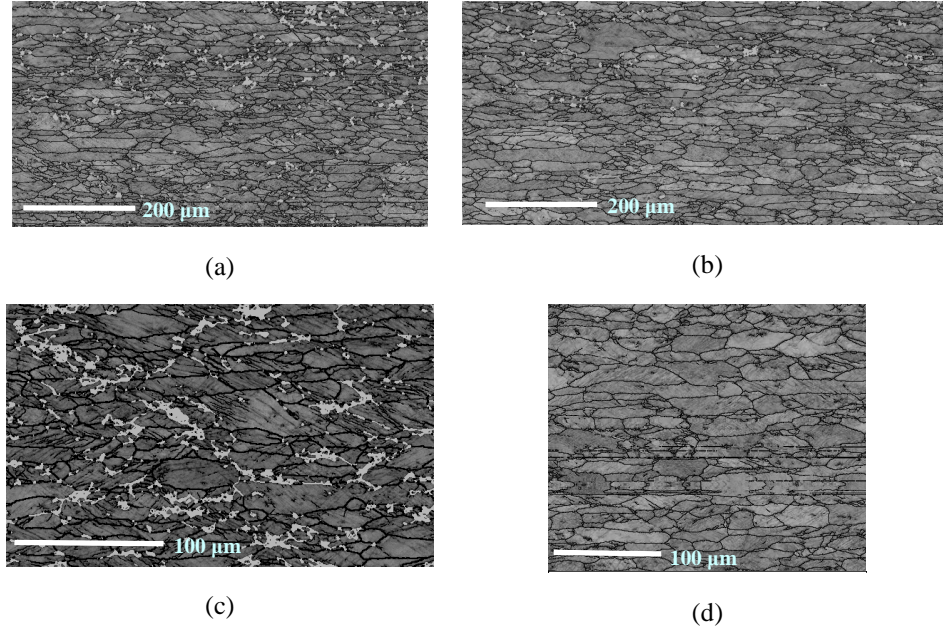
Figure 5.6: Band contrast maps on TD section of PSC specimens. B material of T4 temper deformed at a strain rate of 0.1 s^{-1}. (a) 6016 at RT (b) 6016 at 250°C (c) 6061 at RT and (d) 6061 at 250°C.

From figure 5.6 it can be noticed that the temperature has no significant effect on the evolution of grain morphology during PSC. The band contrast maps in figure 5.6 also reveal that after 30% deformation the substructure inside the grain is mainly composed of series of parallel bands. The maximum misorientation across the deformation traces or bands have been found to be 3°. Deformation bands, sometimes referred to as microbands have been reported in PSC specimens [27]. The misorientation of the microbands have been reported to be about 2-3°. This value did not increase consistently with strain which corroborates with the present observations. After PSC the microbands have been found to be oriented at 35° to the rolling direction [28]. Another study [29] revealed this angle to be 65°. These observations are in contradiction with the present investigation. It can be readily noticed from figure 5.6 that the bands are actually directed in various angles to the rolling direction. In most of the cases the bands are unidirectional inside a single grain. Families of bands with different directions in a grain can also be observed, though limited in number.

(a)
(b)
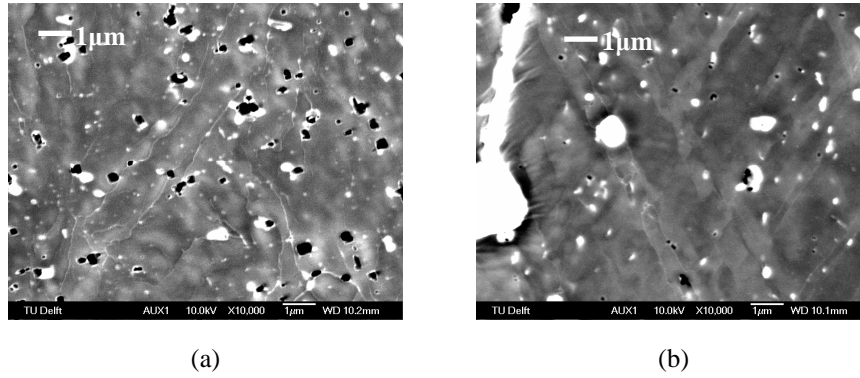
Figure 5.7: GEM-SEM photograph on TD plane of the PSC specimen deformed at 250°C, after 2 hours from Ga deposition for (a) 6016-T4-B and (b) 6061-T4-B

Figure 5.7 shows evidence of the start of subgrain formation for both the samples. Both above pictures show features inside a single grain. Very thin lines of white gallium are seen separating different shades. The situation did not change even after a waiting period of one day.

5.3.3   **Warm Deep Drawing**

(a)   (b)
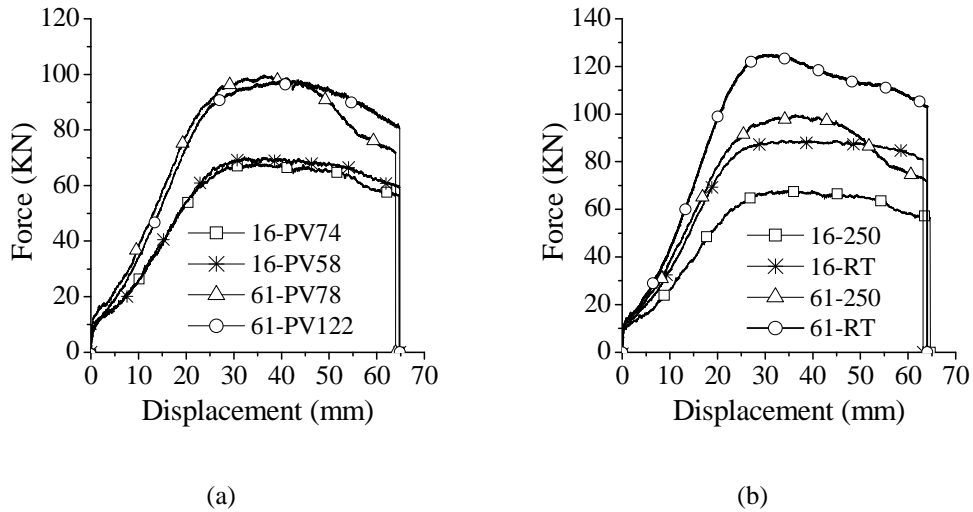
Figure 5.8: Effect of (a) punch velocity at 250°C and (b) temperature on force-displacement response after 30 seconds of holding for sheet of T4 condition.

Punch velocity

Figure 5.8a describes the variation of force-displacement plots with punch velocity for both the alloys. Varying punch velocity from 58 to 78 mm/min for 6016-T4 or from 74 to 120 mm/min for 6061-T4 does not seem to have any effect on the force-displacement plot. The small increase of stress with strain rate visible during tensile test at 250°C has, therefore, no noticeable influence on the punch force during deep drawing tests.

Temperature

The effect of temperature on the force displacement response for both the alloys is shown in figure 5.8b. Clearly the higher the temperature, the softer is the material for all situations.

Work-hardening on microstructure

(a)   (b)

(c)   (d)
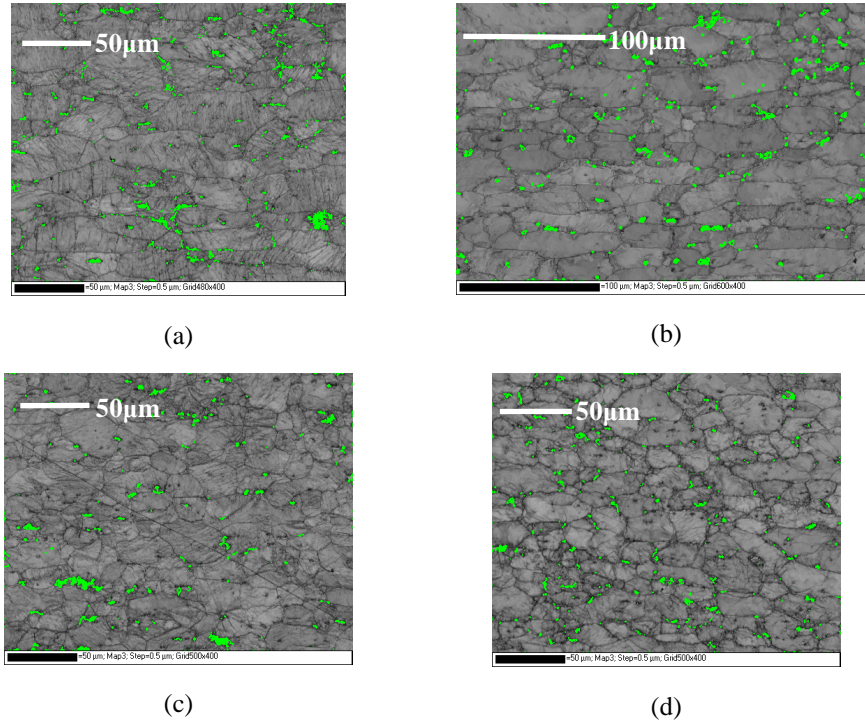
Figure 5.9: Band contrast maps for the DD specimens on TD (horizontal axis –RD and vertical axis ND) section for (a) 6016 at RT (b) 6016 at 250°C (c) 6061 at RT and (d) 6061 at 250°C.

Band contrast maps from EBSD measurements on the deep drawn specimens at a location 3 mm from the edge of the flange are shown in figure 5.9.

From the band contrast map above it can be noticed that the microstructure is very much similar for 6016 and 6061 at both temperatures. The microstructure shows parallel bands with average band spacing of 5 to 7 μm and misorientation less than 5° from one side to another side of a grain at room temperature, while the band density reduces significantly at 250°C along with misorientation to a value of 3°. After DD the substructure made up of bands is not as clear as after PSC, although the amount of deformation at the flange is close to 30%. The elapsed time between the end of drawing and quenching for warm DD tests may have causes added recovery compared to room temperature drawing.

<div align="center">(a)   (b)</div>
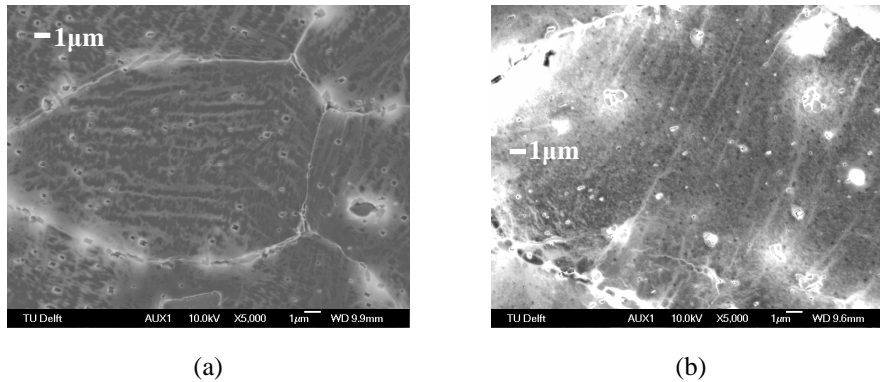
Figure 5.10: GEM-SEM photograph of the DD specimen on the TD plane, after 2 hours from gallium application for (a) 6016-S at RT and (b) 6061-S at 250°C.

In cups drawn at RT, (figure 5.10a) gallium seems to diffuse along parallel bands inside the grains, the direction of the bands varying from grain to grain. After drawing at 250°C, (figure 5.10b) gallium is seen to flood the grain boundaries while the intraganular bands are less pronounced and less continuous. At both temperatures, the GEMs show very similar substructures than the ones observed in EBSD contrast maps and confirm the formation of a banded dislocation structure.

From the band contrast maps of tensile, PSC and DD specimens it can be readily concluded that in the majority of cases deformation bands ended at the grain boundary i.e. bands were restricted inside a grain, and orientations were different in different grains. The banding tendency increased with temperature for tensile specimens while an opposite trend was noticed for DD specimens. For PSC specimens it was however difficult to draw any such conclusions.

5.4   Work Hardening Model

The accurate prediction of the material behaviour during plastic deformation requires the combination of a material model, which predicts the strength and work hardening response of the material, and a FEM framework. The work hardening model developed by *Nes* was selected for the present research. In the next sections the reasons for this choice are first discussed, followed by a short description of the model itself.

5.4.1   Selection of the model

A model of work hardening including a physically based description of metal plasticity was first introduced by Kocks [30]. This approach was modified

subsequently by other researchers [31,32,33] and got the final shape in the form of the *mechanical-threshold-strength (MTS)* model [34]. Two other widely used work hardening models have been developed by *Nes-Marthinsen-Holmedal* [13,35,36] and *Roter-Goerdeler-Gottstein* [37,38]. The models are referred to as the m*icrostructural metal plasticity (MMP) model*, currently termed as the *Nes* model, and the *3 internal variable model (3IVM)* respectively. The three models differ in microstructural description, kinetic description and structural evolution. *MTS* relies on a single parameter only. The flow stress at any level is expressed as a function of the average accumulated dislocation density. The way they are arranged is not considered. In the *Nes* model dislocations are arranged inside cell walls and cell interior. With deformation, cell size, cell wall thicknesses and misorientation, dislocation density inside cell wall and cell interior vary and govern the work hardening characteristics. In the *3IVM*, three internal state variables e.g. mobile dislocations, immobile dislocations inside cell interior and cell walls are the main controlling factors. Both *Nes* and *3IVM* models consider interactions between mobile dislocations. Subsequently the dislocation substructure is formed due to both short and long range interactions, while *MTS* only considers short range interactions. The athermal storage of dislocations is taken care of in a similar way for all three models. The statistical approach relied on to this purpose is virtually more complex in *Nes* or *3IVM* owing to the involvement of more microstructural elements. Building of the substructure beyond stage II is extremely complex and the effect of dynamic recovery should include collective migration of dislocations rather than individual effects. The *Nes* model effectively includes the growth rate of the sub boundary structure under dynamic conditions. The effect of solute content, dispersoids and grain boundaries are well counted in the *Nes* model and makes it an obvious choice for modelling. The model also predicts the evolution of the stastistically averaged subgrain size, dislocation density inside the subgrains and the misorientation between the subgrains.

Considering the models, their fundamental and physical basis, the *Nes* model sounds more logical and has been chosen for the present work. One of the main drawbacks of the *MTS* model in its present form is that it does not include explicitly the effect of solute, grain size and particle content. Additionally, the *Nes* model generates a closer fit of the experimental stress strain curves compared to the *3IVM* model, using the versions available at that moment. The possibility of coupling the *Nes* model with the FEM code and also with other material models made it the most suitable candidate for the present project.

5.4.2   Nomenclature

α_1 : Constant, relating dislocation spacing and stress

α_2 : Constant, relating boundary spacing and stress

β : Constant in τ_p expression

$\dot{\gamma}$: Resolved shear strain rate

δ : Average diameter of the subgrains

κ_0 : Geometrical factor for cell walls

κ_2 : Constant in grain boundary contribution to slip length

κ_3 : Constant in particle contribution to slip length

κ_{3p} : Constant in precipitate contribution to slip length

υ : Poisson ratio

υ_D : Debye frequency

ξ_ρ : Scaling parameter for dislocation dipole separation distance

ξ_δ : Scaling parameter for activation volume for subgrain growth

ρ_i : Initial value of dislocation density within the cells

ρ : Total density of dislocations stored in the material

ρ_b : Dislocation density within the sub-grain boundaries

ρ_m : Mobile dislocation density

τ_t : Stress due to thermal short-range interactions between mobile and stored dislocations

τ_p : Stress increment due to the presence of precipitates

$\hat{\tau}_a$: Athermal flow stress contribution

τ_{cl} : Solute clustering contribution to true stress

φ : Average misorientation of the subgrain boundaries

φ_c : Critical misorientation for subboundary energy

φ_{IV} : Saturation misorientation in stage IV

ω_s : Constant in relaxation length and activation volume expression

ω_t : Constant in activation volume and relaxation distance for thermal stress

ΔU_s : Binding energy between solute atoms and dislocations

A : Constant in τ_p equation

B_ρ : Pre-exponential factor for dislocation velocity during dipole annihilation

$B_\delta^{(pm)}$: Pre-exponential factor for subgrain growth in pure metals

$B_\delta^{(s)}$: Pre-exponential factor for subgrain growth in solute

B_δ : Pre-exponential factor in the expression of subgrain growth rate

B_t : Pre-exponential factor for dislocation velocity in the thermal stress expression

b : Length of Burgers vector

C : Dislocation storage parameter

c_{sc} : Mg solute concentration near the dislocation core

c : Mg solute concentration

c_0 : Total solute concentration of Si and Cu

D : Average grain diameter

e_δ : Concentration exponent in expression of dynamic recovery by subgrain growth

e_ρ : Concentration exponent in expression of dynamic recovery by dislocation dipole annihilation

e_t : Concentration exponent in thermal stress expression

f : Volume fraction of cell walls during stage II

f_{sc} : Volume fraction of material for which scaling relations hold

f_r : Volume fraction of precipitates

k : Boltzmann's constant

G : Shear modulus

K_{II} : Parameter in the misorientation variation rate expression, which is function of the scaling parameters.

L_{eff} : Effective dislocation mean slip length

L_D : Slip length due to grain size

L_ρ : Slip length due to dislocations

L_P : Slip length due to particles

l : Mean effective particle spacing in the slip plane along bending dislocation

l_ρ : Relaxation length for dislocation dipole annihilation

l_t : Relaxation length for solute-mobile dislocation interaction

M : Taylor factor

m : Constant, ratio between mobile and stored dislocation density $\langle$ 1

$q_{IV,S}$: Constant in the expression of S vs. subboundary misorientation

$q_{IV,\delta}$: Controls the maximum possible subgrain size during subgrain growth

q_b : Scaling parameter in stage II

q_c : Scaling parameter in stage II

r : Mean radius of precipitates

r_c : Transition radius for shearing – by-passing

T : Temperature

U_{SD} : Activation energy for self diffusion

U_t : Thermal activation energy

U_s : Activation energy for diffusion of atoms in solution

V_δ : Activation volume for subgrain growth

V_ρ : Activation volume for dislocation dipole annihilation

V_t : Activation volume for solute-mobile dislocation interaction

5.4.3   Description of the Nes model

The general philosophy of the work hardening model was proposed by *Nes* [13] and was subsequently developed by other investigators [39,40]. The main objective of this model was to develop a unified theory of deformation that can predict the stress-strain behaviour for fcc metals or alloys under any level of strain rate and temperature. The theory is based on the detailed description of the microstructure evolution during different stages of deformation. Addressing the problem of athermal storage of dislocations on a statistical approach and combining this with models of dynamic recovery a general internal state variable description has been developed. The effects due to non-deformable precipitates and solid solutions have also been included. *Nes* assumed that at small strain (stage II) dislocations arrange themselves in a cell structure having cell or subgrain size δ, dislocation density

inside the cells ρ_i, dislocation density inside cells walls ρ_b, and wall thickness h (figure.5.11). With increasing strain, cell walls collapse in to sub-boundaries with well defined misorientation φ.
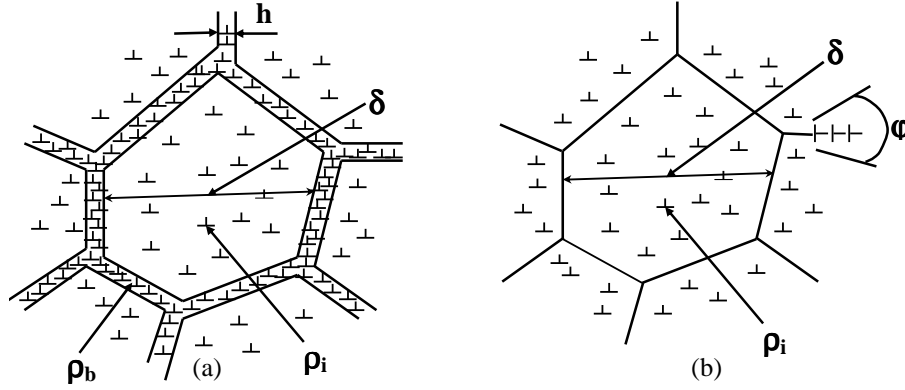
Figure 5.11: Microstructural parameters for (a) small deformations and (b) large deformations [13]

The flow stress for a known microstructure can be defined as the summation of its thermal (τ_t) and athermal ($\hat{\tau}_a$) components. The thermal component is generated due to short range interaction of mobile dislocations with intersecting stored dislocations. The athermal component is the stress contribution due to precipitates or particles (τ_p), solute clusters (τ_{cl}), dislocations (τ_d) and boundaries (τ_b) which are considered as long range barriers.

$$\tau = \tau_t + \hat{\tau}_a = \tau_t + \tau_p + \tau_{cl} + \tau_d + \tau_b \tag{5.1}$$

In pure metals short range interactions are only associated with cutting of trees and dragging of jogs. In alloys, the amount of solute atoms in solution and their thermal activation are expected to control the speed of moving dislocation. In both situations, the thermal stress can be derived from the Orowan equation:

$$\tau_t = (\frac{kT}{V_t})\text{arcsinh}[\frac{(\dot{\gamma}/\upsilon_D)\exp(U_t/kT)}{2bl_t\rho_m B_t}] \tag{5.2}$$

It is assumed that the mobile dislocation density (ρ_m) is proportional to the stored dislocation density (ρ) i.e. $\rho_m = m\rho$. For solid solutions, the activation energy U_t is the summation of activation energy for solute diffusion (U_s) and interaction

energy between solute and dislocation (ΔU_s). v_D is Debye frequency. The activation volume, V_t, and relaxation distance, l_t, are given by:

$$V_t = \frac{\omega_t b^3}{c_{sc}^{e_t}} \tag{5.3}$$

Here ω_t represents the constant in activation volume and relaxation distance for thermal stress, b is the length of Burgers vector, c_{SC} Mg solute concentration near the dislocation core and e_t is concentration exponent.

$$l_t = \frac{b}{\omega_t c_{sc}^{1-e_t}} \tag{5.4}$$

As already mentioned the athermal contribution of the flow stress equation contains four terms:

(a) Contribution due to non-shearable particles (τ_p)

$$\tau_p = \left(\frac{AGb}{1.24 x 2\pi} \right) \frac{\ln(\lambda/b)}{\lambda} \tag{5.5}$$

A is a constant and λ the distance between non-shearable particles. The adaptation of this term to the case of AA6xxx will be discussed in section 5.4.4.

(b) The clustering stress τ_{cl}, due to the formation of clusters by low diffusivity alloying elements e.g. Fe, Mn, Si.

(c) Contribution from forest dislocations approximated by the Taylor equation, $\alpha_1 Gb\sqrt{\rho}$

(d) Contribution from the dislocation interaction with sub-grain and grain boundaries, $\alpha_2 Gb(\frac{1}{\delta} + \frac{1}{D})$

The last two terms change with the amount of deformation because the dislocation density and subgrain size change during work hardening.

At the beginning of deformation a rapid increase of dislocation density controls the athermal part while the effect of spacing between sub-boundaries, i.e. subgrain size, becomes dominant when the dislocation density inside the cell saturates and cell size decreases. To ensure a smooth transition between these two stages a statistical distribution of the subgrain size has been considered. Based on this assumption, equation 5.1 has been modified as follows.

$$\tau = \tau_t + \hat{\tau}_a = \tau_t + \tau_P + \tau_{cl} + \alpha_1 Gb\left[\Gamma_1(\frac{q_c}{\delta\sqrt{\rho_i}})\sqrt{\rho_i} + \Gamma_2(\frac{q_c}{\delta\sqrt{\rho_i}})\frac{q_c}{\delta}\right] + \hat{\alpha}_2 Gb\left(\Gamma_2(0)\frac{1}{\delta} + \frac{1}{D}\right)$$

$$(5.6)$$

$\Gamma_1(x)$ and $\Gamma_2(x)$ are functions related to the subgrain size distribution, G is the shear modulus and $\hat{\alpha}_2$ is given by:

$$\hat{\alpha}_2 = f_{SC}\alpha_1(\sqrt{f(q^2{}_b - 1) + 1} - 1)q_c + (1 - f_{SC})\alpha_2$$

$$(5.7)$$

with α_1 a constant, relating dislocation spacing and stress and α_2 a constant, relating boundary spacing and stress, f_{sc} the volume fraction of the material in which scaling relations hold.
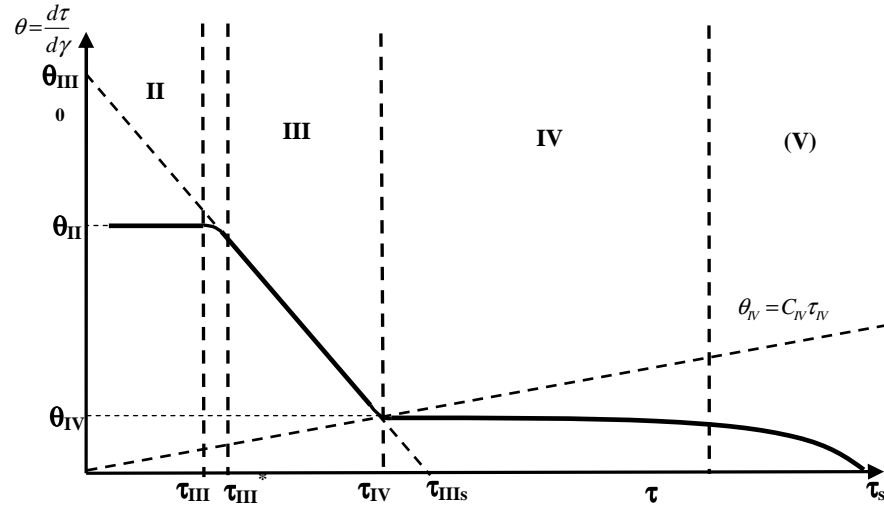
Figure 5.12: Schematic drawing for strain hardening and flow stress relationship
with indication of the successive deformation stages
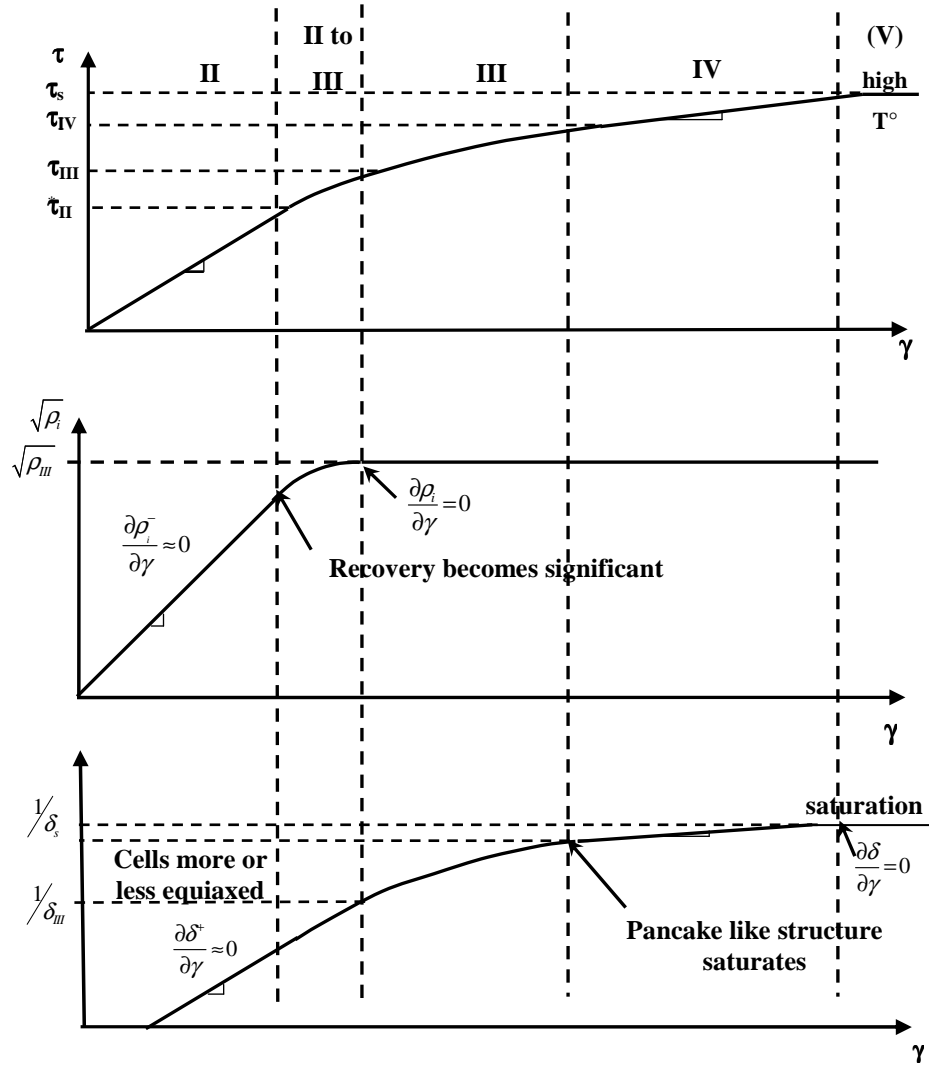
Figure 5.13: Changes in flow stress, dislocation density and cell size during different stages of deformation.

The flow pattern at low temperature consists of four stages as described in figure 5.12. In case of single crystals, the early stage of deformation depends particularly

on the testing temperature, purity and orientation. The region of easy glide is favoured by slip in single crystals. During deformation of polycrystals stage II, III and IV can be readily observed [41]. Stage II is characterized by constant and high strain hardening rate of the order of *G/200* due to accumulation of dislocations. The strain hardening rate is weakly sensitive to temperature and the strain rate and dislocation storage is supposed to be the sole working mechanism and this continues to the next stages until a stable subgrain structure is formed. Starting of dynamic recovery leads to stage III during in which the work hardening rate decreases linearly with stress. The transition from stage II to stage III, for most commercial alloys, is difficult to distinguish due to the effect of grain size and particle distribution which contributes to hardening during stage II. During stage II the structure remains similar and only changes in size, so the scaling principle can be applied during this stage. At the beginning of stage III the dislocation density inside the cell becomes saturated, the misorientation increases rapidly and the cell size decreases (figure 5.13). The strain hardening rate becomes constant again during stage IV. The work hardening rate at this stage is typically 2×10^{-4} *G*, which is much smaller than in stage II. During stage V the rate of dislocation storage and recovery becomes equal.

So the shape of the work hardening and stress-strain plot is dependent on the relative dominance of the dislocation storage and recovery. This competition is translated in the *Nes* model into a set of differential equations, governing the evolution of dislocation density and subgrain size.

$$\frac{d\rho_i}{d\gamma} = \frac{d\rho_i^+}{d\gamma} + \frac{d\rho_i^-}{d\gamma} \tag{5.8}$$

$$\frac{d\delta}{d\gamma} = \frac{d\delta^-}{d\gamma} + \frac{d\delta^+}{d\gamma} \tag{5.9}$$

Figure 5.13 shows in a schematic diagram the changes in flow stress, dislocation density and cell size during deformation. Dislocations are found to be stored in three ways: in the cell interior, forming new boundaries or in old boundaries. Storage inside the cell interior is described by the following equation:

$$\frac{d\rho_i^+}{d\gamma} = \frac{1}{(1+f(q_b^2-1))} \frac{2}{bL_{eff}} \tag{5.10}$$

The effective mean slip length, L_{eff} , is a function of the density of obstacles (forest dislocations, precipitates and grain boundaries) on the slip plane and is given by:

$$\left(\frac{1}{L_{eff}}\right)^2 = \left(\frac{1}{L_\rho}\right)^2 + \left(\frac{1}{L_p}\right)^2 + \left(\frac{1}{L_D}\right)^2 = \left(\frac{\sqrt{\rho}}{C}\right)^2 + \left(\frac{\kappa_3 2 f_r}{r}\right)^2 + \left(\frac{\kappa_2}{D}\right)^2 \qquad (5.11)$$

L_P, L_ρ and L_D are the slip length due to dislocations, particles and grain size respectively, κ_2 is a constant in grain boundary contribution to slip length and κ_3, a constant in particle contribution to slip length.

Some dislocations contribute in forming new boundaries while stored, which results in subgrain refinement:

$$\frac{d\delta^-}{d\gamma} = -\frac{2\delta^2 \rho_i}{\kappa_0 \varphi} \frac{SC^2}{L_{eff} \rho} \qquad (5.12)$$

with S a storage parameter that depends on the subboundary misorientation. When dislocations are consumed at old boundaries they are supposed not to contribute to hardening, but rather have an impact on the misorientation of the boundaries. The model gives the following equation for sub-boundary misorientation evolution:

$$\frac{d\varphi}{d\gamma} = \left(f_{II} \frac{bK_{II}}{\varphi L_{eff}} + (1 - f_{II}) K_{III} \right)\left(1 - (\frac{\varphi}{\varphi_{IV}})^5\right) \qquad (5.13)$$

f_{II} is a function of the microstructure and equals 1 during stage II and vanishes at larger deformation. The misorientation storage parameter K_{III} is an increasing function of temperature as in stage III dynamic recovery gains importance.

At room temperature, where subgrain growth can be neglected, dynamic recovery by dislocation annihilation in the subgrain interior is the predominant mechanism. Dynamic recovery associated with a 3D dislocation network requires thermally activated cross slip and climb. The annihilation rate of dislocations is expressed as:

$$\frac{d\rho_i^-}{d\gamma} = -\rho_i \xi_\rho \sqrt{\rho_i} v_\rho \frac{1}{\dot{\gamma}} \qquad (5.14)$$

ξ_ρ is a scaling parameter relating the dipole separation distance to the average distance between stored dislocations. The migration rate, v_ρ, of dislocations during dipole annihilation depends on the exact controlling step, either glide (g) or climb (c):

$$v_\rho^{(g)} = l_\rho^{(g)} B_\rho^{(g)} v_D \exp\left(\frac{-U^*}{kT}\right) 2\sinh\left(\frac{Gb\sqrt{\rho_i} V_\rho^{(g)}}{2\pi kT}\right) \qquad (5.15)$$

$$v_\rho^{(c)} = \sqrt{\rho_i} b l_\rho^{(c)} B_\rho^{(c)} v_D \exp\left(\frac{-U^*}{kT}\right) 2\sinh\left(\frac{Gb\sqrt{\rho_i} V_\rho^{(c)}}{kT}\right) \qquad (5.16)$$

with l_ρ the relaxation distance, B_ρ a pre-exponential factor, U^* the activation energy, and V_ρ the activation volume. For pure metals, dislocation climb is the limiting process and $U^* = U_{SD}$, $l_\rho = b$, and $V_\rho = 2\xi_\rho b^3$. For solid solutions, $U^* = U_s + \Delta U_s$. If glide is the controlling process, then $l_\rho = b/\omega_s c_{sc}^{1-e_\rho}$, and $V_\rho = \xi_\rho \omega_s b^3 c_{sc}^{-e_\rho}$. On the other hand, if climb is the controlling process, then $l_\rho = b/\omega_s c_{sc}$, and $V_\rho = 2\xi_\rho b^3$. The parameters B_ρ and ξ_ρ are different for pure metal and solid solution cases and for glide and climb processes.

Although subgrain growth at room temperature is negligible, it may become an important mechanism at higher temperature. In the current model the average sub grain size in a dynamic situation will increase at a rate:

$$\frac{d\delta^+}{d\gamma} = \frac{B_\delta b \upsilon_D}{\dot\gamma} \exp\left(-\frac{U^*}{kT}\right) 2\sinh\left(\frac{pV_\delta}{kT}\right) \tag{5.17}$$

The activation volume for pure metal is $V_\delta = \xi_\delta b^3$ and for solid solution, it is $V_\delta = \xi_\delta b^3 c_{sc}^{-e_\delta}$. The driving force for recovery is related to subgrain size and misorientation and is given by:

$$p = \frac{Gb\varphi}{\delta\pi(1-\upsilon)} \ln\left(\frac{e\varphi_c}{\varphi}\right) \tag{5.18}$$

The parameters B_δ and ξ_δ are different for pure metal and solid solution cases

In the present version of the *Nes* model the thermal, dislocation and subgrain stress contributions are added linearly (equation 5.1) [42]. The linear addition is commonly accepted when adding stresses originating from obstacles of different strength [43]. In literature, a power law, in which each term of eq. 5.1 is elevated to a certain power n, is often proposed for adding the effect of precipitates to the dislocation hardening term [44]. In particular, when precipitates become stronger it is often assumed that they have a similar individual strength than forest dislocations and then a power law should be applied. Similarly, in the case of adding the contribution of several populations of non-shearable precipitates, it was shown that the linear addition gives rise to an overestimation of the total stress and a power law is closer to the exact solution [45]. The effect of the power exponent value is small on yield strength due to the low dislocation density but significant on the total stress at larger strain and on work hardening rate. Results in literature also show that the power exponent value depends on the relative strength of the precipitates compared to other obstacles [43]. However, there is no method yet to find the power exponent

value other than by fitting, and therefore the linear addition law is kept in the current model, even for T6 materials.

5.4.4   Modifications of the existing model

For the present work version V201 of the model was used and the code was received from the group of E. *Nes* of NTNU, Norway. After careful observation, it can be seen that equation 5.5 which is proposed to calculate the shear stress due to non shearable particles in the *Nes* model is unable to predict the contribution of the smaller precipitates. Rather, the equation proposed by *Myhr* [46] (equation 5.19) generates a realistic solution where the stress first increases with the precipitate radius for radii below a critical value and then decreases due to coarsening of the precipitates. Therefore the original equation for the contribution of dispersoids to the yield stress (equation 5.5) has been replaced by equation 5.19, which is more suitable for the smaller precipitates present in heat treatable alloys [47,48].

$$\sigma_P = M \left(\frac{3 f_r}{2\pi} \right)^{\frac{1}{2}} 2\beta G \frac{b}{r} \min \left(\frac{r}{r_c}, 1 \right)^{\frac{3}{2}} \tag{5.19}$$

β is a parameter related to the dislocation line tension and r_c is the critical radius of the precipitates at which dislocations start to bypass the precipitates.

The *Nes* model uses a statistical treatment to calculate the mean slip length of dislocation. The contribution of precipitates to the mean slip length is given by

$$L_P = \frac{1}{\kappa_3} \frac{r}{2 f_r} \tag{5.20}$$

with κ_3 a constant. In AA6xxx alloys, precipitates smaller than r_c can be sheared and consequently do not contribute to the slip length. Assuming that precipitates have a size distribution, only those precipitates larger than r_c contribute to dislocation storage. Furthermore, by-pass by dislocations of non-shearable precipitates, as the ones present in T6 condition, leaves Orowan loops around the precipitates. Experimental results, however, show that the initial work hardening rate (θ_0) of T6 or peak-aged materials is minimum meaning the precipitates present at this stage are not efficient in storing dislocations. Following the treatment of Simar [48], it is assumed that Orowan loops can still shear a precipitate if the precipitate size is smaller than the size of fully incoherent precipitates. An efficiency factor (φ) was defined as the proportion of Orowan loops that do not annihilate by shearing. It is assumed that the dislocation density increase due to precipitates, which is proportional to κ_3, also scales with the proportion of Orowan loops that remain around the precipitates. The κ_3 parameter is then modified according to

$$\kappa_3 = \kappa_{3p}\varphi(\overline{r_c})\frac{r}{\overline{r_c}}\frac{f_c}{f_r} \tag{5.21}$$

with $\overline{r_c}$ the mean radius and f_c the volume fraction of non shearable precipitates (i.e. precipitates larger than r_c), and κ_{3p} a constant parameter. φ depends on the size of the non-shearable precipitate. As in [49], φ is assumed to vary linearly from 0 to 1 when the precipitate radius varies from r_c to the radius of fully incoherent precipitates, r_{cl}.

$$\varphi(\overline{r_c}) = \frac{\overline{r_c} - r_c}{r_{cl} - r_c} \tag{5.22}$$

5.5 Material inputs

Grain size (D) and Taylor factor (M) are determined from experimental measurements (table 5.2). The details of the grain size measurements has been discussed in chapter 2, section 2.1.3. The Taylor factor was calculated using the MTM-FHM software system developed by P. Van Houtte taking the texture data measured by XRD.

Table 5.2: Grain Size and Taylor factor for different alloys

Alloy	Grain Size (m)	M
16-T4-S	$18.7 \cdot 10^{-06}$	2.98
16-T6-S	$19.5 \cdot 10^{-06}$	3.02
61-T4-S	$15.8 \cdot 10^{-06}$	2.95
61-T6-S	$15.4 \cdot 10^{-06}$	2.98

Clusters formed during natural ageing (NA) are treated as small precipitates. Consequently, τ_{cl}=0 MPa.

Other inputs like precipitate size (r), number density (N) and volume fraction (f_r) were determined by fitting independently the room temperature yield strength calculated with the model proposed by *Myhr* [46] to experimental data for the conditions listed in table 5.3. This model uses a simple addition of pure metal stress ($\tau_0 = 10$ MPa), solute stress (τ_s) and precipitate stress (τ_p), the latter being the same than equation 5.19. The *Myhr* model was already validated for the yield strength of

AA6xxx alloys. The parameter values so generated were $\beta = 0.36$ and $r_c = 5$ nm. For T4 materials, precipitates are considered as Guinier Preston (GP) zones or naturally aged clusters and hence they are shearable. The stoichiometry of GP zones in AA6016 (excess Si) is taken as $Al_7Mg_2Si_2$ (Mg:Si = 1:1) and in AA6061 (balanced alloys) as $Al_9Mg_2Si_1$ (Mg:Si = 2:1) [50]. Knowing that these precipitates are smaller than the critical radius, r_c, and the density is around $\sim 10^{24}$ m^{-3} the values in table 5.3 are found to produce a good fit of the yield strength (figure 5.14). For T6, precipitates are β''. The stoichiometry is taken as Mg_5Si_6 [51] r is the equivalent circular radius of the needle shaped β''. Existing results from literature indicate that the precipitate size should be around 5 nm, the density in the order of 10^{22} m^{-3} and the solute content of either Mg or Si should be close to the equilibrium concentration. Based on this information, the values in table 5.3 were found by fitting (figure 5.14).

Table 5.3: Volume fraction and radius of precipitates for different alloys

Alloy	f_r	R (m)
16-T4-S	0.0049	$0.8 \cdot 10^{-9}$
16-T6-S	0.0098	$4.5 \cdot 10^{-09}$
61-T4-S	0.0094	$0.8 \cdot 10^{-9}$
61-T6-S	0.0081	$4.8 \cdot 10^{-9}$

Solute concentrations of Mg (c) and Si were calculated from the mass balance (table 5.4). The amount of Si used for the formation of intermetallics with Fe and Mn is subtracted in the same way than in [46]. Cu is assumed to remain in solid solution. Assuming the accuracy of the solute concentration calculation being 0.02 wt% for each element the resulting accuracy for τ_t is found to be less than 2 MPa, which is low compared to observed variations of τ_t with alloy and temper.

Table 5.4: Solute concentration for different alloys under investigation

Alloy	c [at frac]	C_0 [at frac]
16-T4-S	0.0038	0.0080
16-T6-S	0.0001	0.0034
61-T4-S	0.0089	0.0046
61-T6-S	0.0068	0.0009
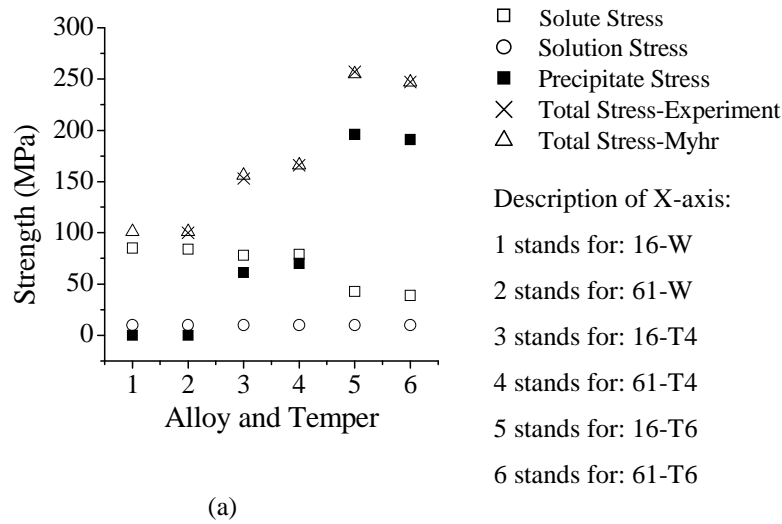
Figure 5.14: Fitting of yield strength at room temperature with model from *Myhr*
[46]

The contribution of dispersoids to the increase of true stress is in the range of 3-4 MPa and hence this effect is neglected. Also for constituents the effect is negligible. Assuming the initial dislocation density (ρ_i) in undeformed metals between 10^9 and 10^{12} m^{-2} and the volume fraction of cell walls to be 0.1 can be considered reasonable values.

5.6   Model parameters

The *Nes* model has already been applied to 1xxx, 2xxx, 3xxx and 5xxx aluminium alloys. Consequently the model parameters exist for these series, but no set of data is available for 6xxx alloys. The purpose of this section is to determine the parameters applicable to 6xxx alloys. The study started with the parameters controlling the yield strength and in the next section doing the same with work hardening.

5.6.1   Parameters controlling yield strength

Model parameters were first determined by fitting the yield strength at room temperature followed by refitting some parameters at higher temperature. The yield strength in the *Nes* model, which is the flow stress at zero strain, is found

comparable to the experimental $YS_{0.2\%}$ value. According to the model, the yield strength mainly depends on the thermal stress and the precipitate stress. The athermal contribution is small (~ 5 MPa). As it will be explained in this section, only two parameters are used to fit the yield strength. First, the concentration exponent in the activation volume and relaxation distance expressions used for the thermal stress calculation is obtained by fitting the yield stress at room temperature ($e_t = 0.58$). Second, the temperature dependence of the yield stress is adjusted by making the transition radius, r_c, temperature dependent, with a value of 5 nm at room temperature and 6.4 nm at 250ºC. All other parameters are taken from literature.

The thermal stress depends on temperature and solute content. The assumption made in the current application of the model, is the absence of dynamic strain ageing (DSA) meaning that no Mg segregates to dislocations. Therefore, the solute concentration near dislocations is $c_{sc} = c + c_0$. Considering the relatively low level of Mg in solid solution the potential effect of DSA on τ_t was found to be limited and hence supports the assumption.

The main parameters in the thermal stress expression (equation 5.2) are B_t, U_t, ω_t and e_t. τ_t is approximately proportional to $T \times ln(B_t^{(s)})$ so the influence of B_t is small and the default value used for other alloys is chosen ($B_t = 57$). The activation energy (U_t) used in calculating the thermal stress (τ_t) is the addition of the activation energy for solute diffusion (U_s) and the interaction energy between dislocation and solute atoms (ΔU_s). For Mg, values for U_s ranging from 120 kJ/mol to 140 kJ/mol have been reported in various research articles [40,41]. The value of ΔU_s should be in the order of 10 kJ/mol [39,40]. Therefore the value of 160 kJ/mol for U_t proposed in previous application of the *Nes* model [39] seems too high and a value of 150 kJ/mol was chosen for the present version. It is found that a variation of the activation energy, U_t, of 10 kJ/mol only changes the thermal stress of a few MPa independently of temperature. The two remaining parameters, e_t and ω_t, control the temperature dependence and overall level of τ_t and have similar effects. Therefore, the value of ω_t has been taken from literature [40] and only the concentration exponent, e_t, is used to fit simultaneously the room temperature yield strength for the two alloys and two tempers. A value of 0.58 is obtained and is within the expected range [0.5 – 1].

Keeping the value of the parameters controlling the yield strength within their expected ranges and only making the shear modulus temperature dependent, it was found that the effect of temperature on thermal stress and precipitate stress is not enough to account for the observed yield strength decrease with temperature. Consequently, it was chosen to use the critical radius as a temperature dependent parameter. This parameter depends on the type of force acting during shearing of precipitates (i.e. the interaction mechanism between dislocation and precipitate), which may depend on temperature. Furthermore the expression used for τ_p (equation

5.5) is a rough approximation, which does not consider the exact interaction mechanism between dislocation and precipitate. The temperature dependence of τ_p is not well established and can be fitted by adjusting r_c. The fitting has been made simultaneously for two alloys and two tempers between room temperature and 250°C, keeping the value of 5 nm at room temperature (table 5.5). The radius increase for temperatures higher than 180°C means that the resistance of precipitates to shearing decreases with increasing temperature.

Table 5.5: Critical radius with temperature

Temperature (°C)	r_c (nm)
130	5.0
150	5.0
180	5.0
250	6.4

5.6.2   Parameters controlling work hardening

The σ-ε curve from the *Nes* model can be compared to the experimental true σ-ε plot (up to necking). In the *Nes* model, work hardening is modelled as the result of the competition between dislocation storage and dynamic recovery. Several dynamic recovery mechanisms are possible depending on the amount of solute in the matrix; the mechanism giving the slowest recovery rate being the controlling one. Previous simulations assumed that recovery in aluminium alloys with moderate amount of alloying element, e.g. AA1xxx and AA3xxx [52], is controlled by dislocation climb as in pure metals. Although the amount of Mg in solid solution in the currently investigated AA6xxx is lower than in typical 5xxx alloys, simulations showed solute drag and pinning reactions give the slowest recovery rate and control recovery, as for 5xxx alloys.

A sensitivity study of the model revealed that variation of the values of the pre-exponential parameters B_ρ and B_δ within their acceptable range does not have much effect on the simulation results. In the same way, the parameter $q_{IV,\delta}$ controls the dynamic recovery by subgrain growth mainly during stage IV and has negligible effect on the current simulations, which does not go beyond stage III. On the other hand, the parameters ξ_ρ, ω_s, e_ρ, controlling the dislocation annihilation inside

dislocation cells and the parameters e_δ and ξ_δ controlling subgrain growth may have a significant effect on the simulation output depending on the simulation conditions. The sensitivity study, however, also showed that variation of the value of these parameters within acceptable ranges does not improve the overall fitting of the model with the experiment. According to the model, all these parameters are also supposed to be independent of solute content. For these reasons, the values of dynamic recovery parameters already reported for Al-Mg alloys [52] were used as default, except for U_s and ΔU_s which are the same than for thermal stress (cf. 5.6.1).

The sensitivity study with regard to the dislocation storage parameters also showed that the model is not very sensitive to the value of the cell wall geometrical parameter κ_0, the saturation misorientation in stage IV, φ_{IV}, and the parameter controlling the saturation of the subgrain size in stage IV, S_{IV}. These last two parameters are important for deformation larger than the one reached with the current simulations. Default values were then used for these parameters [52].

One of the most important physical variables controlling the dislocation storage rate is the mean slip length. As explained in section 5.4.3, the mean slip length is controlled by the distribution of forest dislocations, precipitates and grain boundaries. The influence of precipitates is determined by the parameter κ_3. In AA6xxx alloys, shearable and non-shearable precipitates interact differently with dislocations and, therefore, have a different effect on the dislocation storage. In the current version, this effect has been included by making the parameter κ_3 dependent on the precipitate distribution. Table 5.6 gives the value of parameter κ_3 for the investigated alloys and tempers, as well as the corresponding precipitate contribution to the mean slip length, L_p. The results were obtained by assuming a log normal precipitate size distribution with a standard deviation $\Delta r = 0.2r$ [47,49] and by taking $\kappa_{3p} = 1.5$ [52], r_c determined (cf. section 5.6.1), and $r_{cl} = 25$ nm [49]. From the results in table 5.5, it can be noticed that for the material in T6 conditions at 20°C, the average radius is close to the critical radius and about half of the precipitates are non-shearable. L_p is small enough to expect the precipitates to contribute to work-hardening. The chosen value for κ_{3p} and Δr are then important. For the other conditions the average radius is small enough compared to the critical radius so that only a very small fraction of precipitates are non-shearable and contribute to L_p.

Table 5.6: Parameters κ_3, φ and L_p calculated with $\kappa_{3p} = 1.5$ and a critical radius for shearing/by-passing of $r_c = 5$ nm (20°C) and 6.4 nm (250°C).

Alloy	T (°C)	r (nm)	f_r	$\bar{r_c}$ (nm)	f_c	φ	κ_3	L_p (nm)
6016-T4	20 / 250	0.8	0.0049	-	0	0	0	∞
6016-T6	20	4.5	0.0098	5.7	0.0042	0.03	0.017	14
6016-T6	250	4.5	0.0098	6.9	0.0008	0.03	0.002	96
6061-T4	20 / 250	0.8	0.0094	-	0	0	0	∞
6061-T6	20	4.8	0.0081	5.7	0.0045	0.04	0.025	11
6061-T6	250	4.8	0.0081	7.0	0.0012	0.03	0.004	63
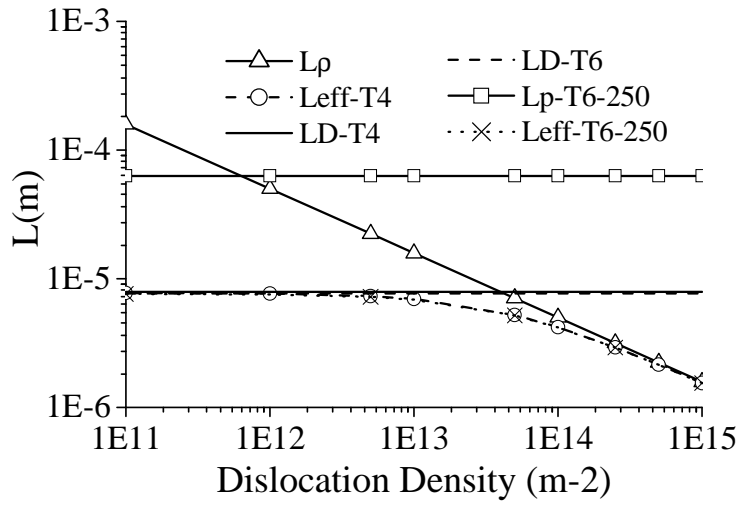
Figure 5.15: Comparison of the forest dislocation, L_ρ, precipitates, L_p, and grain size, L_D, contributions and effective slip length vs. dislocation density for 6061

The forest dislocations, precipitates and grain size contributions to the effective mean slip length are compared in figure 5.15. The grain size contribution has been calculated with $\kappa_2 = 2$ [52], meaning that the average location of dislocation sources is in the centre of the grain. The forest dislocation contribution is controlled by the

statistical parameter C, which is inversely proportional to the chance for a dislocation to become stored inside the cell. This parameter depends on the solute content; the higher the solute content, the smaller the mean free path should be, meaning the smaller the parameter C. A typical value of $C = 50$ is used in figure 5.15. For T4 material, L_p is infinitely large (table 5.6) as the precipitates are small and can be easily sheared, meaning that they do not contribute to work-hardening (fraction of non-shearable precipitates is negligible). In the same way, L_p for T6 materials deformed at 250ºC is still large compared to L_D and precipitates have negligible influence while at RT L_p becomes comparable to L_D and the presence of precipitates contribute to L_{eff}. Figure 5.15 also shows that at small value of dislocation density or very small deformation, L_D is the smallest of the three mean free paths and hence grain size is the controlling factor. With increasing dislocation density or deformation L_p decreases rapidly and eventually forest dislocation density becomes the controlling factor. The parameter C is therefore an important model parameter. It is found that an increment of C from 30 (corresponding to AA5xxx) to 80 (typical for commercially pure aluminium) decreases the flow stress in the order of 40 MPa and extend the range of stage II. For the application of the *Nes* model to AA6xxx, C is chosen as a fitting parameter.

The only remaining parameter of relevance is the dislocation storage q_c. This parameter is the ratio between the cell size and the distance between dislocations inside the cell and, therefore, determines the distribution of dislocations in the microstructure. q_c is also related to q_b, the second scaling parameter. Previous applications of the *Nes* model [52] showed that q_c should increase with increasing solute content, which means that the dislocation network inside the cells becomes relatively denser compared to the cell size. The effect of q_c on the work-hardening is complex because it influences simultaneously the dislocation density, ρ_i, the cell size, δ, and the misorientation, φ. The sensitivity study shows that the effect on cell size dominates and an increasing q_c value increases the cell size and reduces the work-hardening rate. Since q_c depends on solute content, it is used as the second fitting parameter for work-hardening.

The experimental true stress - true strain response of the two alloys, 6016 and 6061, in T4 and T6 conditions, at two temperatures, 20ºC and 250ºC, and at a strain rate of 0.01 s^{-1} were used to fit the *Nes* model. The dislocation storage parameter, C, and the scaling parameter, q_c, depend on solute content. However, for the current fitting, these parameters are assumed independent of alloy composition but are fitted separately for T4 ($C = 30$ and $q_c = 9$) and T6 ($C = 50$ and $q_c = 7$) materials.

(a)

(b)

Figure 5.16: Fitting of experimental true stress- true strain response for T4 temper
(a) 6016 and (b) 6061 with the *Nes* model applied at two different temperatures.

(a)

(b)

Figure 5.17: Fitting of experimental work hardening rate for T4 temper (a) 6016 and
(b) 6061 with *Nes* model at two different temperatures

Figure 5.16 and figure 5.17 show the quality of the fit for the true stress-true strain
response and the work hardening rate at room temperature and 250°C for T4 temper
of both alloys. At room temperature, the simulated work hardening rates of both
alloys are approximately the same the only difference being the yield strength. This

is in accordance with experimental results. A good fit is obtained for both alloys with the same set of parameter values although the simulated stage II is longer than in the experiment. When the temperature increases from room temperature to 250°C, the model predicts a decrease of the work hardening rate for both alloys. This is also qualitatively in accordance with the experimental results. At 250°C for 6016, the work hardening rate is relatively well reproduced. There is only a constant shift between modelled and experimental flow stresses that comes from the initial shift between the fitted and experimental yield strength. At 250°C for 6061, the simulated work hardening rate is too low during stage III. The model does not capture the experimental fact that, when the temperature increases, the work hardening rate decreases less for 6061 than 6016.

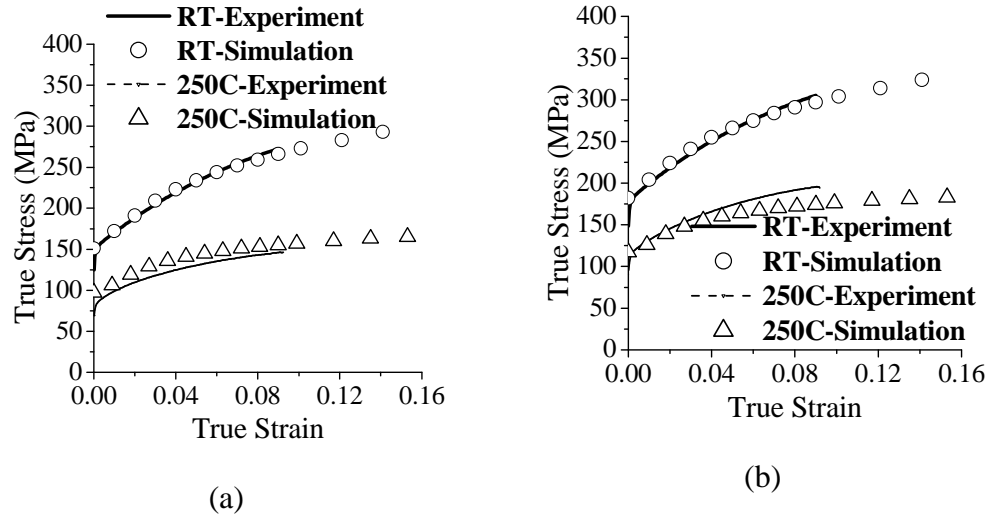(a)   (b)
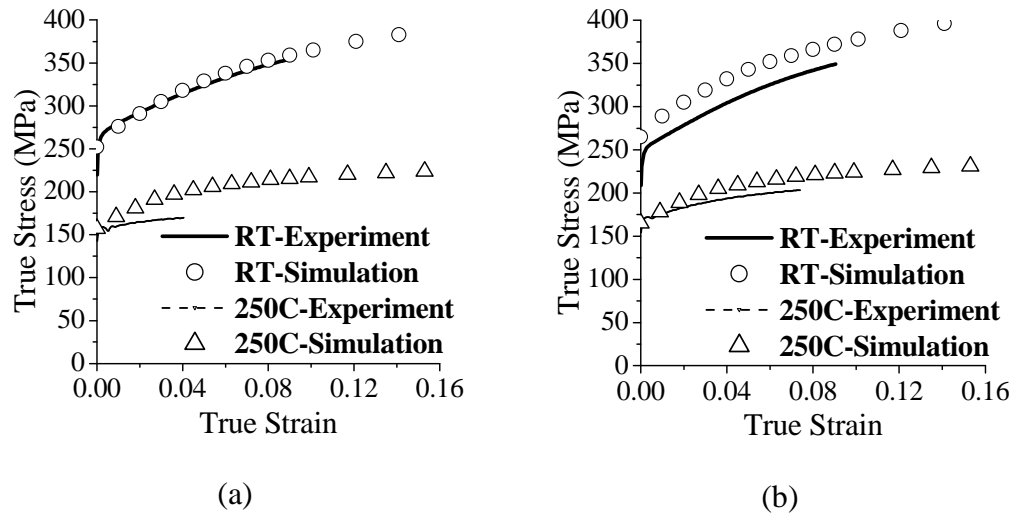
Figure 5.18: Fitting of experimental true stress-true strain response for T6 temper
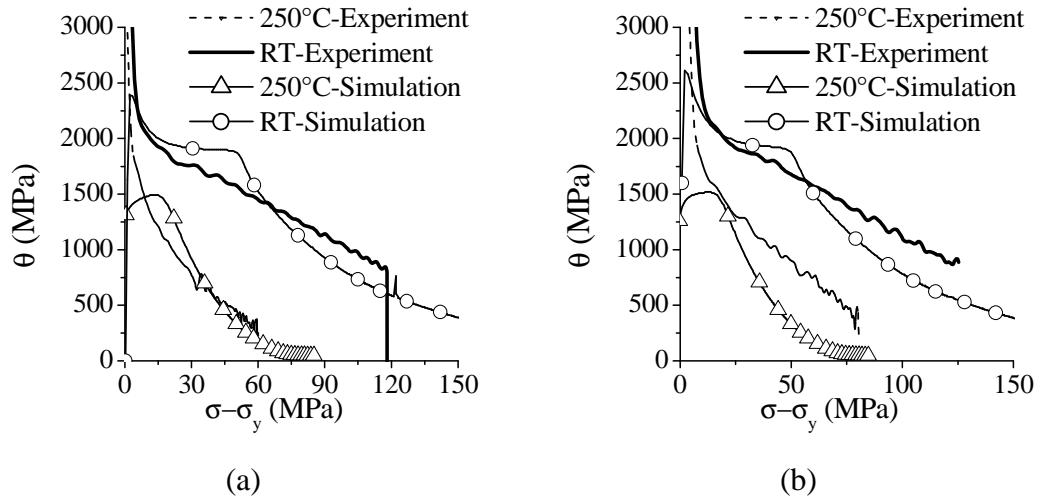(a) 6016 and (b) 6061 with the *Nes* model applied at two different temperatures
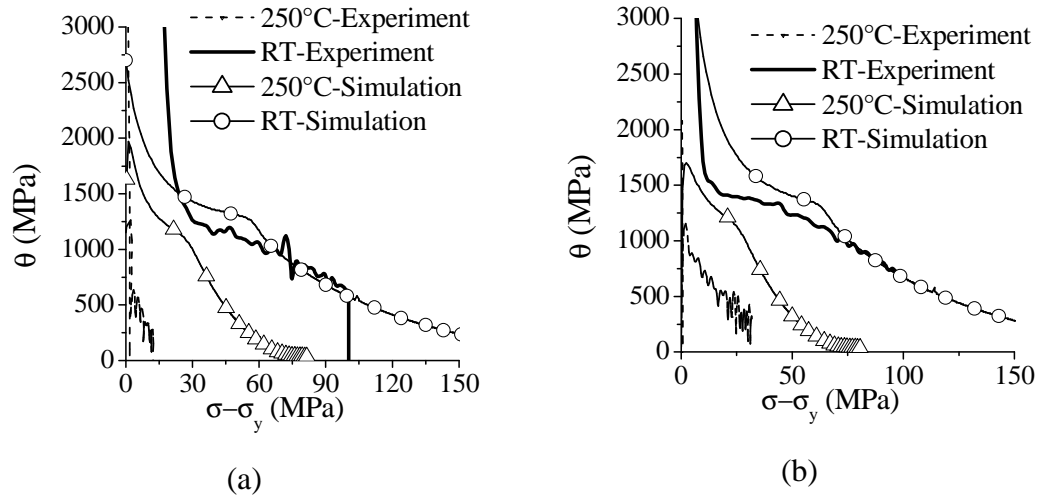
Figure 5.19: Fitting of experimental work hardening rate for T6 temper (a) 6016 and (b) 6061 with *Nes* model at two different temperatures

Figure 5.18 and figure 5.19 show the quality of the fit for the true stress-true strain and work hardening rate curves at room temperature and 250°C for T6 temper of both alloys. At room temperature, a good fit is obtained for the work-hardening rate, although stage II predicted by the model is longer than observed experimentally. The shift between experimental and simulated stress-strain curves of 6061-T6 comes from a shift between the fitted and experimental yield strength. The model also gives a decrease of the work-hardening rate with increasing temperature to 250°C but not as much as observed experimentally. However, a better fit could not be obtained with a single set of parameter values for C and q_c.

When changing from T4 to T6 temper, precipitates grow and solutes are depleted. In the literature [50,53], depletion of solutes during ageing is supposed to be responsible for the experimentally observed decrease of the initial work-hardening rate; solute depletion results in an increase of the mean free path, which is translated in the *Nes* model by an increase of the C parameter. The higher fitted C value for T6 condition compared to T4 reflects this effect of solutes. A relatively low C value ($C = 30$) is found for T4 materials compared to Al-Mg and 5xxx alloys ($C > 35$) [52], meaning that the mean free path is relatively smaller in AA6xxx. The fitted C value for T6 materials ($C = 50$) is in accordance with values reported for low Al-Mg alloys ($C > 45$) [52]. The scaling parameter, q_c, relates the dislocation cell size with the dislocation density inside the cells. The continuous decrease of the fitted q_c values when going from 5xxx [39] to 6xxx-T4 and to 6xxx-T6 show that increasing the amount of precipitates and/or decreasing the amount of solutes promotes the

formation of cell walls at the expense of the storage of dislocation inside the cells. This results in a decrease of subgrain size and an increase of the stress and work-hardening rate in stage III, partially balancing the effect of C (the effect of C still dominates). The fitted values of q_c for T4 ($q_c = 9$) and T6 ($q_c = 7$) conditions are lower than the values already reported for Al-Mg binary alloys with similar total solute content (resp. $q_c = 12$ and 9) [52], meaning that the dislocation cell size is smaller in 6xxx compared to Al-Mg alloys.

Experimental results showed that (section 5.3.1), when going from T4 to T6 temper, the dynamic recovery rate during room temperature deformation slightly decreases (e.g. β parameter of Voce equation decreases). This is usually explained as the result of the competition between solute depletion and precipitate growth. The *Nes* model, however, only includes the effect of solutes on dynamic recovery and therefore predicts faster dynamic recovery rate for T6 compared to T4 materials. However, with the chosen parameters values, the effect is small. During deformation at 250°C, the *Nes* model also predicts very similar dynamic recovery rates for T4 and T6 conditions while experimental measurements showed much faster rates for T6 compared to T4. More generally, with increasing temperature, the work-hardening rates of T4 and T6 tempers calculated with the *Nes* model converge to each other while the experimental results showed the opposite. This explains the quantitative differences between calculated and experimental strain-stress curves at 250°C. The reason for this discrepancy is, however, not yet understood and still needs to be investigated further.

5.6.3   Parameters and Values

The parameter values used in this model are presented in the following table (table 5.7). The meaning of the symbols was given in 5.4.2.

Table 5.7: Value of the parameters used in the model

Symbol	Value range	Unit	Symbol	Value range	Unit
ω_ρ	25	-	e_ρ	0.67	-
ν_D	$1.0 \cdot 10^{13}$	s^{-1}	$B_\delta^{(s)}$	100	-
b	$2.86 \cdot 10^{-10}$	m	$\xi_\delta^{(s)}$	40	-
k	$1.38 \cdot 10^{-23}$	$J.K^{-1}$	e_δ	0.65	-
κ_3	Refer Table 5.6	**-**	$q_{IV,S}$	0.5	-
ν	0.33	-	$q_{IV,\delta}$	2	-
c_0	Refer Table 5.4	atom. frac.	φ_{IV}	0.052	Rad
ΔU_{sc}	0	$J.mol^{-1}$	ω_t	20	-
q_c	Cf. text	-	m	0.8	-
C	Cf. text	-	$B_\rho^{(sg)}$	0.23	-
f	0.1	-	r_{cl}	$25 \cdot 10^{-9}$	M
α_1	0.3	-	ρ_i	$1.0 \cdot 10^{11}$	m^{-2}
α_2	3	-	τ_{cl}	0.0	Pa
κ_0	3.5	-	q_b	Calculated	-
U_t	150000	$J.mol^{-1}$	$B_\rho^{(sc)}$	0.23	-
U_{sd}	130000	$J.mol^{-1}$	φ_c	0.349	Rad
U_S	150000	$J.mol^{-1}$	$B_\rho^{(sc)}$	0.23	-
ΔU_S	0	$J.mol^{-1}$	$\xi_\rho^{(sg)}$	80	-
κ_2	2.0	-	$\xi_\rho^{(sc)}$	80	-
β	0.36	-	ω_s	1	-
$B_t^{(s)}$	57	-	e_t	0.58	-

5.7 Validation and Discussion

After fitting the *Nes* model for 6016 and 6061 alloys at room temperature and 250°C with a strain rate of 0.01 s^{-1}, the validity of the model has been studied at other temperatures (130°C, 150°C and 180°C) and strain rate (0.1 s^{-1}) for the same alloys. The use of the *Nes* model at lower strain rate (≤ 0.001 s^{-1}) at 250°C is not possible as experimental results show evidence of dynamic precipitation for T4 tempers, a mechanism which is not yet implemented in the model.

(a)

(b)

(c)

(d)
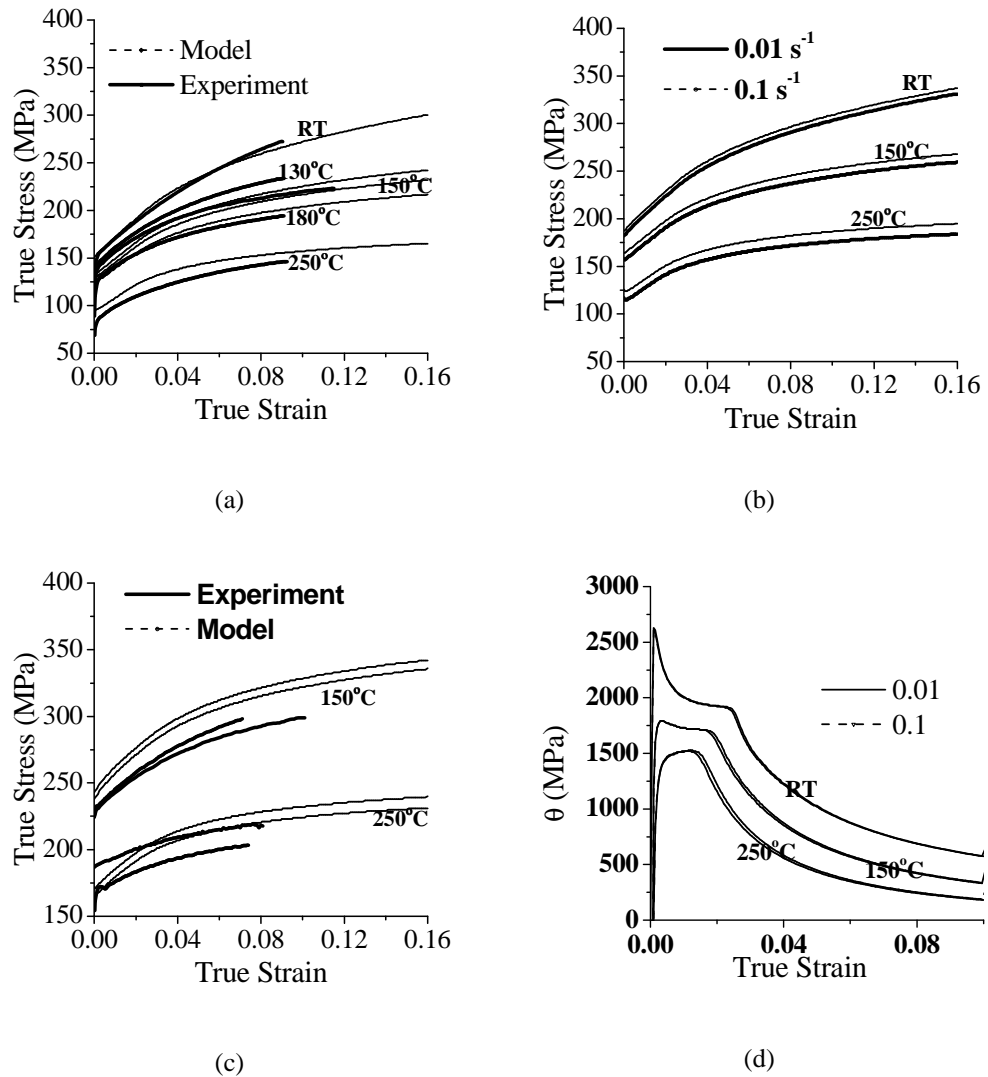
Figure 5.20: Model predictions (a) comparison with experimental results for 6016-T4 at 0.01 s^{-1} (b) simulation results for 6061-T4 (c) comparison with experimental results for 6061-T6 (d) simulated work hardening rate for 6061-T4. At each temperature the curve located above corresponds to a strain rate of 0.1 s^{-1} and the one below to 0.01 s^{-1} both for experiment and modelling.

Figure 5.20a depicts the quality of model predictions for three different temperatures at a strain rate of 0.01 s^{-1} for the alloy 6016-T4. The fitted curves (at room temperature and 250°C) are also shown on the same figure in order to have a better feeling about the suitability of the model within the range of temperatures of interest. It can be clearly seen that the model successfully predicts the decrease of

work hardening rate with temperature. The shift observed between simulated and experimental stress-strain curves at some temperatures is mainly due to a shift in yield strength. As it was explained in 5.6.1 the temperature dependence of yield strength has been fitted simultaneously for the two investigated alloys and tempers with only one parameter and the match was not perfect for all conditions. Similar conclusions are obtained for 6061-T4. In 5.6.2 it was shown that a good fit of the model for T6 tempers at both room temperature and 250°C was not possible; a good fit was obtained at room temperature but the very low work hardening rate at 250°C could not be well reproduced. Figure 5.20c shows that the model slightly overestimates the work-hardening rate of T6 materials at 150°C but the relative effect of temperature on work hardening rate is well captured.

Figure 5.20b, shows the effect of strain rate at several temperatures for 6061-T4. Similar results are obtained for 6016 and for T6 conditions. From experiment (figure 5.1) it was noticed that the yield strength at room temperature is independent of strain rate and that it increases with strain rate at higher temperature. For T6 conditions at 250°C an increase of strength of about 20 MPa was noted with increase of strain rate from 0.01 to 0.1 s^{-1} (figure 5.1). The model also predicts an increase of the initial stress with increasing strain rate but overestimates this effect at room temperature and underestimates it at higher temperature (figure 5.20c). These differences are, however, relatively small. Simulation results also show that, when temperature increases, the work hardening rate increases with increasing strain rate, although this effect is small (figure 5.20.d). This is in accordance with experimental data (see figure 5.1 and figure 4.5 in chapter 4) except for the T4 conditions at 250°C for which a small effect of dynamic precipitation was noticed.

5.8   Conclusions

The main objective of this chapter was to investigate the effect of temperature and strain rate on work hardening behaviour and to develop a numerical model applicable to 6xxx aluminium alloys. Work hardening is related to strain rate sensitivity through the formation of substructure at different levels of strain. Tensile results show that the strain rate sensitivity is zero for both the alloys at RT and slightly positive at 250°C. Temperature influences the flow stress in a most noticeable manner. Both yield point and work hardening rate decrease with increasing temperature. An analysis with the Voce equation revealed that the decrease of work hardening rate is related to both a decrease of dislocation storage efficiency and to the thermal activation of dynamic recovery. Subsequently, the material softens considerably with an increasing drawing temperature leading to a very weak substructure formation owing to larger dynamic recovery at 250°C.

The *Nes* work hardening model has been selected and adapted to 6xxx aluminium alloys by modifying the yield stress expression and considering the different contributions of shearable and non-shearable precipitates on the dislocation mean slip length. The model has been fitted for two alloys and two tempers at RT to 250°C. Overall, the model reproduces well the effect of strain rate and temperature although some quantitative differences remain. For instance, the predicted yield strength slightly deviates from the experiment results for a few particular situations as e.g. for 6016 under T4 condition tested at 250°C, 6061 in T6 state tested at RT and at 150°C at $0.01s^{-1}$ strain rate. The calculated work hardening rate also fits well the experimental results at RT but the correspondence at 250°C needs to be improved. At slow strain rate ($0.001s^{-1}$) some evidence of dynamic precipitation has been recorded (Chapter 4, section 4.3.1) at 250°C for both the alloys. As dynamic precipitation is ignored in the present form of the model, there was no possibility to address this issue. The validity of the model has not been checked for other alloys and temperatures over 250°C. The prediction capability of the model is still limited by the dependence of two parameters on solute content. Indeed, to have a model applicable for any AA6xxx and any temper, the dependence of q_c and C with solute content needs to be known. The assumption made in the present investigation regarding the use of identical parameter values for both alloys of the same temper also needs further attention. Therefore a sub-model involving q_c and C as a function of solute content can be added for improving the current version of the model. With these proposed modifications the model could be extended to predict stress-strain response under peak age and over age conditions.

References

1. **Hansen N. and Jensen D**, Development of microstructure in FCC metals during cold work, *Philosophical Transactions of Royal Society. of London*, **A357**, 1999, p. 1447

2. **Hansen N., Huang X. and Hughes D.A.,** Microstructural evolution and hardening parameters, *Materials Science and Engineering*, **A317,** 2001, p. 3

3. **Hansen N.**, Cold deformation microstructures, *Materials Science and Technology,* **27**, 1990, p. 1039

4. **Hughes D.A.**, Microstructure evolution, slip patterns and flow stress, *Materials Science and Engineering A*, **319-321**, 2001, p. 46

5. **Hughes D.A.**, Microstructure and flow stress of deformed polycrystalline metals, Scripta Metallurgica et Materialia, **27**, 1992, p. 969

6. **Andrade E. and Henderson C.,** The mechanical behaviour of single crystals of certain face-centred cubic metals, *Philosophical Transactions of the royal Society of London series a-mathematical and physical sciences*, **244,** 1951, p. 177

7. **Honeycombe R.W.K**., The Plastic Deformation of Metals, 2nd ed., Butler & Tanner, Ltd., London, 1984

8. **Lomer W.M.**, A dislocation reaction in the face-centred cubic lattice, *Philosophical Magazine*., **42**, 1951, p.1327

9. **Cottrell A.H**., The formation of immobile dislocations during slip, *Philosophical Magazine*, **43**, 1952, p.645

10. **Mecking H. and Kocks U.F**., Kinetics of Flow and Strain-Hardening, *Acta Metallurgica*, **29**, 1981, p.1865

11. **Hiwatashi S., Van Bael A., Van Houtte P., Teodosiu C.**, Prediction of forming limit strains under strain-path changes: application of an anisotropic model based on texture and dislocation structure, *International Journal of Plasticity*, **14**, 1998, p.647

12. **Estrin. Y.**, Unified constitutive laws for plastic deformation, Academic press, London, 1996

13. **Nes E.**, Modelling of work hardening and stress saturation in fcc metals, *Progress in Materials Science,* **41**, 1998, p.129

14. **Hagström J., Mishin O.V. and Hutchinson B.**, Gallium enhanced microscopy for revealing grain boundaries and dislocation subboundaries in aluminium alloys, *Scripta Materialia,* **49**, 2003, p.1035

15. **Hagström J. and Hutchinson B.**, Recrystallization process in aluminium revealed by Gallium treatment, *Materials Science Forum*, **396-402**, 2002, p.539

16. **Ludwig W., Nielsen S.F., Poulsen H.F. and Bellet D.**, Direct Observation of Grain Boundary Wetting by Synchrotron Radiation Imaging Techniques, *Defect and Diffusion forum*, 2001, **194-199**, p.1319

17. **Mahmudi R.**, Grain boundary strengthening in a fine grained aluminium alloy, *Scripta Metallurgica and Materialia*, **32**, 1995, p. 2061

18. **Blaz L. and Evangelista E.**, Strain rate sensitivity of hot deformed Al and AlMgSi alloy, *Materials Science and Engineering A*, **207**(2), 1996, p.195

19. **Wagoner RH.**, A new description of strain-rate sensitivity, *Scripta Maetallurgica.*, **15**, 1981, p.1135

20. **Ayres R.A. and Wenner M.L**, Strain and strain rate hardening effects in punch stretching of 5182-O aluminium at elevated temperatures, *Metallurgical Transactions A*, **10A**, 1979, p.41

21. **Ayres R.A. and Wenner M.L**, Strain and strain rate hardening effects on punch stretching of 5182-O aluminium at elevated temperatures, *Sheet Metal Forming and Formability:10th Biennial Conference of the International Deep-drawing Research Group*, University of Warwich, England, 1978, p.187

22. **Ayres R.A. and Wenner M.L**, Strain and strain rate hardening effects in punch stretching of 5182-O aluminium at elevated temperatures, *Sheet Metal Industries*, 1978, p.1208

23. **Fuchs E.A. and Williams D.R.**, Strain measurements at elevated temperature and high strain rates, 5th Annual and hostile Environments and High Temperature Measurements Conference Proceedings, Society for Experimental Mechanics (Costa Mesa, CA,) 1988, p.42

24. **Bolt P.J., Werkhoven R. and van den Boogaard A.H.**, Warm forming of aluminium sheet, *NIMR report*, project number MC1.02106, 2005

25. **Li D. and Ghosh A.**, Tensile deformation behaviour of aluminium alloys at warm forming temperatures, *Materials Science and engineering A*, **352**(1-2), 2003, p.279

26. **Lee C.S., Duggan B.J. and Smallman R.E.**, A theory of deformation banding in cold-rolling, *Acta Metallurgica and Materialia*, **41**, 1993, p. 2265

27. **Hutchinson B.**, Deformation substructures and recrystallization, *Materials Science Forum*, **558-559**, 2007, p. 13

28. **Akbari G.H., Sellars C.M. and Whiteman J.A.**, Microstructural development during warm rolling of an IF steel, *Acta Materialia*, 45, 1997, p.5047

29. **Zhu Q. and Sellars C.M.**, Evolution of microbands in high purity aluminium-3% magnesium during hot deformation testing in tension-compression, *Scripta Materialia*, **45**(1), 2001, p.41

30. **Kocks U.F.**, Laws for Work-hardening and Low-temperature Creep, *Journal of Engineering. Material. and.Technology. (ASME-H)*, **98**, 1976, p.76

31. **Kocks U.F. and Mecking H.**, A mechanism for static and dynamic recovery, 5th International Conference on the Strength of Metals and Alloys, eds. P. Haasen et al., Pergamon Press, Oxford, vol. 1, 1979, p. 345

32. **Mecking H.**, in Dislocation Modelling of Physical Systems, eds. M.F. Ashby et al., Pergamon Press, Oxford, 1981, p. 197

33. **Estrin Y. and Mecking H.**, A unified phenomenological description of work hardening and creep based on one-parameter models, *Acta Metallurgica*, **57**, 1984, p. 57

34. **Chen S.R., Stout M.G., Kocks U.F.**, **MacEwen S.R. and Beaudoin A.J.**, in Hot deformation of Aluminium alloys II, eds. T.R. Bieler et al., The Minerals, Metals and Materials Scoiety, Rosemont, Illinois, 1998, p.171

35. **Nes E., Marthinsen K. and Holmedal B.**, The effect of boundary spacing on substructure strengthening, *Materials Science and Technology*, **20**, 2004, p 1377

36. **Marthinsen K. and Nes E.**, The AFLOW-model – A microstructural approach to constitutive plasticity-modelling of aluminium alloys, *Materials Science Forum*, **331-337**, 2000, p.1231

37. **Roters F., Raabe D. and Gottstein G.**, Work hardening in heterogeneous alloys - a microstructural approach based on three internal state variables, *Acta Materialia*, **48**, 2000, p.4181

38. **Goerdeler M. and Gottstein G.**, A microstructural work hardening model based on three internal state variables, *Materials Science Engineering A*, **309-310**, 2001, p. 377

39. **Marthinsen K. and Nes E.**, Modelling strain hardening and steady state deformation of Al-Mg alloys, *Materials Science and Technology*, **17**, 2001, p. 376

40. **Nes E. and Marthinsen K.**, Modeling the evolution in microstructure and properties during plastic deformation of f.c.c.-metals and alloys an approach towards a unified model**,** *Materials Science Engineering A,***322**, 2002,p.176

41. **Rollett A.D. and Kocks U.F.,** Stage IV Work Hardening in Cubic Metals, *Solid State Phenomena***, 35-36**, 1994, p.1

42. **Nes E., Marthinsen K. and Holmedal B.**, The effect of boundary spacing on substructure strengthening, *Materials Science and Technology*, **20**, 2004, p. 1377

43. **Cheng L.M., Poole W.J., Embury J.D., and Lloyd D.J.**, The Influence of Precipitation on the Work-Hardening Behavior of the Aluminum Alloys AA6111 and AA7030, *Metallurgical and Materials Transactions A*, **34A**, 2003, p. 2473

44. **Kocks U.F., Argon A.S. and Ashby M.F.**, in *Progress in Materials Science*, eds. Chalmers B. et al., Pergamon Press, Oxford, vol. 19, 1975

45. **Monnet G.**, Investigation of precipitation hardening by dislocation dynamics simulations, *Philosophical Magazine*, **86**, 2006, p. 5927

46. **Myhr O. R. and Grong Ø**, Modelling of non-isothermal transformations in alloys containing a particle distribution, *Acta materialia*, **48**, 2000, p.1605

47. **Friis J., Holmedal B., Ryen Ø., Nes E., Myhr O.R., Grong Ø., Furu T. and Marthinsen K.**, Work hardening behaviour of heat treatable Al-Mg-Si alloys, *Materials Science Forum*, **519-521**, 2006, p.1901

48. **Myhr O.R., Grong Ø. and Andersen S.J.**, Modelling of the age hardening behaviour of Al-Mg-Si alloys, *Acta Materialia*, **49**, 2001, p.65

49. **Simar A., Bréchet Y., Meester B. de, Denquin A., Pardoen T.**, Sequential modeling of local precipitation, strength and strain hardening in friction stir welds of an aluminum alloy 6005A-T6, *Acta Materialia*, **55**, 2007, p.6143

50. **Murayama M, and Hono K.**, Pre-precipitate clusters and precipitation processes in Al-Mg-Si alloys, *Acta Materialia*, **47**, 1999, p.1537

51. **Chen J. H., Costan E., van Huis M. A., Xu Q., Zandbergen H. W.**, Atomic Pillar–Based Nanoprecipitates Strengthen AlMgSi Alloys, **312,** *Science*, 2006, p.416

52. **Holmedal B., Nes E. and Ryen Ø.**, Modelling of Work Hardening, *Report European project Vir[Fab]*, deliverable D23 and 27, NTNU, 2004

53. **Llyod D.J.**, The Work Hardening of Some Commercial Al Alloys, Materials Science Forum, **519-521**, 2006, p. 55

CHAPTER 6

PLASTIC ANISOTROPY IN AA6XXX SHEETS

Plastic anisotropy observed during tensile, plane strain compression and deep drawing tests at room temperature and 250°C is discussed. The possible causes for such anisotropy were investigated by studying the dependence of the r-value on the tensile direction, texture, and yield locus. The shape of the r-value profile and the position of cup ears are independent of the forming temperature. The texture also did not show much change when deformed at 250°C in comparison to RT. The average r-value and ear amplitude, however, depend on temperature. The activation of extra slip systems with temperature increase was suspected as the possible reason for this observation. Experimentally measured r-values and textures have also been used for validating the *crystal plasticity* based *Visco-Plastic Self-Consistent* (*VPSC*) model and subsequently the model has been used to predict the yield locus between room temperature and 250°C.

6.1   Introduction

Plastic anisotropy has an important effect on strain distribution during deformation. Normal plastic anisotropy controls the thinning and formability of most sheet metals [1] and should therefore be taken into account in order to obtain the final geometry of the products within specified tolerance. The appearance of ears is also a well known consequence of plannar anisotropy during deep drawing (DD) of metallic sheet, which is of technological relevance. The development of ears creates additional scrap and induces inhomogeneous properties along the walls of the cups. They can be related to the r-value measured during tensile tests and considered as a basic tool to characterize anisotropy. It is well known that crystallographic orientation or texture in polycrystals is one of the parameters that govern plastic anisotropy and formability of aluminium alloys; a texture derived yield locus combined with FEM is therefore necessary to successfully explain and predict the influence of plastic anisotropy during drawing.

Deep drawing is an important industrial process for sheet forming and also a good test to evaluate strain distribution resulting from plastic anisotropy. The appearance of the undulating pattern at the periphery of the deep-drawn cup with a number of distinct high points called ears and an equal number of low points known as troughs are termed as earing. Ears appear during deep-drawing due to different radial elongations generated by the sheet texture and may lead to several undesirable effects like thickness variations, or change of tolerance in order to maintain volume conservation. In case of rolled Al sheets the ideal situation to minimize earing and increase the deep-drawing formability would be the presence of random or {111} fibre crystallographic texture. This seems too optimistic primarily because during sheet processing the texture does not remain random nor includes {111} components. A more practical solution may be the control of texture components. In order to achieve good formability, the recrystallization structure needs to be present in addition to a suitable crystallographic texture. The typical texture after recrystallization of Al sheets is usually dominated by the Cube {100} <001> or Goss {110} <001> components. These two components promote pronounced earing at 0º (RD) and/or 90º (TD) directions [2,3]. The ear shape of Goss is found to be shifted 15º away towards the transverse direction. All orientations between cube and Goss, i.e. <100> parallel to the rolling directions, inhibit 45° earing. In an attempt to identify the texture responsible for the minimization of in-plane anisotropy, it was revealed that the Cube texture may be beneficial when combined with rolling texture components. Such combination of Cube and rolling texture components can be obtained during annealing depending on the alloy composition, hot or cold rolling conditions, annealing heat-treatment etc [4,5,6]. Rolling texture components, Cu

{112} <11$\bar{1}$>, S {123} <63$\bar{4}$>, and Bs {110} <1$\bar{1}$2>) promote earing at 30°, 45°, 60° respectively with respect to the rolling direction [7,8]. A mixed texture with annealing and rolling components can therefore lead to a more balanced earing profile with eight, six or two fold symmetry. Other investigators have also supported these facts [9].

Another simple parameter to characterize anisotropy is the r-value derived from uniaxial tensile experiments. The r-value or Lankford coefficient is defined as the ratio of true plastic strain along width to that along thickness. For anisotropic materials, it depends on the tensile direction with respect to the rolling direction. The limit drawing ratio (LDR), which estimates the deep-drawability, is influenced greatly by the r-value. A higher average r-value[1] is always encouraged in order to increase the LDR and hence the drawability. But the average r-values from conventionally rolled and annealed aluminium alloys is less than 1, typically in the range of 0.55 to 0.85 [10,11]. These values are much lower compared to commercial steel sheets and explain the relatively low formability of Al sheets. R-value may depend on the applied tensile strain for AA6xxx alloys [12] and should therefore be expressed for a given specimen elongation. The strain dependency of r value is strongly related to the texture evolution [13] and the grain size and has been a research topic of interest [14] since it may produce changes in anisotropy. The relation between r-value and work hardening and their dependence on the tensile direction has also been investigated by many researchers. Engler and An [15] in their work with AA5005 found that increasing the proportion of deformation texture components makes r-value profiles more asymmetric i.e. r-value along RD decreases and along TD increases compared to the r-value profile of pure annealing textures. Extending the comparison to tensile test results almost no difference of work hardening has been observed for low strain (section 5.3 of chapter 5). Only at 45° work-hardening is slightly higher than for the other two directions at the larger strain. The curves for RD and TD almost superimpose on each other. In another investigation by Li [16] on a material exhibiting a similar r-value profile, the flow curves show maximum strain hardening for extruded direction (ED) compared to TD and the 45° direction, with minimum strain hardening at 45°. Nader [17] found that the flow curves obtained from the tensile experiment with AA3003 along 45° and TD superimpose each other and that the flow stress is higher along RD, while the r-value increases from TD to RD through 45°. They also noticed that the r-value increases almost proportionally with the temperature. So the correlation between strain ratio and strain hardening is not simple and systematic for different alloys.

---

[1] average r-value ($\bar{r}$)=(r_0 +2r_{45} + r_{90})/4

Formation of different dislocation structures influenced by the presence of a different number of active slip systems is supposed to be responsible for the different results.

Temperature is also found to have a significant effect on anisotropy [18]. The changing anisotropic behaviour with temperature can be explained by the activation of additional slip systems. Like other fcc metals aluminium slips principally on the octahedral {111} planes in the <110> directions, but slip on other planes (but always along <110> direction) has been frequently reported, particularly at higher temperatures. At temperature below $0.5 \times T_m$ ($0.7 \times T_m$ [19] or $0.6 \times T_m$ [20] by some investigations) classical {111}<110> systems have the lowest critical resolved shear stress (CRSS) making octahedral glide the only feasible. At higher temperatures the CRSS of the non octahedral systems decreases to values close to {111}<110> making them activated. Perocheau [19] reported that at higher temperature ($\geq$ 400°C) slip on {110} could be slightly easier than on {111} while on {100} slip is always difficult. In contrast Bacroix [21] stated {100} as the most probable one at high temperature because of the fact that {100} plane is the most densely packed plane after {111}. Al deformed in tension or compression at low strain rates showed slip on {110} planes between 225°C and 365°C [22] and on {100} planes at 400°C [23]. Maurice and Driver [24] first reported the evidence of non octahedral slip under large strain rate ($10^{-1}s^{-1}$) by means of channel die compression on Al crystals at 400°C. The possibility of slip on {112} has also been discussed and it was concluded that slip on this plane substantially reduces the octahedral slip. This work has been extended [25] up to a strain rate of $10s^{-1}$. Later Driver [26] in his work with PSC tests at a strain rate of $10s^{-1}$ with Al-1%Mn crystals showed that non-octahedral slip begins on {100} plane after 350°C. An important proof for the activation of the non-octahedral slip system {110}<110> at increased temperature is the stabilization of the cube orientation (>300°C), which is unstable at room temperature [27]. Interestingly glide on {100} planes has been reported [28] even at 170°C for AA6056, when deformed at 2% in compression. Dislocations are able to cross slip on to {001} planes and glide. This corroborates the results of Carrade and Martin [29], finding unstable glide along {100} during creep tests from 180°C and primary {100} glide from 400°C for aluminium single crystals. At 180°C glide on {001} seems difficult because of strong friction on screw dislocation, which disappears with temperature.

In current forming simulations with FEM, plastic anisotropy effects can be introduced by the use of an appropriate yield function. Since plastic anisotropy is related to the crystallographic texture and slip system activation, *crystal plasticity* models are preferred to compute the effect of plastic anisotropy on the yield locus. The first noticeable work related to plastic anisotropy was performed by Taylor [30]. He assumed each and every grain to experience the same shape change as the whole

polycrystal. All five possible combinations of the {111}<110> slip systems has been considered in his model in order to calculate the amount of slip. Bishop and Hill [31] revised Taylor's work with the statement that only a limited number of states can activate all five {111}<110> slip systems simultaneously in a fcc crystal. The YL for randomly oriented fcc crystals using this approach lies between those of the Tresca and von Mises criteria. Applying this approach Hosford and Backofen [32] calculated the plastic behaviour of textured materials showing the effect of textural components on yielding. Various assumptions have been made for the selection of activated slip systems related to the texture development and each yield somewhat different results [33]. Banabic [34], Barlat and Cazacu [35], Barlat [36], Lopes [37] then refined the model accommodating the effect of shear stresses along the symmetry axes. But all efforts to tract the yield locus have been restricted to room temperature and very few have been done at high temperature because of the difficulty of performing tests at hot or warm temperature. With increasing use of warm or hot forming processes it becomes necessary to describe more precisely and accurately the plastic deformation behaviour and consequently the shape of yield locus at high temperature. Tetsuo [38] investigated the effect of temperature on yield locus and found that the size of the yield locus drastically reduces with increasing temperature due to the decrease of yield strength. The Logan-Hosford or Barlat model have been found to be a better choice compared to Hill's or Von Mises' to predict the yield locus at higher temperature.

Plastic anisotropic behaviour of 6xxx is not well known. Some research has been done for RT applications but studies at high temperature are really scarce. Therefore, the main objective of this chapter is to understand the anisotropic behaviour of heat treatable 6xxx aluminium alloys from RT to 250°C both from experiment and modelling results. This chapter also aims to generate a temperature dependent yield locus to be used as an input for FEM modelling. In the first part of the chapter, tensile and deep drawing tests were used to study the plastic anisotropy and its temperature dependence. Efforts have been made to investigate any textural change after deformation with temperature that might affect anisotropy. The possible activation of extra slip systems with temperature has been determined from the EBSD measurements and subsequently, using this knowledge, the *Visco-Plastic Self-Consistent* (*VPSC*) model has been validated based on r-value and texture results and used for the prediction of the yield locus in the temperature range between RT to 250°C.

6.2   Experimental Conditions

Tensile, PSC and deep-drawing tests have been performed at temperatures between RT and 250°C. The general description and procedure of the mechanical tests have been elaborately described in chapter 3. Respective r-values have been measured on tensile specimens after deformation. From the results of the deep-drawing tests, the earing anisotropy has been looked at in detail. Earing profiles from 3 different series of experiments have been calculated and compared with experimental results. The textures of the deformed samples were compared and subsequently band contrast maps generated from the EBSD measurements were used to identify the slip systems activated at room temperature and 250°C.

6.3 Experimental Results

6.3.1   Tensile tests
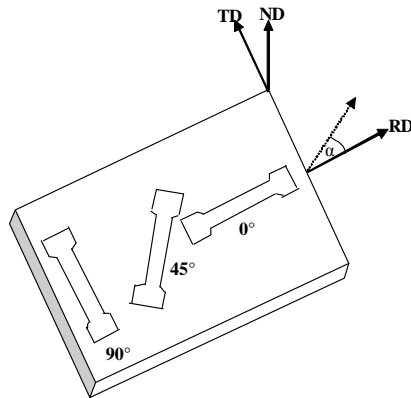
Figure 6.1: Schematic of tensile tests with different in-plane angles α.

Tensile experiments were done by varying the in-plane angle (figure 6.1) between RD and the tensile direction at temperatures between RT and 250°C for both alloys. Specimens of both S and B with 1 mm and 3 mm thicknesses respectively showed similar stress-strain behaviour and only results from the tensile experiments for S material are presented.

Stress strain response
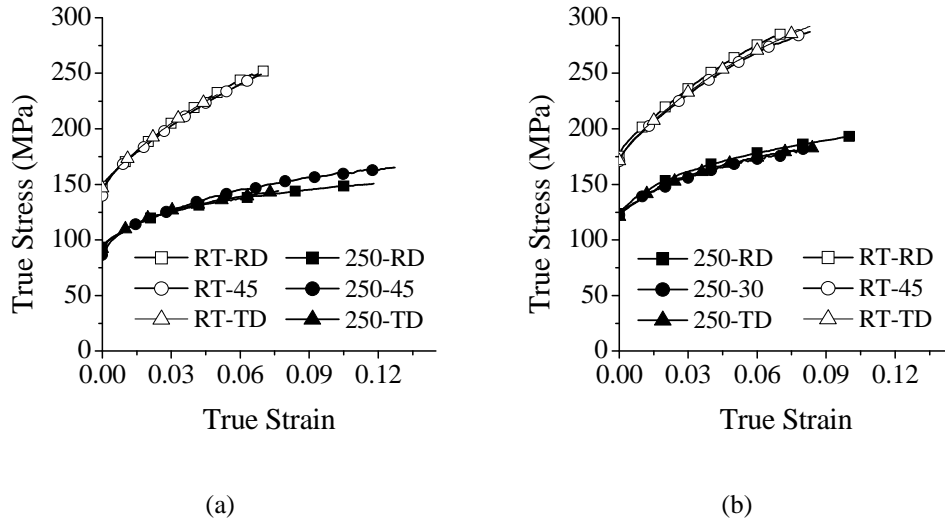
Figure 6.2: True stress-true strain curves at RT and 250°C and 0.1 s^{-1} for different tensile directions for (a) 6016-T4 and (b) 6061-T6.

In the present investigation, as depicted in figure 6.2, there is almost no difference in flow curves along three different directions at room temperature for both alloys. At 250°C the curve along 45° departs at larger strain only very slightly from the other two directions for 6016. Observations were identical with a strain rate of 0.01 s^{-1}.

r-value

(a)   (b)
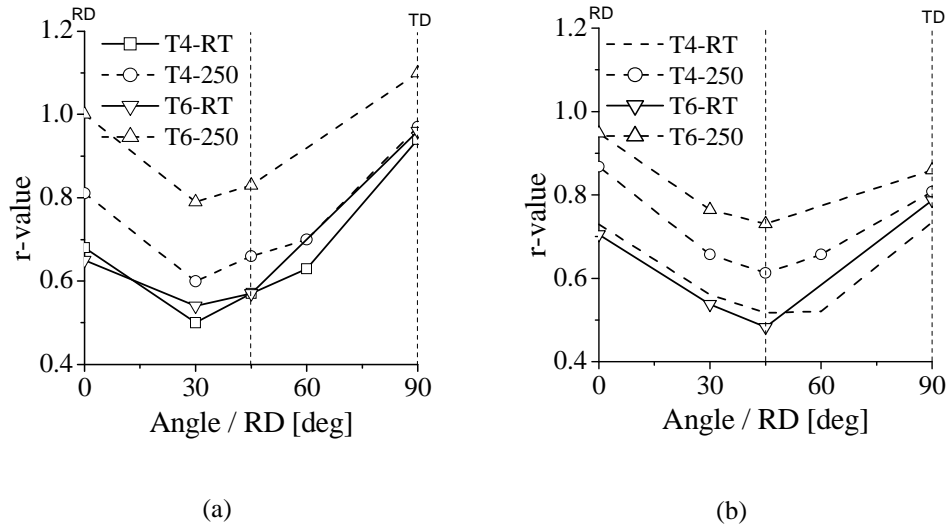
Figure 6.3: Experimental r-value as a function of the angle between the tensile and RD for (a) 6016 and (b) 6061 directions.

The dimensions of the tensile specimens deformed up to 10% strain with a strain rate of 0.01 s^{-1} were measured and used to calculate the total final true strains and consequently the r-values. All the curves for both alloys (figure 6.3) show the maximum r-values along RD and TD and the minimum around 30° for 6016 and 45° for 6061. The r-values along TD are always higher than the ones along RD for 6016. At 250°C, the r-values increase compared to the RT values for all measured angles. This increase is more pronounced for T6 materials. However, the direction dependence of r-values, i.e. the planar anisotropy, remains the same.

6.3.2   Deep-Drawing tests
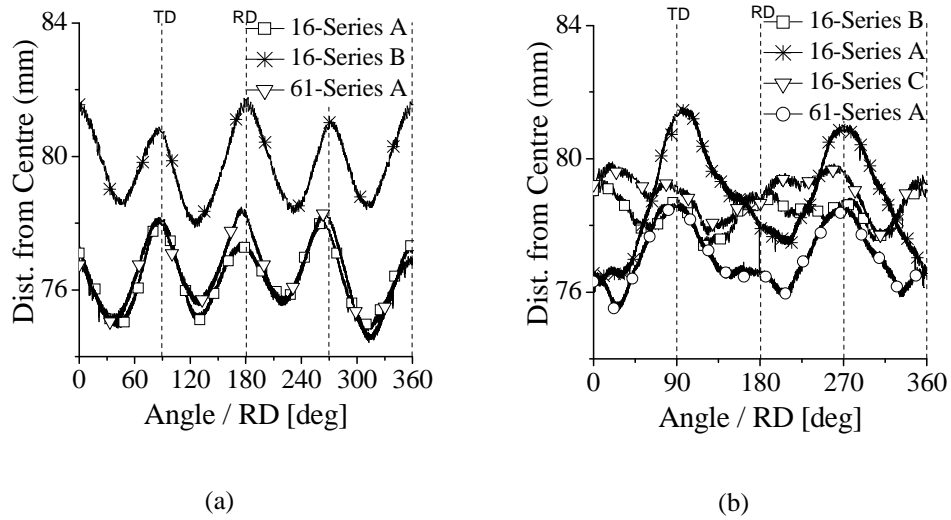
Figure 6.4: Earing profile for T4 materials of different series at (a) RT and (b) at 250°C

Room temperature deep drawing was done for both materials in T4 temper condition. Figure 6.4a, shows the appearance of four ears at RD and TD directions and troughs at 45° and equivalent directions. The number, position and amplitude of ears were found to be independent of alloy composition. Similar results are obtained for different series showing the reproducibility of the test. At 250°C, (figure 6.4b) the results from series A, (refer section 3.4.2 for different DD series) for both the alloys, exhibit two ears at TD and troughs close to RD positions. At 180°C the materials produced similar earing profiles like the ones observed at 250°C.
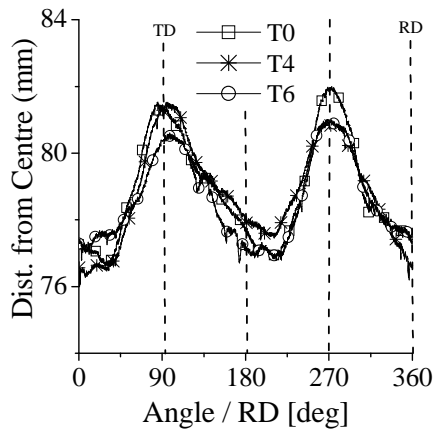
(a)
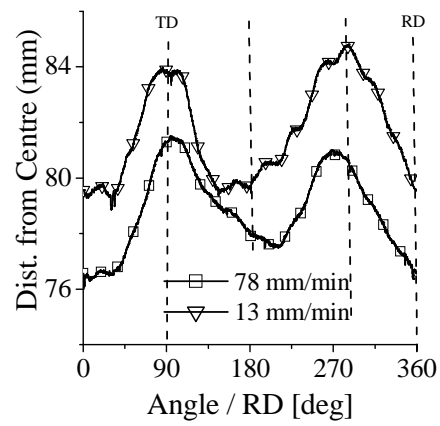
(b)
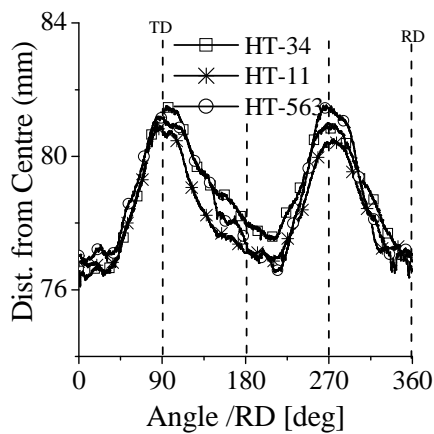
(c)
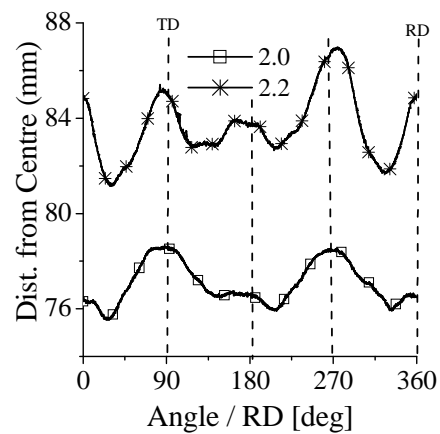
(d)

Figure 6.5: Effect of test parameters on earing profiles observed at 250°C from series A (a) varying temper condition for 6016 (b) punch velocity for 6016-T4 (c) holding time for 6016-T4 (d) and drawing ratio for 6061-T4

During series A the effect of some process parameters on anisotropy at 250°C was investigated (figure 6.5). Difference in temper, punch velocity and holding time does not produce any change in the number and position of ears. For 6061, there is a tendency to maintain also ears at RD and this tendency is more pronounced with higher drawing ratio.

The ear profile at 250°C from the two others series are different than the one observed in series A (figure 6.4b). In series B, the earing profile is similar to the room temperature one, while in series C, the ear profile is more irregular with two ears approximately around 30° and 260°. The three series were done using the same test parameters and configuration and only the tools were unmounted and remounted between two series. These unexpected large differences of earing profile between series at 250°C shows that plastic anisotropy at warm temperature is extremely sensitive to small variations in tests conditions. Possible differences originating from the unmounting and remounting of the tools produce small variations in the alignment of the tools or in the temperature gradients in the die and blank holder. However, no direct measurement is available to identify the exact cause of the observed differences.

Effect of blank orientation

In order to study the possible influence of tool alignment, distortion, or departure from cylindrical symmetry on appearance of earing, series B of deep-drawing tests has been done by aligning either the RD, 35° and TD direction of the blank with a reference direction on the tool, i.e. rotating the blank with respect to the tool.
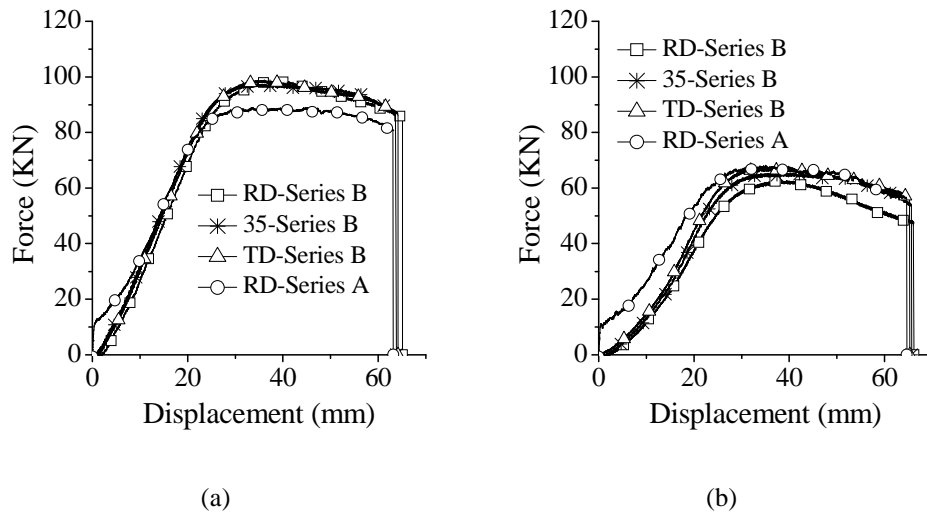
Figure 6.6: Force-displacement curves at different directions for 6016-T4 drawn at
(a) RT and (b) 250°C

In figure 6.6, force displacement curves from series A and B at RT and 250°C are
compared. Figure 6.6a shows that there is absolutely no effect of blank direction at
RT. A larger scattering is observed at 250°C (figure 6.6b) with the maximum force
varying between 62 kN and 67 kN for different blank directions. The difference
between two tests with different blank directions is of the same order than the
difference between two tests with same blank direction. Furthermore a soft tendency
of decreasing the maximum force with increasing distance between the centre of the
bottom of the cup (BC) and the centre of the outer circumference of the cup (MC)
(cf. page 48) has been noticed for the tests done at 250°C so the observed
differences are unlikely to be due to blank direction, and therefore to the tool
geometry.
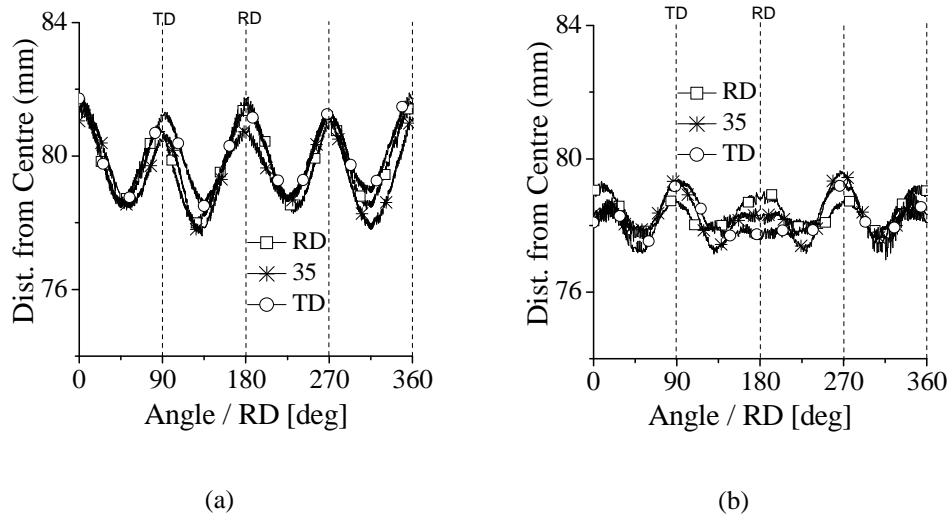
Figure 6.7: Ear profile for different positions of the blank from series B for 6016-T4
at (a) RT and (b) 250°C

For series B four nearly identical earing ear profiles are observed at RT whatever the
direction of the blank (figure 6.7a). At 250°C the reproducibility of the earing
profile was lower than at RT but, unlike series A, all tests show approximately a 4
ear profile with ears at RD and TD and troughs at 45° and equivalent positions
(figure 6.7b). Since the ear profile is independent of the blank direction at both
temperatures it can be concluded that for series B the earing profile is controlled by
the material anisotropy and not by the tool geometry. Therefore, increasing the
drawing temperature from RT to 250°C does not change the type of anisotropy but
reduces the height of the ears showing that the material behaves more isotropically.

Effect of friction

(a)

(b)

(c)
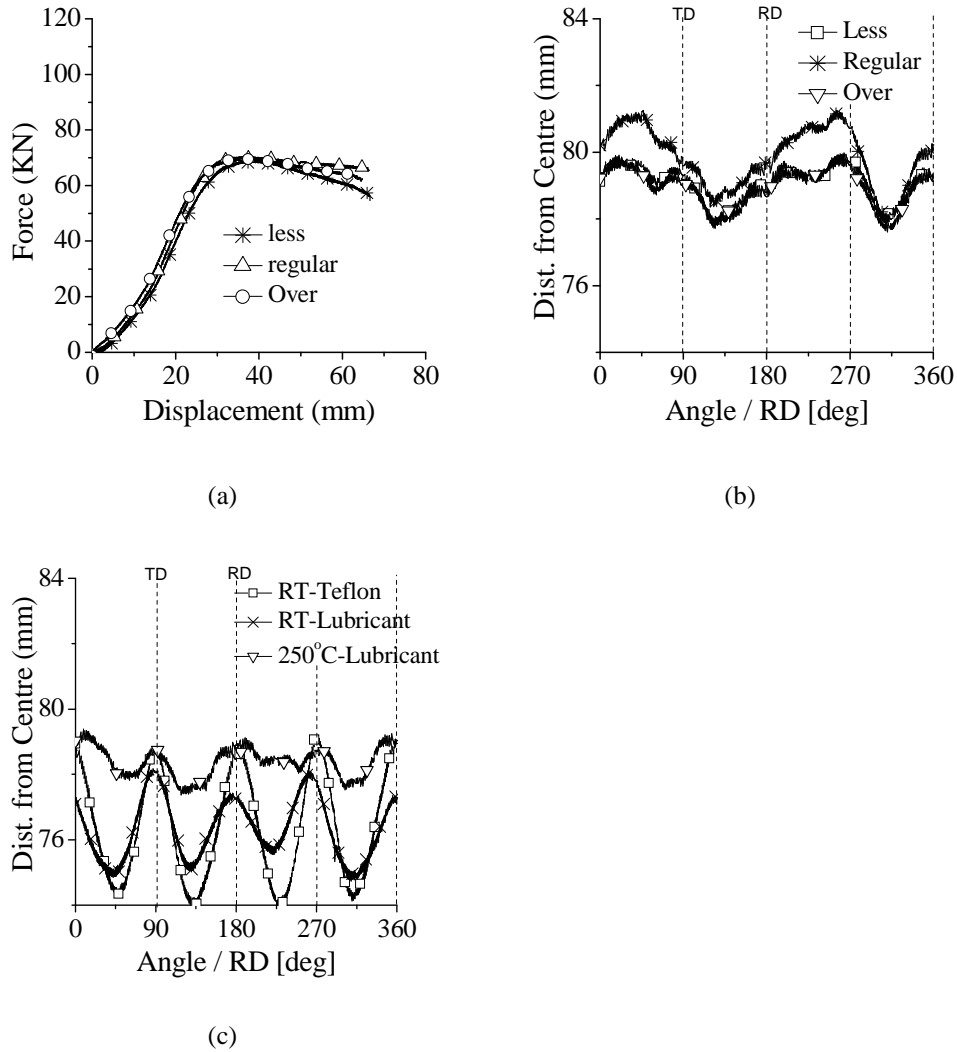
Figure 6.8: Effect of amount of lubricant or friction for 6016-T4 (a) on force-displacement at 250°C from series C and (b) on ear profile at 250°C from series C and (c) on ear profile.

Effect of friction at 250°C has been studied by varying the amount of lubrication with respect to the regular amount employed during the other series. It can be clearly noticed that, for the amount of lubricant used, friction does not have an effect on force displacement (figure 6.8a) or earing profile (figure 6.8b). The effect of friction has been investigated further by comparing tests done at RT and 250°C with regular

amount of lubricant and a test done at RT with Teflon sheets between the blank and the tools in addition to the lubricant (figure 6.8c). It can be noticed that the amplitude of the ear decreases when friction increases, i.e. from RT with Teflon sheets, to RT with lubricant and to 250°C with lubricant.

Thickness distribution

(a)

(b)
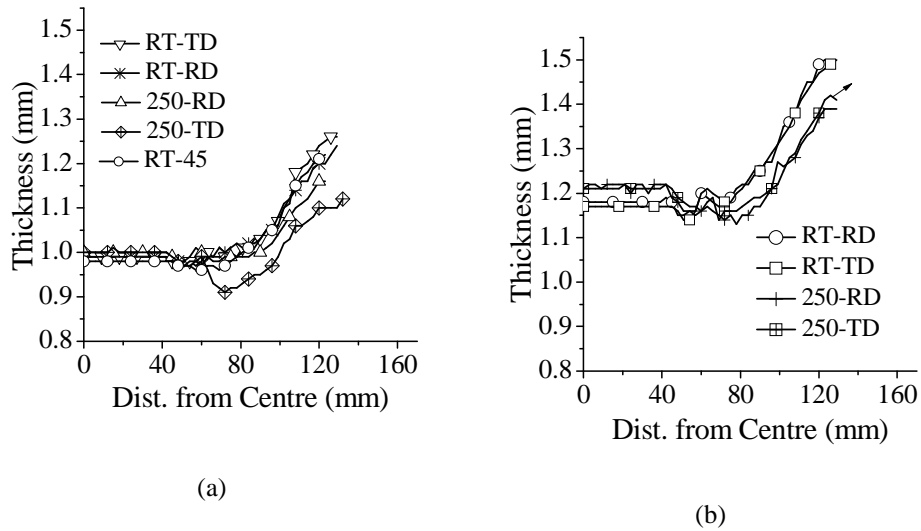
Figure 6.9: Anisotropy in thickness distribution from series A for (a) 6016-T4 and (b) 6061-T4

Figure 6.9 shows that for all RT deep drawing tests the thickness decreases only slightly after the first curvature. Also, no thickness difference along RD and TD has been noticed. At 250°C the thickness of the cups decreases at the point of first curvature before to increase along the cup wall. The thickness values along RD and TD are almost the same for alloy 6061 compared to slight difference of thickness along TD and RD for alloy 6016.

6.3.3   Texture evolution during deformation

Textures after tensile, plane strain compression and deep drawing tests have been compared with the textures of the initial undeformed materials to search for any evidence of change of deformation mechanisms with deformation temperature. Texture measurements were also used for model validation. All textures after deformation were measured by EBSD and the data were processed using the

Channel5 acquisition system of HKL. ODFs were calculated in the way described in 2.1.5. The volume fraction (%) of selected orientations has been calculated with the MTM-FHM software system developed by P. Van Houtte using a spread of 11° around each selected orientation. All ODF calculations were performed assuming the orthotropic sample symmetry [39] and by consequence the full texture can be represented in the Euler subspace $0° \leq \{\varphi_1, \varphi, \varphi_2\} \leq 90°$. The total number of grains involved during the texture measurements by EBSD for all deformed specimens was between 150 and 200. The application of orthotropic sample symmetry actually quadruples the number of grains used for the ODF calculations.

Texture after tensile deformation

(a)   (b)
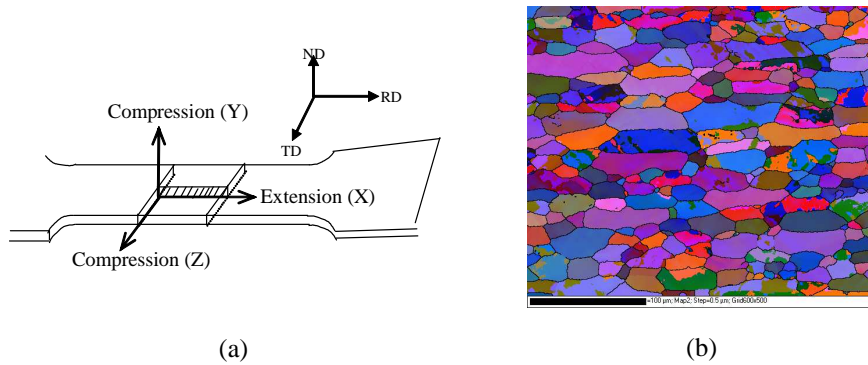
Figure 6.10: (a) Schematic view of the section of the tensile specimen considered for EBSD measurement and (b) OIM image of the tensile samples 6016-T4 deformed at 250°C

EBSD measurements have been performed right at the middle of the gauge length and mid thickness on the (X,Y) plane indicated in figure 6.10a. All EBSD measurements were performed on specimens with the tensile direction parallel to the rolling direction. Textures have been calculated in the (RD, TD, ND) reference frame as shown in figure 6.10a.

(a)

(b)

(c)
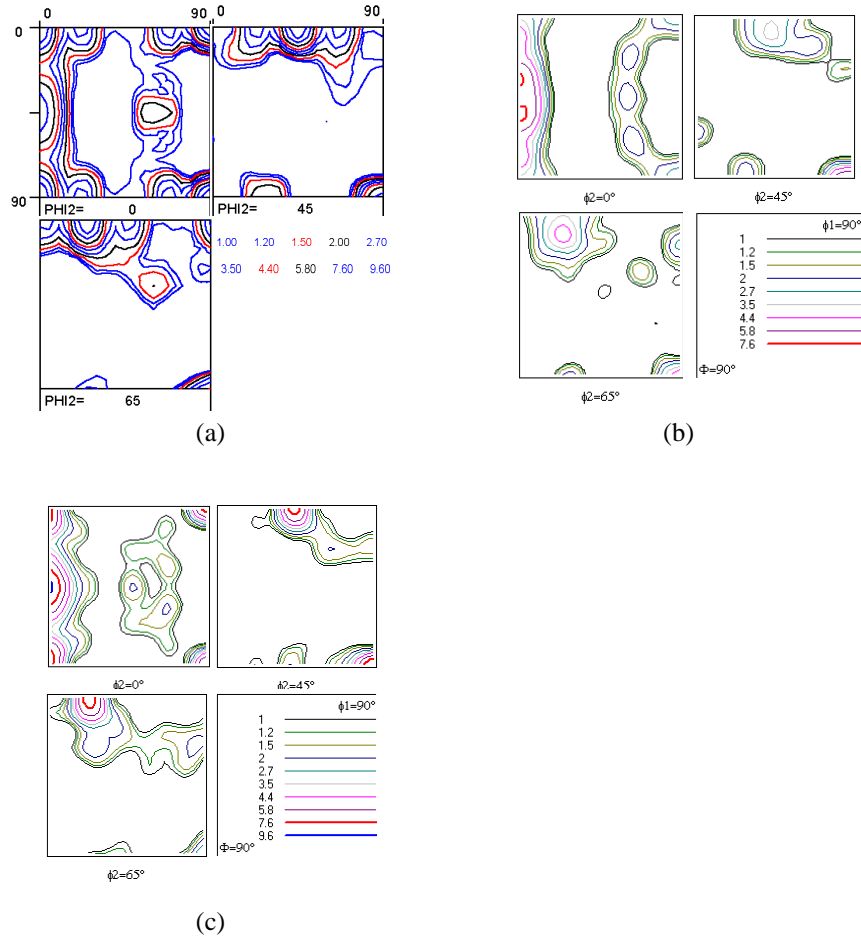
Figure 6.11: ODF for 6016-T4-S (a) as received (b) after 10% deformation at RT
and (c) after 10% deformation at 250°C

Table 6.1: Volume fraction of the texture components in 6016-T4 before and after
tensile deformation.

Sample	Cube	Goss	Br	S	Cu	P	R	I-G	D
16-T4-S	5.7	4.5	1.5	5	1.8	3	4.5	0.5	2.3
16-T4-RT	3.7	5.4	1.4	3.4	2.1	3.2	3.5	0.4	2.6
16-T4-250	4.8	5.8	2.3	4.9	2.6	3	4.8	0.2	3.4

Figure 6.11 and table 6.1 depict the texture before and after 10% tensile deformation
at a strain rate of 0.1 s^{-1} both at RT and at 250°C for 6016-T4 material, chosen as a
representative example. The as-received cold rolled-solution treated and

recrystallized material consists of a typical recrystallization texture composed of Cube, R, P and Goss. The textural changes for RT and 250ºC specimens due to 10% tensile deformation are small and the textures remain qualitatively the same. It has been noticed that the trends of texture change for both alloys are also very similar. It is evident from the ODFs that there is a tendency for the Cube component volume fraction to decrease and the Goss volume fraction to increase after tensile deformation compared to as-received material; the Goss component has the maximum volume fraction after deformation compared to Cube in the as-received material. Also ODFs are similar in terms of presence of Goss and P component on the α-fibre. The slightly higher volume fraction of Brass, Cu, S and D after tensile elongation at 250ºC compared to RT does not necessarily bring significant difference. The microstructure after 10% deformation shown in Figure 6.10b is clearly not much different from the initial undeformed microstructure. The grains are slightly elongated along the rolling direction like the as-received material. These observations allow to drawing the conclusions that 10% tensile deformation does not produce noticeable change in materials microstructure and texture.

Texture after plane strain compression
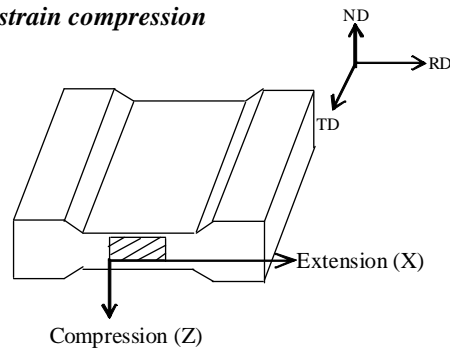
Figure 6.12: Schematic view of the half cross-section of the PSC specimen considered for EBSD measurement after deformation

EBSD measurements were done at the centre of PSC specimens on the TD plane as shown in figure 6.12. Textures have been calculated before and after PSC using, the extension direction as X-axis and compression direction as Z-axis, which also means textures are calculated in the conventional (RD, TD, ND) reference frame as shown in figure 6.12.

(a)   (b)

(c)
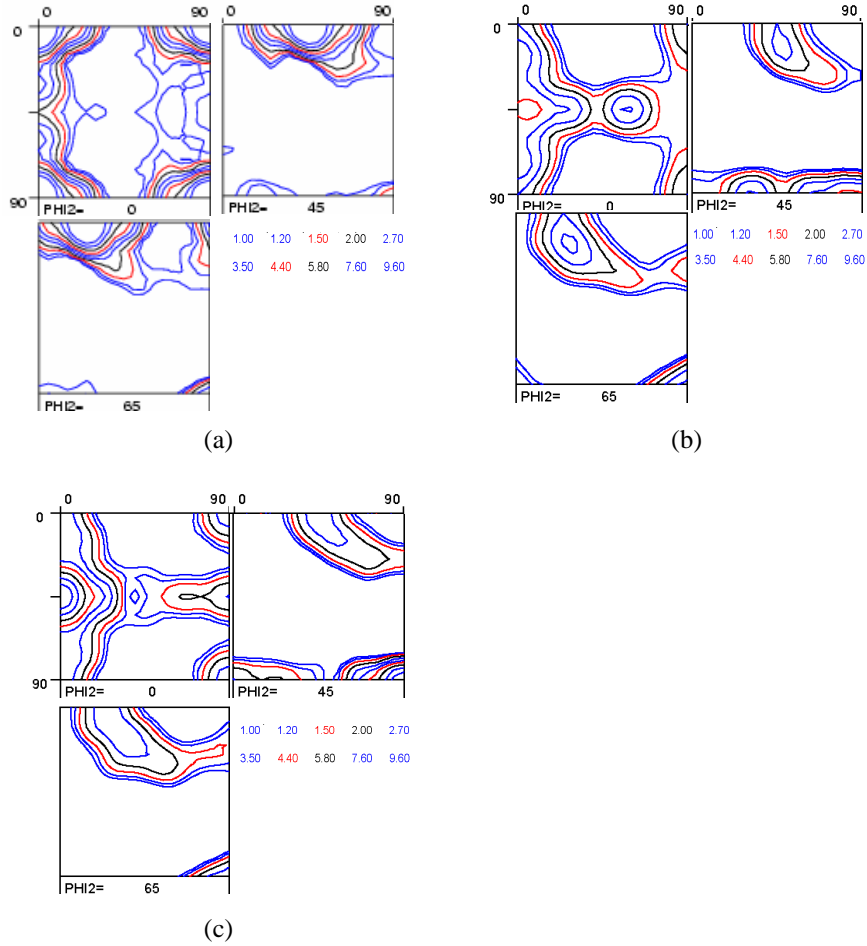
Figure 6.13: ODF for 16-T4-B (a) as-received (b) after PSC at RT and (c) after PSC at 250°C, both at 0.1 s^{-1} strain rate and 35% deformation

Table 6.2: Volume fraction of the texture components from PSC experiments

Sample	Cube	Goss	Br	S	Cu	P	R	I-G	D
16-T4-B	9.7	1.7	0.4	1.7	1.9	1.5	1.6	1.1	2.3
16-PSC-RT	2.9	3.5	4.0	5.9	2.1	4.4	6.5	1.4	2.5
16-PSC-250	3.0	6.3	3.1	6.0	2.1	2.6	6.6	1.8	3.2
61-T4-B	7.3	1.4	0.6	1.9	1.8	1.9	1.3	1.0	2.5
61-PSC-RT	2.2	3.2	3.4	8.7	2.9	3.3	7.9	3.8	3.9
61-PSC-250	3	2.7	3.2	7.0	3.1	2.7	7.3	0.7	2.0

The as-received materials show (figure 6.13a and table 6.2) the presence of a strong cube component. With 35% deformation the volume fraction of Cube is found to be

reduced significantly, while the volume fractions of Goss, Brass, R and S increase. No significant difference can be noticed between the textures generated after deformation at RT and 250°C, which is a significant result considering the limited number of grains involved in measurement. For all situations, the η-fibre is present from Goss to Cube with a maximum intensity for the Goss component. Goss and P are the two main components on the α-fibre in the deformation texture, although the α-fibre is absent in as-received texture. It can also be noticed that no β-fibre is found after PSC.

Texture after deep drawing
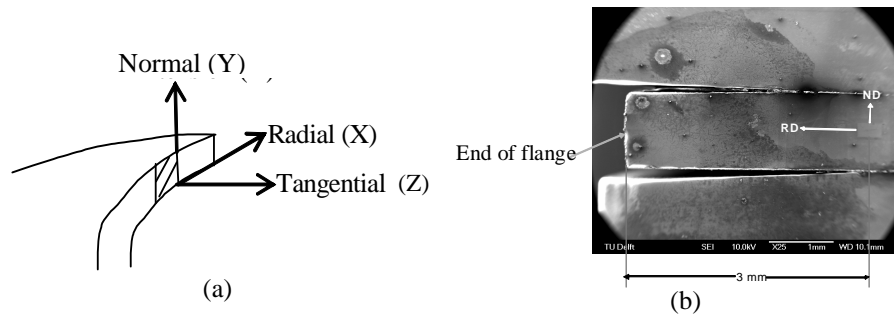
Figure 6.14: (a) Schematic position of EBSD scans at the flange (b) a typical example

EBSD measurements were done on the cross section of the deep-drawing cup in the flange region as shown in figure 6.14a and b, 3 mm away from the end of the flange (i.e. edge of the cup). During deep drawing this part of the flange underwent approximately 30% of tangential compressive deformation. ODFs have been calculated in the (Radial, Normal, Tangential) or (X,Y,Z) reference frame to be consistent with PSC tests, i.e. to have the extension direction as X-axis and compression direction as Z-axis.

(a)   (b)

(c)   (d)

(e)   (f)
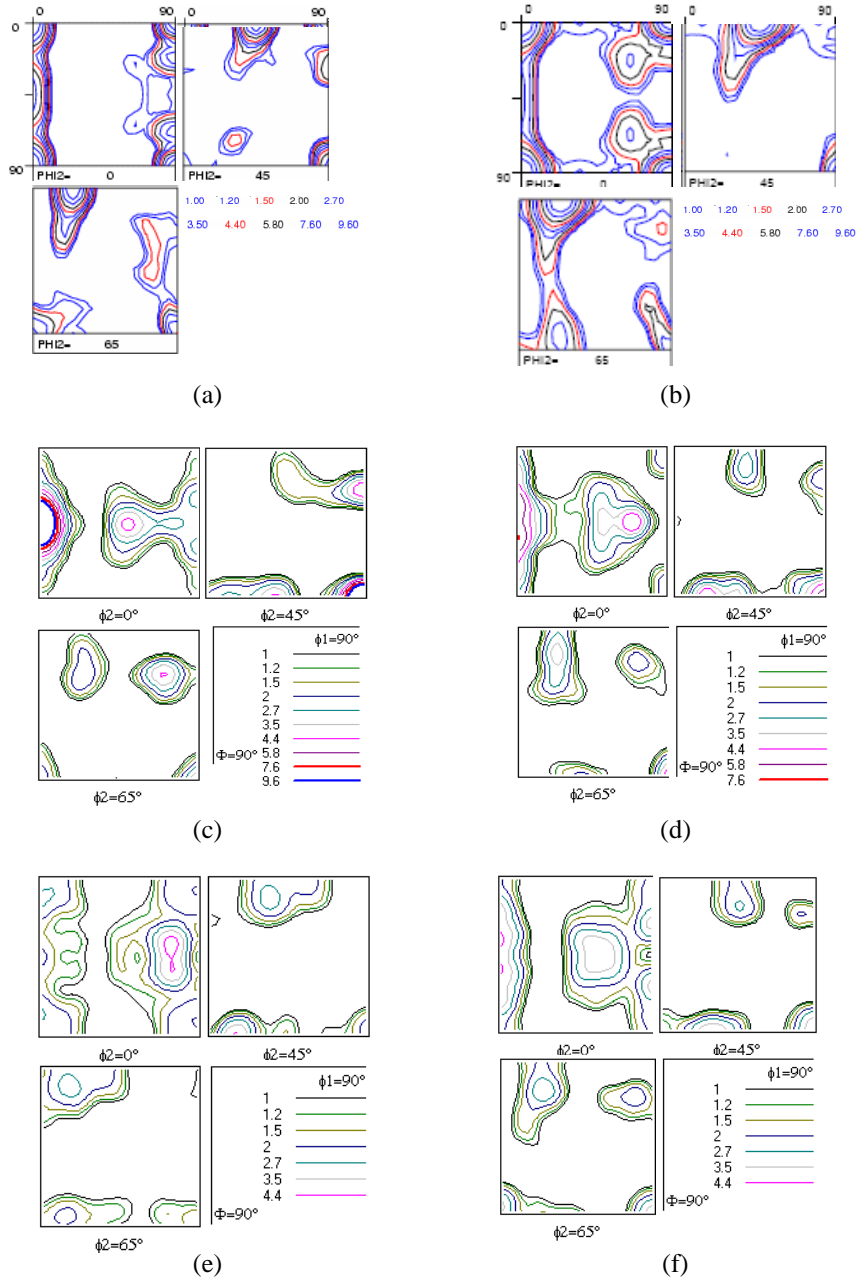
Figure 6.15: ODF of deep-drawing specimens for (a) as received 16-T4-S (b) as received 61-T4-S (c) 6016-T4 at RT and (d) 6016-T4 at 250°C (e) 6061-T4 at RT (f) 6061-T4 at 250°C

Table 6.3: Volume fraction of the texture components from deep-drawing experiments

Sample	Cube	Goss	Br	S	Cu	P	R	I-G	D
16-T4-S	5.7	4.5	0.5	2.9	3.0	1.8	2.4	1.3	3.4
16-DD-RT	1.4	9.0	2.5	5.2	3.8	5.1	3.5	2.0	5.7
16-DD-250	2.3	4.8	2.7	3.1	2.2	5.2	3.3	1.1	3.3
16-TD-250	5.3	1.0	2.7	5.4	2.0	3.1	5.7	0.8	4.0
61-T4-S	6.7	2.3	0.5	1.7	1.5	2.0	1.6	0.7	2.0
61-DD-RT	3.2	1.9	2.3	2.0	0.8	3.6	1.9	2.4	1.3
61-DD-250	2.4	3.6	2.1	2.8	1.6	5.7	2.0	2.0	2.9

Figure 6.15 presents the textures measured on samples cut along RD, for which the reference frame (X,Y,Z) corresponds to (RD, ND, TD). For comparison, the as-received textures in figure 6.15a and b have also been recalculated in the (RD, ND, TD) reference frame. Comparing the ODFs (figure 6.15) and the volume fraction of the texture components (table 6.3) it can be concluded that both alloys show Goss and P dominated textures after room temperature and warm temperature drawing, while the dominance of cube has reduced drastically. Like for tensile and PSC tests, the accuracy of texture measurement by EBSD on deep drawn cups is lower compared to as-received materials because of the limited number of measured grains. For instance, the extremely large intensity of the Goss component for 6016 material drawn at RT is due to the presence of a group of Goss orientated grains under the area examined. Therefore, qualitatively there is no major texture difference between cups of 6016 drawn at room and warm temperature. Apart from the η-fibre exhibiting a maximum at the Goss component, other components close to the β-fibre (Br, S and Cu or D) are also observed. Deep drawing of 6061 at warm temperature produces similar textures than in 6016 alloy but is dissimilar at room temperature with respect to the presence of a maximum at P, a smaller Goss intensity and the absence of β-fibre orientations.

(a)   (b)
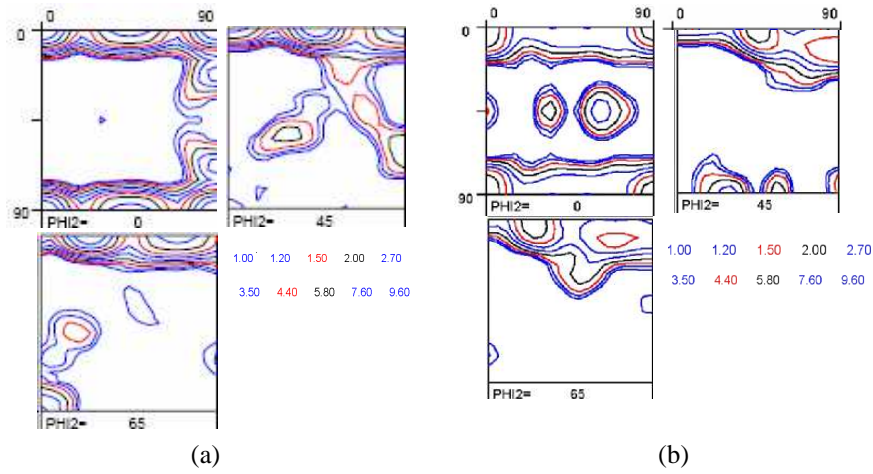
Figure 6.16: Odf for the (a) as received 16-T4-S (b) deep drawn sample 16-T4
along TD at 250°C

Figure 6.16 depicts the ODF measured on a cup cut along TD. The reference frame
(X,Y,Z) corresponds then to (TD, ND, RD). The texture of the as-received material
is also recalculated in this reference frame. It can be noticed that the intensity of H
and to less extend cube components decreases, while grains with P orientation and
with orientations close to the β fibre (Br, approximately S and D) appear. A small
amount of Goss grains are also formed. Although the initial texture in the blank
along the TD direction is different than the one along the RD direction when
calculated in a reference frame linked to the deformation directions, the texture after
deformation are more similar.

6.3.4   Temperature and active slip systems

An attempt has been made in the present investigation to identify the activated slip
systems by using the bands visible as black parallel lines on EBSD band contrast
maps (figure 6.17) of deformed specimens. The principle of the calculation is to
verify which crystallographic plane, among a list of possible slip planes, contains the
direction of the observed bands. After importing the EBSD data in the TSL$^{®}$
software a vector $\vec{ab}$ is drawn on top of the band. The local crystallographic
orientation measured at the origin of the vector $\vec{ab}$ is then used by the TSL software
to calculate the coordinates of $\vec{ab}$ with respect to the crystal reference frame. This
vector is then compared to a list of slip plane normals <hkl>. If the angle between
$\vec{ab}$ and <hkl> is 90°±5° then {hkl} is considered as containing the direction (ab).
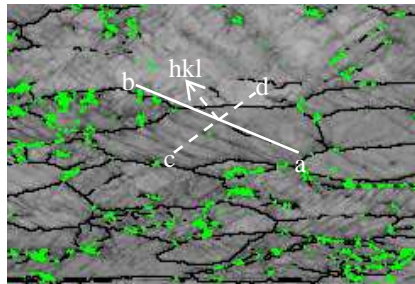
a-b: vector drawn on the deformation band

c-d: slip plane trace

hkl: normal to the slip plane

Figure 6.17: Band contrast map used for the identification of slip systems.

The measured bands measurements have been obtained for PSC and deep drawing tests both at RT and 250°C. In order to calculate the accuracy of the measurement, the procedure has been repeated for five vectors starting at different points on a single band and this has been repeated on other bands as well. The average interval of confidence obtained was 5° for a confidence level of 95%. This includes the effect of accuracy on local crystallographic orientation measurement and the accuracy of manually plotting the band direction.

Table 6.4: Probability of activation of slip systems

AA	Def	T (°C)	{111}	{112}	{110}	{100}
6016	PSC	RT				
6016	PSC	250				
6061	PSC	250				
6016	DD	250				

	Frequently a solution		Sometimes a solution		Not a solution

Several grains and bands per grain have been analysed for each condition. Results are summarized in Table 6.4, which indicates how frequently the slip planes contain the observed bands. From table 6.4 it can be noticed that at RT bands are mostly parallel to {111}. As {111}<110> should be the predominant slip system at room temperature, this result suggests that the observed bands are indeed correlated to the active slip systems. Assuming the validity of this correlation holds at 250°C it can be concluded that {112}<110> is activated at 250°C. However, the slip systems {111}, {110}, and {100}<110> cannot be excluded. These findings also corroborate the literature reports mentioned in the introduction of this chapter. The slip systems found will be used as input for the *VPSC* model which is discussed in section 6.5.

6.4 Discussion on Anisotropy from Experiments

The effect of plastic anisotropy on mechanical behaviour has been first investigated from tensile experiments. Typically the true stress - true strain curves and r-values have been used for this purpose. During deep drawing tests, the earing profiles have been considered as a measure of anisotropy. Deformation textures have also been compared for different conditions to reveal any possible change of anisotropy. The influence of several parameters on anisotropy was studied: alloy, temper condition, punch velocity, holding time, friction, etc. Among these parameters, the predominant effect was temperature and friction condition, followed by the effect of precipitates.

Texture, r-value and ears

For the investigated conditions the shape of r-value profile did not change with temperature and in most cases the values lie typically below 1. The r-value is maximum along RD and TD and minimum along 45°. It has also been observed that ears were formed at RD and TD while troughs were observed at 45°. This is commensurate with the observation made by Engler and An [15]. Since the stress state in the outer flange is pure circumferential compression, it is expected that ears will occur at locations that are orthogonal to the direction of maximum r-value in the tensile test, i.e. at RD and TD. The maximum r-values along RD and TD are due to the cube texture of the as-received materials. The appearance of asymmetric r-value profiles for 6016 with higher maximum along TD and minimum at 30° compared to the symmetric r-value profile for 6061 with minimum at 45° can be attributed to the presence of a higher fraction of Goss orientation in alloy 6016. Indeed, this component is found to produce the highest in-plane anisotropy of r-values among the texture components appearing in aluminium sheets [16]. The pure Goss component gives rise to a strong increase of r-values in the range of 55º to 90º. The presence of Cube and Goss domination and the absence of a β-fibre in as-received textures also explain the four fold symmetry and the appearance of ears at RD and TD after deep drawing according to the previous observations reported in section 6.1. However, unlike r-value profiles, the texture difference between 6016 and 6061 has no effect on the measured earing profiles at RT. Although the type of r-values and earing profiles did not change with temperature, r-values are found to increase with increasing temperature (figure 6.3), while the amplitude of the ears decreases (figure 6.7). As noticed in section 6.3.4, the deformation mechanism is sensitive to temperature. At RT {111}<110> is the predominant slip system while at 250°C three extra slip systems seem to be active. The possible relation between slip system

activation and r-value and ears will be investigated in section 6.5. The observed effect of temperature on the amplitude of the ears could not be distinguished from the effect of friction, since friction also increases with temperature. The effect of friction between the blank and the tool seems complicated and very much dependent on texture. It changes not only the ear height but also their location and shape. It has been reported [40] that with increasing friction the ear height of Goss, S or Brass dominated textures decreases along RD and diagonal directions and increases along TD. The asymmetry of the ear profile is then enhanced. For Cube textures the ear height reduces symmetrically along RD and TD due to the symmetry of this orientation with respect to RD and TD. The observed decrease of the amplitude of the ears with increasing friction can then be explained by the Cube texture of the as-received material. The larger decrease of ear amplitude along RD compared to TD observed at RT when increasing friction (Figure 6.8c) can be related to the presence of the Goss component in 6016-T4 material.

Texture after deformation

Textures after tensile, PSC and deep drawing tests at RT and 250°C were measured and compared. Savoie and co-workers [13] showed that during the early stage of drawing the tensile component of the stress tensor dominates in the flange and the texture at this stage are expected to be similar to the tensile one while at the later stage of drawing the outer part of the flange is subjected to a stress state close to uniaxial circumferential compression and this tends to dominate the earing pattern. Since the force in the flange during deep drawing is compressive in nature, texture after PSC and deep drawing were calculated using the same reference frame with the Z-axis being the compressive axis. Observing the ODFs for different deformation modes and temperatures it can be concluded that texture changes during deformation but in none of the cases the difference between the textures after deformation at RT and 250°C was significant. During both PSC and deep drawing, the deformed texture changed with respect to the as received texture principally by the decrease of Cube and increase of Goss volume fraction. P, R, S and Brass components were also found to increase. The textures are also commonly characterized by the presence of the η fibre. Texture evolution during tensile, PSC and DD at RT is well documented while the same for warm temperature is not. The decrease of Cube and the increase of S orientations with deformation is in strong agreement with the observation of Driver [26]. The reason for this behaviour is the splitting of Cube grains by strong TD rotations and with further deformation leading to four symmetrically equivalent S {123}<412> orientations. The reduction of the Cube orientation has also been reported during warm PSC test with AA1050 [41]. From the results of the tensile experiments it has been noticed that tensile deformation up to 10% produces qualitatively similar texture both at room temperature and at 250ºC. The same

observation has been reported [42] with AA1145 for tensile deformation up to 30%. The independence of deformation texture on temperature contrasts with the effect of temperature on r-value, earing amplitude and slip system activation. This apparent difference will be investigated further with a numerical model in section 6.5.

Precipitates, ears and r-values

A change of anisotropy with temperature can be associated with a change in precipitate shape and morphology. In an investigation by Jobson and Roberts [43] on Al-4% Cu alloy to study the change in earing profile after solution treatment and ageing for different time spans, it has been reported that the height of the ears changes with the nature of precipitates but the nature of 4 fold symmetry remains unchanged under any circumstances. In presence of θ' precipitates, the height of the ears diminishes to a very low level and increases again in the presence of θ precipitates. More interestingly, no significant texture changes have been noticed among different conditions implying that the variation of earing behaviour can be attributed to the presence of different precipitates and θ' precipitates tend to make the material behaving in a more isotropic manner. Almost the same effect has been reported by Hosford and Zeisloft [44] for Al-Cu alloys where the reduction in plastic anisotropy due to the presence of θ' precipitates depends on both shape and habit plane of the precipitates. In section 6.3.2 the effect of precipitates on anisotropy during deep drawing has been investigated by varying temper, holding time before deformation, and punch velocity. From figure 6.5, it can be clearly noticed that at 250°C not only the number of ears but also their height did not change with different precipitates for the investigated alloys. Therefore, the present experimental observation at 250°C does not comply with the literature in terms of height of the ears.

Concerning the effect of precipitates on r-values in different directions, investigations showed (figure 6.3) that r-values can be influenced by the microstructure of the alloy. With Al-4% Cu alloy [45] the introduction of θ' phase reduces the normal anisotropy like β' in Al-Mg-Si alloys, although γ' platelets in Al-15%Ag did not reduce the anisotropy compared to solution treated condition, bearing the fact that the overall strengthening by γ' is similar to θ'. Hence, the habit plane of the precipitates is also important apart from the nature of the precipitates. Referring to figure 6.3 it can be readily noticed that for both alloys at RT the r-value remained unchanged for different precipitate populations (T4 and T6). At 250°C, although the r-value profile remained the same, the T6 state yields higher r-values for both alloys compared to the T4 condition, the difference being larger for 6016.

The difference in r-values at 250°C is purely due to differences in size, amount and stoichiometry of precipitates as well as a different solute content between the two materials.

6.5   Modelling Effect of Temperature on Plastic Deformation

Driven by the objective to study the effect of temperature on plastic deformation resulting from temperature dependent slip system activity, the use of a *Crystal Plasticity (CP)* approach is essential. It enables the interpretation of deformation characteristics using all possible combinations of CRSS. In the *crystal plasticity* approach, the properties of grains are considered identical with respect to the crystallographic reference system. In polycrystalline aggregates heterogeneity arises owing to the crystallographic orientation of different grains. The assumption of identical deformation in every grain irrespective of its orientation throughout the polycrystal by Taylor [46], results in an upper bound to the stress. This *full constrain (FC)* model is famous because of the possibility of multiple slip and reasonable texture predictions. Simultaneously the model assumes that the deformation in each grain is equal to the macroscopic deformation. So the *FC* model only accounts for strain compatibility, whilst it violates stress equilibrium between the grains during plastic deformation. The *relaxed constrain* (*RC*) [47] approach considers grain shape effects on grain interaction and has been found satisfactory for rolling and torsion at large strain. It allows generation of local strain incompatibilities among neighboring grains to gain a better stress homogeneity on a phenomenological basis. From mechanical view point neither of the two shows a convincing theoretical solution to polycrystal deformation in view of the fact that stress equilibrium and full strain compatibility was not maintained. Alternatively, the *visco-plastic self-consistent crystal plasticity* model does not suffer from these drawbacks as the relaxed stress component(s) for each grain individually does not have to be specified beforehand. Hence, for this reason the *VPSC* model was applied in the current investigation.

6.5.1   Description of Visco-plastic Self-Consistent Model (VPSC)

The fully anisotropic *visco-plastic self-consistent* (*VPSC*) model used for the present work was developed by Lebensohn and Tomé (1993) [48] based on the work of Molinari (1987) [49]. Version 6 of the *VPSC* code (2003) has been used. The *VPSC* model was initially developed for low symmetry materials but has been extended for higher symmetry materials. The model considers each individual grain as a viscoplastic ellipsoidal inclusion embedded in a homogeneous, incompressible effective medium (HEM) representing the surrounding grains. The interaction between the inclusions and HEM is considered to be local but each individual grain

deforms in a way making the average deformation equal to the imposed one, which is known as the self-consistent (SC) approach. The strength of such interaction is reflected in the respective accommodation of plastic deformation by the grains and the surroundings. The anisotropy of the grains and the matrix both will contribute to such interaction. The stress and strain rate distribution within the inclusion and the matrix are homogeneous while the resulting stress and strain fields are heterogeneous. *VPSC* accounts for plastic deformation by the mechanism of slip and twinning. It also includes the effect of hardening and texture. Neglecting elastic effects at large plastic strains, the material behaviour is assumed to be governed by a visco-plastic equation. The local and the overall response are independent of hydrostatic pressure component and the deformation takes place without volume change. Therefore the model is described in the 5 dimensional deviatoric stress and strain rate spaces.

6.5.2   Inputs and simulation conditions

The main input for the model was the initial experimental texture, which was discretized in 2000 orientations. Calculations were based on the assumption that no work-hardening was present. The visco-plastic behaviour was modeled by using a rate sensitive constitutive law with a rate sensitivity parameter equal to 1/20. The accommodation tensor of the self consistent model is calculated by assuming the strength of the interaction between individual grains and the matrix to be intermediate between the secant and tangent approximations (n_{eff} = 10). It is assumed that temperature controls the CRSS and thus the number of activated slip systems.

6.5.3   Model fitting and validation

Experimental results of section 6.3 showed that, although temperature does not seem to influence the plastic anisotropy character, the number of active slip system families might be temperature dependent. A comparison of the experimental and calculated r-values has been used to fit the CRSS. The model has then been validated by comparing the experimental and predicted textures after 35% deformation by PSC at RT and 250°C.

r-value

(a)

(b)

(c)

(d)
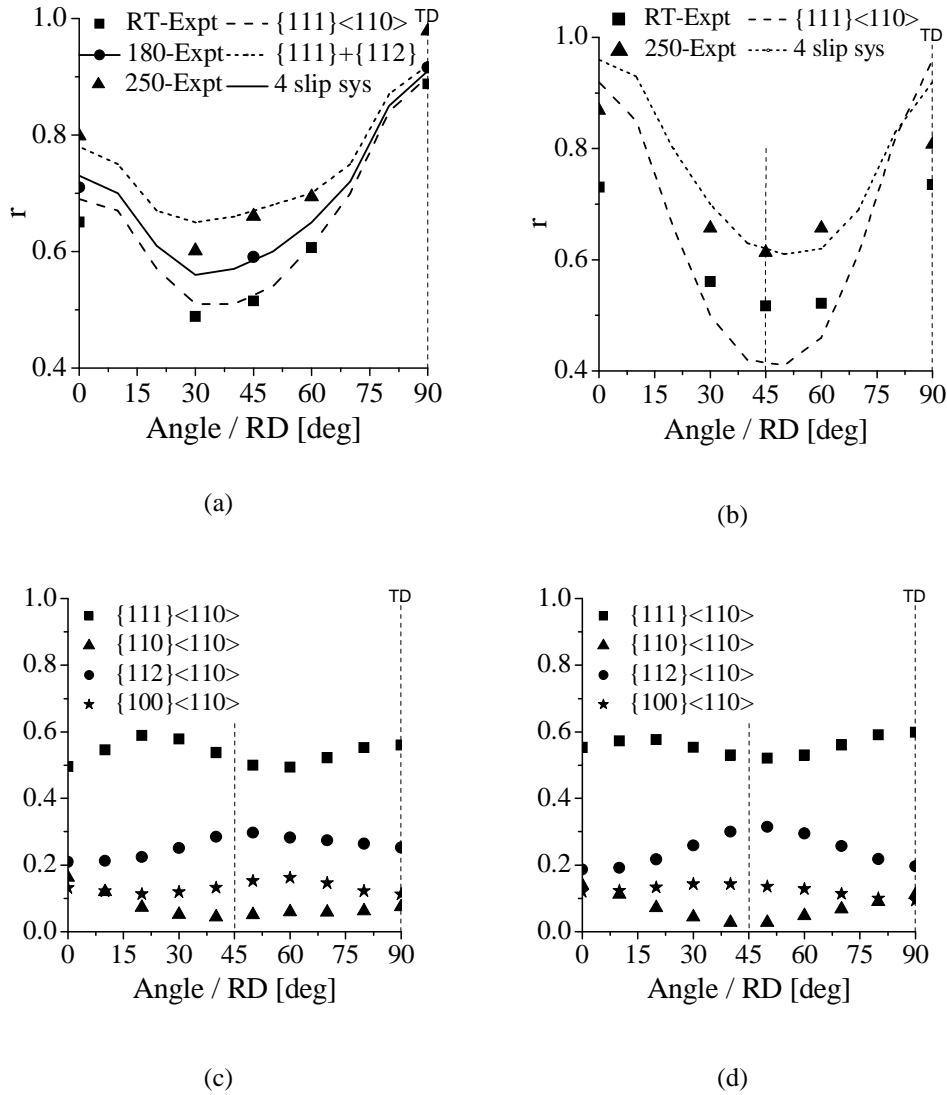
Figure 6.18: Comparison of experimental and calculated r-values for (a) 6016-T4 and (b) 6061-T4 alloys (c) slip activity for 6016-T4 at 250°C and (d) slip activity for 6061-T4 at 250°C

Plastic deformation of aluminium alloys at RT is known to take place by slip on the octahedral slip system, {111}<110>. R-value calculations with the *VPSC* model assuming only {111}<110> slip system predicts well the r-values measured at RT for 6016-T4 (figure 6.18a). For the 6061 alloy, the model predicts properly the symmetry of the r-value profile but underestimates the RT r-value at 45° and over

estimates it at RD and TD. Despite these differences, the model can be considered as reliable. The best fit of the experimental r-values at 180°C is obtained by adding an additional slip system family, {112}<110>, with a CRSS ratio of the {111}<110> and {112}<110> slip system families of 1:1.2. Four families of slip systems {111},{110},{100} and {112}<110> with CRSS ratios 0.9:1:1.1:1 were found to produce a good fit of experimental r-values at 250°C for both alloys. With these conditions, the model predicts the highest slip activity for {111}<110> and the lowest for {110}<110> (figure 6.18c and d). The slip activity is nearly the same for both alloys.

Texture

Using the same CRSS values obtained after fitting the r-value profiles, textures corresponding to 35% PSC deformation were calculated for both alloys and compared to the experimental counterparts at RT and 250°C.

(a)   (b)
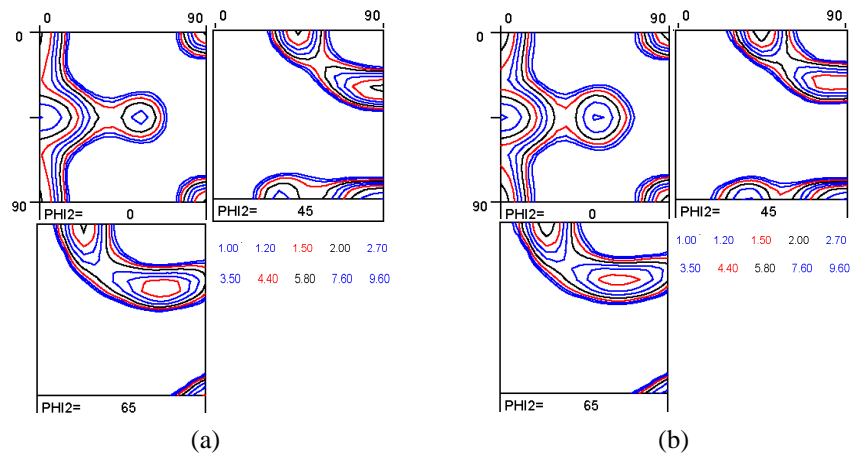
Figure 6.19: ODF calculated with the *VPSC* model after 35% PSC for 6016-T4-B
with (a) only {111}<110> slip and with (b) 4 slip system families

Figure 6.19 shows that the textures predicted by the model with one or four families of slip systems are qualitatively similar to the textures observed from experiments at RT and 250°C (figure 6.13). Like experimental observation there is no significant difference between deformation textures at different deformation temperatures. Here, the η-fibre spreads from Goss to Cube. Goss and P are the main components on the α-fibre, whereas the β-fibre is absent which corresponds well with the experimentally observed textures.

(a)

(b)

(c)

(d)
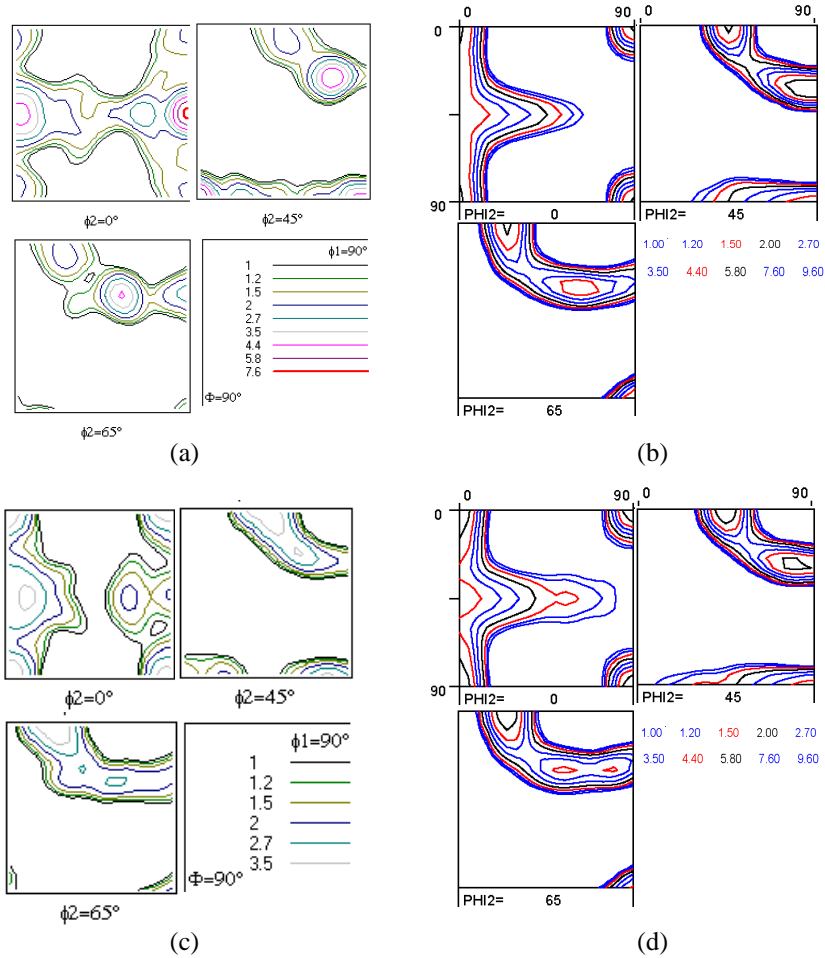
Figure 6.20: Comparison of texture for 6061-T4 specimen after PSC of 35% deformation at RT (a) from experiment (b) from *VPSC* and at 250°C (c) from experiment (d) from *VPSC*

Figure 6.20 represents the comparison of experiment and model for 6061-T4 material for both RT and 250°C. The predictions are close in terms of relative intensities of Cube and Goss components, the presence of the η-fibre and the absence of the β-fibre. The presence of the Inverse Goss (I-G) component has not been predicted for this alloy.

6.6   A modelling Approach to Calculate the Yield Locus

After proper fitting of the CRSS ratios of different slip planes the *VPSC* model was used to determine the stress factors, namely tensile, plane strain, bi-axial and shear

factors which are the yield stress for each deformation mode normalized by the uniaxial tension yield stress.

These factors along with r-values and equi-biaxial strain ratios were then used for the calculation of the yield locus according to the Vegter equation. At RT the experimental yield locus was compared with the simulated one, while at 250°C the yield locus was only predicted.

6.6.1   Determination of the Yield Locus
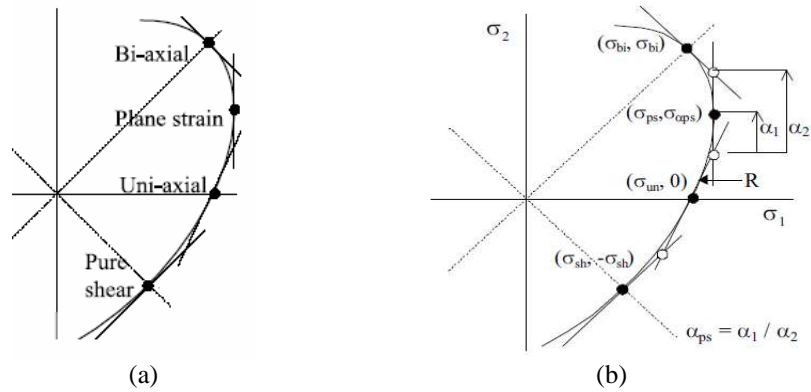
Figure 6.21: Schematic of Yield locus (a) four test points (b) showing the input parameters

To explain the plastic behaviour of isotropic materials, the Von Mises or Tresca yield functions are considered sufficient. However, for sheet metal forming some additional parameters are needed to describe the plastic anisotropy. These parameters are obtained from a set of selected mechanical tests and can be used to construct a yield surface. A yield surface is defined as a hyper surface that describes the elastic region in 6 dimensional stress space. Assuming all out of plane components of the stress vector to be zero at the time of sheet metal forming, the yield criteria can be defined in plane stress space. The yield locus for the present investigation has been calculated with the Vegter yield equation. In constructing the yield surface, the Vegter yield criterion [50] is considered as one of the most accurate yield functions for aluminium alloys. The model predicts much better results in terms of plastic behaviour compared to others based on uni-axial yield stress and r-values. The Vegter yield locus calculation uses as input the yield stress of four different states of stress along particular loading directions namely, pure shear, plane strain tension, uniaxial tension and equi-biaxial (figure 6.21a). This

gives four reference points along the yield locus in the region where σ1 > σ2. The corresponding reference points in the region where σ2 > σ1 can be obtained either by assuming symmetry of the yield locus in respect to the first diagonal or from the yield stresses of the same four stress states after rotating the loading direction by 90°. The reference points in the compression region of the yield locus are usually obtained by assuming that the yield stress in compression is equal to the one in tension. A Bezier curve is used to describe the points in between the reference points. Considering the normals to the yield locus as the direction of the plastic strain rate (Drucker's postulate), the set of Bezier curve is constructed in such a way that the yield locus is continuous. The gradient at the uni-axial stress point is a function of r-value. The gradient at the plane strain point is infinite and hence fixed. As it is difficult to measure the gradient at a simple shear point, the gradient is fixed. The gradient at the equi-biaxial point is directly related to strain during the test, $\rho = \dot{\varepsilon}_2 / \dot{\varepsilon}_1$. The intersection of the two tangents at the reference points defines the hinge point $\vec{\sigma}_h$ (Figure 6.21b). Hence, the yield locus between two reference stress points $\vec{\sigma}_i$ and $\vec{\sigma}_j$ is defined by

$$\vec{\sigma_{loc}} = \vec{\sigma}_i + 2\mu(\vec{\sigma}_h - \vec{\sigma}_i) + \mu^2(\vec{\sigma}_i + \vec{\sigma}_j - 2\vec{\sigma}_h) \tag{6.1}$$

with $\mu \in [0,1]$.

Finally, a yield function is constructed by defining an equivalent stress σ_{eq} that is implied for any plane stress state by the relation

$$\vec{\sigma} = \frac{\sigma_{eq}}{\sigma_f}\vec{\sigma_{loc}} \tag{6.2}$$

Where σ_f is the current flow stress. A function ϕ needs to be defined as follows,

$$\phi(\sigma, \varepsilon_{eq}) = \sigma_{eq}(\sigma) - \sigma_f(\varepsilon_{eq}) \tag{6.3}$$

The function ϕ fulfils the condition that $\phi = 0$ on the yield locus and $\phi < 0$ in the elastic regime. The direction of the plastic strain rate can be calculated from the derivative of ϕ to the stress σ. Since ϕ is continuously differentiable, the plastic strain rate direction is continuous.

The planar anisotropy can be modeled by allowing all reference stress points and corresponding normals to depend on θ, i.e. the angle between the first principal stress and the rolling direction. The reference stress points and normals are defined by an interpolation, based on Fourier series.

The four reference stresses, r-value and strain ratio at the equi-biaxial point for the calculation of a yield locus curve can be obtained either from experimental pure

shear, plane strain tension, uniaxial tension and equi-biaxial tests or from *crystal plasticity* simulations of these deformation modes. The input data are usually given as stress factors in respect to the uniaxial tension yield strength.

6.6.2   Validation of yield locus at room temperature

A very accurate calculation of the yield locus at RT based on experiments has already been documented by Vegter [50] and Barlat [51]. The yield locus at RT of the investigated materials were constructed by determining the stress ratios from uniaxial, plane strain, simple shear and normal compression experiments and by joining the points with the Vegter equation. R-values and equi-biaxial strain ratios were measured directly on the specimens. The mechanical tests were done with the loading direction parallel to RD, at 45° to RD or parallel to TD. The yield locus for $\theta = 0$, 45 and 90° could then be directly obtained using results from perpendicular tests. In this section, the *VPSC* model is also used to simulate the same set of deformation tests considering only the {111}<110> slip systems, which are assumed to be the only one active at RT. Stress ratios, r-values and equi-biaxial strain ratios were derived and used to calculate the yield locus. There is a possibility to choose two options for the hardening law implicitly inside the code. One is the Voce law or alternatively the one predicted by the *mechanical-threshold-strength (MTS)* model. The main advantage of the model is the possibility to also predict the YL at elevated temperature using the activated slip system at that temperature. This model has already been successfully used by Engler [52] in a 5xxx alloy with much lower experimental effort compared to Vegter and Barlat '91. For the present investigation no work hardening has been used to calculate the stress factors.

(a)   (b)

(c)
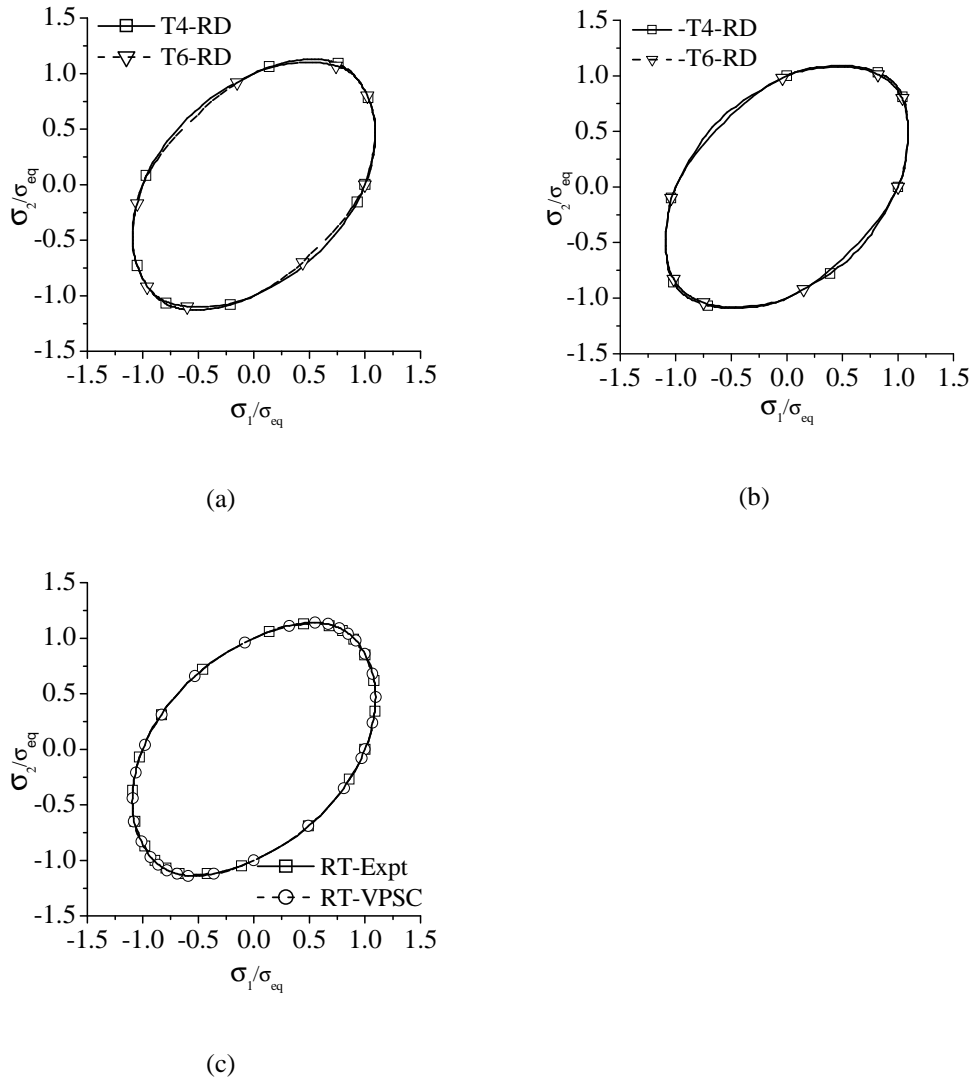
Figure 6.22: Normalized experimental yield locus at two different tempers for (a) 6016 and (b) 6061; Comparison with model for (c) 6016-T4

The yield locus derived from experiment for 6016 and 6061 using the Vegter equation is presented in figure 6.22a and b for the case corresponding to $\theta = 0^\circ$ (labeled "RD"). The figures show that there are only small shape changes in yield surface due to changes of temper condition. For 6016 the curves slightly differ at the bi-axial and pure shear points while for 6061 only at pure shear points a difference is observed. From figure 6.22 it can be seen that the yield locus derived from *VPSC* calculations is in close agreement with the experimental one and it validates the numerical method used.

6.6.3   Temperature dependence of yield locus

Change in size, position and shape of yield locus with temperature may be associated with a change of plastic deformation response. Position and shape remaining constant, the change in size can be modelled with isotropic hardening or softening. The change of yield locus shape reflects the change of plastic anisotropy. Owing to the difficulty in carrying out experiments at elevated temperatures very limited data are available about high temperature yield loci. In the present investigation, the *VPSC* model has been used to predict the yield locus in the same way than at RT; uniaxial, plane strain, simple shear and normal compression deformations are simulated to derive the stress factors, r-value and equi-biaxial strain ratio after 10% deformation. These output data are used to construct the yield locus according to the Vegter method. The general description of the *VPSC* model is given in section 6.5.1. The temperature dependence of the CRSS ratios were obtained by fitting the r-value, as discussed in section 6.5.3. The model uses only one octahedral slip system {111}<110> at RT and 130°C. At 180°C an additional slip system family {112}<110> is introduced. The CRSS ratio of the {111}<110> and {112}<110> slip system families is 1:1.2. Four families of slip systems {111}, {110},{100} and {112}<110> are used at 250°C with the CRSS ratios 0.9:1:1.1:1.

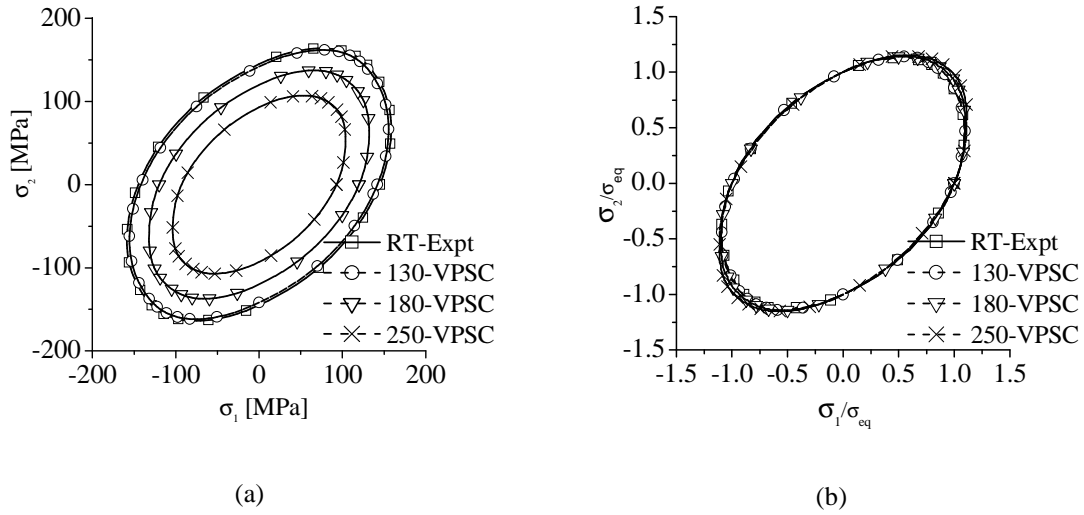|	
(a)	(b)

Figure 6.23: Effect of temperature on yield locus for 6016-T4 along RD (a) actual (b) normalized

Figure 6.23a shows that the yield locus reduces in size with increasing temperature, which is a direct consequence of the temperature dependence of the yield strength.

At RT and 130°C the yield locus overlaps since both yield strength and CRSS are the same in this temperature range. Figure 6.23b shows the yield locus normalized with respect to equivalent uniaxial stress to identify the shape change. It can be noticed that, with increasing temperature, the yield locus becomes more elongated along the equi-biaxial direction.

6.6.4   Discussion

The activation of different slip systems was proposed to explain the temperature dependence of plastic deformation and anisotropy. Experimental r-values at different angles to RD were well fitted by the *VPSC* model in the temperature range RT-250°C. The model was subsequently successfully validated by the prediction of PSC textures at 35% deformation at RT and 250°C and the yield locus at RT. Using the determined temperature dependence of the slip systems, the model can generate the yield loci at the temperatures needed for the FE modelling of warm forming.

An effort has been made in section 6.3.4 to determine experimentally from the band contrast maps of the deformed samples the active slip systems and compare them with the predicted slip system activity by the *VPSC* model depending on the CRSS ratios. In the model the highest activity at 250°C has been noticed on the {111}<110> system followed by {112}, {110} and {100}. The activity level, however, of {110} and {100} are very low and close to each other. From experiment, it appeared difficult to conclude such a straight forward ranking about the relative activity of the slip planes but the activity of {111} has been reduced while changing from RT to 250°C. This supports the conclusion of Maurice [24] that the introduction of slip on {112} reduces the activity of {111} considerably. According to Perocheau [19] the difficulty of slip on {100} is highest which also is commensurate with present observation.

The normalized yield locus curves (figure 6.23b) reveal that, when temperature is increased, the yield locus expands along the equi-biaxial point compared to the remaining uniaxial tension, shear or compression points. Expansion of the yield surface at the biaxial point (equivalent to the bottom of the cup in terms of stress state) with temperature means that the material becomes relatively stronger at the bottom compared to the other parts of the cup. Although the change of the yield locus with temperature looks small, it is to be kept in mind that even a small apparent change may have a significant impact on plastic anisotropy.

6.7   Conclusions

The most interesting conclusions which can be drawn from this chapter are outlined below:

1. No change in the type of anisotropy with temperature has been noticed from the mechanical test results. The true stress, true strain curves or the r-value profile generated from the tensile experiments supports the above statement. An absence of change in earing profile in terms of number of ears and relative position, in the deep drawing experiments also supports the same conclusion.

2. Although the deformed texture changed compared to the initial texture for all modes of deformation, no significant effect of the deformation temperature on texture evolution could be observed.

3. The earing profiles from three different series of deep drawing tests at room temperature were found to be the same while they are different at 250°C. Series A and C revealed two fold symmetry while series B showed four fold symmetry with lesser amplitude. It has been concluded that these differences are caused by undetected differences in the tool geometry or alignment. It revealed that plastic anisotropy at warm temperature is very sensitive to test conditions.

4. The observation of the band orientation on the band contrast maps after deformation suggested the activation of extra slip system families with increasing temperature.

5. The *VPSC* model successfully predicts the deformed texture after PSC at 35% deformation for room and warm temperatures and both alloys using the CRSS ratios of different slip planes determined after fitting the r-value profiles. A good match is obtained between the experimental and calculated yield locus at RT and the model is then used to predict the yield locus at 250°C.

References

1. **Hu J., Ikeda K. and Murakami T**., Effect of texture components on plastic anisotropy and formability of aluminium alloy sheets, *Journal of Materials Processing Technology*, **73**, 1998, p. 49

2. **Zhao Z., Mao W., Roters F. and Raabe D**., A texture optimization study for minimum earing in aluminium by use of a texture component crystal plasticity finite element method, *Acta Materialia*, **52** 2004, p.1003

3. **Zhou. Y., Jonas. J. J., Savoie. J., Makinde. A. and MacEwen. S.R.**, Effect of texture on earing in fcc metals: finite element simulations, *International Journal of Plasticity*, **14**, 1998, p.1

4. **Engler O., Hirsch J. and Lücke K.**, Texture development in Al-1.8 wt% Cu depending on the precipitation state—II. Recrystallization textures, *Acta Metallurgica and Materialia*, **43**, 1995, p. 121

5. **Engler O., Chavooshi A., Hirsch J. and Gottstein G.**, Formation of recrystallization textures and plastic anisotropy in AL-MG-SI alloys, *Materials Science Forum*, **157-162**, 1994, p. 939

6. **Hirsch J. and Engler O.**, *Proceedings 16th Risø International Symposium on Material Science*, Risø National Laboratory (eds. N.Hansen et al.) Roskilde, Dänemark, **49**, 1995

7. **Oscarsson A and Bate P**, Texture variations through the thickness of AA3004 and its effects on earing behaviour, *Materials Science Forum*, **217-222**, 1996, p.559

8. **Wagner P and Lucke K**, Quantitative correlation of texture and earing in Al-Alloys, *Materials Science Forum*, **157-162**, 1994, p.2043

9. **Engler O and Hirsch J**, Polycrystal plasticity simulation of six and eight ears deep-drawing aluminium cups, *Materials Science and Engineering A*, **452-453**, 2007, p.. 640

10. *Formability of aluminium alloy sheets*, ed. by Metal Forming Section, (Japan Institute of Light Metals, Tokyo, 1985

11. **Uno T**., *Sumitomo Light Metal Technical Reports*, **42**, 2001, p. 100

12. **Ekström H-E., Furu T., Mishin O. V**., T. Pettersen an dB Olsson, *Aluminium*, **78**, 2002, p. 930

13. **Savoie J., Jonas J. J., MacEwen S. R. and Perrin R**., Evolution of r-value during the tensile deformation of aluminum, *Textures Microstructure*, **23**, 1995, P.149

14. **Stachowicz, F.F.**, On the mechanical and geometric inhomogeneity and formability of aluminium alloy sheets, *Archives of Metallurgy*, **41**, 1996, p.60.

15. **Engler O., An Y.**, Correlation of texture and plastic anisotropy in the Al-Mg alloy AA5005, *Solid State Phenomena*, **105**, 2005, p..277.

16. **Li S., Engler O. and Van Houtte P**., Plastic anisotropy and texture evolution during tensile testing of extruded aluminium profiles, *Modelling Simulation Materials Science and Engineering*, **13**, 2005, p.783.

17. **Abedrabbo N., Pourboghrat F. and Carsley J.**, Forming of aluminium alloys at elevated temperatures – part I, *Material Characterization, International Journal of Plasticity*, **22 (2)**, 2006, p.314

18. **Jahazi M and Goudarzi M**, The Influence of thermomechanical parameters on the earing behaviour of 1050 and 1100 aluminium alloys, *Journal of Materials Processing Technology* **63**, 1997, p.610

19. **Maurice Cl. and Driver J.H**., Hot rolling textures of f.c.c. metals—Part II. Numerical simulations, *Acta Materialia*, **45**, 1997, p.4639

20. **Perocheau F. and Driver J.H.**, Slip system rheology of Al-1%Mn crystals deformed by hot plane strain compression, *International Journal of Plasticity*, **18**, 2002, p.185

21. **Bacroix B. and Jonas J.J**., The influence of non-octahedral slip on texture development in fcc metals, *Texture and Microstructure*, **8&9**, 1988, p. 267

22. **Hazif R. Le. and Poirier J.P.**, Cross-slip on {110} planes in aluminum single crystals compressed along <100> axis, *Acta Metallurgica*, **23**, 1975, p.865

23. **Carrard M. and Martin J.L**., "A study of (001) glide in [112] aluminium single crystals II. Microscopic mechanism", *Philosophical Magazine A*, **58**, 1988, p.491

24. **Maurice Cl. and Driver J.H.**, High temperature plane strain compression of cube oriented aluminium crystals, *Acta Metallurgica et Materialia*, **41**, 1993, p..1653

25. **Perocheau F.**, Etude et simulation de textures de déformation à chaud d'alliage d'aluminium, Ph.D. Thesis (1999) EMSE-INPG, France

26. **Driver J., Perocheau F. and Maurice Cl.**, Modelling hot deformation and textures of aluminium alloys, *Materials Science Forum*, **331-337**, 2000, p.43

27. **Maurice Cl. and Driver J.H.**, Hot rolling textures of Aluminium, *Materials Science Forum*, **157-162**, 1994, p.807.

28. **Delmast F., Majimel J., Vivast M., Molenat G., Couret A. and Coujou A**., Cross slip and glide in {001} planes of Al-Mg-Si alloy 6056, *Philosophical Magazine Letters*, 83, No. 5, 2003, p. 289

29. **Carrard M. and Martin J. L**., A study of (001) glide in [112] aluminium single crystals 11. Microscopic mechanism, *Philosophic Magazine A*, , **58**, No. 3, 1988, p. 491

30. **Taylor G.I**., *Journal of Inst. Met*., **62**, 1938, p. 307

31. **Bishop J.F.W. and Hill R.**, A theoretical derivation of the plastic properties of a polycrystalline face-centred metal, *Philosophical magazine series 7*, **42**, 334, 1951, p.1298

32. **Hosford W.F. and Backofen W.A.**, *Fundamentals of Deformation Processing*, Syracuse U. Press, 1964, p.259

33. **Leffers T., Asaro A.J., Driver J.H., Kocks U.F., Mecking M, Tomé and van Houtte P.**, *The Eighth International Conference on Texture of Materials*, TMS, Warrendale PA, 1988, p. 265

34. **Banabic D., Bunge H.J., Pöhlandt K., Tekkaya A.E**., *Formability of Metallic Materials*, ed BanabicD., 2000, Springer Verlag, Berlin

35. **Cazacu O., Barlat F**., Application of the theory of representation to describe yielding of anisotropic aluminium alloys, *International of Engineering Science*, **41**, 2003, p.1367

36. **Barlat F., Brem J.C., Yoon J.W., Chung K., Dick R.E., Lege D.J., Pourboghrat F., Choi S.H. and Chu E**., Plane stress yield function for aluminium alloy sheets, part 1:formulation, *International Journal of Plasticity*, **19**, 2003, p. 1297

37. **Lopes A.B., Barlat F., Gracio J.J., Ferreira Duarte, J., Rauch E.F**., Effect of texture and microstructure on strain hardening anisotropy for aluminium deformed in uniaxial tension and simple shear, *International Journal of Plasticity*, **19**, p. 419

38. **Naka T., Nakayama Y., Uemori T., Hino R. and Yoshida F**., Effects of temperature on yield locus for 5083 aluminium alloy sheet, *Journal of Materials Processing Technology*, **140**, 2003, p.494

39. **Zhou. Y., Jonas. J. J., Savoie. J., Makinde. A. and MacEwen. S.R**., Effect of texture on earing in fcc metals: finite element simulations, *International Journal of Plasticity*, **14**, 1998, 1-3, p. 117

40. **Engler O. and Kalz S.**, Simulation of earing profiles from texture data by means of a visco-plastic self-consistent polycrystal plasticity approach, *Materials Science and Engineering A*, **373**, 2004, p. 350.

41. **Vernon-Parry K.D., Furu T., Jensen D.J. and Humphreys F.J.**, Deformation microstructure and texture in hot worked aluminium alloys, *Materials Science and Technology*, November 1996, **12**, p. 889

42. **Savoie J., Zhou Y., Jonas J.J. and Macewen S.R**, "Texture induced by tension and deep drawing in aluminium sheets", *Acta Materialia*, **44 (2)**, 1996, p. 587

43. **Jobson P.and Roberts W.T.**, Directionality in a precipitation-hardened alloy, *Metallurgical transactions A*, **A**, 1977, p.2013.

44. **Hosford W.F. and Zeisloft R.H**., The anisotropy of age-hardened Al-4pct Cu singles crystals during plane strain compression, *Metallurgical Transactions*, **3**, 1972, p.113

45. **Bate P., Roberts W.T. and Wilson D.V.**, The plastic anisotropy of two phase aluminium alloys – I. Anisotropy in unidirectional deformation, *Acta Metallurgica*, **29**, 1981, p.1797.

46. **Taylor G.I.**, *Journal of Institution of Metals*, **62**, 1938, p.307

47. **Honneff H. and Mecking H.**, *Proceedings of sixth international conference on Texture of Materials (ICOTOM-6)*, 1981, p.347

48. **Lebensohn R.A. and Tomé C.N.**, A self-consistent anisotropic approach for the simulation of plastic deformation and texture development of polycrystals: Application to zirconium alloys**,** *Acta Metallurgica and Materialia*, **41**, No.9, 1993, p.2611

49. **Molinari A., Canova G.R. and Ahzi S.**, A self-consistent approach of the large deformation polycrystal viscoplasticity, *Acta Metallurgica*, **35**, 1987, p.2983

50. **Vegter H. and van den Boogaard A.H.,** A plane stress yield function for anisotropic sheet material by interpolation of biaxial stress states, *International Journal of Plasticity,* **22**, 2006, p. 557.

51. **Barlat, F., J. C. Brem, J. W. Yoon, K. Chung, R. E. Dick, D. J. Lege, F. Pourboghrat, S. H. Choi and E. Chu**, Plane stress yield function for aluminum alloy sheets—part 1: Theory, *International Journal of Plasticity*, **19**, 2003, p. 1297.

52. **Engler O., An Y.G.**, Correlation of texture and plastic anisotropy in the Al-Mg alloy AA 5005, *Solid State Phenomena*, **105**, 2005, p. 277

Chapter 7

APPLICATIONS AND CONCLUSIONS

This chapter presents the results of a simulation using a finite element model. The finite element code DiekA developed at the University of Twente (The Netherlands) was linked to the *Nes* and *VPSC* models for the description of the material behaviour. The punch force-punch displacement curves and thickness distribution from deep drawing tests with different conditions were simulated and compared with the experimental results.

7.1 Introduction

The term "simulation" (derived from the Latin word "simulare" meaning "to pretend") in its technical sense means to reproduce a physical or technical process using mathematical and physical models. Simulation is usually cheaper and less hazardous compared to practical experiments. Simulations might produce identical output as experiments when all the steps of the experiments are successfully and logically replicated. Therefore, simulation is considered as a powerful tool when combined with a sufficient level of modern computational power, which is often required to simulate complex technical processes. With the increase of computational power during the last ten years numerical methods are playing now a prominent role. In present day research, finite element modelling (FEM) is widely used as a framework for product design and process optimization. Describing a technical problem in physical terms and subsequently formulating it mathematically, is the first step for modeling. Numerical complexity like poor convergence during iterations should be avoided. The boundary and initial conditions have to be predefined properly. During fabrication as a first tool for industrial product or process design, FEM can solve potential problems and hence save time and money. Also, to understand the complex deformation mechanics during any forming processes numerical analysis is considered as a critical tool. A detailed overview can be found in Belytschko [1], Zienkiewicz and Taylor [2], Simo and Hughes [3], Crisfield [4].

Being a very popular forming process deep drawing (DD) is simulated very frequently with FEM. For production of complex shapes and curvatures, the DD process is frequently of critical importance in car body press forming in the automotive industry. An incorrect tool design may lead to several undesirable effects leading to failure by wrinkling, necking or stretching. However, proper tool design and control of variables during DD is a daunting task and needs several trials to reach to perfection. Consequently, the design of the tool consumes a lot of time and money. FEM can replace the hazards of practical trial and error by a virtual process. An accurate description of the material response, tool geometry and other process variables are essential inputs for the successful and accurate running of the model. This is also the case for the simulation of warm forming processes. Warm forming has been considered as a promising process for improvement of formability compared to room temperature forming. Due to the complex effect of temperature on material response, accurate material models become extremely necessary. A temperature and rate dependent hardening and temperature dependent anisotropic yield function need to be implemented for thermo-mechanical simulation during warm forming. The yield function denotes the initiation of plastic flow under an

arbitrary loading mode while the hardening rule describes the evolution of the yield surface.

Existing research on simulation of warm forming only deals with the influence of temperature on flow stress [5,6,7]. The description of material's anisotropy by the use of the Vegter yield surface [8] was assumed independent on changes in temperature. To be more realistic, the change of yield surface with temperature also needs to be incorporated in the model. Therefore, the global objective of the project was to develop a FEM linked to physically based models that should predict the work hardening and yield locus for several aluminium alloy systems in a wide range of temperature. The material models have been developed at Delft University of Technology, while their coupling with FE code has been done at the University of Twente. The physically based *Nes* model (described in chapter 5) includes the effect of work hardening and the crystal plasticity *VPSC* model (described in chapter 6) gives the coefficients of the yield locus as a function of temperature. The coupling of material models and application to 5xxx and 6xxx aluminium alloys has been presented in details in the Ph.D. thesis of Kurukuri [9]. For instance, the true stress-true strain response of 5754-O obtained from the tensile experiments was also simulated by FEM and the accuracy and necessity of FEM were verified. Two physically based hardening models namely the Bergström and *Nes* models were also compared. Both models can fit well the results of monotonic tensile tests. However, the *Nes* model gives better prediction of the DD process than the Bergström model when they were coupled with the FE code [9]. The aim of the present chapter is to present an application of the FEM linked to the *Nes* and the *VPSC* models presented in chapters 5 and 6. Deep drawing of cylindrical cups of 6xxx was chosen as a case study. The punch force-punch displacement and thickness distribution are compared with the experimental one.
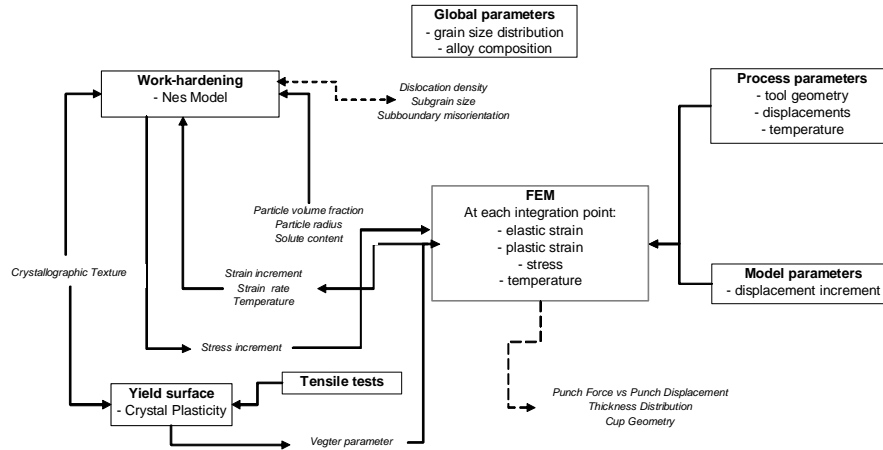
7.2   Description of the model

Figure 7.1: Different models used in the thesis and the way they are related with each other

In the context of the present research, the *Nes* work hardening model and the *VPSC* crystal plasticity model have been linked to the DiekA FEM to simulate warm deep drawing (figure 7.1). The implicit finite element code DiekA [10] has been developed at the University of Twente Laboratory of Applied Mechanics. The code has been specially made for the simulation of forming processes like deep drawing, rolling, extrusion, bending, injection molding and others. The main characteristics of these simulations are strong nonlinearities due to (visco) plastic material behaviour, tool-workpiece contact, large strains and thermo-mechanical coupling. The code has many advantages to work with. It solves a set of thermo-mechanically coupled equations. It also works on the arbitrary Lagrangian Eulerian method. With this method, the displacement of the element mesh can be disconnected from the material displacement. It is possible to calculate problems with large displacements and the temperature can be used as a degree of freedom. For three dimensional calculations bulk elements, membrane elements, plate elements and contact elements have been developed. The tool description can be done with geometric contours and the contact description is done with the help of special interface elements. The FE code uses stress strain curves generated from the *Nes* subroutine together with stress factors and r-values at different angles to the rolling direction from the *VPSC* subroutine. The *Nes* model has been fitted and validated using the tensile test data at room and warm temperatures (chapter 5). The stress factors and r-

values are used to describe the anisotropic behaviour of the sheet by using the Vegter yield function [8] (chapter 6). The parameters of the Vegter yield function were calculated for a limited set of temperatures, i.e. at 25, 150, 180, and 250°C and quadratic interpolating functions were used to determine the parameters at other temperatures.

7.3   Simulation of Deep Drawing

The details of the deep drawing tests have been described in chapter 3. Cylindrical shaped cups were drawn at various temperatures, punch velocity and holding time for different tempers of both 6016 and 6061 aluminium alloys. The experimental results showing the influence of these parameters on the punch force-punch displacement response, the thickness distribution and earing profile have been presented in Chapter 4, Chapter 5 and Chapter 6.

7.3.1   Input

Following the orthotropic symmetry assumption for the material behaviour, a quarter of the blank was modelled and boundary conditions were applied on the displacement degrees of freedom to represent the symmetry. The blanks were modelled with 998 discrete Kirchhoff triangular shell elements with 3 translational, 3 rotational and 1 temperature degree of freedom per node and a typical element edge size of 5mm. The tools were modelled as rigid contours with a prescribed temperature. The model further contains 1996 contact elements, resulting in a total of 10,812 degrees of freedom. The global convergence criterion was set to 0.5% relative unbalanced force. In the simulations punch displacement increments of 0.1 mm were used.

In the presented simulations, room temperature deep drawing was simulated by giving a temperature of 25°C to the punch, the die, and the blank holder. For warm deep drawing, the die and the blank holder were given a temperature 250°C, while the punch was kept at 25°C. As a consequence, the temperature of the bottom of the cup was low while the temperature at the flange was higher maintaining a temperature gradient from the bottom to the flange. In the simulations, the friction between the sheet and the rigid tools (die and cheeks) is described with the Coulomb's friction model. The friction between tool and work-piece is one of the least known parameters in the simulations. Van den Boogaard [11] measured the value experimentally for the used combination of materials and lubricant. He found a value of 0.06 at room temperature and at temperatures above 150°C, the friction

coefficient varied between 0.12 and 0.18 depending on the experiments. In the model, the value of the friction coefficient was 0.06 below 90°C and 0.12 above 110°C. In the transition domain the values were linearly interpolated. Owing to the high heat conduction of aluminium and the low sheet thickness, it is logical to assume that temperature is constant across the sheet thickness. It is also assumed that the tools remain at the prescribed temperature as well as the part of the blank in contact with the tools. Therefore results are not very dependent to the heat transfer coefficient (α) between the tool and the blank and a constant value of α = 140 W/m-K was used.

7.3.2   Results

The experimental punch force-punch displacement response and the thickness profile from cup centre to cup edge are used to validate the DD simulations.

Temperature

The comparison between the FEM predictions and experimental results is made at room temperature and at 250°C.
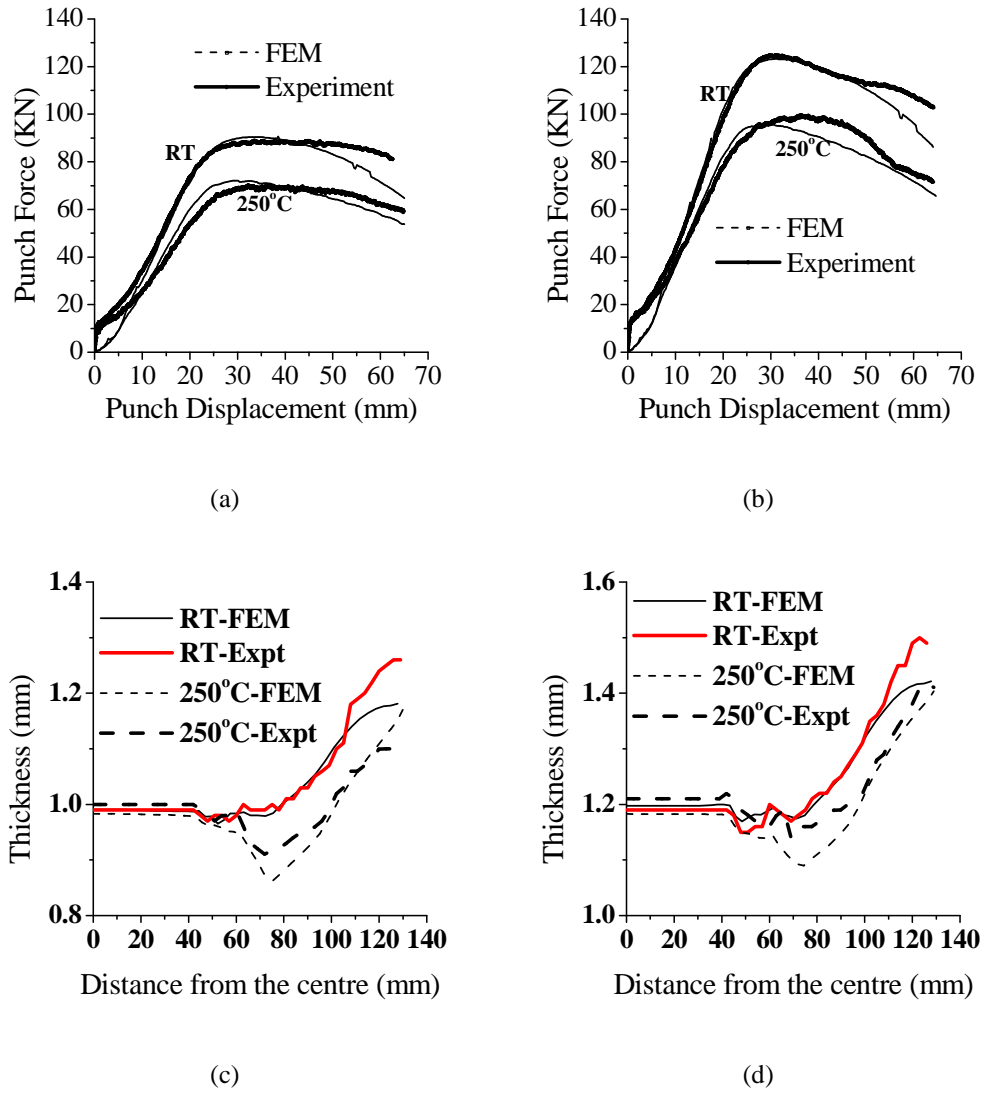
(a)   (b)

(c)   (d)

Figure 7.2: Comparison of FEM simulation and experiment (series A). Punch force
vs displacement curves for T4 alloys at two temperatures for (a) 6016 and (b) 6061;
Thickness distribution for T4 alloys for (c) 6016 and (d) 6061.

Comparing the different punch force–displacement curves (figure 7.2a and figure
7.2b), it can be seen that the model performs well at both the temperatures. At 25°C,
the simulated maximum punch force shows a very good agreement with the
experiment, while the punch force is underestimated at larger drawing depths for
both alloys under T4 conditions. The calculated depth corresponding to maximum

punch force at 250°C is slightly shifted compared to the experimental values for both alloys.

Experimental measurements in figure 7.2c and figure 7.2d show that the bottom (part of the curve from 0 to 45 mm) is thinner after room temperature drawing than after warm drawing. The reason is that during warm drawing, the flange is warmer and therefore softer than the bottom and carries relatively more deformation than in case of room temperature drawing. The FEM model, however, predicts the same bottom thickness for both drawing temperatures. FE simulations also show that the trends along the wall (curve from 45 to 120 mm) and flange (curve above 120 mm) with changing temperature are well predicted. A significant drop in thickness at the middle of the cup wall at 250°C compared to the room temperature thickness, has been noticed by the experiment and subsequently supported by the model. The minimum wall thickness is, however, underestimated by the FEM results, which represents an important issue to be considered for further model improvement. Indeed, due to thinning, the cup wall becomes the weakest of the areas and needs careful attention during warm forming to avoid premature failure in this area. The flange thickness becomes thicker than the initial sheet thickness indicating the predominance of the circumferential force. The deep drawing experiments and modelling at 180°C were also found to be in good agreement. The punch force – punch displacement and thickness profile remain in between the curves obtained at room temperature and 250°C for both alloys.

Temper
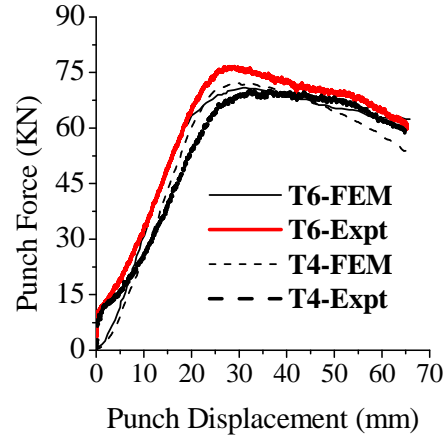
(a)

Figure 7.3: FEM simulation of punch force vs punch displacement curves for T4 and T6 tempers for 6016 at 250°C

In Figure 7.3, the simulated and experimental punch force–displacement curves for 6016 are plotted for different tempering conditions. It can be noticed that the numerical model underestimates the maximum punch force for T6 and slightly overestimates the same for T4. This observation is somehow surprising since, from fitting of the *Nes* model, it has been observed that the *Nes* model overestimates the flow stress for T6 condition at high temperature (figure 5.18) and, therefore, an overestimation of the punch force in T6 condition rather than an underestimation would have been expected during deep drawing simulation. Also, the difference between simulated punch forces of T4 and T6 blanks is low compared to their difference in flow stress. It shows that the relation between flow stress and punch force is complex and further investigation is required to reach a good prediction of the temper effect during deep drawing.

7.4   Conclusions

The effect of temperature, temper and composition on material properties were the three most intensively studied parameters in the present investigation. Experimental results were used to validate the *Nes* and *VPSC* models and subsequently the models

have been coupled with the finite element code DiekA to obtain predictions about the forming process.

Experimentally, the most noticeable change of material properties was produced by temperature. Both yield strength and work hardening were reduced due to an increase of temperature up to 250°C. The maximum punch force and rate of increase of force with displacement also decreased with temperature during deep drawing. Although no change was noticed in the number of ears owing to the change in temperature the amplitude of ears was found to be reduced at 250°C. The thickness distribution from the bottom of the cup to the flange was also different at different temperatures. At 250°C a significant dip in thickness was observed at the lower part of the cup wall.

The effect of temperature has been explicitly included in the *Nes* code and has been captured nicely by the model. Other models, e.g. Bregström, are handicapped by the fact that they need to be fitted for each temperature. From room temperature to 250°C, the work hardening response of the materials can be successfully predicted. An effort has been made to simulate deep drawing after coupling the *Nes* and *VPSC* models with the FE code DiekA. The predictions seem close in terms of punch force vs punch displacement and thickness distribution. Results of FEM simulations still need to be analysed with respect to the influence of temperature on earing profile and plastic anisotropy.

The prediction of the stress strain response for different alloys by only taking into account the change of the precipitate radius and volume fraction, and the solute content is readily done with the *Nes* model while a different fitting schedule has to be followed for other simpler models. Changing the solute content and precipitate distribution also gives a straightforward indication about the change in materials properties due to temper state. Changing the temper state from T4 to T6 was associated with an increase in yield strength and a decrease in work hardening although the effect on work hardening was much restricted at room temperature. FEM simulations of deep drawing properly captured the difference between the two investigated alloys while the prediction of temper effect still needs to be improved.

The specific case study presented in this chapter illustrates that combining physically based material models with FEM can be used to simulate forming processes successfully. The simulation results globally show a good agreement with experiment and demonstrate the potential interest of the modelling approach. This type of models is very flexible and can be easily extended and hence applied to other systems.

References

1. **Belytschko, T., Liu W.K. and Moran B.,** Nonlinear finite elements for continua and structures**, J.** Wiley & Sons, Chichester, 2000**.**

2. **Zienkiewicz, O. C. and Taylor R.L.** The Finite Element Method For solid and structural mechanics, Butterworth–Heinemann, 6 edn., 2005.

3. **Simo, J.C. and Hughes T.J.R.** Computational inelasticity, Interdisciplinary applied mathematics, Springer, NewYork, 2000.

4. **Crisfield, M.A.** Non-linear Finite Element Analysis of Solids and Structures, Vol. 2: *Advanced Topics*, J. Wiley & Sons, NewYork, 1997.

5. **Li D. and Ghosh A.,** Tensile deformation behaviour of aluminium alloys at warm forming temperatures. *Materials Science and Engineering A*.,**352**, 2003, p.279

6. **Takuda H., Mori K., Masuda I., Abeand Y., Matsuo M..** Finite element simulation of warm deep drawing of aluminum alloy sheet when accounting heat conduction. *Journal of Materials Processing Technology*, **120**, 2002, p.412

7. **van den Boogaard A.H. and Huétink J..** Simulation of aluminium sheet forming at elevated temperatures. *Comp. Methods in Applied Mechanics and Engineering*, **195**: 2006, p.6691

8. **Vegter H. and van den Boogaard A. H..** A plane stress yield function for anisotropic sheet material by interpolation of biaxial stress states, *International Journal of Plasticity*, **22**, 2006, p.557

9. **Kurukuri S**., Ph.D. thesis, Simulation of Thermally Assisted Forming of Aluminum Sheet, University of Twente, The Netherlands, 2010

10. DiekA Development Group, Section of Applied Mechanics, University of Twente. *DiekA User Manual, Release 9.1 edition*, 2006.

11. **van den Boogaard, A. H.**, Thermally enhanced forming of aluminium sheet, Ph.D. thesis, University of Twente, The Netherlands, 2002

PUBLICATIONS

Journal Papers

1. Warm deep-drawing and post drawing analysis of aluminium 6XXX alloys, M. Ghosh, A. Miroux, and L. Kestens, in preparation.

2. Forming of AA6016 sheet at warm temperature: Modeling and experiments, M. Ghosh, S. Kukukuri, A. G. Miroux, A.H. van den Boogaard and L. Kestens, in preparation.

3. Thermo-mechanical forming of Al-Mg-Si sheet, A.H. van den Boogaard, S. Kukukuri, M. Ghosh, and A. G. Miroux, *Computer Methods in Materials Science*, Vol. 9, no. 1 (2009) p. 5.

4. Effect of temperature on anisotropy in forming simulation of aluminium alloys, S. Kukukuri, A. Miroux, M. Ghosh, and A.H. van den Boogaard, *International Journal of Material Forming*, Vol. 2 Supplement 1, (2009) p. 387

Conference contributions

1. Mechanical and Forming Properties of AA6xxx Sheet from Room to Warm Temperatures, Alexis Miroux, Manojit Ghosh, Srihari Kurukuri, Leo Kestens and Ton van den Boogaard, *Proceedings of the 12th International Conference on Aluminium Alloys*, eds. S. Kumai, O. Umezawa, Y. Takayama, T. Tsuchida, T. Sato, September 5-9, 2010, Yokohama, Japan 2010 The Japan Institute of Light Metals p. 1243

2. Thermo-mechanical Forming of Al–Mg–Si Alloys: Modeling and Experiments, S. Kurukuri, A.H. van den Boogaard, M. Ghosh and A. Miroux, *Proceedings of the 10th International Conference on Numerical Methods in Industrial Forming Processes (NUMIFORM)*, eds. F. Barlat, Y.H. Moon, M.G. Lee, (2010), p. 810

3. Deformation Texture and Plastic Anisotropy of AA6xxx at Warm Temperature, M. Ghosh, A. Miroux, J. Sidor and L. Kestens, *Proceedings of the 2009 TMS Annual Meeting & Exhibition*, eds. W. Yin, S. K. Das, and Z. Long (2009) p. 101.

4. An advanced Material Model for Aluminium Sheet Forming at Elevated Temperatures, S. Kukukuri, A. Miroux, M. Ghosh, A.H. van den Boogaard, *Computational Plasticity X - Fundamentals and Applications (COMPLAS 2009),* eds. E. Oñate, D.R.J. Owen and B. Suárez, (2009), p. (on CD ROM)

5. A Dislocation Based Constitutive Model for Warm Forming of Aluminium Sheet, S. Kukukuri, M. Ghosh and A.H. van den Boogaard, *Proceedings of 9th International Conference on Technology of Plasticity*, ed. D.Y. Yang (2008) p. 333.

6. Textural Changes After Warm Temperature Forming of AA6xxx, M. Ghosh, A. Miroux, R. Werkhoven, P.J. Bolt, J. Sidor and L. Kestens, *proceedings of the 11th International Conference on Aluminium Alloys*, eds. J. Hirsch, B. Skrotski and G. Gottstein, (2008), p. 782.

7. Changes in Deformation Texture and Plastic Anisotropy with Temperature for AA6016, M. Ghosh, A. Miroux and L. Kestens, *Proceedings of the International Symposium for Research Scholars on Metallurgy (ISRS-2008), (*2008), p. 165

Award Received

1. Prof. Dr. Ing.-Dr.Hc. Hans Wilfried Wagener Endowment Award for the paper entitled "Changes in deformation texture and plastic anisotropy with temperature for AA6016" in the conference *International Symposium for Research Scholars (ISRS-2008)*, held from 10 to 12 December 2008 at Indian Institute of Technology, Chennai, India.

CURRICULUM VITAE

Manojit Ghosh

Born December 21st, 1972 in Kolkata, India

Education

2004 – 2008	Doctor of Philosophy in Materials Science and Engineering department, Faculty of 3mE, Delft University of Technology, Delft, The Netherlands
	Thesis: *Microstructurally Controlled Mechanical Properties of Al-Mg-Si Alloys for Warm Forming Applications*
1996 – 1998	Master of Technology in Metallurgical Engineering department, Indian Institute of Technology, Kharagpur, India.
	Thesis: *Preparation of Copper-Tin compacts from a non-conventional warm compaction route*
1992 – 1996	Bachelor of Engineering in department of Metallurgy, Jadavpur University, Kolkata, India.
	Thesis: *Rationalization of process parameters of diamond cutting tools*

Work Experience

2008 - date	Assistant Professor, department of Metallurgy and Materials Engineering, Bengal Engineering and Science University, Shibpur, Howrah, India.
1998 – 2004	Lecturer, department of Metallurgy and Materials Engineering, Bengal Engineering and Science University, Shibpur, Howrah, India.
1998 – 1998	Management trainee, Ispat Profiles India, Pune, India